

**SYNTHESIS, CHARACTERIZATION, AND
ELECTROCHEMICAL PROPERTIES OF Ni(OH)₂-
BASED NANOSTRUCTURES**



**A Thesis Submitted in Partial Fulfillment of the Requirements for the
Degree of Doctor of Philosophy in Physics
Suranaree University of Technology
Academic Year 2018**

การสังเคราะห์ การศึกษาลักษณะเฉพาะและสมบัติทางไฟฟ้าเคมี
ของโครงสร้างนาโนกลุ่มนิกเกิลไฮดรอกไซด์



วิทยานิพนธ์นี้เป็นส่วนหนึ่งของการศึกษาตามหลักสูตรปริญญาวิทยาศาสตรดุษฎีบัณฑิต
สาขาวิชาฟิสิกส์
มหาวิทยาลัยเทคโนโลยีสุรนารี
ปีการศึกษา 2561

**SYNTHESIS, CHARACTERIZATION, AND
ELECTROCHEMICAL PROPERTIES OF Ni(OH)₂-BASED
NANOSTRUCTURES**

Suranaree University of Technology has approved this thesis submitted in partial fulfillment of the requirements for the Degree of Doctor of Philosophy.

Thesis Examining Committee



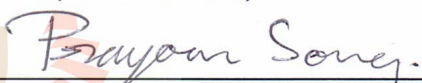
(Assoc. Prof. Dr. Sirichok Jungthawan)

Chairperson

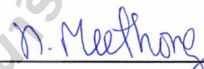


(Prof. Dr. Santi Maensiri)


Member (Thesis Advisor)


(Assoc. Prof. Dr. Prayoon Songsiriritthigul)


Member



(Asst. Prof. Dr. Nonglak Meethong)

Member


(Asst. Prof. Dr. Theeranun Siritanon)

Member


(Assoc. Prof. Capt. Dr. Kontorn Chamniprasart)


(Assoc. Prof. Dr. Worawat Meevasana)

Vice Rector for Academic Affairs
and Internationalization

Dean of Institute of Science

ทองสุข สิชชุมแสง : การสังเคราะห์ การศึกษาลักษณะเฉพาะและสมบัติทางไฟฟ้าเคมีของ
โครงสร้างนาโนกลุ่มนิกเกิลไฮดรอกไซด์ (SYNTHESIS, CHARACTERIZATION, AND
ELECTROCHEMICAL PROPERTIES OF Ni(OH)₂-BASED NANOSTRUCTURES)
อาจารย์ที่ปรึกษา : ศาสตราจารย์ ดร.สันติ แม้นศิริ, 247 หน้า

นิกเกิลไฮดรอกไซด์/วิธีไฮโดรเทอร์มอล/สมบัติทางไฟฟ้าเคมี/ค่าความจุเทียบ/ชั้นแพร่แก๊ส

ในงานวิจัยนี้ได้ทำการสังเคราะห์อนุภาคนาโน $M_xNi_{1-x}(OH)_2$ ($M = Mg, Mn, Cu, Zn, Bi$) ที่ $x = 0.00, 0.05, 0.10$ และ 0.15 ด้วยกระบวนการทางไฮโดรเทอร์มอล และได้ทำการศึกษาโครงสร้างผลึกและสมบัติทางไฟฟ้าเคมีของวัสดุ โครงสร้างนาโนที่สังเคราะห์ได้เหล่านี้ด้วยวิธีที่หลากหลาย ศึกษาลักษณะโครงสร้างผลึกด้วยเทคนิคการเลี้ยวเบนของรังสีเอ็กซ์ (XRD) ร่วมด้วยวิธี Rietveld refinement ศึกษาลักษณะโครงสร้างทางจุลภาคและลักษณะพื้นฐานวิทยาด้วยเทคนิคกล้องจุลทรรศน์อิเล็กตรอนแบบส่องกราด (SEM) และกล้องจุลทรรศน์อิเล็กตรอนแบบส่องผ่าน (TEM) ศึกษาองค์ประกอบทางเคมีและสถานะประจุด้วยเทคนิคโฟโตอิเล็กตรอน (XPS) และเทคนิคการดูดกลืนรังสีเอ็กซ์ (XAS) พื้นที่ผิวจำเพาะและความเป็นรูพรุนที่เกี่ยวข้องกับความสามารถในการกักเก็บประจุถูกวัดค่าด้วยเทคนิคการดูดซับแก๊ส สำหรับการศึกษาสมบัติทางไฟฟ้าเคมีถูกดำเนินการด้วยสามวิธีคือ โวลแทมเมตรี (CV) การชาร์จและดิสชาร์จโดยใช้กระแสคงที่ (GCD) และอิมพีแดนซ์เชิงไฟฟ้าเคมี (EIS)

ผลจากการศึกษาโครงสร้างผลึกด้วยเทคนิค XRD พบว่าการแทนที่ของไอออน $Mg^{2+}, Mn^{2+}, Cu^{2+}, Zn^{2+}$ และ Bi^{3+} ในตำแหน่งไอออนของ Ni^{2+} ส่งผลต่อโครงสร้างผลึก ซึ่งถูกยืนยันผลด้วยการวิเคราะห์แบบ Rietveld refinement เนื่องจากการเปลี่ยนแปลงของค่าแลตทิซพารามิเตอร์และปริมาตรยูนิตเซลล์ การศึกษาโครงสร้างจุลภาคด้วยภาพถ่าย TEM แสดงให้เห็นถึงลักษณะทางพื้นฐานวิทยาและขนาดของอนุภาคที่แตกต่างกันของรูปร่างเฮกซะโกนอลและบาร์ ซึ่งลักษณะที่แตกต่างกันนี้ขึ้นอยู่กับชนิดและปริมาณของสารเจือที่ถูแทนที่ในตำแหน่งของ Ni^{2+} ผลจากการวัดค่าพื้นที่ผิวจำเพาะด้วยเทคนิคการดูดซับแก๊สด้วยวิธี BET พบว่า พื้นที่ผิวจำเพาะอยู่ในช่วง 26-53 ตารางเมตรต่อกรัม โดยการเพิ่มขึ้นของพื้นที่ผิวจำเพาะเป็นผลมาจากการเพิ่มขึ้นของพื้นที่ผิวต่อปริมาตรในอนุภาคที่มีขนาดเล็กกว่า นอกจากนี้ การวิเคราะห์การกระจายตัวของรูพรุนด้วยวิธี BJH แสดงโครงสร้างแบบเมโซพอร์ส (mesoporous) และไมโครพอร์ส (microporous) ในสารตัวอย่างกลุ่มนิกเกิลไฮดรอกไซด์ สำหรับการศึกษาสมบัติทางไฟฟ้าเคมี โครงสร้างแบบไมโครพอร์สช่วยปรับปรุงค่าประสิทธิภาพความสามารถในการคายประจุ (cyclic stability) ซึ่งอาจเป็นผลมาจาก

ไอออนของอิเล็กโทรไลต์ถูกกัก (electrolyte ions confinement) อยู่ในวัสดุ นอกจากนี้ผลจากการศึกษาสมบัติทางไฟฟ้าเคมีด้วยเทคนิค CV พบว่าสารตัวอย่างกลุ่มนิกเกิลไฮดรอกไซด์กักเก็บประจุด้วยกระบวนการแทรกเข้าและแทรกออก (intercalation/deintercalation) ของไอออนของอิเล็กโทรไลต์ สารกลุ่มนิกเกิลไฮดรอกไซด์ที่ผ่านการเจือด้วย Mn^{2+} Cu^{2+} Zn^{2+} และ Bi^{3+} ด้วยปริมาณจำเพาะค่าหนึ่ง แสดงให้เห็นถึงการปรับปรุงค่าการกักเก็บประจุไฟฟ้าเคมีจำเพาะ ซึ่งค่าการกักเก็บประจุไฟฟ้าเคมีจำเพาะที่สูง ไม่สามารถอธิบายด้วยการเพิ่มขึ้นของระยะห่างระหว่างระนาบได้อย่างชัดเจน จากผลการทดลอง พบว่ามีสองแนวทางที่สามารถเพิ่มค่าการกักเก็บประจุไฟฟ้าเคมีจำเพาะของสารกลุ่มนิกเกิลไฮดรอกไซด์ คือ (i) การลดลงของขนาดอนุภาคเพื่อเพิ่มพื้นที่ในการทำปฏิกิริยา (ii) การลดลงของค่าความต้านทานการแลกเปลี่ยนประจุเพื่อส่งเสริมการเคลื่อนที่ของไอออนของอิเล็กโทรไลต์ที่เร็วขึ้น นอกจากนี้ กระบวนการกักเก็บประจุแบบคาปาซิทีฟ (capacitive) ที่โดดเด่นส่งผลให้เกิดการปรับปรุงค่าประสิทธิภาพความสามารถในการอัดและคายประจุ (cyclic stability) ในสารกลุ่มนิกเกิลไฮดรอกไซด์ ดังนั้น ข้อสังเกตที่ประดิษฐ์ขึ้นมีแนวโน้มในการนำไปประยุกต์ใช้งานด้านตัวเก็บประจุไฟฟ้าเคมียิ่งยวด



THONGSUK SICHUMSAENG : SYNTHESIS, CHARACTERIZATION,
AND ELECTROCHEMICAL PROPERTIES OF Ni(OH)₂-BASED
NANOSTRUCTURES. THESIS ADVISOR : PROF. SANTI MAENSIRI,
D.Phil. 247 PP.

NICKEL HYDROXIDE/HYDROTHERMAL METHOD/ELECTROCHEMICAL
PROPERTIES/PSEUDOCAPACITANCE/GAS DIFFUSION LAYER

In this research, M_xNi_{1-x}(OH)₂ (M = Mg, Mn, Cu, Zn, Bi) nanostructures with x = 0.00, 0.05, 0.10, and 0.15 were synthesized by a hydrothermal method. The crystal structure and electrochemical properties of the materials were studied by using several techniques. X-ray diffraction (XRD) technique including a Rietveld refinement was used for the structural analysis. The microstructure and morphology were investigated by scanning electron microscopy (SEM) and transmission electron microscopy (TEM) techniques. The chemical compositions and oxidation states were determined by X-ray photoelectron spectroscopy (XPS) and X-ray absorption spectroscopy (XANES) techniques. The specific surface area and their porosity which relate to the electrochemical performance were evaluated by gas adsorption technique. For the electrochemical studies, cyclic voltammetry (CV), galvanostatic charge discharge (GCD), and electrochemical impedance spectroscopy (EIS) were carried out.

The XRD results demonstrated that the substitutions of Mg²⁺, Mn²⁺, Cu²⁺, Zn²⁺, and Bi³⁺ ions in Ni²⁺ sites had influences on the structure which were confirmed by the Rietveld refinement due to the change of lattice parameters and unit cell volume. TEM images revealed the difference in morphologies and sizes of hexagonal and bar-like

shapes, depending on types and contents of the dopants that were substituted in Ni^{2+} sites. The specific surface area of the materials obtained from Brunauer-Emmett-Teller (BET) method was found to be in the range of 26-53 m^2/g . The higher specific surface area was due to the increase of surface-to-volume ratio in the smaller particle size. Furthermore, pore size distributions from Barrett-Joyner-Halendar (BJH) method presented the mesoporous and microporous structures in the samples. For the electrochemical studies, the microporous structure improved the cyclic stability. This is possibly due to the electrolyte ions confinement in the materials. In addition to the electrochemical studies, the CV analysis revealed the intercalation/deintercalation charge storage mechanism in all samples. The Mn, Cu, Zn, and Bi-doped $\text{Ni}(\text{OH})_2$ with the specific amount showed the improved specific capacitance value. The higher value could not clearly explain by the increased of the interlayer distance. Based on the experimental results, there are two approaches to enhance the specific capacitance values of $\text{Ni}(\text{OH})_2$ -based materials. (i) reducing the particle size providing the large active area. (ii) lowering the charge transfer resistance promoting the faster electrolyte ions transportation. In addition, the dominant capacitive charge storage mechanism resulted in the improved cyclic stability of $\text{Ni}(\text{OH})_2$ -based materials. Therefore, the $\text{M}_x\text{Ni}_{1-x}(\text{OH})_2$ electrodes are promising candidate for electrochemical capacitor applications.

ACKNOWLEDGEMENTS

I would like to express my deepest and sincere gratitude to my advisor, Prof. Dr. Santi Maensiri. None of this work would have been possible without his insightful guidance, advice, and help based upon his expert knowledge and experience. I would like to thank my thesis examination committee members, Assoc. Prof. Dr. Prayoon Songsiriritthigul, Asst. Prof. Dr. Nonglak Meethong, and Asst. Prof. Dr. Theeranun Siritanon for serving on my Ph.D. in reading and providing me with valuable comments.

I would like to thank all members and staffs in Advanced Materials Physics (AMP) Laboratory, the School of Physics, Institute of Science, Suranaree University of Technology, and Synchrotron Light Research Institute (SLRI) for all their help and friendship.

I gratefully acknowledge financial support to the Science Achievement Scholarship of Thailand (SAST) from Thai Government throughout the whole period of my Bachelor and Ph.D. study. Also, I would like to thank the SUT CoE on Advanced Functional Materials (SUT-AFM), Suranaree University of Technology for all supports.

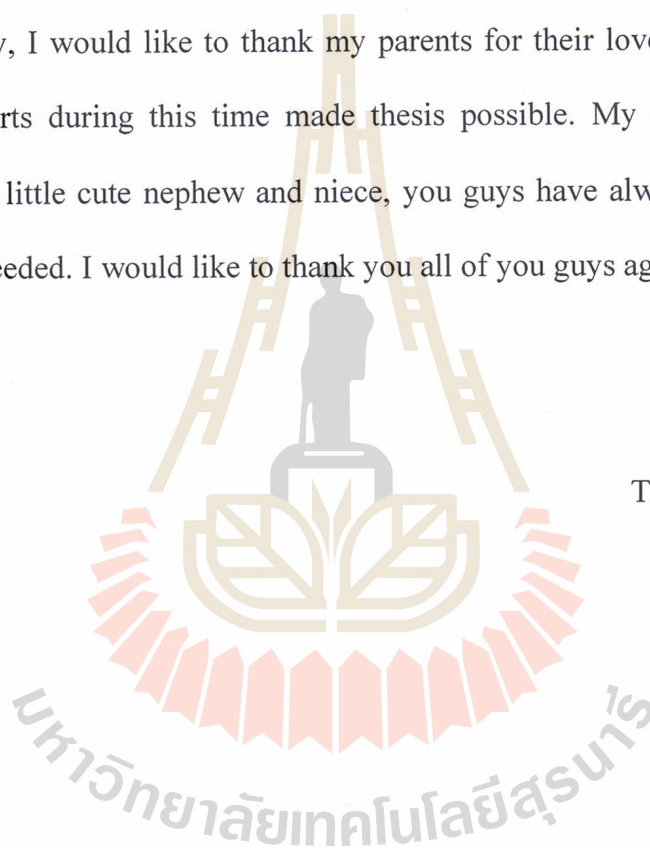
I would like to thank Dr. Wolfgang G. Zeier and his Materials by Design group members, Institute of Physical Chemistry, Justus-Liebig University Giessen, Germany for accepted me to work with his group as a visiting Ph.D. student. There was such an amazing experienced to work with you and your group. During my stay in Germany for

six months, there are many people that I would like to thank, especially Jan Peilstöcker for his help and taking care of me. Also, I would like to thank Florian Ostermaier for always standing by me during my tough time in Germany.

I would like to thank Dr. Jintara Padchasri, Dr. Unchista Wongpratrat, Dr. Benjaporn Yotburut, miss Suphawi Chaisit, miss Ornuma Kalawa, and miss Kwunta Siwawongkasem for their help and friendship during my Ph.D. study.

Finally, I would like to thank my parents for their love and all financial and mental supports during this time made thesis possible. My sister and my brother including my little cute nephew and niece, you guys have always been there for me whenever I needed. I would like to thank you all of you guys again from the bottom of my heart.

Thongsuk Sichumsaeng



CONTENTS

	Page
ABSTRACT IN THAI.....	I
ABSTRACT IN ENGLISH	III
ACKNOWLEDGEMENTS.....	V
CONTENTS.....	VII
LIST OF TABLES.....	XV
LIST OF FIGURES	XXII
LIST OF ABBREVIATIONS.....	XLIII
CHAPTER	
I INTRODUCTION.....	1
1.1 Background and significant of the study	1
1.2 Research objectives.....	3
1.3 Scope and Limitations of the study	3
1.4 Locations of the research.....	4
1.5 Skill and expertise	4
1.6 Dissertation structure.....	5
II LITERATURE REVIEWS.....	6
2.1 Basic of electrochemical capacitors	6
2.1.1 Conventional capacitor	7
2.2.2 Electrochemical capacitor	8

CONTENTS (Continued)

	Page
2.2.2.1 Electric double layer capacitors (EDLCs).....	9
2.2.2.2 Pseudocapacitors	11
2.2 Structure of Ni(OH) ₂	14
2.3 Electrochemical properties of Ni(OH) ₂	16
III RESEARCH METHODOLOGY	22
3.1 Synthesis of pure and M _x Ni _{1-x} (OH) ₂ nanostructures.....	22
3.2 Hydrothermal synthesis.....	25
3.3 Materials characterization	27
3.3.1 X-ray diffraction technique.....	27
3.3.1.1 Structural refinement.....	29
3.3.2 Electron microscopy technique.....	31
3.3.2.1 Scanning electron microscopy (SEM).....	31
3.3.2.2 Transmission Electron Microscopy (TEM).....	32
3.3.2.3 Energy dispersive X-ray spectroscopy (EDS).....	34
3.3.3 Gas adsorption technique.....	34
3.3.4 X-ray photoelectron spectroscopy technique.....	38
3.3.5 X-ray absorption spectroscopy technique	40
3.4 Electrochemical measurement.....	42
3.4.1 Cyclic voltammetry (CV)	44
3.4.1.1 Kinetic analysis for charge storage mechanism	46
3.4.2 Galvanostatic charge/discharge (GCD)	48

CONTENTS (Continued)

	Page
3.4.3 Electrochemical impedance spectroscopy (EIS).....	49
IV RESULTS AND DISCUSSION.....	54
4.1 Effects of various electrolytes on electrochemical properties of Ni(OH) ₂ nanostructures	54
4.1.1 Structural and morphology analysis.....	55
4.1.2 Surface analysis	59
4.1.3 Electrochemical study.....	60
4.1.3.1 Cyclic voltammetry	61
4.1.3.2 Galvanostatic charge/discharge	64
4.1.3.3 Electrochemical impedance spectroscopy	68
4.1.3.4 Cyclic stability.....	69
4.1.3.5 Energy density and power density.....	74
4.2 Electrochemical studies of Ni(OH) ₂ on GDL substrate	75
4.2.1 Electrode preparation of Ni(OH) ₂ on GDL substrate	77
4.2.2 Structural analysis of the prepared Ni(OH) ₂ working electrode.....	78
4.2.3 Microstructure and surface morphologies	80
4.2.4 Electrochemical study.....	81
4.2.4.1 Cyclic voltammetry	81
4.2.4.2 Kinetic analysis for charge storage mechanism	84
4.2.4.3 Galvanostatic charge/discharge	85

CONTENTS (Continued)

	Page
4.2.4.4 Electrochemical impedance spectroscopy.....	86
4.2.4.5 Cyclic stability.....	88
4.2.4.6 Energy density and power density.....	92
4.3 Effect of Mg-doped Ni(OH) ₂ on structure and electrochemical properties.....	93
4.3.1 Structural and morphology analysis.....	94
4.3.2 Chemical compositions and oxidation state analysis.....	103
4.3.3 Specific surface area and porosity analysis	104
4.3.4 Electrochemical study.....	107
4.3.4.1 Cyclic voltammetry	108
4.3.4.2 Kinetic analysis of charge storage mechanism.....	110
4.3.4.3 Galvanostatic charge/discharge	115
4.3.4.4 Electrochemical impedance spectroscopy.....	120
4.3.4.5 Cyclic stability.....	121
4.3.4.6 Energy density and power density.....	125
4.4 Effects of transition metals (Mn, Cu, and Zn) doped Ni(OH) ₂ on structure and electrochemical properties.....	127
4.4.1 Structural and morphology analysis.....	127
4.4.2 Chemical compositions and oxidation states analysis	147
4.4.3 Specific surface area and porosity analysis	152
4.4.4 Electrochemical study.....	158

CONTENTS (Continued)

	Page
4.4.4.1 Cyclic voltammetry	158
4.4.4.2 Kinetic analysis of charge storage mechanism.....	167
4.4.4.3 Galvanostatic charge/discharge test	170
4.4.4.4 Electrochemical impedance spectroscopy	177
4.4.4.5 Cyclic stability	181
4.4.4.6 Energy density and power density.....	183
4.5 Effects of Bi-doped Ni(OH) ₂ on structure and electrochemical properties.....	185
4.5.1 Structural and morphology analysis.....	185
4.5.2 Chemical compositions and oxidation state analysis.....	193
4.5.3 Specific surface area and porosity analysis	198
4.5.4 Electrochemical study	199
4.5.4.1 Cyclic voltammetry	200
4.5.4.2 Kinetic analysis of charge storage mechanism.....	201
4.5.4.3 Galvanostatic charge/discharge	205
4.5.4.4 Electrochemical impedance spectroscopy.....	209
4.5.4.5 Cyclic stability	210
4.5.4.6 Energy density and power density.....	211
V CONCLUSIONS AND SUGGESTIONS	213
5.1 Effect of various electrolytes on electrochemical properties of Ni(OH) ₂ -based nanostructures	213

CONTENTS (Continued)

	Page
5.2 Electrochemical studies of Ni(OH) ₂ on GDL substrate	214
5.3 Effects of Mg-doped Ni(OH) ₂ on structure and electrochemical properties.....	215
5.4 Effects of transition metals (Mn, Cu, Zn) doped Ni(OH) ₂ on structure and electrochemical properties.....	216
5.5 Effect of Bi-doped Ni(OH) ₂ on structure and electrochemical properties.....	217
5.6 Suggestions.....	218
REFERENCES	220
APPENDIX.....	244
CURRICULUM VITAE.....	247

LIST OF TABLES

Table	Page
2.1 A summary of the unit cell parameters of the two known phases Ni(OH) ₂ where $a = b$ and $\alpha = \beta$	15
2.2 List of reports on the specific capacitance value of metal doped β -Ni(OH) ₂	18
2.3 List of reports on morphology dependence electrochemical performance including specific capacitance (C_s) and capacitance retention of β -Ni(OH) ₂ obtained from various preparation methods.	19
3.1 List of starting materials used for the synthesis of Ni(OH) ₂ -based nanostructures, including their molecular weight (M_w), purity, and source.	24
3.2 Comparison of different powder synthesis method (Yoshimura and Byrappa, 2008).....	25.
3.3 Powder diffraction pattern as a function of various crystal structure, specimen, and instrumental parameters (Pecharsky and Zavalij, 2009).	29
3.4 List of adsorption/desorption isotherm types including their features.....	36
3.5 List of EIS definitions adapted from (Lisdar and Schäfer, 2008).	52
4.1 The summarized specific capacitance value of Ni(OH) ₂ electrodes as function of current density in various electrolytes.....	66
4.2 Bare ion size, radius of hydration sphere, ionic mobility and molar ionic conductivity of Na ⁺ and K ⁺ ions (Zhong <i>et al.</i> , 2015).	67

LIST OF TABLES (Continued)

Table	Page
4.3 The dependency of the capacitive and diffusion-controlled mechanisms at different scan rates.	85
4.4 The details of lattice parameter a and c , profile factor (R_p), weighted profile residual (R_{wp}), goodness of fit (GOF), unit cell volume, and crystal density obtained from the Rietveld refinement. The calculated d -spacing of (001), (100), and (101) planes and the calculated crystallite size from Scherrer's equation of $Mg_xNi_{1-x}(OH)_2$ samples with $x = 0.00$, 0.05, 0.10, and 0.15.	98
4.5 Specific surface area (S_{BET}), mean pore diameter (D_{MP}), total pore volume (V_T), mesopore diameter (D_{BJH}), mesopore volume (V_{BJH}), and BET particle size (d_{BET}), of $Mg_xNi_{1-x}(OH)_2$ samples.	106
4.6 The capacitive and diffusion contributions of $Mg_xNi_{1-x}(OH)_2$ samples determined from the oxidation peaks at different scan rates.	114
4.7 The summarized data obtained from the specific capacitance (F/g) and specific capacity (mAh/g) calculations.	119
4.8 The details of solution resistance (R_s), charge transferred resistance (R_{ct}), and the angle of vertical line with x -axis obtained from EIS measurement and cyclic stability and coulombic efficiency obtained from repeating GCD measurement at current density of 5 A/g for 1000 cycles in $Mg_xNi_{1-x}(OH)_2$ samples.	123

LIST OF TABLES (Continued)

Table	Page
4.9 The specific energies (E) and the specific power (P) of $\text{Mg}_x\text{Ni}_{1-x}(\text{OH})_2$ samples at various current densities.....	126
4.10 The details of lattice parameter a and c , profile factor (R_p), weighted profile residual (R_{wp}), goodness of fit (GOF), unit cell volume, and density obtained from the Rietveld refinement including the calculated d -spacing of (001), (100), and (101) planes and the calculated crystallite size from Scherrer's equation of $\text{Mn}_x\text{Ni}_{1-x}(\text{OH})_2$ samples with $x = 0.00$, 0.05, 0.10, and 0.15.....	133
4.11 The details of lattice parameter a and c , profile factor (R_p), weighted profile residual (R_{wp}), goodness of fit (GOF), unit cell volume, and density obtained from the Rietveld refinement including the calculated d -spacing of (001), (100), and (101) planes and the calculated crystallite size from Scherrer's equation of $\text{Cu}_x\text{Ni}_{1-x}(\text{OH})_2$ samples with $x = 0.00$, 0.05, 0.10, and 0.15.....	135
4.12 The details of lattice parameter a and c , profile factor (R_p), weighted profile residual (R_{wp}), goodness of fit (GOF), unit cell volume, and density obtained from the Rietveld refinement including the calculated d -spacing of (001), (100), and (101) planes and the calculated crystallite size from Scherrer's equation of $\text{Zn}_x\text{Ni}_{1-x}(\text{OH})_2$ samples with $x = 0.00$, 0.05, 0.10, and 0.15.....	137

LIST OF TABLES (Continued)

Table	Page
4.13 The summary of the average particle size for $\text{Mn}_x\text{Ni}_{1-x}(\text{OH})_2$, $\text{Cu}_x\text{Ni}_{1-x}(\text{OH})_2$, and $\text{Zn}_x\text{Ni}_{1-x}(\text{OH})_2$ samples with different Mn, Cu, and Zn doping contents.....	146
4.14 Specific surface area (S_{BET}), mean pore diameter (D_{MP}), total pore volume (V_{T}), mesopore diameter (D_{BJH}), mesopore volume (V_{BJH}), and BET particle size (d_{BET}) of $\text{Mn}_x\text{Ni}_{1-x}(\text{OH})_2$ samples.....	157
4.15 Specific surface area (S_{BET}), mean pore diameter (D_{MP}), total pore volume (V_{T}), mesopore diameter (D_{BJH}), mesopore volume (V_{BJH}), micropore diameter (D_{Micro}), and BET particle size (d_{BET}) of $\text{Cu}_x\text{Ni}_{1-x}(\text{OH})_2$ samples.	157
4.16 Specific surface area (S_{BET}), mean pore diameter (D_{MP}), total pore volume (V_{T}), mesopore diameter (D_{BJH}), mesopore volume (V_{BJH}), and BET particle size (d_{BET}) of $\text{Zn}_x\text{Ni}_{1-x}(\text{OH})_2$ samples.....	158
4.17 The specific capacitance of $\text{Mn}_x\text{Ni}_{1-x}(\text{OH})_2$ samples with various current densities.....	174
4.18 The specific capacitance of $\text{Cu}_x\text{Ni}_{1-x}(\text{OH})_2$ samples with various current densities.....	175
4.19 The specific capacitance of $\text{Zn}_x\text{Ni}_{1-x}(\text{OH})_2$ samples with various current densities.....	176

LIST OF TABLES (Continued)

Table	Page
4.20 The details of solution resistance (R_s), charge transferred resistance (R_{ct}), and the angle of inclined line with x -axis obtained from EIS measurement and the cyclic stability obtained from repeating GCD measurement at current density of 5 A/g for 1000 cycles in $Mn_xNi_{1-x}(OH)_2$ samples.	178
4.21 The details of solution resistance (R_s), charge transferred resistance (R_{ct}), and the angle of inclined line with x -axis obtained from EIS measurement and the cyclic stability obtained form repeating GCD measurement at current density of 5 A/g for 1000 cycles in $Cu_xNi_{1-x}(OH)_2$ samples.	179
4.22 The details of solution resistance (R_s), charge transferred resistance (R_{ct}), and the angle of inclined line with x -axis obtained from EIS measurement and the cyclic stability obtained from repeating GCD measurement at current density of 5 A/g for 1000 cycles in $Zn_xNi_{1-x}(OH)_2$ samples.....	180

LIST OF TABLES (Continued)

Table	Page
4.23 The details of lattice parameter a and c , profile factor (R_p), weighted profile residual (R_{wp}), goodness of fit (GOF), unit cell volume, and crystal density obtained from the Rietveld refinement including the calculated d -spacing of (001), (100), and (101) planes and the calculated crystallite size from Scherrer's equation of $\text{Bi}_x\text{Ni}_{1-x}(\text{OH})_2$ samples with $x = 0.00, 0.05, 0.10$, and 0.15	189
4.24 Specific surface area (S_{BET}), mean pore diameter (D_{MP}), total pore volume (V_T), mesopore diameter (D_{BJH}), mesopore volume (V_{BJH}), and BET particle size (d_{BET}) of $\text{Bi}_x\text{Ni}_{1-x}(\text{OH})_2$ samples.	199
4.25 The specific capacitance of $\text{Bi}_x\text{Ni}_{1-x}(\text{OH})_2$ samples with various current densities.....	208
4.26 The details of solution resistance (R_s), the inclined line angle with x -axis obtained from EIS measurement and the cyclic stability obtained from repeating GCD measurement at current density of 5 A/g for 1000 cycles of $\text{Bi}_x\text{Ni}_{1-x}(\text{OH})_2$ samples.	210

LIST OF FIGURES

Figure	Page
2.1 Schemetic illslution of the first low voltage electrolytic capacitor based on porous carbon (Adapetd from (Becker, 1957)).....	6
2.2 The plot between specific power against specific energy known as a Ragone plot for various electrical energy storage devices (Adapted from (Simon and Gogotsi, 2008)).....	8
2.3 Stern model of the electrical double-layer formed at a positively charged electrode in an aqueous electrolyte (Adapted from (Zhang and Zhao, 2009)).....	10
2.4 Different types of reversible redox mechanisms that give rise to pseudocapacitance: (a) underpotential deposition, (b) redox pseudocapacitance, and (c) intercalation pseudocapacitance (Adapted from (Augustyn <i>et al.</i> , 2014)).....	13
2.5 The crystal structure of β -Ni(OH) ₂ represented by (a) unit cell projection and (b) ball-and-stick unit cell of Ni ²⁺ (grey spheres), O ²⁻ (red spheres), and H ⁺ (pink spheres) (Hall <i>et al.</i> , 2015).....	14
2.6 The crystal structure of α -Ni(OH) ₂ represented by (a) unit cell projection and (b) ball-and-stick unit cell of Ni ²⁺ (grey spheres), OH ⁻ (red spheres), and H ₂ O (blue spheres) (Hall <i>et al.</i> , 2015).....	15

LIST OF FIGURES (Continued)

Figure	Page
2.7 Schematic illustration for the electrochemical processes of nickel hydroxide (Adapted from (Hall <i>et al.</i> , 2015)).....	16
2.8 (a) The CVs curve at a scan rate of 2 mV/s and (b) cycle performance at a galvanostatic current density of 1 A/g of the $\text{Al}_x\text{Ni}_{1-x}\text{LDH}$ electrode (Adapted from (Huang <i>et al.</i> , 2013)).....	17
2.9 Comparison (a) CV curves of $\beta\text{-Ni(OH)}_2$ nanoparticles of different sizes at a scan rate of 20 mV/s. (b) Discharge curves of $\beta\text{-Ni(OH)}_2$ nanoparticles at a current density of 1 A/g. (c) Slope region proportion for different sized Ni(OH)_2 nanoparticles in the total discharging region at current densities of 1 and 20 A/g, respectively. (d) Specific capacity of Ni(OH)_2 nanoparticles of different sizes as a function of the discharge current (Adapted from (Wang <i>et al.</i> , 2015)).....	21
3.1 Schematic overview of the synthesized $\text{M}_x\text{Ni}_{1-x}(\text{OH})_2$ nanostructures by a hydrothermal method.....	23
3.2 Schematic diagram of the mini-stainless steel autoclave and the Teflon container.....	26
3.3 (a) Schematic principle of XRD measurement of the materials and (b) the description of Bragg's diffraction law.....	27
3.4 The different typical signals in SEM technique consisting of secondary electrons, backscattered electrons, and X-rays elemental information.....	32

LIST OF FIGURES (Continued)

Figure	Page
3.5 The different typical signals in TEM technique including inelastic and elastic scattering, incoherent scattering, and transmitted electrons.	33
3.6 (a) Six types of isotherms and (b) four types of hysteresis loops according to IUPAC classification (Adapted from (Gregg and Sing, 1982)).	35
3.7 (a) Schematic principle of XPS measurement and (b) the photoelectric effect in XPS technique.	39
3.8 Schematic illustration of the XAS technique. (a) X-ray is absorbed by an electron in a core level followed by photoelectron emission and (b) Fluorescence X-ray.	40
3.9 Typically X-ray absorption spectrum with different regions of XANES and EXAFS.	41
3.10 A schematic illustration of X-ray absorption measurement of (a) Transmission mode and (b) Fluorescence mode.	41
3.11 An overview of the electrochemical workstation consisting of a computer, PSTAT/GSTAT, and electrochemical cell.	43
3.12 (a) The potential waveform is applied to the working electrode in the cyclic voltammetry and (b) a typical CV curve.	44
3.13 A schematic diagram of charge and discharge curve for an ideal electrochemical capacitor.	48

LIST OF FIGURES (Continued)

Figure	Page
3.14 Nyquist plot of a simple Randles equivalent circuit for an electrochemical cell.	51
4.1 XRD pattern of the synthesized Ni(OH) ₂ nanostructures.	56
4.2 (a-d) TEM bright field images, (e) the corresponding SAED diffraction pattern, and (f) the estimated nanoplates size of the synthesized Ni(OH) ₂ nanostructures.	56
4.3 Schematic illustration of the formation of porous Ni(OH) ₂ platelets.	57
4.4 (a) N ₂ adsorption/desorption isotherm and (b) the pore size distribution of Ni(OH) ₂ calculated from BET and BJH methods, respectively.	58
4.5 (a) The survey XPS spectrum and the high resolution XPS spectrum of (b) C 1s region, (c) O 1s region and (d) Ni 2p region of the Ni(OH) ₂ nanoplates.	60
4. 6 (a-d) CV curves of the Ni(OH) ₂ electrodes measured in different aqueous electrolytes and scan rate (mV/s).	62
4.7 (a-d) The plot between log (<i>i</i>) vs. log (<i>v</i>) of the Ni(OH) ₂ electrodes in 1M NaOH, 2M KOH and 1M KOH + 0.5M Na ₂ SO ₄ , respectively.	63
4.8 Comparison of CV curves of Ni(OH) ₂ electrodes measured at scan rate of 2 mV/s.	64

LIST OF FIGURES (Continued)

Figure	Page
4.9 (a) Comparison of charge and discharge curves measured at current density of 1 A/g and (b) the calculated specific capacitance obtained from the discharge curves of Ni(OH) ₂ electrodes.....	65
4.10 The calculated coulombic efficiency of Ni(OH) ₂ electrodes in various electrolytes.	67
4.11 (a) Nyquist plots and (b) Bode plots of Ni(OH) ₂ electrodes measured at the frequency range of 0.1 Hz to 100 kHz.	68
4.12 Comparison of capacitance retention of Ni(OH) ₂ electrodes measured in different electrolytes at 5 A/g for 1000 cycles.....	70
4.13 FE-SEM images and their corresponding EDS results of the Ni(OH) ₂ electrodes (a) before the electrochemical measurements and (b) after GCD test for 1000 cycles in 1M KOH and (c) 1M KOH + 0.5M Na ₂ SO ₄ electrolytes.	72
4.14 (a-c) FE-SEM images with different magnifications of the Ni(OH) ₂ electrodes after 1000 GCD cycles test at current density of 5 A/g in 1M NaOH electrolytes and (d-e) the corresponding EDS results of the Ni(OH) ₂ electrodes in different detected areas.	73
4.15 Ragone plots of Ni(OH) ₂ electrodes compared in various electrolytes.	75

LIST OF FIGURES (Continued)

Figure	Page
4.16 Schematic overview of (a) typical Ni-foam substrate adapted from (Li <i>et al.</i> , 2014) and (b) GDL substrate of non-woven straight carbon fibers type.....	77
4.17 Schematic representation for the electrode preparation of Ni(OH) ₂ on GDL substrate.	78
4.18 XRD patterns of (a) XRD holder, (b) bare GDL substrate, (c) powder Ni(OH) ₂ , and (d) the prepared working electrode.	79
4.19 FE-SEM images of (a) bare GDL substrate and (b-d) the prepared working electrode with different magnifications.	81
4.20 (a) Comparison CV curves of Ni foam and GDL substrate, (b) CV curves of Ni(OH) ₂ on GDL substrate at different scan rates, (c) the scan rate dependent of peaks current, and (d) the contribution of capacitive and diffusion-controlled mechanism.....	83
4.21 (a) Charge and discharge curves of Ni(OH) ₂ on GDL substrate at different current densities and (b) the calculated specific capacitance obtained from the discharge curves.	86
4.22 Nyquist plots of bare GDL and Ni(OH) ₂ on GDL substrate measured at the frequency range of 0.1 Hz to 100 kHz.	88

LIST OF FIGURES (Continued)

Figure	Page
4.23 The capacitance retention and coulombic efficiency of $\text{Ni}(\text{OH})_2$ on GDL substrate measured in 1M NaOH at current density of 5 A/g for 1000 cycles.....	89
4.24 (a-d) Surface morphologies and (e-f) the corresponding EDS spectra of $\text{Ni}(\text{OH})_2$ on GDL substrate after repeating GCD measurements for 1000 cycles.....	91
4.25 The schematic representation of (a) uncrack, (b) crack, and (c) severe crack on the electrode surface of $\text{Ni}(\text{OH})_2$ on GDL substrate.	92
4.26 The compared Ragone plot of $\text{Ni}(\text{OH})_2$ with the well-known Ragone plot of Kötz (Adapted from (Kötz and Carlen, 2000)).....	93
4.27 XRD patterns of $\text{Mg}_x\text{Ni}_{1-x}(\text{OH})_2$ samples with (a) $x = 0.00$, (b) $x = 0.05$, (c) $x = 0.10$, and (d) $x = 0.15$ and their corresponding enlarged view of the diffraction peaks in 2θ ranging from 18.5 to 20.0 degree.....	95
4.28 Rietveld refinement of $\text{Mg}_x\text{Ni}_{1-x}(\text{OH})_2$ samples with $x = 0.00, 0.05, 0.10$, and 0.15.....	97
4.29 (a) Lattice parameters a and c , (b) c/a ratio, (c) unit cell volume, and (d) crystallite size as function of Mg content (x) obtained from Rietveld refinement.	99

LIST OF FIGURES (Continued)

Figure	Page
4.30 TEM bright field images and their corresponding SAED patterns of $\text{Mg}_x\text{Ni}_{1-x}(\text{OH})_2$ samples with (a) $x = 0.00$, (b) $x = 0.05$, (c) $x = 0.10$, and (d) $x = 0.15$, respectively.	101
4.31 Lattice fringes from HRTEM of $\text{Mg}_x\text{Ni}_{1-x}(\text{OH})_2$ samples with (a) $x = 0.00$, $x = 0.05$, $x = 0.10$, and $x = 0.15$, respectively.	102
4.32 The average particle size of $\text{Mg}_x\text{Ni}_{1-x}(\text{OH})_2$ samples with $x = 0.00$, 0.05 , 0.10 , and 0.15	103
4.33 (a) The survey XPS spectra and (b) the high resolution XPS spectra in Mg 2s region of $\text{Mg}_x\text{Ni}_{1-x}(\text{OH})_2$ samples with $x = 0.00$, 0.05 , 0.10 , and 0.15	104
4.34 (a) N_2 adsorption/desorption isotherms and (b) pore size distribution of $\text{Mg}_x\text{Ni}_{1-x}(\text{OH})_2$ samples with $x = 0.00$, 0.05 , 0.10 , and 0.15 , respectively. ..	105.
4.35 CV curves of $\text{Mg}_x\text{Ni}_{1-x}(\text{OH})_2$ samples with (a) $x = 0.00$, (b) $x = 0.05$, (c) $x = 0.10$, and (d) $x = 0.15$ at different scan rates of 1, 2, 3, 4, 5, 10, and 20 mV/s.	109
4.36 Comparison CV curves of $\text{Mg}_x\text{Ni}_{1-x}(\text{OH})_2$ samples at scan rates of 2 mV/s.	110
4.37 The scan rate dependence of peaks current of $\text{Mg}_x\text{Ni}_{1-x}(\text{OH})_2$ samples at different scan rates of 1, 2, 3, 4, 5, 10, and 20 mV/s.	111

LIST OF FIGURES (Continued)

Figure	Page
4.38 Dependence of b -values obtained from oxidation and reduction process as function of Mg content (x).....	111
4.39 The contributions from capacitive and diffusion process varying with scan rates in $\text{Mg}_x\text{Ni}_{1-x}(\text{OH})_2$ samples.....	112
4.40 The relative contributions of capacitive and diffusion-controlled mechanisms at scan rate of 1 mV/s of $\text{Mg}_x\text{Ni}_{1-x}(\text{OH})_2$ samples.	115
4.41 GCD curves at different current densities of $\text{Mg}_x\text{Ni}_{1-x}(\text{OH})_2$ with (a) $x = 0.00$, (b) $x = 0.05$, (c) $x = 0.10$, and (d) $x = 0.15$	116
4.42 (a) The comparison of GCD curves and (b) their corresponding IR drop at current density of 1 A/g in $\text{Mg}_x\text{Ni}_{1-x}(\text{OH})_2$ samples.	117
4.43 The calculated specific capacitance as function of current density in $\text{Mg}_x\text{Ni}_{1-x}(\text{OH})_2$ samples.	118
4.44 Nyquist plots of $\text{Mg}_x\text{Ni}_{1-x}(\text{OH})_2$ samples measured at the frequency range of 0.1 Hz to 100 kHz. Inset shows an enlarged view of Nyquist plots.....	120
4.45 Comparison of (a) capacitance retention and (b) coulombic efficiency as function of cycle number of $\text{Mg}_x\text{Ni}_{1-x}(\text{OH})_2$ samples measured at current density of 5 A/g for 1000 cycles.....	122
4.46 Comparison of Nyquist plot before and after the GCD measurement at current density of 5 A/g for 1000 cycles in sample of $x = 0.05$	124

LIST OF FIGURES (Continued)

Figure	Page
4.47 Comparison of Nyquist plot before and after the GCD measurement at current density of 5 A/g for 1000 cycles in sample of $x = 0.15$. Number 1 and 2 indicate the presence of two semicircles in the sample.....	124
4.48 (a) The Ragone plot of $\text{Mg}_x\text{Ni}_{1-x}(\text{OH})_2$ samples and (b) the comparison of Ragone plot of $\text{Mg}_x\text{Ni}_{1-x}(\text{OH})_2$ samples with a well-known Ragone plot of Kötzt (Kotz and Carlen, 2000).	125
4.49 XRD patterns of $\text{Mn}_x\text{Ni}_{1-x}(\text{OH})_2$ samples with (a) $x = 0.00$, (b) $x = 0.05$, (c) $x = 0.10$, and (d) $x = 0.15$ and their corresponding enlarged view of the diffraction peaks in 2θ ranging from 18.5 to 20.0 degree.....	128
4.50 XRD patterns of $\text{Cu}_x\text{Ni}_{1-x}(\text{OH})_2$ samples with (a) $x = 0.00$, (b) $x = 0.05$, (c) $x = 0.10$, and (d) $x = 0.15$ and their corresponding enlarged view of the diffraction peaks in 2θ ranging from 18.5 to 20.0 degree.....	128
4.51 XRD patterns of $\text{Zn}_x\text{Ni}_{1-x}(\text{OH})_2$ samples with (a) $x = 0.00$, (b) $x = 0.05$, (c) $x = 0.10$, and (d) $x = 0.15$ and their corresponding enlarged view of the diffraction peaks in 2θ ranging from 18.5 to 20.0 degree.....	129
4.52 Rietveld refinement of $\text{Mn}_x\text{Ni}_{1-x}(\text{OH})_2$ samples with $x = 0.00, 0.05, 0.10$, and 0.15.....	132
4.53 Rietveld refinement of $\text{Cu}_x\text{Ni}_{1-x}(\text{OH})_2$ samples with $x = 0.00, 0.05, 0.10$, and 0.15.....	134

LIST OF FIGURES (Continued)

Figure	Page
4.54 Rietveld refinement of $\text{Zn}_x\text{Ni}_{1-x}(\text{OH})_2$ samples with $x = 0.00, 0.05, 0.10,$ and 0.15	136
4.55 (a) Lattice parameter a , (b) Lattice parameter c , (c) c/a ratio, and unit cell volume obtained from the Rietveld refinement. (e) The calculated crystallite size as function of Mn, Cu, and Zn content (x) obtained from Scherer's equation.....	138
4.56 TEM bright field images and their corresponding SAED patterns of $\text{Mn}_x\text{Ni}_{1-x}(\text{OH})_2$ samples with (a) $x = 0.00$, (b) $x = 0.05$, (c) $x = 0.10$, and (d) $x = 0.15$, respectively.	142
4.57 TEM bright field images, lattice fringes and their corresponding SAED patterns of $\text{Cu}_x\text{Ni}_{1-x}(\text{OH})_2$ samples with (a) $x = 0.00$, (b) $x = 0.05$, (c) $x = 0.10$, and (d) $x = 0.15$, respectively.	143
4.58 TEM bright field images and their corresponding SAED patterns of $\text{Zn}_x\text{Ni}_{1-x}(\text{OH})_2$ samples with (a) $x = 0.00$, (b) $x = 0.05$, (c) $x = 0.10$, and (d) $x = 0.15$, respectively.	144
4.59 The average particle size of $\text{Mn}_x\text{Ni}_{1-x}(\text{OH})_2$ samples as function of Mn content (x).	145
4.60 The average particle size of $\text{Cu}_x\text{Ni}_{1-x}(\text{OH})_2$ samples as function of Cu content (x).	145

LIST OF FIGURES (Continued)

Figure	Page
4.61 The average particle size for $\text{Zn}_x\text{Ni}_{1-x}(\text{OH})_2$ samples as function of Zn content (x).	146
4.62 The survey XPS spectrum of $\text{Mn}_x\text{Ni}_{1-x}(\text{OH})_2$ samples with (a) $x = 0.00$, (b) $x = 0.05$, (c) $x = 0.10$, and (d) $x = 0.15$	147
4.63 The survey XPS spectrum of $\text{Cu}_x\text{Ni}_{1-x}(\text{OH})_2$ samples with (a) $x = 0.00$, (b) $x = 0.05$, (c) $x = 0.10$, and (d) $x = 0.15$	148
4.64 The survey XPS spectrum of $\text{Zn}_x\text{Ni}_{1-x}(\text{OH})_2$ samples with (a) $x = 0.00$, (b) $x = 0.05$, (c) $x = 0.10$, and (d) $x = 0.15$	148
4.65 XANES spectra including pre-edge (region I) and white line region (region III) of Zn-doped $\text{Ni}(\text{OH})_2$ at Ni K-edge measured in transmission mode.	150
4.66 The first derivative plots of Zn-doped $\text{Ni}(\text{OH})_2$ at Ni K-edge measured in transmission mode.	151
4.67 XANES spectra of Zn-doped $\text{Ni}(\text{OH})_2$ samples at Zn K-edge measured in fluorescence mode.	151
4.68 The first derivative plots of Zn-doped $\text{Ni}(\text{OH})_2$ at Zn K-edge measured in transmission mode.	152

LIST OF FIGURES (Continued)

Figure	Page
4.69 (a, c, e) N ₂ adsorption/desorption isotherm and (b, d, f) the pore size distribution of Mn _x Ni _{1-x} (OH) ₂ , Cu _x Ni _{1-x} (OH) ₂ , and Zn _x Ni _{1-x} (OH) ₂ samples calculated from BET and BJH methods, respectively. The inset indicates the presence of hysteresis loops and micropore distributions.	155
4.70 Schematic representation of the decrease of mean pore diameter (D_{mp}) and total pore volume (V_T) after Cu doping	156
4.71 (a, c, e, g) CV curves and (b, d, f, h) their scan rate dependent of peaks current of Mn _x Ni _{1-x} (OH) ₂ samples with x = 0.00, 0.05, 0.10, and 0.15, respectively.	161
4.72 (a, c, e, g) CV curves and (b, d, f, h) their scan rate dependent of peaks current of Cu _x Ni _{1-x} (OH) ₂ samples with x = 0.00, 0.05, 0.10, and 0.15, respectively.	162
4.73 (a, c, e, g) CV curves and (b, d, f, h) their scan rate dependent of peaks current of Zn _x Ni _{1-x} (OH) ₂ samples with x = 0.00, 0.05, 0.10, and 0.15, respectively.	163
4.74 Comparison CV curves of Mn _x Ni _{1-x} (OH) ₂ samples at scan rates of 2 mV/s.....	164
4.75 Comparison CV curves of Cu _x Ni _{1-x} (OH) ₂ samples at scan rates of 2 mV/s.....	164

LIST OF FIGURES (Continued)

Figure	Page
4.76 Comparison CV curves of $\text{Zn}_x\text{Ni}_{1-x}(\text{OH})_2$ samples at scan rates of 2 mV/s.....	165
4.77 Dependence of b -values obtained from oxidation and reduction process as function of Mn content (x).....	165
4.78 Dependence of b -values obtained from oxidation and reduction process as function of Cu content (x).	166
4.79 Dependence of b -values obtained from oxidation and reduction process as function of Zn content (x).....	166
4.80 The relative contributions of capacitive and diffusion-controlled mechanisms at scan rate of 1 mV/s in $\text{Mn}_x\text{Ni}_{1-x}(\text{OH})_2$ samples.....	168
4.81 The relative contributions of capacitive and diffusion-controlled mechanisms at scan rate of 1 mV/s in $\text{Cu}_x\text{Ni}_{1-x}(\text{OH})_2$ samples.	169
4.82 The relative contributions of capacitive and diffusion-controlled mechanisms at scan rate of 1 mV/s in $\text{Zn}_x\text{Ni}_{1-x}(\text{OH})_2$ samples.....	169
4.83 (a) Comparison of GCD curves at current density of 1 A/g and (b) their corresponding IR drop of $\text{Mn}_x\text{Ni}_{1-x}(\text{OH})_2$ samples.	171
4.84 (a) Comparison of GCD curves at current density of 1 A/g and (b) their corresponding IR drop of $\text{Cu}_x\text{Ni}_{1-x}(\text{OH})_2$ samples.....	171
4.85 (a) Comparison of GCD curves at current density of 1 A/g and (b) their corresponding IR drop of $\text{Zn}_x\text{Ni}_{1-x}(\text{OH})_2$ samples.	172

LIST OF FIGURES (Continued)

Figure	Page
4.86 The calculated specific capacitance as function of current density in $\text{Mn}_x\text{Ni}_{1-x}(\text{OH})_2$ samples.	174
4.87 The calculated specific capacitance as function of current density in $\text{Cu}_x\text{Ni}_{1-x}(\text{OH})_2$ samples.	175
4.88 The calculated specific capacitance as function of current density in $\text{Zn}_x\text{Ni}_{1-x}(\text{OH})_2$ samples.....	176
4.89 Nyquist plots of $\text{Mn}_x\text{Ni}_{1-x}(\text{OH})_2$ samples measured at the frequency range of 0.1 Hz to 100 kHz. Enlarged views of Nyquist plot showing the solution resistance (R_s) and charge transfer resistance (R_{ct}).	178
4.90 Nyquist plots of $\text{Cu}_x\text{Ni}_{1-x}(\text{OH})_2$ samples measured at the frequency range of 0.1 Hz to 100 kHz. Enlarged views of Nyquist plot showing the solution resistance (R_s) and charge transfer resistance (R_{ct}).	179
4.91 Nyquist plots of $\text{Zn}_x\text{Ni}_{1-x}(\text{OH})_2$ samples measured at the frequency range of 0.1 Hz to 100 kHz. Enlarged views of Nyquist plot showing the solution resistance (R_s) and charge transfer resistance (R_{ct}).	180
4.92 Comparison of capacitance retention as function of cycle number for $\text{Mn}_x\text{Ni}_{1-x}(\text{OH})_2$ samples measured at current density of 5 A/g for 1000 cycles.....	182

LIST OF FIGURES (Continued)

Figure	Page
4.93 Comparison of capacitance retention as function of cycle number for $\text{Cu}_x\text{Ni}_{1-x}(\text{OH})_2$ samples measured at current density of 5 A/g for 1000 cycles.....	182
4.94 Comparison of capacitance retention as function of cycle number for $\text{Zn}_x\text{Ni}_{1-x}(\text{OH})_2$ samples measured at current density of 5 A/g for 1000 cycles.....	183
4.95 (a) The Ragone plot of $\text{Mn}_x\text{Ni}_{1-x}(\text{OH})_2$ samples and (b) the comparison of Ragone plot of $\text{Mn}_x\text{Ni}_{1-x}(\text{OH})_2$ samples with a well-known Ragone plot of Kötzt (Kötzt and Carlen, 2000).	184
4.96 (a) The Ragone plot of $\text{Cu}_x\text{Ni}_{1-x}(\text{OH})_2$ samples and (b) the comparison of Ragone plot of $\text{Cu}_x\text{Ni}_{1-x}(\text{OH})_2$ samples with a well-known Ragone plot of Kötzt (Kötzt and Carlen, 2000).	184
4.97 (a) The Ragone plot of $\text{Zn}_x\text{Ni}_{1-x}(\text{OH})_2$ samples and (b) the comparison of Ragone plot of $\text{Zn}_x\text{Ni}_{1-x}(\text{OH})_2$ samples with a well-known Ragone plot of Kötzt (Kötzt and Carlen, 2000).	185
4.98 XRD patterns of $\text{Bi}_x\text{Ni}_{1-x}(\text{OH})_2$ samples with (a) $x = 0.00$, (b) $x = 0.05$, (c) $x = 0.10$, and (d) $x = 0.15$ and their corresponding enlarged view of the diffraction peaks in 2θ ranging from 17 to 21 degree.....	186
4.99 Rietveld refinement of $\text{Bi}_x\text{Ni}_{1-x}(\text{OH})_2$ samples with $x = 0.00, 0.05, 0.10$, and 0.15	187.

LIST OF FIGURES (Continued)

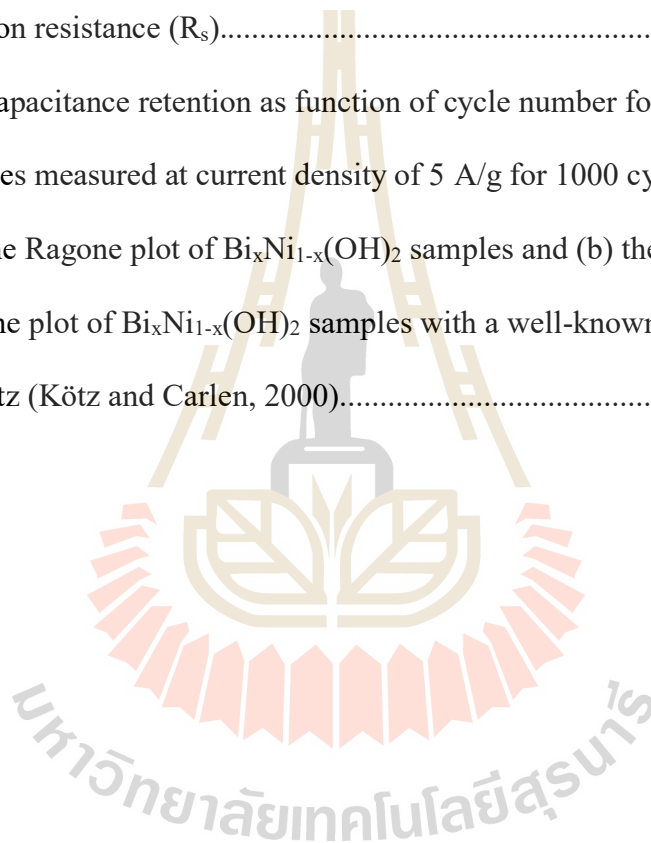
Figure	Page
4.100 (a) Lattice parameters a and c , (b) c/a ratio, (c) unit cell volume, and (d) crystallite size as function of Bi content (x).	190
4.101 TEM bright field images and their corresponding SAED patterns of $\text{Bi}_x\text{Ni}_{1-x}(\text{OH})_2$ samples with (a) $x = 0.00$, (b) $x = 0.05$, (c) $x = 0.10$, and (d) $x = 0.15$, respectively.	192
4.102 The average particles size of $\text{Bi}_x\text{Ni}_{1-x}(\text{OH})_2$ samples as a function of Bi content (x).	193
4.103 The survey XPS spectrum of $\text{Bi}_x\text{Ni}_{1-x}(\text{OH})_2$ samples with different Bi content of $x = 0.00$, (b) $x = 0.05$, (c) $x = 0.10$, and (d) $x = 0.15$	194
4.104 The normalized XANES spectra including pre-edge (region I) and white line region (region III) of Bi-doped $\text{Ni}(\text{OH})_2$ at Ni K-edge measured in transmission mode.	196
4.105 The first derivative plots of Bi-doped $\text{Ni}(\text{OH})_2$ at Ni K-edge measured in transmission mode.	196
4.106 The normalized XANES spectra including pre-edge (region I) and white line region (region III) of Bi-doped $\text{Ni}(\text{OH})_2$ samples at Bi M_5 -edge measured in fluorescence mode.	197
4.107 The first derivative plots of Bi-doped $\text{Ni}(\text{OH})_2$ at Bi M_5 -edge measured in transmission mode.	197

LIST OF FIGURES (Continued)

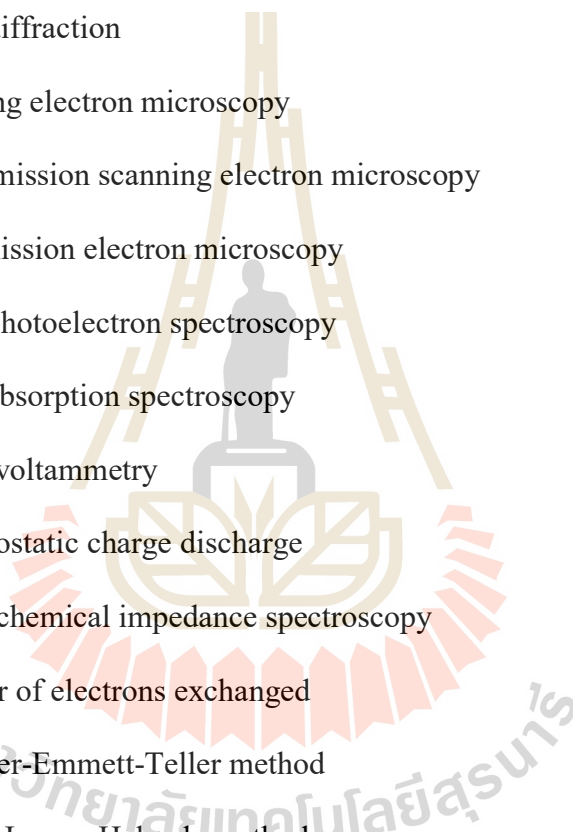
Figure	Page
4.108 (a) N ₂ adsorption/desorption isotherm and (b) the pore size distribution of Bi _x Ni _{1-x} (OH) ₂ samples calculated from BET and BJH methods, respectively.	199
4.109 (a, c, e, g) CV curves and (b, d, f, h) their scan rate dependent of peaks current of Bi _x Ni _{1-x} (OH) ₂ samples with x = 0.00, 0.05, 0.10, and 0.15, respectively.	202
4.110 Comparison CV curves of Bi _x Ni _{1-x} (OH) ₂ samples at scan rates of 2 mV/s...203	203
4.111 Dependence of b-values obtained from oxidation and reduction process as function of Bi content (x).	203
4.112 The relative contribution of capacitive and diffusion-controlled mechanisms at scan rate of 1 mV/s in Bi _x Ni _{1-x} (OH) ₂ samples.	204
4.113 (a) Comparison of GCD curves at current density of 1 A/g and (b) their corresponding IR drop of Bi _x Ni _{1-x} (OH) ₂ samples.....	206
4.114 The calculated specific capacitance as function of current density in Bi _x Ni _{1-x} (OH) ₂ samples.	206.
4.115 (a) The GCD curves of Bi _x Ni _{1-x} (OH) ₂ with x = 0.10 at different current densities and (d) the corresponding IR drop of all Bi _x Ni _{1-x} (OH) ₂ samples as function of a current density.	207.

LIST OF FIGURES (Continued)

Figure	Page
4.116 Nyquist plots of $\text{Bi}_x\text{Ni}_{1-x}(\text{OH})_2$ samples measured at the frequency range of 0.1 Hz to 100 kHz. Enlarged views of Nyquist plot showing the solution resistance (R_s).....	209
4.117 The capacitance retention as function of cycle number for $\text{Bi}_x\text{Ni}_{1-x}(\text{OH})_2$ samples measured at current density of 5 A/g for 1000 cycles.....	211
4.118 (a) The Ragone plot of $\text{Bi}_x\text{Ni}_{1-x}(\text{OH})_2$ samples and (b) the comparison of Ragone plot of $\text{Bi}_x\text{Ni}_{1-x}(\text{OH})_2$ samples with a well-known Ragone plot of Kötz (Kötz and Carlen, 2000).....	212



LIST OF ABBREVIATIONS



ECs	Electrochemical capacitors
EDLCs	Electrical double layer capacitors
XRD	X-ray diffraction
SEM	Scanning electron microscopy
FE-SEM	Field emission scanning electron microscopy
TEM	Transmission electron microscopy
XPS	X-ray photoelectron spectroscopy
XAS	X-ray absorption spectroscopy
CV	Cyclic voltammetry
GCD	Galvanostatic charge discharge
EIS	Electrochemical impedance spectroscopy
NEE	Number of electrons exchanged
BET	Brunauer-Emmett-Teller method
BJH	Barrett-Joyner-Halenda method
XANES	X-ray near edge structure
EXAFS	Extended X-ray absorption fine structure
CB	Carbon black
PVDF	Polyvinylidene difluoride
NMP	N-methyl pyrrolidone
OER	Oxygen evolution reaction

CHAPTER I

INTRODUCTION

1.1 Background and significant of the study

Recently, electrochemical capacitors (ECs) also known as supercapacitors or ultracapacitors have attracted increasing attention as one of the energy storage devices due to their high power density, long cycle life, and low maintenance cost (Wu *et al.*, 2015; Lang *et al.*, 2011). Basically, ECs can be classified into two types based on their energy storage mechanisms that are electrical double layer capacitors (EDLCs) and pseudocapacitors.

EDLCs store energy based on the reversible adsorption/desorption of ions at the interface between the electrolyte and electrode materials (Liu *et al.*, 2015; Merlet *et al.*, 2012). On the other hand, pseudocapacitors or redox supercapacitors store energy from a fast and reversible surface or near surface reactions of the electrode materials (Simon and Gogotsi, 2008). There are three different types of pseudocapacitive mechanisms those are (i) underpotential deposition, (ii) surface redox reaction, and (iii) intercalation reaction (Augustyn *et al.*, 2014; Sankar *et al.*, 2015). For nanostructured layered metal hydroxides, the specific capacitance arises generally from the intercalation/deintercalation process because of the several nanometers of interlayer spacing of the hydroxides that allow the electrolyte ions to move into and out of the electrode matrix (Yin and Tang, 2016). Nickel hydroxide (Ni(OH)_2) is known as a

layered structure pseudocapacitive material which is interesting for electrochemical applications because of its low cost, easy processing, and its high theoretical specific capacitance value within the potential window of about 0.5 V (Singh *et al.*, 2014; Ji *et al.*, 2013).

Generally, Ni(OH)_2 can be identified into two phases known as β and α crystal structure. The electrochemical performance of $\alpha\text{-Ni(OH)}_2$ was reported to be higher than the β -phase. However, the $\alpha\text{-Ni(OH)}_2$ materials were never used in practical applications because of their long-term cyclic stability problem and the unstable phase of $\alpha\text{-Ni(OH)}_2$ (Audemer *et al.*, 1997). From this point of view, improving the electrochemical performances of $\beta\text{-Ni(OH)}_2$, especially in terms of specific capacitance and cyclic stability, are focused on the present work. The electrochemical performances of $\beta\text{-Ni(OH)}_2$ were found to be significantly improved by substitution of nickel ions by other metal ions (Huang *et al.*, 2013; Ramesh and Kamath, 2008). However, there are a few works that have been reported on improving the electrochemical performance of the $\beta\text{-Ni(OH)}_2$ by metal ions substitution and the electrochemical mechanism has not been clearly understood yet.

In this research, $\text{M}_x\text{Ni}_{1-x}(\text{OH})_2$ nanostructures (M = Mg, Mn, Cu, Zn, and Bi) with different contents of $x = 0.00, 0.05, 0.10$, and 0.15 were synthesized by a hydrothermal process. The crystal structure and morphology of the synthesized $\text{M}_x\text{Ni}_{1-x}(\text{OH})_2$ were characterized by X-ray diffraction (XRD), scanning electron microscopy (SEM), and transmission electron microscopy (TEM). The specific surface area and porosity of the synthesized $\text{M}_x\text{Ni}_{1-x}(\text{OH})_2$ were examined by nitrogen gas absorption technique. The surface chemical compositions and oxidation state were determined by X-ray photoelectron spectroscopy (XPS) and X-ray absorption

spectroscopy (XAS) techniques. For electrochemical studies of the synthesized $M_xNi_{1-x}(OH)_2$, three well-known techniques including cyclic voltammetry (CV), galvanostatic charge discharge (GCD) and electrochemical impedance spectroscopy (EIS) were carried out.

1.2 Research objectives

1.2.1 To synthesize the $M_xNi_{1-x}(OH)_2$ ($M = Mg, Mn, Cu, Zn, \text{ and } Bi$) nanostructures for $x = 0.00, 0.05, 0.10, \text{ and } 0.15$ by a hydrothermal process.

1.2.2 To characterize the synthesized $M_xNi_{1-x}(OH)_2$ ($M = Mg, Mn, Cu, Zn, \text{ and } Bi$) nanostructures.

1.2.3 To study the electrochemical properties of $M_xNi_{1-x}(OH)_2$ ($M = Mg, Mn, Cu, Zn, \text{ and } Bi$) nanostructures.

1.3 Scope and Limitations of the study

1.3.1 This study focuses on the synthesis of $M_xNi_{1-x}(OH)_2$ ($M = Mg, Mn, Cu, Zn, \text{ and } Bi$) nanostructures for $x = 0.00, 0.05, 0.10, \text{ and } 0.15$ by using a hydrothermal process.

1.3.2 The hydrothermal process was carried out only at $160\text{ }^{\circ}\text{C}$ for 20 h.

1.3.3 Study of structure, morphology and phase composition of the synthesized $M_xNi_{1-x}(OH)_2$ ($M = Mg, Mn, Cu, Zn, \text{ and } Bi$) nanostructures by using the XRD, SEM, and TEM techniques.

1.3.4 Study of surface chemical compositions and oxidation state of the synthesized $M_xNi_{1-x}(OH)_2$ ($M = Mg, Mn, Cu, Zn, \text{ and } Bi$) nanostructures by using XPS and XAS techniques.

1.3.5 Investigation of the electrochemical properties of the doping Ni(OH)_2 with Mg, Mn, Cu, Zn, and Bi electrodes via CV, GCD and EIS techniques and compared with those of the pure Ni(OH)_2 .

1.4 Locations of the research

1.4.1 Advanced Materials Physics (AMP) laboratory, School of Physics, Institute of Science, Suranaree University of Technology, Nakhon Ratchasima, 30000, Thailand.

1.4.2 The Center for Scientific and Technological Equipment, Suranaree University of Technology, Nakhon Ratchasima, 30000, Thailand.

1.4.3 Synchrotron Light Research Institute (Public Organization), Nakhon Ratchasima, 30000, Thailand.

1.4.4 Research Instrument Center, Khon Kaen University, Khon Kaen, 40002, Thailand.

1.5 Skill and expertise

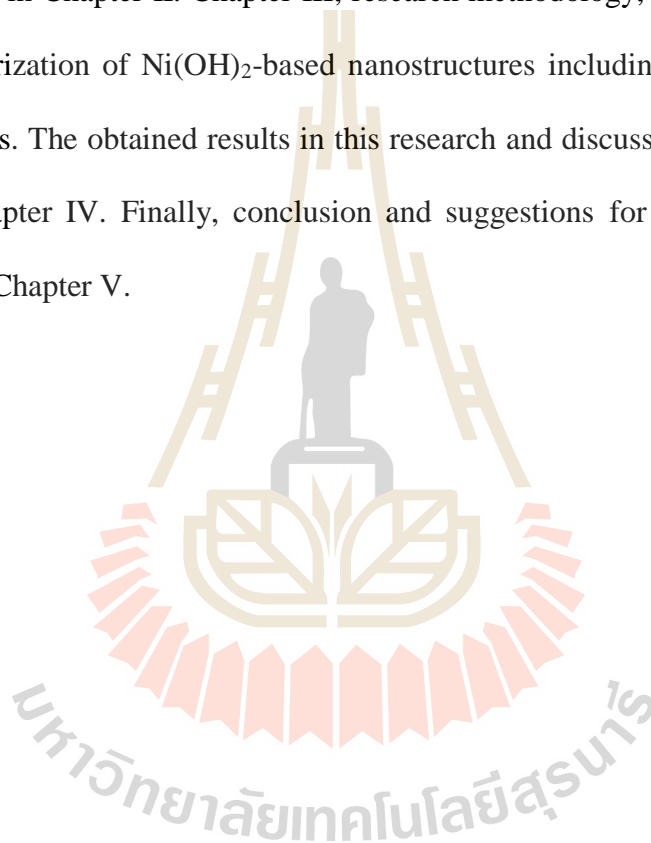
1.5.1 Skill and expertise from synthesis and characterization of the Ni(OH)_2 -based nanostructures.

1.5.2 Understanding of the electrochemical mechanism and properties of Ni(OH)_2 -based nanostructures.

1.5.3 Publications in International ISI journals.

1.6 Dissertation structure

This dissertation is divided into five chapters. The introduction chapter including an overview of this research is given in Chapter I. Reviews of the literature which is relevant to this research, including basic of electrochemical capacitors, structure of Ni(OH)_2 , and the electrochemical properties of Ni(OH)_2 -based materials are presented in Chapter II. Chapter III, research methodology, presents the synthesis and characterization of Ni(OH)_2 -based nanostructures including the electrochemical measurements. The obtained results in this research and discussions of the results are given in Chapter IV. Finally, conclusion and suggestions for the future works are described in Chapter V.



CHAPTER II

LITERATURE REVIEWS

2.1 Basic of electrochemical capacitors

Electrochemical capacitors, also known as ultracapacitors or supercapacitors, have been known for many years. In 1957, the first patent of electrochemical capacitors based on a high specific surface area of carbon was described by Becker (Kötz and Carlen, 2000). The schematic image of carbon-based electrochemical capacitor is shown in Figure 2.1. A pair of porous carbon electrodes are partially immersed in the electrolyte and are connected with an insulating container. This electrolytic capacitor showed a capacitance of 6 F within the potential window of 1.5 V due to the energy stored on the surface and in the pore of the porous carbon electrodes.

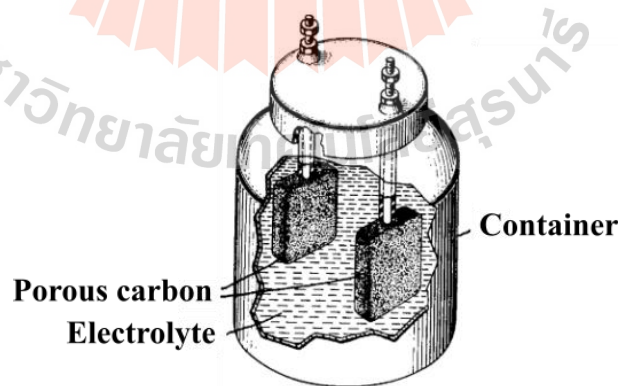


Figure 2.1 Schematic illslution of the first low voltage electrolytic capacitor based on porous carbon (Adapetd from (Becker, 1957)).

Later, a commercial device of electrochemical capacitor was first invented by Standard Oil Company of SOHIO in 1966 (Long *et al.*, 2011) and they were further developed under the name of “*supercapacitor*” in 1971 by NEC company which were primary used for memory backup. For a redox system, known as pseudocapacitors, a RuO₂ films were first studied in an aqueous electrolyte in 1971 (Trasatti and Buzzanca, 1971; Melbourne, 1978).

2.1.1 Conventional capacitor

A conventional capacitor consists of two conducting plates which are separated by a vacuum or dielectric material. When a voltage is applied to a capacitor, the opposite charges accommodate on the surface of the electrodes producing an electric field. Therefore, the capacitance (C) is the ratio of electric charge (Q) on each electrode with the potential (V) different between them as follows:

$$C = \frac{Q}{V} \quad (2.1)$$

The charge store is directly proportional to the surface area (A) of each electrode and inversely proportional to the distance between the electrodes (d). Hence, the capacitance can be rewritten as follows.

$$C = \frac{\epsilon_0 \epsilon_r A}{d} \quad (2.2)$$

Where ϵ_0 is the dielectric constant in a vacuum and ϵ_r is the relative dielectric constant of the material. According to equation 2.2, the capacitance depends on the dielectric constant, the electrode surface area, and the distance between the plates. In addition, the calculated work done by a potential difference between the plates leads to the energy stored in a capacitor which can be expressed following the relation.

$$E = \frac{1}{2} CV^2 \quad (2.3)$$

2.2.2 Electrochemical capacitor

Electrochemical capacitors are one of the energy storage devices that can be fully charged and discharged in seconds, leading to a very high specific power when compared with Li-battery as shown in Figure 2.2. Electrochemical capacitors are similar to batteries in design and manufacture, which consist of two electrodes (anode and cathode) separated by an ion exchange membrane (separator) and an electrolyte connecting both electrodes.

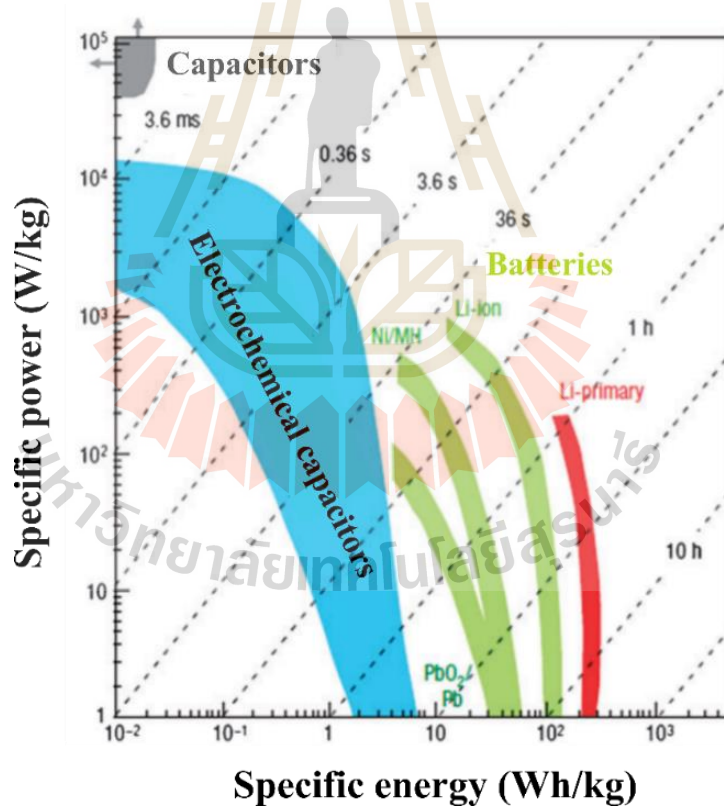


Figure 2.2 The plot between specific power against specific energy known as a Ragone plot for various electrical energy storage devices (Adapted from (Simon and Gogotsi, 2008)).

Depending on charge storage mechanism, electrochemical capacitors can be classified into two main groups those are electric double layer capacitors (EDLCs) and pseudocapacitors.

2.2.2.1 Electric double layer capacitors (EDLCs)

EDLCs store the charge based on the electrostatic force using the reversible adsorption of electrolyte ions onto active materials that have a highly accessible specific surface area and are electrochemically stable (Simon and Gogotsi, 2008). The concept of electric double layer was first described by von Helmholtz. The Helmholtz model states that two layers of opposite charge form at the electrode/electrolyte interface and both of them are separated by an atomic distance. The specific capacitance (C) is due to the occurrence of charge separation on polarization at the electrode/electrolyte interface which can be described as follows (Chmiola *et al.*, 2006):

$$C = \frac{\epsilon A}{d} \quad (2.4)$$

where ϵ is the dielectric constant of the electrolyte, d is the effective thickness of the double layer, and A is the electrode surface area.

After that the capacitance model of diffuse layer was further developed by Gouy (Gouy, 1910) and Chapman (Chapman, 1913) on consideration of a continuous distribution of electrolyte ions in the solution due to thermal fluctuation. Later, the combination of the Helmholtz and Gouy and Chapman model was proposed by Stern (Stern-Hamburg, 1924). The following two regions of ion distribution are inner Helmholtz plane (IHP) or Stern layer and outer Helmholtz plane (OHP) or diffuse

layer as shown in Figure 2.3. In IHP region, ions (generally anions) are strongly adsorbed by the electrode while the non-specifically adsorbed ions are referred to OHP.

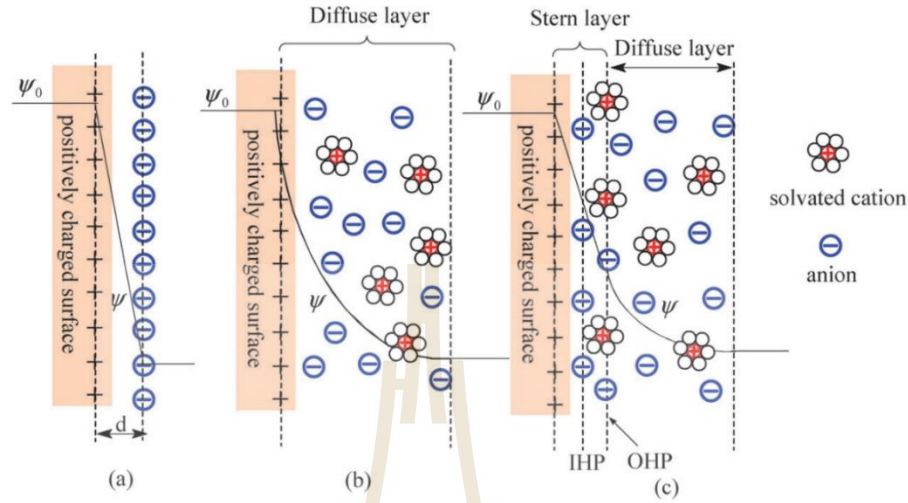


Figure 2.3 Stern model of the electrical double-layer formed at a positively charged electrode in an aqueous electrolyte (Adapted from (Zhang and Zhao, 2009)).

Therefore, the total capacitance in the EDL is given as follows (Zhang and Zhao, 2009):

$$\frac{1}{C_{DL}} = \frac{1}{C_H} + \frac{1}{C_D} \quad (2.5)$$

where C_H is the capacitance from the Helmholtz layer and C_D is the capacitance from the diffuse layer (Béguin *et al.*, 2014).

As mentioned before, the specific surface area of the electrode material plays an important role on the electrochemical performances of EDLCs. Because of their high specific surface area and rectangular shape of the charge storage mechanism, carbon-based materials such as reduced graphene oxide (Ramesh *et al.*, 2018), graphene (Stoller *et al.*, 2008), carbon nanotubes (Izadi-Najafabadi *et al.*, 2010), and activated carbon (Sim *et al.*, 2015) are reported for EDLC types.

2.2.2.2 Pseudocapacitors

They are known as a new type of electrochemical capacitors which were first discovered in RuO₂ thin film electrode in 1971 (Trasatti and Buzzanca, 1971). Pseudocapacitors use faradaic oxidation and reduction reactions at specific potential windows during charge and discharge to store the energy. The redox reactions occur at the surface or near surface of an electrode. Pseudocapacitance arises through a thermodynamically and kinetically electrochemical redox reaction. The redox reaction depends on the electrode potential which the change in charge (dq) has a relationship with the electrode potential (dV). Therefore, pseudocapacitance created by the redox reaction is the ratio of dq/dV and the behavior of the redox reaction is similar to batteries.

By assuming that the redox material is uniformly distributed on the electrode layer. The oxidized species (O_x) and reduced species (R_d) are insoluble in the electrolyte, so the redox reaction can be expressed as follows (Yu *et al.*, 2013):



where n is the number of electrons transferred. According to thermodynamics theory, the reversible electrode potential induced by the reaction can be expressed as follows (Yu *et al.*, 2013):

$$E = E^0 + \frac{RT}{nF} \ln \left(\frac{C_{ox}}{C_{red}} \right) \quad (2.7)$$

where E^0 is the standard electrode potential. C_{ox} and C_{red} are the concentrations of oxidized and reduced species within the electrode layer, respectively. E is the electrode potential. R is the gas constant and T is the temperature. Equation 2.7 indicates that when the electrode potential E changes over time, the oxidized and reduced species

concentration will change accordingly, resulting in a current flow through the electrode. The current density passing through the electrode can be expressed as follows (Yu *et al.*, 2013):

$$i = nFd \frac{dC_{ox}}{dt} \quad (2.8)$$

where A is the area of the electrode layer and d is the thickness of the electrode layer. Moreover, the theoretical specific capacitance value of pseudocapacitive materials can be calculated according to the following equation (Zhi *et al.*, 2013).

$$C = \frac{nF}{MV} \quad (2.9)$$

Where n is the number of electrons transferred in the redox reaction, F is the Faraday constant, M is the molar mass, and V is the potential window.

Conway first identified the three different faradic mechanisms of pseudocapacitive materials (Conway, 1999) as shown in Figure 2.4. These are underpotential deposition, redox pseudocapacitance and intercalation pseudocapacitance as shown in Figure 2.4.

Underpotential deposition occurs when metal ions form an adsorbed monolayer at a different metal's surface well above their redox potential. Redox pseudocapacitance occurs when ions are electrochemically adsorbed onto the surface or near surface of material with a concomitant faradaic charge-transfer. Intercalation pseudocapacitance occurs when ions intercalate into the tunnels or layers of a redox-active material accompanied by a faradaic charge-transfer with no crystallographic phase change (Augustyn *et al.*, 2014).

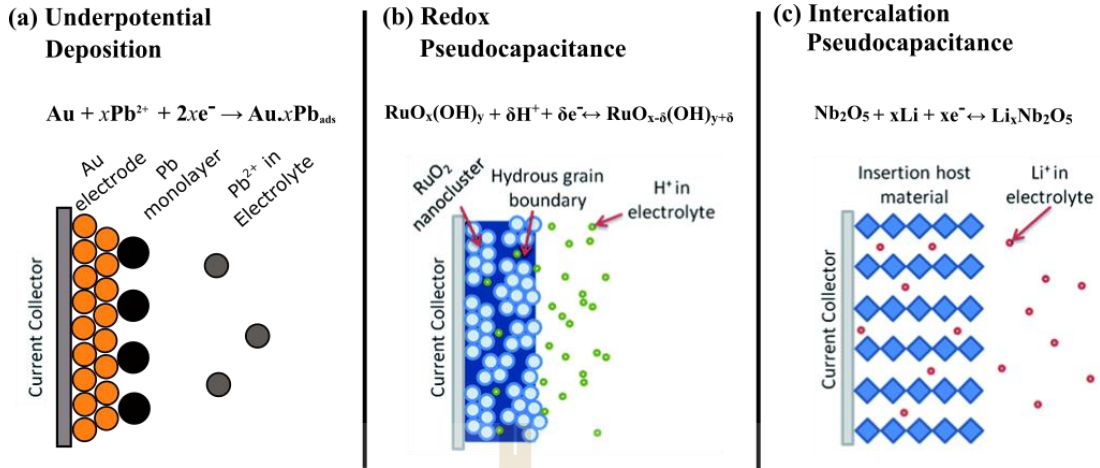
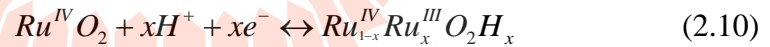
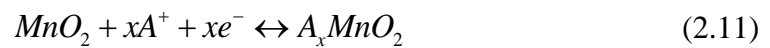


Figure 2.4 Different types of reversible redox mechanisms that give rise to pseudocapacitance: (a) underpotential deposition, (b) redox pseudocapacitance, and (c) intercalation pseudocapacitance (Adapted from (Augustyn *et al.*, 2014)).

Well-known examples of pseudocapacitive materials are ruthenium oxide (RuO_2) and manganese oxide (MnO_2). The pseudocapacitive behavior of RuO_2 is generally described as a fast, reversible electron-transfer reaction that is coupled with absorption of protons at or near the electrode surface as follows (Long *et al.*, 2011):



For manganese oxide, the charge storage mechanism occurs through the redox couple of Mn^{+4} and Mn^{+3} at the surface or in the bulk as follows:



where A represents an alkali metal cation. Another example of pseudocapacitive material is a nanostructured layered metal hydroxide such as $\text{Co}(\text{OH})_2$ (Tang *et al.*, 2010) and $\text{Ni}(\text{OH})_2$ (Sun *et al.*, 2015). The hydroxides of divalent transition metal oxides, $\text{M}^{2+}(\text{OH})_2$, tends to form lamellar structures that generally consist of MO_6 octahedra separated by hydrogen atoms. When the oxidation state of transition metals

is +3, the additional positive charge of the slabs can be compensated by the intercalation of anion species into the interlayer spacing forming a layered double hydroxide (Augustyn *et al.*, 2014). The interlayer spacing of the hydroxides is several nanometers. Therefore, it allows the ions to intercalate reversibly into tunnels or layers of redox active materials.

2.2 Structure of $\text{Ni}(\text{OH})_2$

$\text{Ni}(\text{OH})_2$ is isostructural with the brucite $\text{Mg}(\text{OH})_2$, consisting of metal cations surrounded approximately octahedrally by hydroxide anions. These octahedral units form infinite layers, with the hydroxide ions sitting perpendicular to the layers (Li *et al.*, 2006). Bode and co-workers (Bode *et al.*, 1966) first identified two known pseudopolymorphs of $\text{Ni}(\text{OH})_2$ denoted as β and α phase. As shown in Figure 2.5, β - $\text{Ni}(\text{OH})_2$ consists of brucite-type layers well-ordered along the c -axis with c -spacing of 4.8 Å.

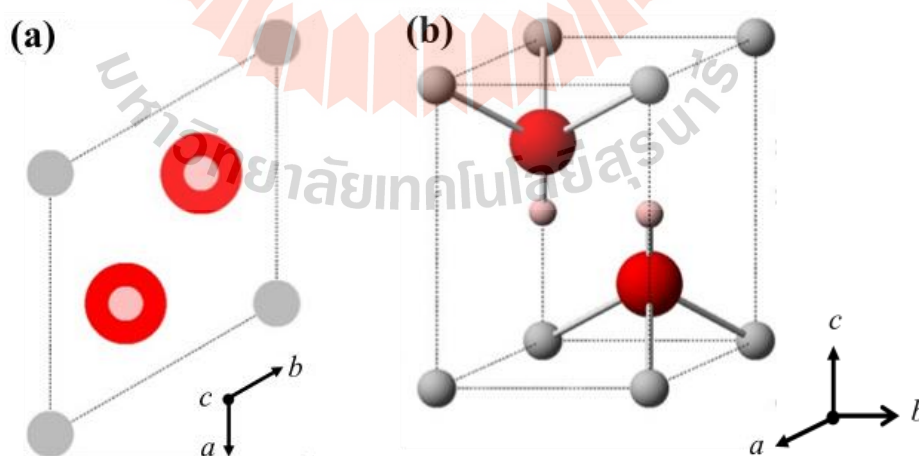


Figure 2.5 The crystal structure of β - $\text{Ni}(\text{OH})_2$ represented by (a) unit cell projection and (b) ball-and-stick unit cell of Ni^{2+} (grey spheres), O^{2-} (red spheres), and H^+ (pink spheres) (Hall *et al.*, 2015).

On the other hands, α -Ni(OH)₂ consists of brucite-type layers randomly stacked along the c -axis with the intercalation of water molecules between the layers as shown in Figure 2.6. The water molecule acts as a glue that holds together the Ni(OH)₂ layers with c -spacing of 7.6 Å (Hall *et al.*, 2015). The unit cell parameters of Ni(OH)₂ are listed in Table 2.1.

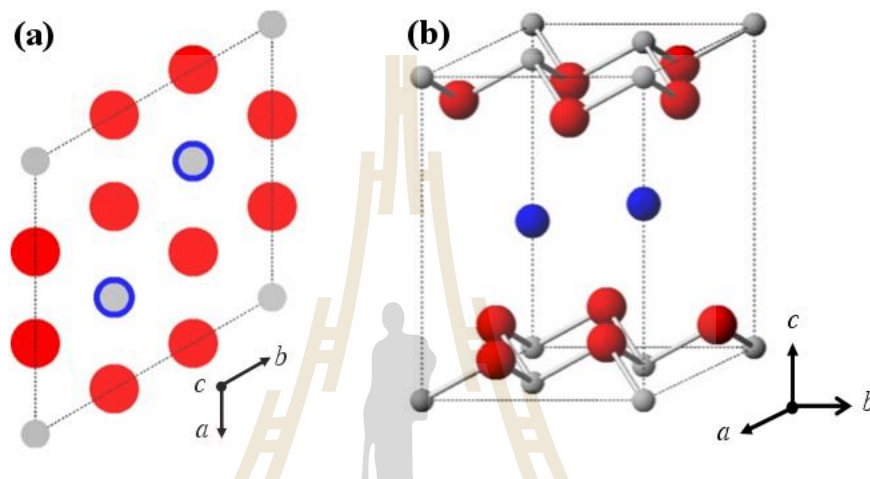


Figure 2.6 The crystal structure of α -Ni(OH)₂ represented by (a) unit cell projection and (b) ball-and-stick unit cell of Ni²⁺ (grey spheres), OH⁻ (red spheres), and H₂O (blue spheres) (Hall *et al.*, 2015)

Table 2.1 A summary of the unit cell parameters of the two known phases Ni(OH)₂ where $a = b$ and $\alpha = \beta$.

Materials	Space group	Lattice parameters		Angle		References
		a (Å)	c (Å)	α	γ	
β -Ni(OH) ₂	P $\bar{3}$ ml	3.13	4.61	90°	120°	(McEwen, 1971)
α -Ni(OH) ₂	P $\bar{3}$ lm	3.08	8.00	90°	120°	(Pandya <i>et al.</i> , 1990)

2.3 Electrochemical properties of $\text{Ni}(\text{OH})_2$

It has been known for a long time that nickel hydroxide was used as the active materials for positive electrodes in nickel-based rechargeable batteries including Ni - Cd, Ni - Fe, Ni - Zn, and Ni - MH (Hall *et al.*, 2015; Song *et al.*, 2005). In recent years, nanosized $\text{Ni}(\text{OH})_2$ has been identified as a very promising material for supercapacitor applications (Li *et al.*, 2013). Bode and co-workers (Bode *et al.*, 1966) first proposed the schematic to explain the electrochemical reaction of two phases known as β and α - $\text{Ni}(\text{OH})_2$ as shown in Figure 2.7. During the charging, β and α - $\text{Ni}(\text{OH})_2$ phases transform into β - NiOOH and γ - NiOOH , respectively.

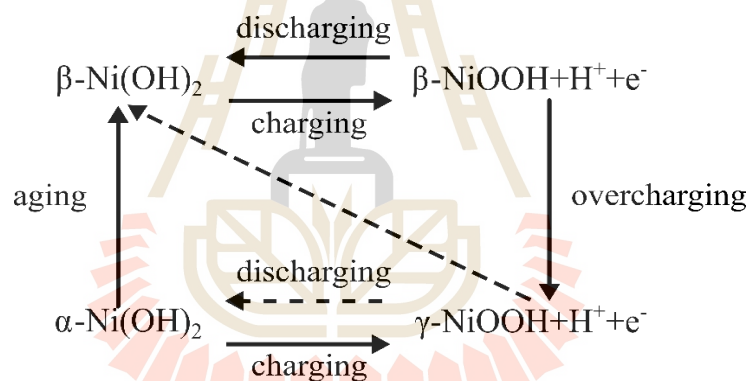


Figure 2.7 Schematic illustration for the electrochemical processes of nickel hydroxide (Adapted from (Hall *et al.*, 2015)).

In 1988, the electrochemical properties of α - $\text{Ni}(\text{OH})_2$ phase were reported to be better than β - $\text{Ni}(\text{OH})_2$ because they could exchange 1.2 electrons per nickel against 1 electron for the β -type phase (Audemer *et al.*, 1997). However, the α - $\text{Ni}(\text{OH})_2$ materials were never used in practical applications. The main reasons for this were due to the long-term cyclic stability problems and the unstable phase of α - $\text{Ni}(\text{OH})_2$ that easily transformed to β -phase after a few cycles. The electrochemical performance of

β -Ni(OH)₂ was found to be significantly improved by increasing the number of electrons exchanged per Ni metal atom (NEE) value. Audemer and co-workers (Audemer *et al.*, 1997) reported on the increase NEE of β -Ni(OH)₂ by cobalt substitution. They found that the β -Ni(OH)₂ substituted with cobalt provided a better electrochemical performance than pure nickel hydroxide. Recently, Huang and co-workers (Huang *et al.*, 2013) reported on improving the electrochemical performance of β -Ni(OH)₂ with increasing specific capacitance from 941.7 to 2122.6 F/g by the addition of 3.4 mol.% Al as shown in Figure 2.8.

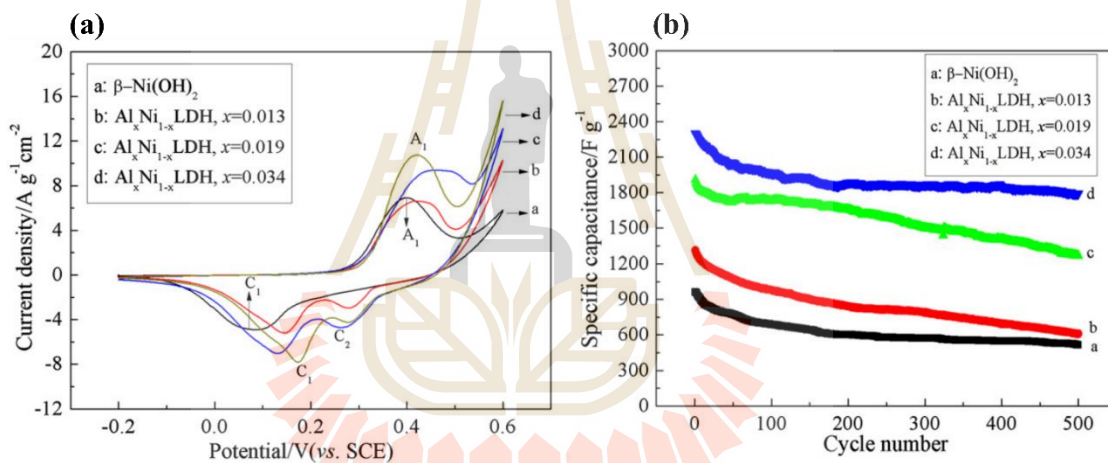


Figure 2.8 (a) The CVs curve at a scan rate of 2 mV/s and (b) cycle performance at a galvanostatic current density of 1 A/g of the Al_xNi_{1-x}LDH electrode (Adapted from (Huang *et al.*, 2013)).

Due to the substitution of larger ionic radius of Ni²⁺ with smaller ionic radius of Al³⁺, lattice parameter a was found to be gradually decreased with increasing Al³⁺ contents while the lattice parameter c increased. The increase in the interlayer distance, which related to the lattice parameter c , was found to be the main reason for increasing specific capacitance value of β -Ni(OH)₂. This could be explained by the increase of Al

in the mole content as the interlayer distance increased leading to a higher specific capacitance value because of intercalated species (water and anions) within the interlayer of nickel hydroxide. The partial substitution of nickel ions with metal ions has been reported as summarized in Table 2.2.

Table 2.2 List of reports on the specific capacitance value of metal doped β -Ni(OH)₂.

Dopants	Methods	C _s	References
Zn-Co	Co-precipitation	160 F/g	(Park <i>et al.</i> , 2006)
Co	Hydrothermal	209 mAh/g	(Ramesh and Kamath, 2008)
La	electrodeposition	840 F/g	(Shao <i>et al.</i> , 2009)
Co-Zn	precipitation	257 mAh/g	(Yue <i>et al.</i> , 2012)
Co	Template-free growth	1464.7 F/g	(Liu <i>et al.</i> , 2013)
Al	Hydrothermal	2122.6 F/g	(Huang <i>et al.</i> , 2013)
Fe	Hydrothermal	3.51 F/cm ²	(Li <i>et al.</i> , 2018)
La	Hydrothermal	586 F/g	(Chakrabarty and Chakraborty, 2019)

Not only the substitution of metal ions affected the electrochemical performance of β -Ni(OH)₂, but also the morphology (Dubal *et al.*, 2012), particle size (Wang *et al.*, 2015) and specific surface area (Li *et al.*, 2010). The summarized data on the electrochemical performance of β -Ni(OH)₂ with various preparation methods and morphologies are listed in Table 2.3.

Table 2.3 List of reports on morphology dependence electrochemical performance including specific capacitance (C_s) and capacitance retention of β -Ni(OH)₂ obtained from various preparation methods.

Method	Morphology	C_s	Retention (%)	Reference
Electro-deposition	Thin film	578 F/g at 2.5 mA	95.5% retained after 400 cycles	(Zhao <i>et al.</i> , 2007)
Hydrothermal	Flowerlike	1715 F/g at 5 mV/s	79.9% retained after 2000 cycles	(Jiang <i>et al.</i> , 2011)
	Stacked nanoplates	1268 F/g at 5 mV/s	77.2% retained after 2000 cycles	
	Hexagonal nanoplates	1029 F/g at 5 mV/s	78.6% retained after 2000 cycles	
Precipitation	Spherical microstructure	255 mAh/g at 2 C	73.5% retained after 200 cycles	(Yue <i>et al.</i> , 2012)
Growth on Ni foam	nanosheets	2384.3 F/g at 1A/g	75% retained after 3000 cycles	(Xiong <i>et al.</i> , 2015)
Directly oxidized Ni foam	Irregular hexagonal aggregates	6.4 F/cm ² at 2.5 mA/cm ²	70.4% retained after 2000 cycles	(Zhou <i>et al.</i> , 2016)
Solvothermal-precipitation	3D porous	2110 F/g at 1.0 A/g	53% retained after 2000 cycles	(Liu <i>et al.</i> , 2018)

For example, Jiang and co-workers compared the electrochemical performance of Ni(OH)₂ with different morphologies of flowerlike nanostructured, stacked nanoplates, and hexagonal nanosheet (Jiang *et al.*, 2011). They found that the flowerlike structure showed the highest specific capacitance value due to the ultrathin superstructures of interconnected nanoflakes forming a flowerlike structure with many

macropores. Hence, the flake-like structure shortened the ion diffusion pathway within the active materials leading to a high specific capacitance value. They concluded that the thickness had a very important effect for the improvement of specific capacitance of β -Ni(OH)₂. As the thickness decreased, resulting in the increase of specific capacitance value. Moreover, Kiani and co-workers (Kiani *et al.*, 2010) reported on the increase in the electrochemical performance of β -Ni(OH)₂ due to the decrease of particle size. They compared the electrochemical performance of β -Ni(OH)₂ between microparticles and nanoparticles. The results showed that β -Ni(OH)₂ nanoparticles exhibited a superior cycling reversibility and improved capacity. Also, Wang and co-workers studied the effect of nanoparticle size on electrochemical performance of β -Ni(OH)₂ (Wang *et al.*, 2015). The increase of electrochemical performance as the particle size decreased until it reached at critical size was observed as shown in Figure 2.9. The particle size was less than the critical value that corresponded to a rapid decrease in conductivity. The conductivity of electrode materials was closely related to the diffusion of protons through the nanoparticles and the redox reaction rate on the surface.

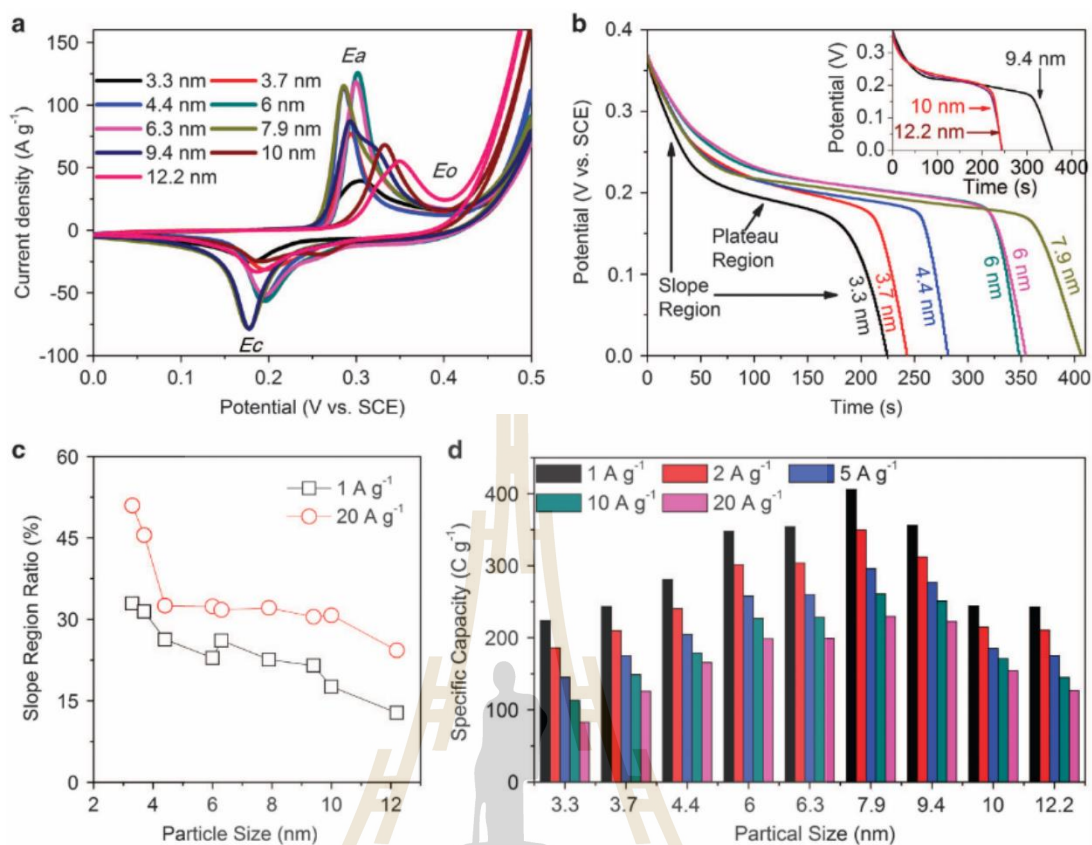


Figure 2.9 Comparison (a) CV curves of β -Ni(OH)₂ nanoparticles of different sizes at a scan rate of 20 mV/s. (b) Discharge curves of β -Ni(OH)₂ nanoparticles at a current density of 1 A/g. (c) Slope region proportion for different sized Ni(OH)₂ nanoparticles in the total discharging region at current densities of 1 and 20 A/g, respectively. (d) Specific capacity of Ni(OH)₂ nanoparticles of different sizes as a function of the discharge current (Adapted from (Wang *et al.*, 2015)).

CHAPTER III

RESEARCH METHODOLOGY

This chapter explains the experimental procedure for the synthesis of Ni(OH)_2 -based nanostructures. The materials characterization with various techniques consisting of XRD, SEM, TEM, XAS, XPS, and nitrogen adsorption/desorption including the electrochemical measurements are also described in this chapter.

3.1 Synthesis of pure and $\text{M}_x\text{Ni}_{1-x}(\text{OH})_2$ nanostructures

Pure Ni(OH)_2 and $\text{M}_x\text{Ni}_{1-x}(\text{OH})_2$ ($\text{M}=\text{Mg, Mn, Cu, Zn, and Bi}$) nanostructures were prepared by the hydrothermal route. For Mg, Mn, Cu, and Zn doping, the sulfate source was used as alternative material sources while the chloride source of nickel was used for the Bi doping. Their molecular weight and purity of all starting materials are listed in Table 3.1. For the synthesis, the starting materials were first dissolved in DI water under vigorous stirring for several minutes until a clear solution was obtained. For each sample, the weight percent of M:Ni was kept corresponding to the nominal composition of $\text{M}_x\text{Ni}_{1-x}(\text{OH})_2$ nanostructures ($x = 0.00, 0.05, 0.10, \text{ and } 0.15$) and then a precipitating agent of NaOH solution was added to the above solution. In order to remove Na^+ ions, Cl^- ions, SO_4^{2-} ions, and other impurities, the obtained $\text{M}_x\text{Ni}_{1-x}(\text{OH})_2$ suspension was washed with DI water several times until the $\text{pH} \sim 7$. After washing, the NaOH solution was directly added to the obtained $\text{M}_x\text{Ni}_{1-x}(\text{OH})_2$ and then

the mixture was immediately transferred to a Teflon-lined stainless-steel autoclave. The autoclave was sealed and heated at 160 °C for 20 h. The resultant precipitate of $M_xNi_{1-x}(OH)_2$ nanostructures was washed with DI water and ethanol several times until the pH became neutral and it was then dried in a vacuum oven at 70 °C overnight. The schematic overview of the synthesized $M_xNi_{1-x}(OH)_2$ nanostructures is shown in Figure 3.1.

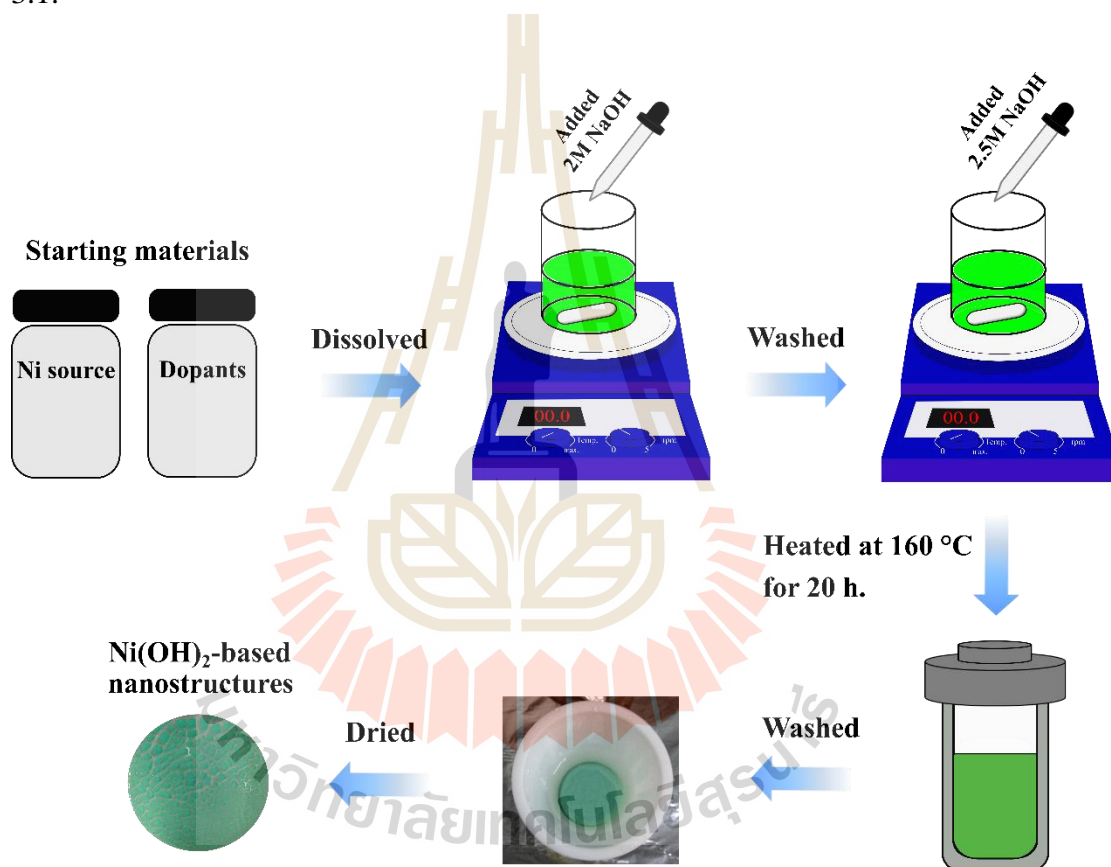


Figure 3.1 Schematic overview of the synthesized $M_xNi_{1-x}(OH)_2$ nanostructures by a hydrothermal method.

Table 3.1 List of starting materials used for the synthesis of Ni(OH)₂-based nanostructures, including their molecular weight (M_w), purity, and source.

Materials	M _w (g/mol)	Purity	Source
Nickel (II) Sulfamate Tetrahydrate (C ₄ H ₆ .NiO ₄ .4H ₂ O)	322.91	98%	Fluka
Nickel (II) chloride hexahydrate (NiCl ₂ .6H ₂ O)	237.71	>98%	Sigma-Aldrich
Magnesium Sulfate Hexahydrate (MgO ₄ .S.6H ₂ O)	228.45	99%	Fluka
Manganese (II) Sulfate Monohydrate (MnO ₄ .S.H ₂ O)	169.00	99%	Fluka
Cupric Sulfate Pentahydrate (CuO ₄ .S.5H ₂ O)	249.68	99%	Fluka
Zinc Sulfate Monohydrate (O ₄ .S.Zn.H ₂ O)	179.45	99%	Fluka
Bismuth (III) acetate (C ₂ H ₃ O ₂ .3Bi)	386.12	99.99%	Sigma-Aldrich
Sodium Hydroxide (NaOH)	40.00	97%	Ajax Finechem

3.2 Hydrothermal synthesis

It is well known that the properties of materials depend on their shape/morphology and size. From this point of view, a several synthetic routes have been used for the synthesis of nanostructured including solid state reactions, co precipitation, sol-gel, and hydrothermal methods. Among these methods, hydrothermal method has advantages of high crystallinity and purity with good compositional and morphology control, and narrow particle size distribution. The comparison of various powder synthesis methods is listed in Table 3.2.

Table 3.2 Comparison of different powder synthesis method (Yoshimura and Byrappa, 2008).

Parameter	Solid state reaction	Co-precipitation	Sol-gel	Hydrothermal
Cost	Low to moderate	Moderate	High	Moderate
Compositional control	Poor	Good	Excellent	Good/Excellent
Morphology control	Poor	Moderate	Moderate	Good
Powder reactivity	Poor	Good	Good	Good
Purity (%)	<99.5	>99.5	>99.5	>99.5
Annealing step	Yes	Yes	Yes	No

Hydrothermal synthesis is one of the most important techniques which is used to synthesize nanostructure materials with a variety of shapes/morphologies and sizes. The term of “*hydrothermal*” was first used by the British geologist Sir Roderick Murchison to describe the action of water under elevated temperature and pressure, in

bringing about changes in the earth's crust, leading to the formation of rocks and minerals (Yoshimura and Byrappa, 2008). Byrappa (Byrappa, 2013) defined the term of hydrothermal synthesis as “any heterogeneous chemical reaction in the presence of solvent or minerals, whether it is aqueous and non-aqueous, above room temperature and at pressure greater than 1 atm in a closed system”. The crystal growth of the hydrothermal process under a given hydrothermal conditions in the autoclaves can be carried out in two ways. One is a recrystallization of the solid substance, including dissolution in the liquid phase and convective mass transfer of the dissolved part of the substance to the growth zone or seed. Another way is the dissolution of the mixture of the nutrient components with the help of their convective mass transport into the growth zone and interaction of the dissolved components on the seed surface (Byrappa, 2013).

In this research, all starting materials and the precipitating reagent of NaOH solution were filled in a Teflon container. The filled Teflon was then placed in the autoclave as illustrated in Figure 3.2. The autoclave was heated up to the temperature of 160 °C and maintained at this temperature for 20 h.

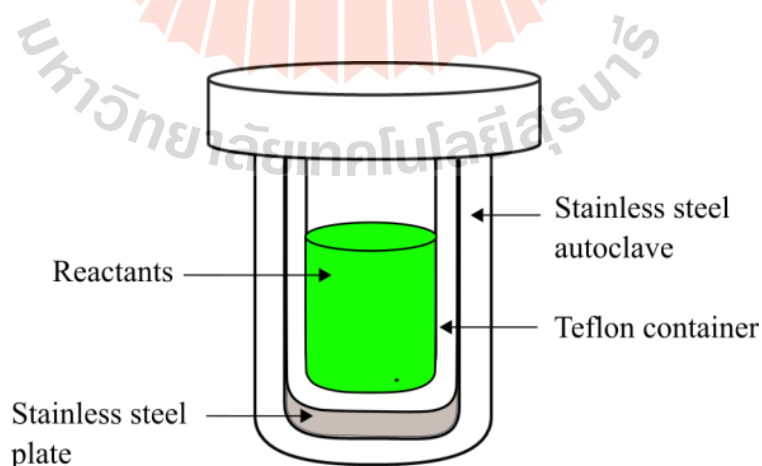


Figure 3.2 Schematic diagram of the mini-stainless steel autoclave and the Teflon container.

3.3 Materials characterization

This section presents an overview of materials characterization by various techniques. The principle of each technique is explained in the following sections.

3.3.1 X-ray diffraction technique

X-ray diffraction (XRD) is a well-known technique which is used to determine crystal structure of the materials. This technique involves the intensity measurement of X-ray which is scattered from electrons bond to atoms. The scattered waves at atom with different positions are detected, so the measured intensities give the structural information that relate to their positions. The schematic principle of X-ray diffraction measurements is illustrated in Figure 3.3.

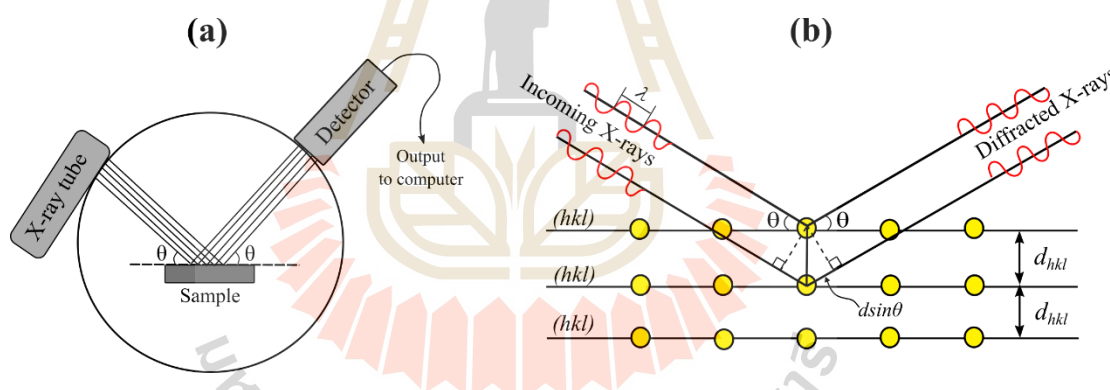


Figure 3.3 (a) Schematic principle of XRD measurement of the materials and (b) the description of Bragg's diffraction law.

The structural information is known via Bragg's equation, which described the principle of X-ray diffraction in terms of a reflection of X-rays by sets of lattice planes. Lattice planes are characterized by the Miller indices (hkl) . Parallel planes have the same indices and are equally spaced, separated by the distance (d_{hkl}), Bragg analysis treats X-rays being like visible light that reflected by the surface of a

mirror. The X-rays penetrate deep inside the material where additional reflections occur at thousands of consecutive planes. Since all X-rays are reflected in the same direction, superposition of the scattered X-rays occurs (Dinnebier and Billinge, 2008). Therefore, the Bragg's equation is as follows:

$$n\lambda = 2d \sin \theta \quad (3.1)$$

where d is the interplanar spacing and 2θ is the diffraction angle or the angle between the incoming and outgoing X-ray beams.

According to the structural information, the crystallite size can be calculated from the broadening of peak in a diffraction pattern by using the following Scherrer's equation.

$$\beta_{hkl} = \frac{K\lambda}{L_{hkl} \cos \theta} \quad (3.2)$$

Where K is a scale factor which depends on the shape of the grains (e.g., $K = 0.89$ for a sphere shape and $K = 0.94$ for a cubic shape). L_{hkl} is the crystallite size and β_{hkl} is a full width at half maximum. The general information obtained from a powder diffraction pattern is summarized in Table 3.3. The interplanar distance (d_{hkl}) or d -spacing in terms of their Miller indices can be separately calculated for each crystal system. For hexagonal system, the d -spacing is as follows:

$$\frac{1}{d^2} = \frac{4}{3} \frac{h^2 + hk + k^2}{a^2} + \frac{l^2}{c^2} \quad (3.3)$$

Table 3.3 Powder diffraction pattern as a function of various crystal structure, specimen, and instrumental parameters (Pecharsky and Zavalij, 2009).

Pattern component	Crystal structure	Specimen property	Instrumental parameter
Peak position	Unit cell parameters (a, b, c, α , β , γ)	Absorption Porosity	Radiation (wavelength) Instrument/sample alignment Axial divergence of the beam
Peak intensity	Atomic parameters (x, y, z, B, etc.)	Preferred orientation Absorption Porosity	Radiation (Lorentz polarization)
Peak shape	Crystallinity Disorder Defects	Grain size Strain Stress	Radiation (spectral purity) Geometry Beam conditioning

3.3.1.1 Structural refinement

The Rietveld refinement is known as the method used to determine the structural information including lattice parameters, atomic coordinates, atomic occupancy, bond length, and bond angle. This method is based on a minimization of the difference between observed and calculated profiles using a least square technique following the relation:

$$S = \sum_i w_i (y_{i,o} - y_{i,c})^2 \quad (3.4)$$

where S is the weighted difference between the observed intensity ($y_{i,o}$) and the calculated intensity ($y_{i,c}$) at point i of a diffraction pattern and w_i is the statistical weight quality which is equal to $1/y_i$. The calculated intensity ($y_{i,c}$) is presented as sum of all individual detected Bragg reflections plus an appropriate background function.

Individual peak profiles are described by one of the common peak shape functions, typically pseudo-Voigt or Pearson-VII. The pseudo-Voigt function is a

simply linear combination of Lorentzian and Gaussian components (McCusker *et al.*, 1999). The Rietveld algorithm optimizes the model function to minimize the weighted sum of squared differences between the observed and calculated intensity values or S value. The best fit between a raw and calculated diffraction pattern is attributed nearly evenly both above and below the zero-difference line. The crystallographic information file (CIF) is generally used for the structural model. The quality of the structural refinement is indicated by some residual functions of profile factor (R_p), Weighted profile residual (R_{wp}), Expected R -value (R_{exp}), and Goodness of fit (GOF) as follows (Toby, 2006):

$$R_p = \frac{\sum_{i=1,n} |y_{i,o} - y_{i,c}|}{\sum_{i=1,n} |y_{i,o}|} \quad (3.5)$$

$$R_{wp} = \left[\frac{\sum_{i=1,n} w_i (y_{i,o} - y_{i,c})^2}{\sum_{i=1,n} w_i y_{i,o}^2} \right]^{\frac{1}{2}} \quad (3.6)$$

$$R_{exp} = \left[\frac{N - P}{\sum_i w_i y_{i,o}^2} \right]^{\frac{1}{2}} \quad (3.7)$$

$$GOF = \chi^2 = \left[\frac{R_{wp}}{R_{exp}} \right]^2 \quad (3.8)$$

In this work, X-rays diffraction measurements were performed using Bruker D2 Phaser with Cu K_α radiation ($\lambda = 1.5406 \text{ \AA}$) at scanning rate of $0.02^\circ/\text{min}$ in the 2θ range from 10 to 80° . A freely available of JANA2006 program was used for the structural refinement. The peak-shape function of pseudo-Voigt and the standard CIF file of $\beta\text{-Ni(OH)}_2$ were used for the refinement.

3.3.2 Electron microscopy technique

An electron microscopy is a typically technique that uses electron beam to eliminate specimen and create an enlarged image. The electron microscopy uses electrostatic and electromagnetic lenses to form an image by controlling the electron beam to focus on or through a specific plane relative to the specimen. As a result, electron microscopy images provide the information on the structural basis of the specimen via both qualitative and quantitative analyses.

3.3.2.1 Scanning electron microscopy (SEM)

SEM is one type of electron microscopy techniques that images the sample surface by scanning it with a high energy of electron beam. As a brief overview, the electron beam is produced by an electron gun and it is accelerated by an anode. The primary beam is scanned across the sample surface and the beam penetrates and interacts with atom that makes up the sample material. The electrons from the primary beam spread out in the sample to form the interaction volume. The interaction volume depends on the accelerating voltage of the primary electron beam with the larger interaction volume results from the larger accelerating voltage. As illustrated in Figure 3.4, secondary electrons are produced from the sample surface. Additionally, backscattered electrons and X-rays come from the top half of the interaction volume and in whole of the interaction volume, respectively. These secondary electrons, backscattered electrons, and X-rays are collected by a detector and they are converted into a signal to form an image. Therefore, this technique reveals the information about the sample's surface morphology, elemental composition, and the orientation at different regions of the sample.

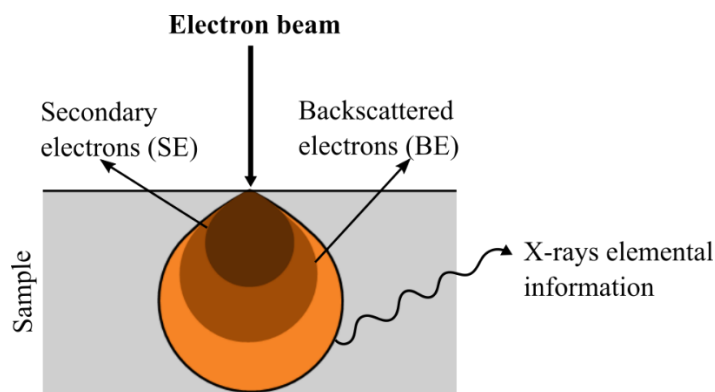


Figure 3.4 The different typical signals in SEM technique consisting of secondary electrons, backscattered electrons, and X-rays elemental information.

In this work, the samples were placed on a metal stub without gold coating. A field emission scanning electron microscope (FE-SEM, AURIGA, Carl Zeiss) coupled with dispersive X-ray spectroscopy (EDS) was employed to investigate the morphology including shape, size, porous, and elemental compositions of the samples.

3.3.2.2 Transmission Electron Microscopy (TEM)

TEM is used to determine the structure, chemical compositions, and specimen orientations, and the properties of the specimen in submicron detail through high-resolution and high magnification image. In this technique, the electron beam is transmitted through a thin specimen and the transmitted electrons are detected as shown in Figure 3.5. The TEM images are formed via the scattering of an incident electron beam by a specimen through an objective lens. The primary image is formed and it is magnified using additional lenses to form a highly magnified final image. The electrons are collected from below the sample onto a phosphorescent screen or thorough a camera.

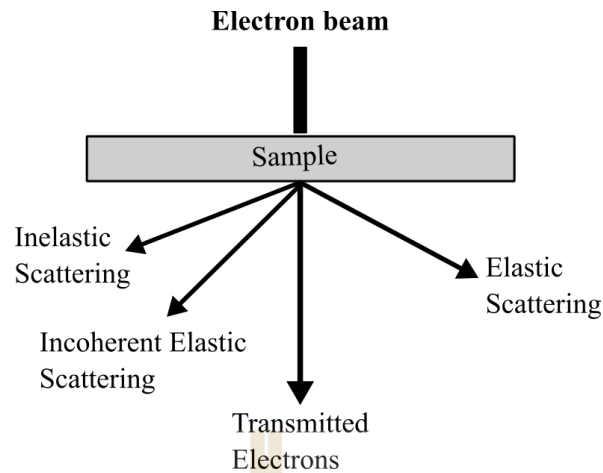


Figure 3.5 The different typical signals in TEM technique including inelastic and elastic scattering, incoherent scattering, and transmitted electrons.

The diffraction pattern is produced at its back focal plane in the process of forming the primary image using an objective lens. Fourier transform of the scattered electron produces a diffraction pattern. The diffraction angle in TEM is very small (usually $\theta < 1^\circ$) because the reflecting lattice planes are nearly parallel to the primary beam. Using the approximation of $\sin \theta \approx \theta$, so the Bragg's law can be rewritten as follows:

$$\lambda = 2d\theta \quad (3.9)$$

$$\lambda L = Rd \quad (3.10)$$

where L is the camera length or the distance between the crystal and photographic plate of camera. λL is called as the camera constant of the TEM. Therefore, the spacing of the planes d is calculated by measuring the radius R , which is the distance from the central spot of the transmitted beam to diffraction spot via equation 3.10.

In this work, the samples were dispersed in ethanol, and then dropped on a copper grid and dried in order to obtain an enough thin sample for electron beam

transmittance. Bright Field Transmission Electron Microscopy (TEM, FEI Tecnai G2) with an acceleration voltage of 200 kV was used to reveal the morphology and the corresponding electron diffraction patterns (SAED) of the materials.

3.3.2.3 Energy dispersive X-ray spectroscopy (EDS)

EDS technique is used to provide an information on the chemical composition of a sample. Basically, an electron beam is focused on the sample surface in either SEM or TEM. The primary electron beam penetrates the sample and interacts with the electrons that making up the material. An X-rays are produced and detected by an energy dispersive detector. In this view, an electron of the inner shell of the atom is removed by an electron from the primary beam and then an electron from the outer shell fills the inner shell. The emission of an X-ray is detected and the detected signals display as a spectrum of X-ray intensity versus X-ray energy. The energies of the characteristic X-rays allow the elements making up the sample to be identified, while the intensities of the Characteristic X-ray provide the elemental compositions.

In this research, the elemental compositions of the samples were characterized by SEM-based EDS.

3.3.3 Gas adsorption technique

Gas adsorption technique is one of the important techniques used for porous materials characterization. The specific surface area, mean pore diameter, total pore volume, and pore size distribution can be evaluated by this technique. For a brief overview, a solid sample is placed in a closed system of the gas. At a given pressure, a solid sample begins to adsorb the gas. The amount of the gas molecules adsorbed on the sample surface increases with increasing of the pressure. The pressure becomes constant at the value P and the amount of the gas adsorbed can be calculated by

application of the universal gas law. Thus, adsorption isotherm is obtained. Whereas the decrease of pressure results in the desorption isotherm. In generally, the isotherm can be classified into six types according to IUPAC classification which is shown in Figure 3.6(a). Moreover, the hysteresis loop which depends on pore size distribution, geometry, and connectivity can be classified into four types as presented in Figure 3.6(b).

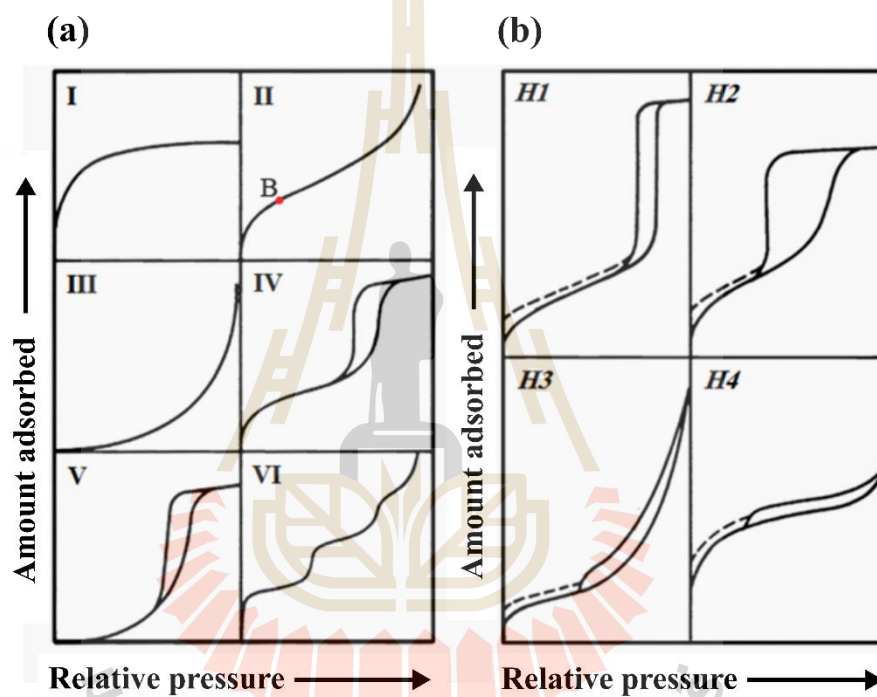


Figure 3.6 (a) Six types of isotherms and (b) four types of hysteresis loops according to IUPAC classification (Adapted from (Gregg and Sing, 1982)).

As shown in the above figure, adsorption/desorption isotherms are classified based on the strength of the interaction between the sample surface and the adsorbate and the existence or absence of pores. Generally, pores in materials are classified into three groups according to pore size distributions. Those are micropore

(pore size < 2 nm), mesopore (2-50 nm), and macropore (>50 nm). The summarized data of adsorption/desorption isotherm with various features are listed in Table 3.4.

Table 3.4 List of adsorption/desorption isotherm types including their features.

Type	Features	
	Interaction between sample surface and adsorbate	Porosity
I	Relative strong	Micropores
II	Relative strong	Nonporous
III	Weak	Nonporous
IV	Relative strong	Mesopores
V	Weak	Mesopores Micropores
VI	Relative strong Sample surface has an even distribution of energy	Nonporous

A well-known BET method (Brunauer *et al.*, 1938) has been extensively used for a specific surface area determination. The principle measurement of the BET method is based on the physical adsorption of gas on the sample surface and by calculation the amount of adsorbate gas corresponding to a monolayer on the surface. For BET method, the phenomenon of adsorption can be expressed via the following equation.

$$\frac{1}{W \left[\left(\frac{P_0}{P} \right) - 1 \right]} = \frac{1}{W_m C} + \frac{C-1}{W_m C} \left(\frac{P}{P_0} \right) \quad (3.11)$$

where W is the volume of the gas adsorbed, P is equilibrium pressure, P_0 is the saturation pressure, W_m is the volume of adsorbate as monolayer, and C is the BET constant.

The BET plot of $1/W[(P/P_0)-1]$ against P/P_0 (relative pressure) showing a straight line where slope and intercept can be obtained according to a linear equation. Hence, two parameters of W_m and C are obtained via the following relation.

$$W_m = \frac{1}{\text{slope} + \text{intercept}} \quad (3.12)$$

$$C = \frac{\text{slope}}{\text{intercept}} + 1 \quad (3.13)$$

Therefore, the specific surface area (S_{BET}) can then be derived as follows:

$$S_{\text{BET}} = \frac{W_m N A_{\text{CS}}}{m V_0} \quad (3.14)$$

where W_m is the monolayer volume, N is Avogadro's number (6.023×10^{23}), A_{CS} is the cross-section area of the surface occupied by individual gas molecules (16.2 \AA^2 for nitrogen), m is the sample mass, and V_0 is the molar volume of gas ($22414 \text{ cm}^3/\text{molar}$ at atmospheric pressure).

The total pore volume (V_T) is calculated from the amount of vapor adsorbed at a relative temperature close to unity by the following equation:

$$V_T = \frac{P_a V_{\text{ads}} V_m}{RT} \quad (3.15)$$

where V_T is the volume of liquid N_2 in total pore, P_a is ambient pressure, V_{ads} is the volume of gas adsorbed, V_m is molar volume of liquid adsorbate, R is gas constant ($8.314 \text{ J.K}^{-1}.\text{mol}^{-1}$), and T is ambient temperature.

The average pore size (r_p) is estimated from the total pore volume (V_T) by assuming pores as a cylindrical shape which can be expressed as follows:

$$r_p = \frac{2V_T}{S_T} \quad (3.16)$$

In addition, the pore size distribution is determined by Barrett-Joyner-Halenda (BJH) method (Barrett *et al.*, 1951) by applying the Kelvin model. This model based on the assumption that the mesopores have cylinder shape. Therefore, it works only in type IV of the adsorption and desorption isotherms.

In this work, a BEL SORP mini II instrument was used to examine the BET specific surface area and pore size distribution via BET and BJH methods, respectively. Before the measurement could be started, the $M_xNi_{1-x}(OH)_2$ samples were degassed at 120 °C for 3 h.

3.3.4 X-ray photoelectron spectroscopy technique

XPS is a widely used surface analytical technique that it allows to determine the chemical compositions, stoichiometry and the empirical formula of the material, and the chemical and electronic state of the elements on the sample surface. This technique is based on a photoelectric effect. Each atom has core electron with the characteristic binding energy (E_B) equal to the ionization energy of that electron. When an X-ray beam is shone on the sample surface, the energy of the X-ray photon is completely adsorbed by the core electron of an atom. If the photon energy ($h\nu$) is large enough, so the core electron will then escape from the atom and emit out of the surface.

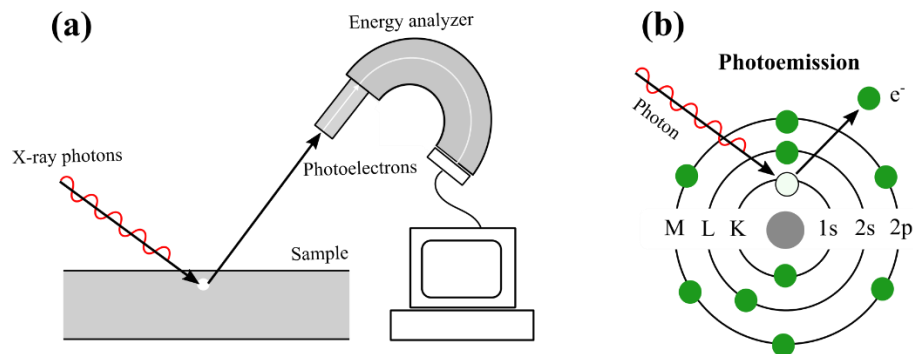


Figure 3.7 (a) Schematic principle of XPS measurement and (b) the photoelectric effect in XPS technique.

As shown in Figure 3.7, the emitted electron with the kinetic energy (E_k) is referred as a photoelectron. The binding energy of the core electron is given via the following Einstein relation.

$$h\nu = E_B - E_{kin} - \phi \quad (3.17)$$

$$E_{kin} = h\nu - E_B - \phi \quad (3.18)$$

Where $h\nu$ is the X-ray photon energy. E_B is binding energy of the electron in the material (i.e. energy required to remove an electron). E_{kin} is the kinetic energy of photoelectron and ϕ is the work function which is defined as the minimum amount of energy needed to move an electron from the Fermi level (at $E_{kin} = 0$) into vacuum level.

As described before, XPS technique is used for the kinetic measurement of the ejected inner or valence electron by an incident X-ray photon of known energy ($h\nu$). Therefore, the binding energy (E_B) is calculated which is characteristic of the chemical bonds in a compound. In this work, the chemical compositions and oxidation state of the samples were carried out by using X-ray photoelectron spectra (XPS) with PHI Versa Probe II XPS system (ULVAC-PHI) with an Al K α radiation (1486.6 eV).

3.3.5 X-ray absorption spectroscopy technique

XAS technique is used to study the local structure of the material. It is a technique which probes the core-shell electrons of an atom, typically a *K*-edge (*1s*) electron, by the beam of X-ray photons. The photon energy is typically higher than the binding energy of the deep core level. As a result, the electron is excited by absorption the photon energy and move to an empty state emitted a photoelectron which is called the photoelectric effect. After that an electron from the *L* or *M* shell jumps in to fill the vacancy at *K* shell with X-ray fluorescence emission as shown in Figure 3.8.

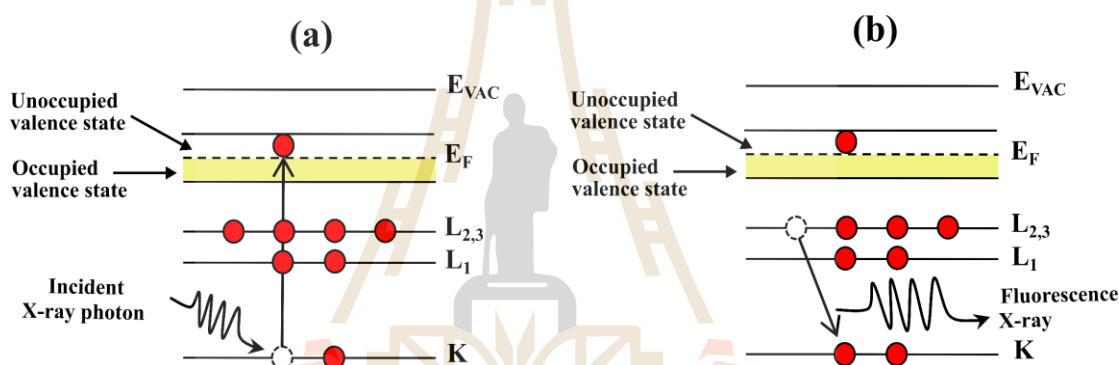


Figure 3.8 Schematic illustration of the XAS technique. (a) X-ray is absorbed by an electron in a core level followed by photoelectron emission and (b) Fluorescence X-ray.

Generally, the XAS spectrum consists of two main regions known as X-ray absorption near-edge spectroscopy (XANES) and extended X-ray absorption fine-structure (EXAFS) as illustrating in Figure 3.9. XANES region provides information about the oxidation state and the coordination number of the absorbing atoms. EXAFS region gives information about the interatomic distance, coordination number, and species of neighboring atoms.

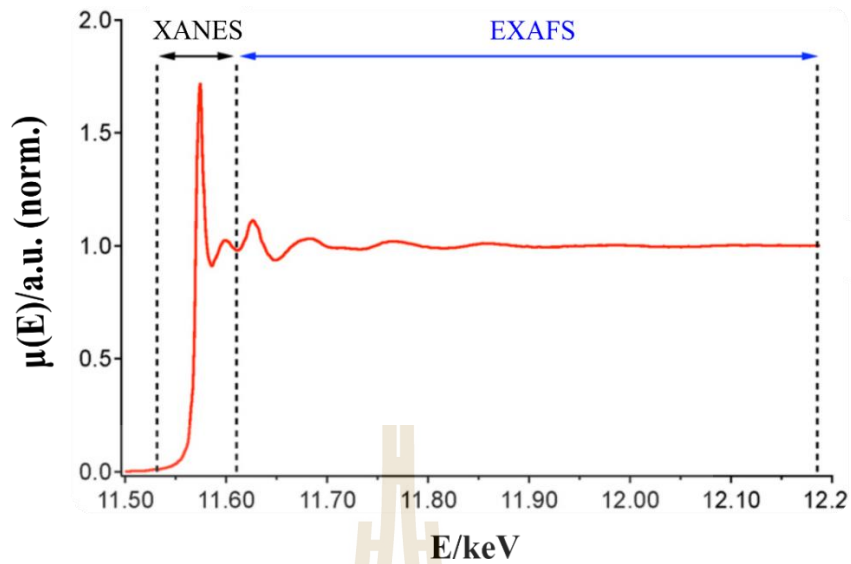


Figure 3.9 Typically X-ray absorption spectrum with different regions of XANES and EXAFS.

In general, XAS measures the absorption of X-ray as a function of X-ray energy ($E=h\nu$). When the X-ray beam (I_0) passes through a material in transmission mode, the X-ray beam intensity (I) will be decreased by an amount which is determined by the absorption characteristic of the material as shown in Figure 3.10.

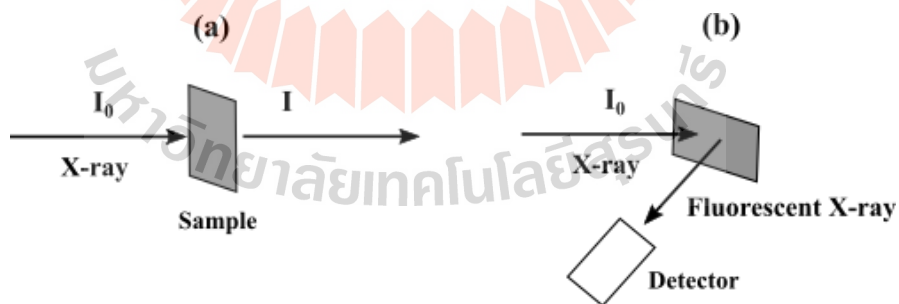


Figure 3.10 A schematic illustration of X-ray absorption measurement of (a) Transmission mode and (b) Fluorescence mode.

The X-ray absorption coefficient $\mu(E)$ is determined from the decay in the X-ray beam intensity (I) with distance (x) following the Lambert's law (Koningsberger *et al.*, 2000).

$$I = I_0 e^{-\mu(E)x} \quad (3.19)$$

$$\mu(E)x = \ln\left(\frac{I_0}{I}\right) \quad (3.20)$$

The plot between the absorption coefficients (μ) as a function of energy (E) is shown in a normalized XAS spectrum with three main features: (i) a sharp rise from the absorption or the increase in absorption is called the absorption edge (E_{edge}) which is the kinetic energy (E_{kin}) is defined to be equal to E_0 , (ii) a region from the onset of X-ray absorption to approximately 30 eV beyond is the X-ray Absorption Near Edge (XANES). In this region, a core electron is photo-excited into an empty valence state. Hence, the characteristic of the oxidation state results from its shape and intensity, and (iii) beyond the XANES region, the small oscillations in the intensity is called the Extended X-ray Absorption Fine Structure spectrum (EXAFS). This region can be analyzed to give the number and type of neighboring atoms and their distance to the absorbing atom because the oscillations in absorption are related to neighboring atoms.

In this work, XANES spectra of the samples were collected at the Synchrotron Light Research Institute (BL 5.2 SUT-NANOTEC-SLRI, XAS) of Thailand and they were compared with the standard data. The oxidation state was evaluated by using Athena software.

3.4 Electrochemical measurement

Electrochemical capacitor or supercapacitors are electrochemical storage devices which their charge storage mechanism, performances, and other properties are usually investigated through three well-known techniques including cyclic voltammetry (CV), galvanostatic charge/discharge (GCD), and electrochemical

impedance spectroscopy (EIS). Figure 3.11 gives a schematic overview of a cell connected to an electrochemical workstation which is composed of a potentiostat/galvanostat (PSTAT/GSTAT), a computer, and electrochemical cell.

Three-electrode system including counter electrode (also known as auxiliary electrode) (CE), reference electrode (RE), and working electrode (WE) is one of important components in electrochemical measurement. The role of counter electrode is to complete the electrical circuit. The most commonly used for counter electrodes are glassy carbon, silver (Ag), and platinum (Pt.) wire/plate. For a reference electrode, it is used as a point of reference for measuring and controlling the potential window of the electrode without passing any current. Therefore, reference electrode should be an ideal non-polarizable electrode. The most commonly used for reference electrodes are saturated calomel electrode (SCE), the standard hydrogen electrode (SHE), and the Ag/AgCl electrode. Working electrode (WE) is the electrode which is the electrochemical reaction taking place. Hence, different electrode materials can also lead to different electrochemical responses.

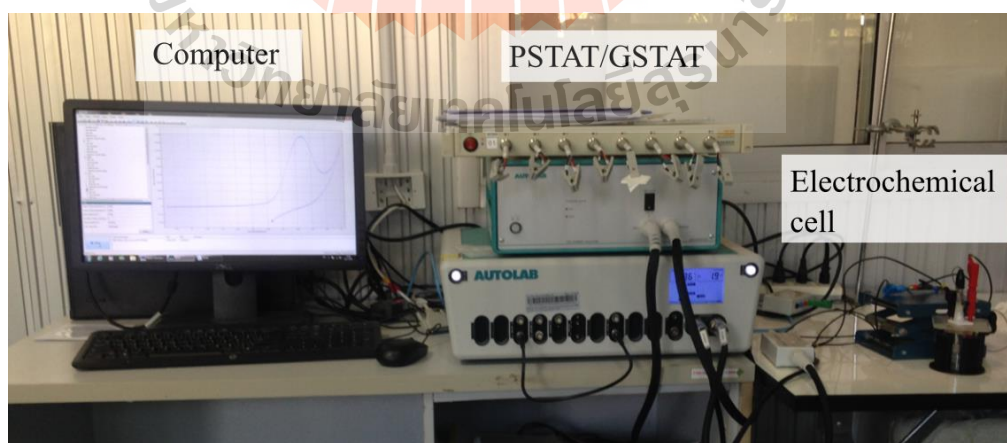


Figure 3.11 An overview of the electrochemical workstation consisting of a computer, PSTAT/GSTAT, and electrochemical cell.

3.4.1 Cyclic voltammetry (CV)

CV is a widely used electrochemical technique which yields information about surface and solution electrochemical reactions including electrochemical kinetics, reaction reversibility, and reaction mechanisms. It has been extensively used to characterize the performance of various electrical energy storage devices like electrochemical capacitors, batteries, and fuel cell.

In this technique, the potential is applied between the working electrode and reference electrode in both forward and reverse directions and then the resulting current which measured between working electrode and counter electrode is plotted as a function of the potential (Kounaves, 2015). When asymmetrical triangular potential waveform is applied to a working electrode as shown in Figure 3.12(a), then a plot of current density versus potential has a characteristic shape which is known as cyclic voltammetry (CV) as seen in Figure 3.12(b). The shape of CV represents the characteristic of the capacitive and redox reaction mechanism. CV curve displays a rectangular shape for an ideal EDLC and the peaks in the CV curves indicate the redox reaction that occurs at the working electrode.

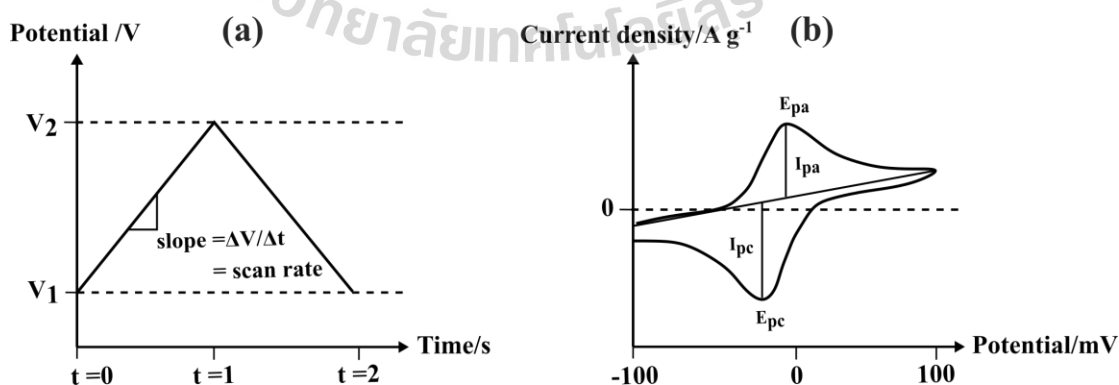


Figure 3.12 (a) The potential waveform is applied to the working electrode in the cyclic voltammetry and (b) a typical CV curve.

For redox reaction mechanism, the positive potential is applied and the electroactive species loses an electron giving rise an oxidation peak (also known as anodic peak). On the other hand, the reduction peak is observed when the negative potential is applied (also known as cathodic peak). As the reaction taking place at the electrode/electrolyte interface leads to an electron or charge transfer. There are three types of electron transfer process including reversible process, irreversible process, and quasi-reversible process.

In reversible process, the peak of oxidation and reduction is observed. The rate of electron transfer is fast in both forward and reverse scan. The current is directly proportional to the concentrations and increases with the square root of scan rate. The peak current is given by Randles-Sevcik equation as follows (Xing *et al.*, 2017):

$$i_p = 2.69 \times 10^5 n^{3/2} A D^{1/2} C v^{1/2} \quad (3.22)$$

where n is the number of electron transferred, A is the electrode area (cm^2), D is the diffusion coefficient (cm^2/s), C is the concentration (mol/cm^3), and v is the scan rate (V/s). The position of peaks on the potential axis (E_p) relates to the formal potential of the redox process (E^0) and it is centered between peak potentials of anodic (E_{pa}) and cathodic (E_{pc}) as follows:

$$E^0 = \frac{E_{pa} + E_{pc}}{2} \quad (3.23)$$

The potential separation (ΔE_p) between anodic and cathodic peaks is then given by the following relation.

$$\Delta E_p = E_{pa} - E_{pc} = \frac{0.059}{n} V \quad (3.24)$$

In irreversible process, only oxidation or reduction peak is observed. The rate of electron transfer is slow. The peak current is given by

$$i_p = 2.99 \times 10^5 n(\alpha n_a)^{1/2} AD^{1/2} C v^{1/2} \quad (3.25)$$

where α is the transfer coefficient and n_a is the number of electrons involved in the charged transfer process. For a quasi-reversible process, the current is controlled by both mass transfer and charge transfer process. The CV shape is a combination between the reversible process (fast v) and irreversible process (slow v).

According to CV curve, the capacitance for the variation of voltage with time is given by

$$\frac{dQ}{dt} = C \frac{dV}{dt}; C = i/V \quad (3.26)$$

where dQ/dt is the current (i) and dV/dt is the scan rate (V). Therefore, the specific capacitance in CV technique is obtained following the relation.

$$C_{cv} = \frac{1}{mv\Delta V} \int I(V)dV \quad (3.27)$$

The term of $\int I(V)dV$ refers to the area surround the CV curve, m is the mass of the active material within the electrode, v is the scan rate and ΔV is the potential window.

3.4.1.1 Kinetic analysis for charge storage mechanism

In CV curve, the total current measured under the potential scan rate can be interpreted as the sum of the current from capacitive and diffusion-controlled processes (Liu *et al.*, 2018). The current in CV curve is related to the scan rate following the power-law relation (Lindström *et al.*, 1997; Forghani and Donne, 2018) :

$$i = av^b \quad (3.28)$$

$$\log(i) = \log(a) + b \log(v) \quad (3.29)$$

where i is the peak current, a and b are the adjustable parameters, and v is the scan rate. The value of b can be obtained from the slope of the plot between $\log(i)$ versus $\log(v)$. There are two meanings of b -value. A $b = 0.5$ implies that the current is affected by diffusion-controlled such as the intercalation/deintercalation mechanism (Wang *et al.*, 2007; Sankar *et al.*, 2015; Xiao *et al.*, 2016) due to the current is proportional to the square root of the scan rate according to the following equation (Wang *et al.*, 2007).

$$i = nFAC^* D^{1/2} v^{1/2} (\alpha nF / RT)^{1/2} \pi^{1/2} \chi(bt) \quad (3.30)$$

where n is the number of electrons involved in the electrode reaction, F is Faraday's constant, C^* is the surface concentration of the electrode material, α is the transfer coefficient, D is the diffusion coefficient, R is the molar gas constant, T is the temperature, and $\chi(bt)$ function represents the normalized current for a totally irreversible system as indicated by the CV response.

In contrast, a $b = 1$ indicates that the obtained CV current is due to a capacitive mechanism because the current is proportional to the scan rate following the relation (Wang *et al.*, 2007).

$$i = vC_d A \quad (3.31)$$

where C_d is the capacitance and A is the surface area of the electrode material. From CV kinetic analysis, the total charge storage has been assumed to be the combination of capacitive ($k_1 v$) and diffusion-controlled or intercalation/deintercalation ($k_2 v^{1/2}$) mechanism following the relation (Lindström *et al.*, 1997 and Forghani and Donne, 2018):

$$i_p = k_1 v + k_2 v^{1/2} \quad (3.32)$$

$$\frac{i_p}{v^{1/2}} = k_1 v^{1/2} + k_2 \quad (3.33)$$

Where the k_1 and k_2 values are determined from the slope and intercept of the plot between $i_p/v^{1/2}$ versus $v^{1/2}$, respectively. Therefore, the contributions of capacitance arising from capacitive and diffusion-controlled intercalation/deintercalation mechanisms can be distinguished.

In this work, the CV measurements were performed at room temperature over the different scan rates. The peak current of each scan rate was used to identify the charge storage mechanism in the $M_xNi_{1-x}(OH)_2$ samples.

3.4.2 Galvanostatic charge/discharge (GCD)

GCD is one of the most reliable techniques for specific capacitance, energy density, powder density, and cycle life evaluation. In general, GCDs are performed by applying a constant current density and the potential is recorded as a function of charging/discharging time as seen in Figure 3.13.

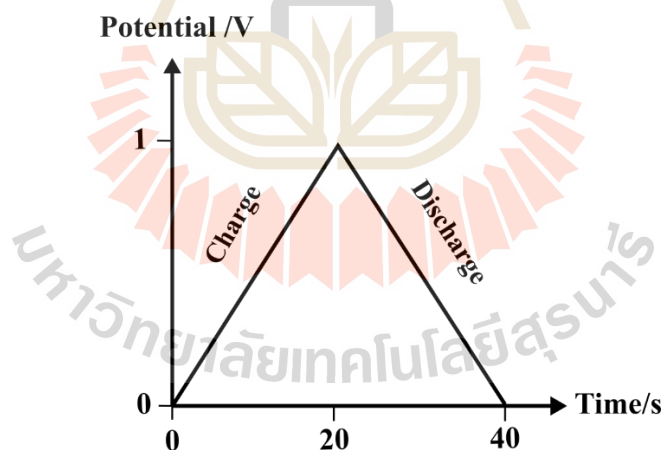


Figure 3.13 A schematic diagram of charge and discharge curve for an ideal electrochemical capacitor.

For an ideal linear charge/discharge curves, the specific capacitance is estimated from the current (I) and slope ($\Delta V/\Delta t$) of the discharge curve following the relation.

$$C_s = \frac{I\Delta t}{m\Delta V} \quad (3.34)$$

Where m is mass of the active material within the electrode. The specific energy or energy density (E , Wh/kg) and specific power or power density (P , W/kg) are calculated via the following relation.

$$E = \frac{1}{2} CV^2 \quad (3.35)$$

$$P = \frac{E}{t} \quad (3.36)$$

In this work, the GCD measurements of $M_xNi_{1-x}(OH)_2$ samples were performed in 1M NaOH. The charge and discharge between the selected potential windows were carried out at different current densities. The specific capacitance value, energy density, and power density of the samples were determined by using equation 3.34, 3.35, and 3.36, respectively. The cyclic stability was evaluated by repeating charge and discharge at a constant current density for 1000 cycles. The electrochemical performance of all $M_xNi_{1-x}(OH)_2$ samples was evaluated and compared with pure $Ni(OH)_2$.

3.4.3 Electrochemical impedance spectroscopy (EIS)

EIS is a powerful technique of determining the complex electrical resistance of a system. It has been extensively used in electrochemical research for characterization of bulk and interfacial properties of the system (Dhillon and Kant, 2017) and the corrosion analysis (Randviir and Banks, 2013).

According to Ohm's law, the resistance is defined as the ratio between the voltage (V) and current (I) following the relation of $R = V/I$. The equation represents the ideal resistance of only one circuit. In AC circuit, the word of "resistance" is

replaced by “impedance” which is more general circuit. Like resistance, impedance is defined as the ability of a circuit to resist the flow of electrical current. Generally, electrochemical impedance is determined by applying a sinusoidal potential of small amplitude to the electrode cell and the current response is measured. The sinusoidal potential and current as a function of time can be expressed as follows:

$$V_t = V_0 \sin(\omega t) \quad (3.37)$$

$$I_t = I_0 \sin(\omega t + \phi) \quad (3.38)$$

where V_0 and I_0 are the amplitude of the signal and current, respectively. V_t and I_t are the potential and current at time t , respectively. ω is the angular frequency ($\omega = 2\pi f$) and ϕ is the phase shift between the current response and potential. The complex impedance can then be defined according to Ohm's law as follows:

$$Z = \frac{V_t}{I_t} = |Z| \frac{\sin(\omega t)}{\sin(\omega t + \phi)} = |Z| e^{j\phi} = |Z| (\cos \phi + j \sin \phi) = Z' + jZ'' \quad (3.39)$$

Where Z' is the real part of the complex impedance and $-Z''$ is the imaginary part of the complex impedance. The plot between imaginary part and real part gives the modulus $|Z|$ and the phase angle ϕ which can be expressed as follows:

$$|Z| = \sqrt{(Z')^2 + (Z'')^2} \quad (3.40)$$

$$\phi = \tan^{-1} \left(\frac{Z''}{Z'} \right) \quad (3.41)$$

where the capacitance in term of real part (C'), imaginary part (C''), and in complex system (C) are presented as follows:

$$C' = \frac{Z'}{\omega |Z|^2} \quad (3.42)$$

$$C'' = -\frac{Z'}{\omega|Z|^2} \quad (3.43)$$

$$C = \frac{Z''}{\omega|Z|^2} - j\left(\frac{Z'}{\omega|Z|^2}\right) = C' - jC'' \quad (3.44)$$

The EIS measurement results are presented by the plot between the real part (Z') versus the imaginary part ($-Z''$) which is well known as the Nyquist plot as shown in Figure 3.14 and the Bode plot of the modulus of the impedance (Z) as a function of the log frequency which is used to investigate the electrical or electrode-kinetic relaxation processes.

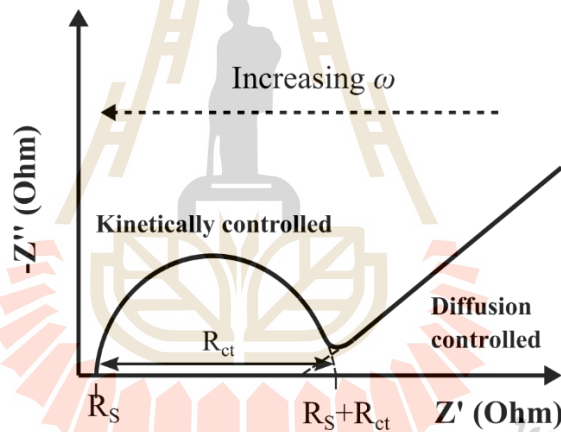


Figure 3.14 Nyquist plot of a simple Randles equivalent circuit for an electrochemical cell.

In electrochemical impedance spectroscopy, four elements consisting ohmic resistance (R), capacitance (C), constant phase element (CPE), and Warburg impedance (Z_w) are usually used to describe the impedance behavior. The definitions of these elements are summarized in Table 3.5.

When the electrode immersed in the electrolyte, impedance will arise from the solution resistance (R_s), charge transfer resistance (R_{ct}), the double layer

capacitance (C_{dl}), and the Warburg impedance (Z_w) which is known as a Randles circuit (Randviir and Banks, 2013). R_s is observed at the highest frequency where the real-axis is intersected. R_{ct} is observed in the mid-to low-frequency region which is marked as the kinetically controlled region and it relates to the heterogeneous electron transfer rate constant (k^0) following the relation.

$$R_{ct} = \frac{RT}{F^2 k^0 C} \quad (3.45)$$

Where R is the gas constant, T is the temperature, F is the Faraday constant and C is the concentration of the electroactive species. C_{dl} is estimated at the maximum of Z'' axis at of the semi-circle. Warburg impedance accounts for the diffusion of the ions in solution in an electrochemical reaction. The Warburg impedance is generally seen in the low frequency which is marked in the diffusion-controlled region in the Nyquist plot.

Table 3.5 List of EIS definitions adapted from (Lisdar and Schäfer, 2008).

Impedance element	Definition	Phase angle
R	$Z = R$	0°
C	$Z_C = \frac{1}{j\omega C}$	90°
CPE	$Z_{CPE} = \frac{1}{A(j\omega)^\alpha}$	$0^\circ - 90^\circ$
Z_w^*	$Z_w = \frac{\sigma}{\sqrt{\omega}}(1 - j)$ $\sigma = \frac{RT}{n^2 F^2 \sqrt{2}} \left(\frac{1}{\sqrt{D_0 c_0}} + \frac{1}{\sqrt{D_R c_R}} \right)$	45°

* Where α the dispersion exponent

In this work, EIS measurements of the $M_xNi_{1-x}(OH)_2$ samples were carried out in the frequency range of 0.1 Hz to 100 kHz at amplitude of 0.1 V. The measurements were performed after the galvanostatic charge/discharge measurement.



CHAPTER IV

RESULTS AND DISCUSSION

This chapter presents the experimental results and their discussion. The crystal structure of Ni(OH)₂-based materials obtained from the hydrothermal process is determined by XRD. The microstructure and morphology of the Ni(OH)₂-based materials are revealed by SEM and TEM images. The chemical compositions and oxidation state are investigated by XPS and XAS. Their specific surface area and porosity are evaluated from BET and BJH methods, respectively. The effects of electrolytes, current collectors and Mg, Mn, Cu, Zn, and Bi-doped Ni(OH)₂ are demonstrated in electrochemical results.

4.1 Effects of various electrolytes on electrochemical properties of Ni(OH)₂ nanostructures

Nickel hydroxide (Ni(OH)₂) is one of the pseudocapacitive materials which is interested in the electrochemical applications because of its low cost, easy processing, and its high theoretical specific capacitance value of 2082 F/g within the potential window of 0.5 V (Singh *et al.*, 2014; Ji *et al.*, 2013). The electrochemical properties of Ni(OH)₂ have been studied in different electrolytes. In 1M NaOH electrolyte, the ultra-thin Ni(OH)₂ nanowalls showed the ultra-high specific capacitance value (Lu *et al.*, 2011) while the Ni(OH)₂-based composite electrodes possessed the highest specific

capacitance value in 2M KOH electrolyte (Zhang *et al.*, 2010). Also, the Ni(OH)₂-based electrode materials reached the highest specific capacitance value in the mixed solution of 1M KOH + 0.5M Na₂SO₄ (Ren *et al.*, 2016). For the nanostructured layered nickel hydroxide, the capacitance arises generally from the intercalation/deintercalation mechanism, which is involved the moving of electrolyte ions into/out the electrode matrix and undergo redox reaction (Augustyn *et al.*, 2014; Sankar *et al.*, 2015). However, there are a few works that reported on the effects of the different electrolytes on the electrochemical properties of Ni(OH)₂ (Soserov *et al.*, 2017; Zhao and Zheng, 2015; Inamdar *et al.*, 2011).

In this work, a simple hydrothermal synthesis of hexagonal Ni(OH)₂ nanoplates and the material characterizations are reported. In particular, the electrochemical properties of the Ni(OH)₂ electrodes are studied and discussed in various alkaline electrolyte including 1M NaOH, 1M KOH, 2M KOH, and 1M KOH + 0.5M Na₂SO₄ based on the previous reports.

4.1.1 Structural and morphology analysis

XRD pattern of the synthesized Ni(OH)₂ nanostructures is presented in Figure 4.1. All the diffraction peaks can be indexed and well matched with the standard diffraction pattern of hexagonal β -Ni(OH)₂ (JCPDS file no. 14-0117). The observed diffraction peaks at $2\theta = 19.29, 33.04, 38.54, 52.15, 59.02, 62.64, 69.33, 70.45,$ and 72.69° correspond to the lattice planes of (001), (100), (101), (102), (110), (111), (200), (103), and (201), respectively. In addition, the sharp of diffraction peak indicates high crystallinity of the prepared Ni(OH)₂ (Mphuthi *et al.*, 2017). Note that no extra peaks are observed, confirming the high purity phase of Ni(OH)₂.

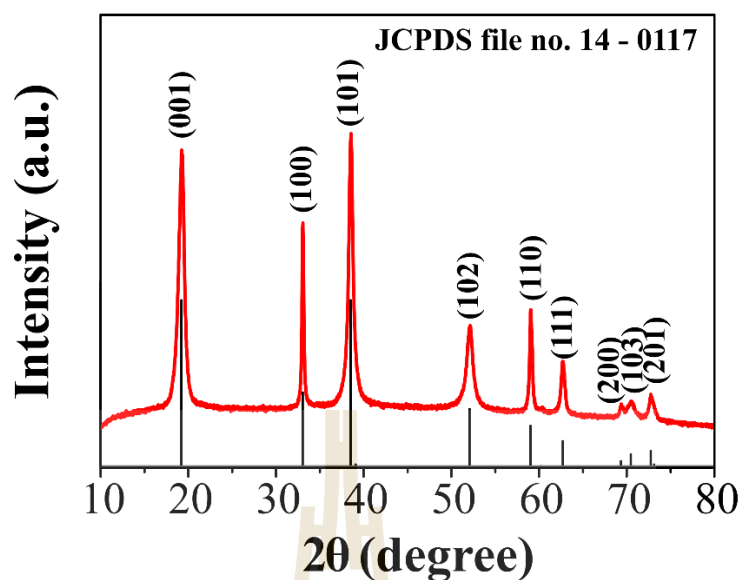


Figure 4.1 XRD pattern of the synthesized $\text{Ni}(\text{OH})_2$ obtained from hydrothermal process.

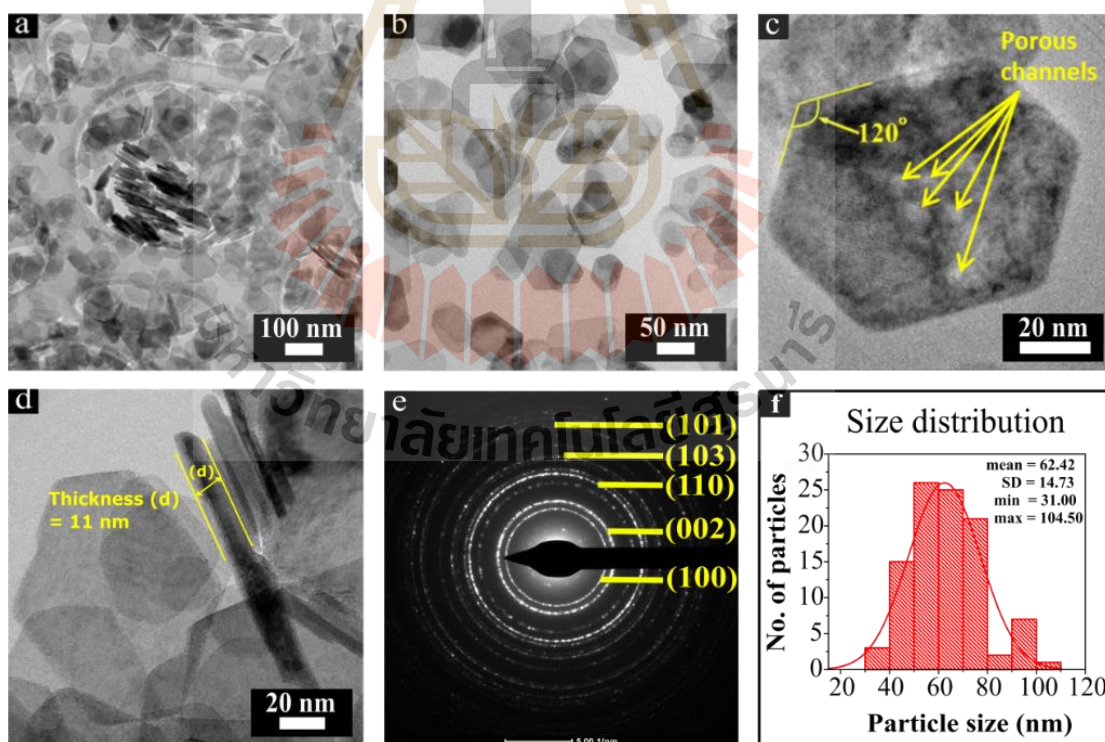


Figure 4.2 (a-d) TEM bright field images, (e) the corresponding SAED diffraction pattern, and (f) the estimated nanoplates size of the synthesized $\text{Ni}(\text{OH})_2$ nanostructures.

Figure 4.2(a-d) shows the TEM bright field images of the synthesized $\text{Ni}(\text{OH})_2$ nanostructures. As shown in Figure 4.2(a-d), TEM images reveal the hexagonal shape of $\text{Ni}(\text{OH})_2$ with an average plate size of about 62 nm. Furthermore, some of the $\text{Ni}(\text{OH})_2$ nanoplates are stacked together into a columnar shape with an average thickness of about 11 nm.

It can be clearly seen from the high magnification TEM image in Figure 4.2(c) that an individual hexagonal is thin and the measured interfacial angle is 120° . More importantly, a porous structure is also observed on the surface of the $\text{Ni}(\text{OH})_2$ nanoplate as can be clearly seen in Figure 4.2(c) which suggests that the generation of pores within the nanoplates could be attributed to the loss of water molecules under hydrothermal conditions and then followed by the formation of nickel-oxygen bond at the interface of the aggregated nanoparticles. The mechanism for hexagonal nanostructure growth is illustrated in Figure 4.3 (Singh *et al.*, 2014).

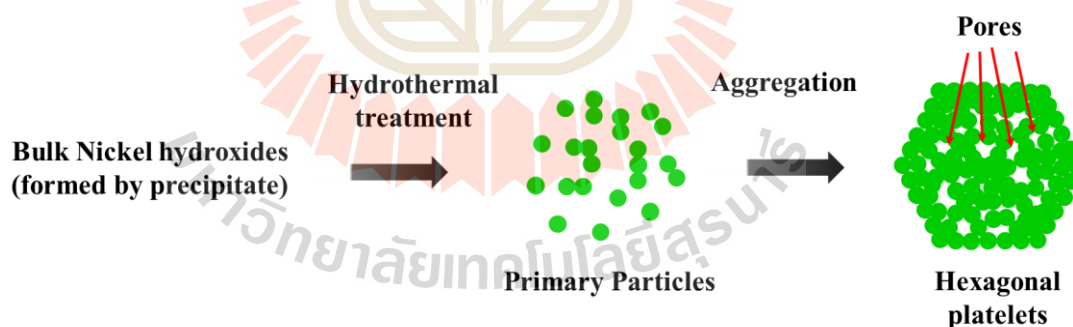


Figure 4.3 Schematic illustration of the formation of porous $\text{Ni}(\text{OH})_2$ platelets.

These pores are very useful for charge storage applications as they can decrease the ionic diffusion length and also the electrolyte resistance (Singh *et al.*, 2014). Figure 4.2(e) shows a spotty ring pattern of the selected area electron diffraction

(SAED) image that confirms the polycrystalline $\text{Ni}(\text{OH})_2$ and the lattice planes of the $\text{Ni}(\text{OH})_2$ phase are in good agreement with the XRD results.

In order to further investigate the type of pores observed in the TEM image, the BET technique was used. Figure 4.4(a) shows the N_2 adsorption/desorption isotherms of the hexagonal $\text{Ni}(\text{OH})_2$ nanoplates. According to IUPAC classifications, the N_2 isotherm curves can be classified as type IV. At the relative pressures ranging from 0.4 to 0.9, the presence of the hysteresis loop is observed, which is characteristic of mesoporous materials (Nagaraju *et al.*, 2017).

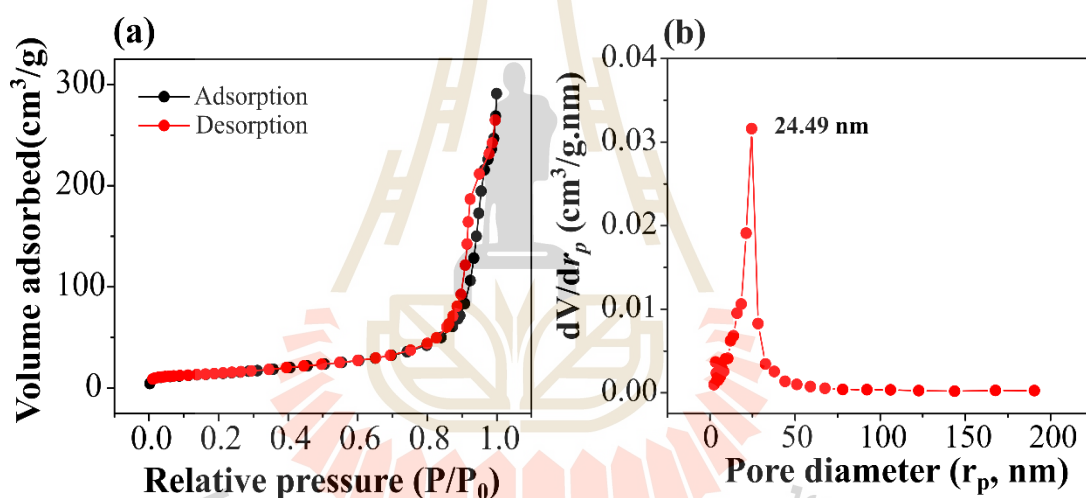


Figure 4.4 (a) N_2 adsorption/desorption isotherm and (b) the pore size distribution of $\text{Ni}(\text{OH})_2$ calculated from BET and BJH methods, respectively.

The calculated BET specific surface area from the N_2 isotherm is found to be $52.80 \text{ m}^2/\text{g}$, which is higher than that of a previous study (Singh *et al.*, 2014). The higher surface area of $\text{Ni}(\text{OH})_2$ nanoplates suggest that to provide a larger contact area with the electrolyte, which is highly beneficial for the delivery of high capacitance for pseudocapacitors (Sun *et al.*, 2015). The calculated pore size distribution from the adsorption branch of the nitrogen isotherm by using the Barrett-Joyner-Halenda (BJH)

method shows that the mean pore diameter of Ni(OH)_2 is centered at 24.49 nm with the mesopore volume of $0.3903 \text{ cm}^3/\text{g}$ as shown in Figure 4.4(b). Therefore, the obtained mean pore diameter indicates the existence of mesopores on the Ni(OH)_2 nanoplates.

4.1.2 Surface analysis

The surface characteristics and chemical compositions of Ni(OH)_2 nanoplates were investigated using XPS technique. As shown in Figure 4.5(a), a survey spectrum of Ni(OH)_2 confirms the presence of C 1s, O 1s, and Ni 2p on the sample surface. The high resolution XPS in C 1s, O 1s, and Ni 2p region are shown in Figure 4.5(b-d). For C 1s peak fitting, peaks located at binding energy of about 284.5 eV is attributed to C-C bond and 288.6 eV is referred to C-C=O bond (Nie *et al.*, 2018). Peak fitting of Ni 2p region shows two main peaks at the binding energy of 855.2 eV (Ni $2p_{1/2}$) and 872.8 eV (Ni $2p_{3/2}$) with the separation of spin energy around 17.6 eV, indicating the characteristics of Ni(OH)_2 phase (Liu *et al.*, 2014; Zhang *et al.*, 2015; Parveen and Cho, 2016). The O 1s peak was observed at the binding energy of 531.0 eV corresponding to Ni-OH (Ratcliff *et al.*, 2011). This result clearly indicates the formation of Ni(OH)_2 .

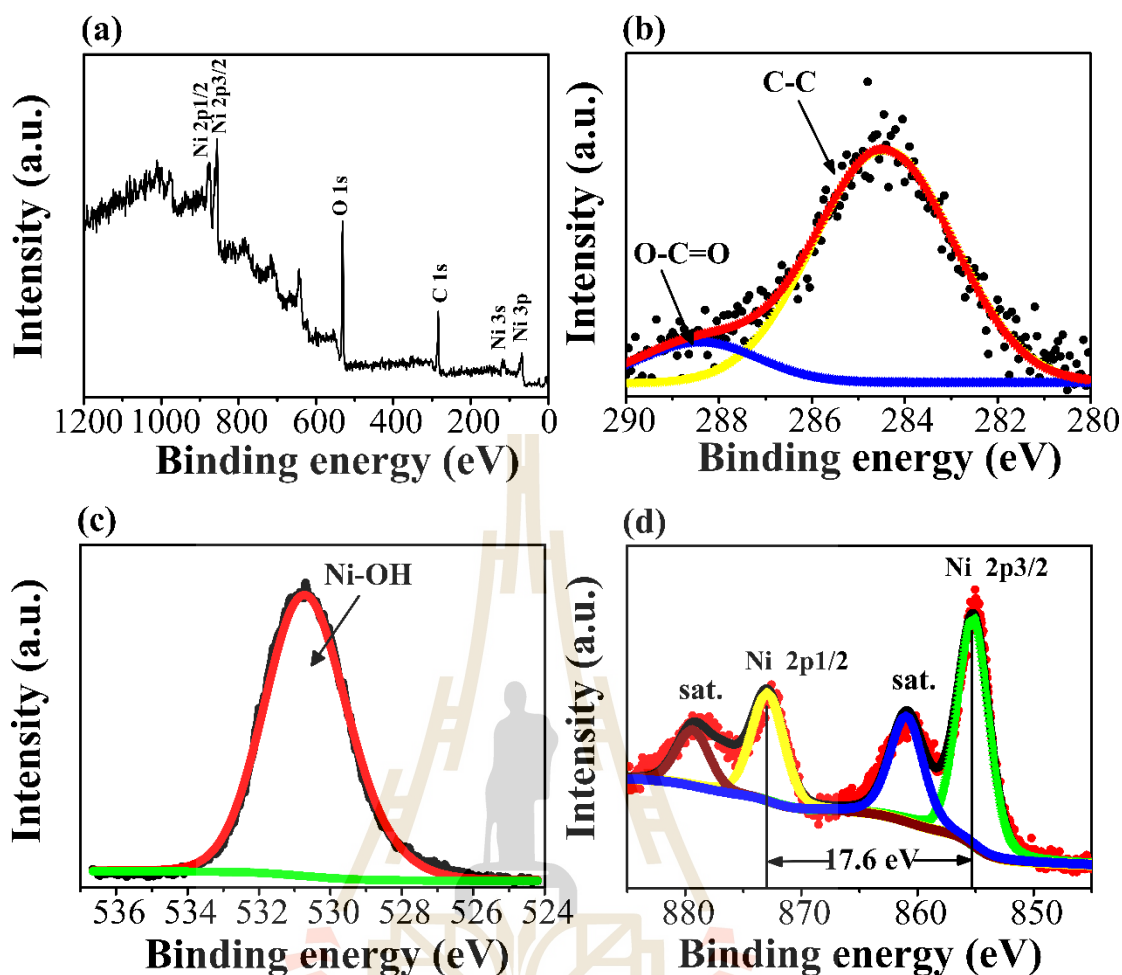


Figure 4.5 (a) The survey XPS spectrum and the high resolution XPS spectrum of (b) C 1s region, (c) O 1s region and (d) Ni 2p region of the Ni(OH)₂ nanoplates.

4.1.3 Electrochemical study

As mentioned before, the selection of suitable electrolytes is very important for electrochemical performance. Therefore, the selected alkaline electrolytes including 1M NaOH, 1M KOH, 2M KOH and 1M KOH mixed with 0.5M Na₂SO₄ were evaluated in a three-electrode system. To prepare working electrode, Ni(OH)₂ (active material), carbon black (conducting agent), and polyvinylidene difluoride (binder) in the mass ratio of 80 : 10 : 10 were mixed in 200 μ L of N-methylpyrrolidone (NMP) solution. The resulting slurry was dropped onto 1 x 2 cm² of Ni foam substrate. The

prepared working electrode was dried in a vacuum oven at 70°C overnight and pressed at 5 MPa for 1 min with the obtained mass loading of Ni(OH)₂ about 2 mg.

4.1.3.1 Cyclic voltammetry

Figure 4.6(a-d) shows a CV curves of the Ni(OH)₂ electrodes measured in different aqueous electrolytes. The observed redox peaks are presented in all aqueous electrolytes. It is also observed that the redox peaks shift to higher and lower potential with increasing scan rate (mV/s). The shift of redox peaks with increasing scan rate ranging from 2 to 20 mV/s was used to identify the charge storage mechanism of the Ni(OH)₂ electrodes in 1M NaOH, 1M KOH, 2M KOH, and 1M KOH + 0.5M Na₂SO₄ electrolytes.

The scan rate dependence of CV peak current can be expressed as $i = av^b$ where i is the CV peak current (A/g), a and b are the adjustable parameters, and v is the scan rate (V/s). The value of b was determined from the slope of the plot of $\log(i)$ versus $\log(v)$. There are two meanings of b -value. The value of b is 1, indicating the obtained CV current is due to a capacitive mechanism. While the value of b is 0.5, the obtained CV current is due to the diffusion-controlled intercalation/deintercalation mechanism (Sankar *et al.*, 2015; Li and Liu, 2014; Xiao *et al.*, 2016). As shown in Figure 4.7(a-d), the slopes or the b -values are close to 0.5. Hence, it may be concluded that the Ni(OH)₂ electrodes in 1M NaOH, 1M KOH, 2M KOH, and 1M KOH + 0.5M Na₂SO₄ electrolytes store the charge based on intercalation/deintercalation mechanism.

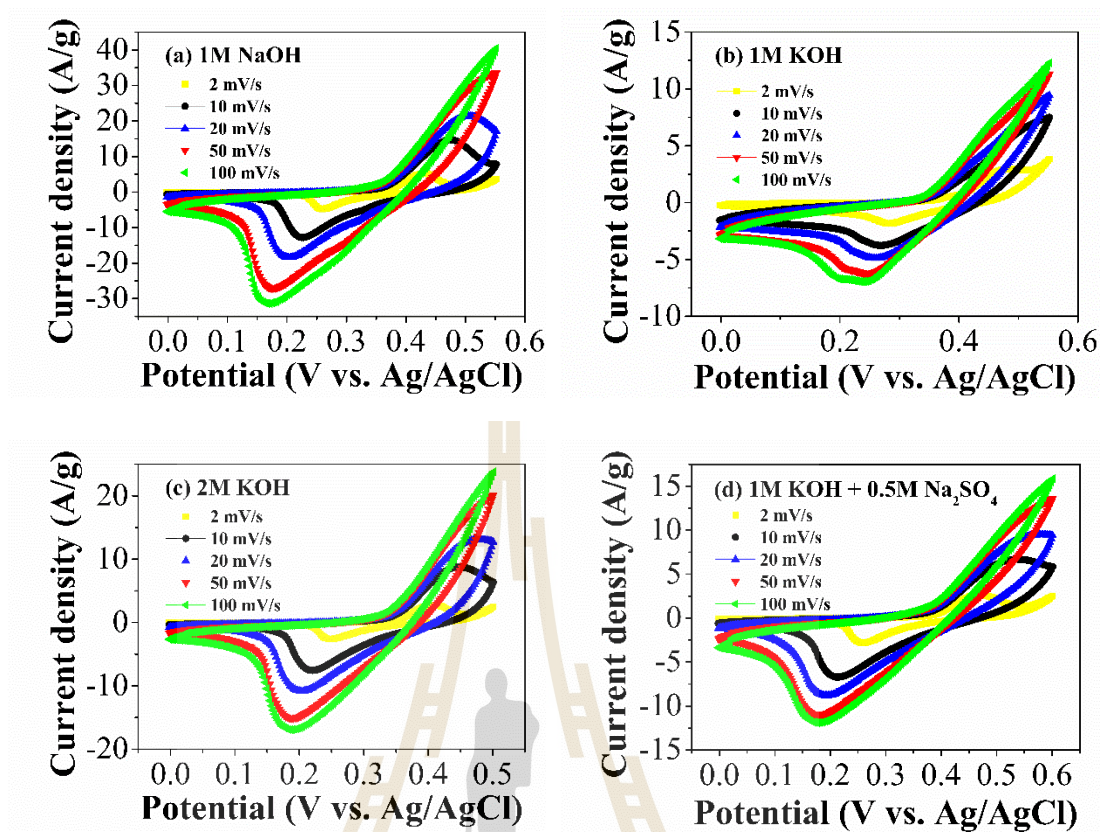


Figure 4.6 (a-d) CV curves of the Ni(OH)_2 electrodes measured in different aqueous electrolytes and scan rate (mV/s).

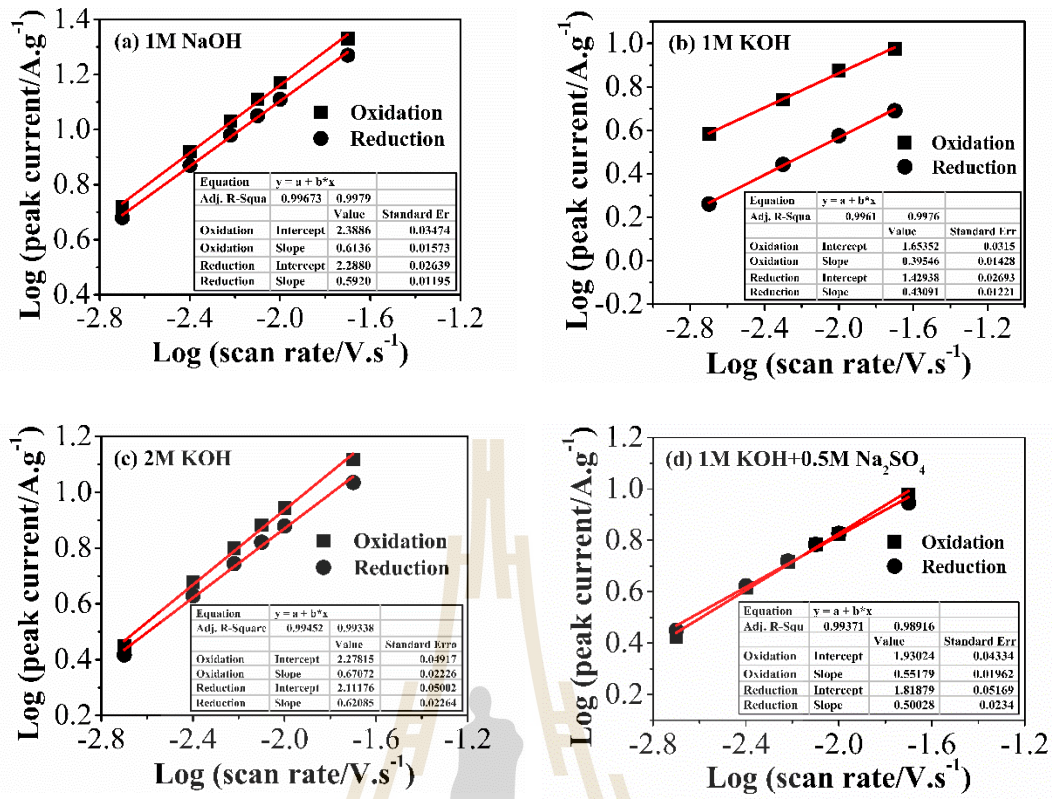
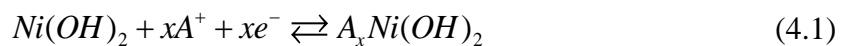


Figure 4.7 (a-d) The plot between log (*i*) vs. log (*v*) of the Ni(OH)₂ electrodes in 1M NaOH, 2M KOH and 1M KOH + 0.5M Na₂SO₄, respectively.

Figure 4.8 shows a comparison of CV curves in different alkaline electrolytes at a scan rate of 2 mV/s. It can be clearly seen that all the CV curves show the oxidation and reduction peaks during both charging and discharging processes, indicating a faradic reaction (Krishnan *et al.*, 2015). The redox peaks of Ni(OH)₂ electrodes correspond to the reversible redox reaction of $\text{Ni}^{2+} \rightleftharpoons \text{Ni}^{3+} + e^-$ (Li *et al.*, 2018). Based on the intercalation/deintercalation charge storage mechanism, the possible mechanism of Ni(OH)₂ electrode in 1M NaOH, 1M KOH, 2M KOH, and 1M KOH + 0.5M Na₂SO₄ aqueous electrolyte is proposed as (Augustyn *et al.*, 2014; Sankar *et al.*, 2015; Pang *et al.*, 2012).



Where A is Na^+ and K^+ ions. This chemical reaction can be explained that during the charging process, the alkaline cation of the electrolyte intercalates into $\text{Ni}(\text{OH})_2$ matrix and releases an electron. Whereas the discharging process, the alkaline cation of the electrolyte deintercalates from $\text{Ni}(\text{OH})_2$ matrix and diffuses into the electrolyte solution (Sankar *et al.*, 2015). Importantly, the larger CV curve is observed in 1M NaOH electrolyte, suggesting that it offers a higher capacitance value.

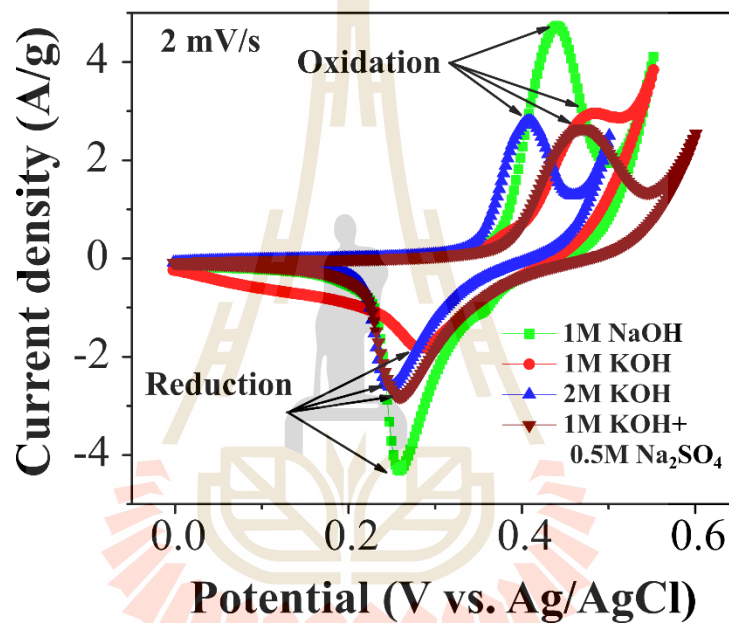


Figure 4.8 Comparison of CV curves of $\text{Ni}(\text{OH})_2$ electrodes measured at scan rate of 2 mV/s.

4.1.3.2 Galvanostatic charge/discharge

Figure 4.9(a) shows a comparison of the charging and discharging curves of the $\text{Ni}(\text{OH})_2$ electrodes measured at a current density of 1 A/g. Non-linear curves are observed, implying that the electrodes store the charge base on redox or intercalation/deintercalation mechanism (Senthilkumar *et al.*, 2014). The longer time for discharging is observed in 1M NaOH electrolyte. Moreover, IR drop which is related to the contact resistance between current collector and electrode material,

solution resistance and charge transfer resistance (Yan *et al.*, 2015) is also observed as shown in the inset of Figure 4.9(a). Clearly seen that Ni(OH)₂ electrode measured in 1M NaOH aqueous electrolyte shows the lowest value of IR drop in which the highest specific capacitance value is expected in the lowest IR drop value.

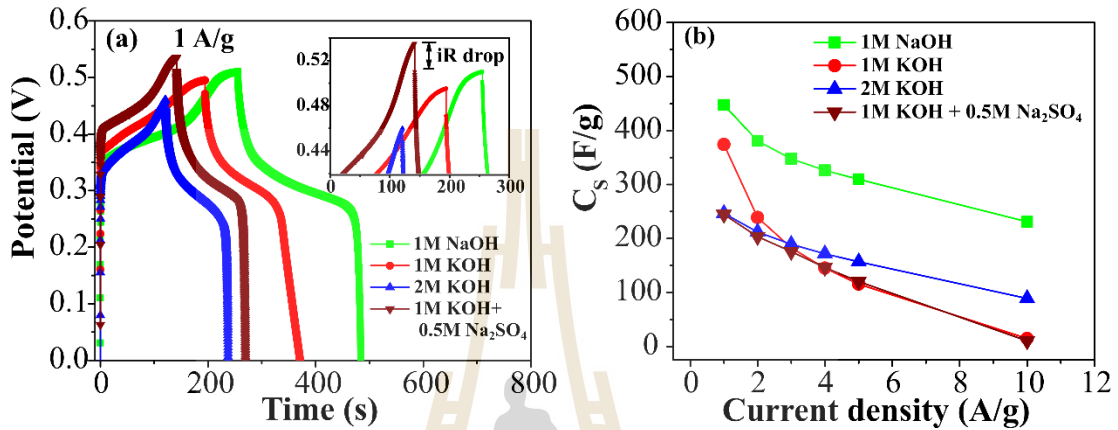


Figure 4.9 (a) Comparison of charge and discharge curves measured at current density of 1 A/g and (b) the calculated specific capacitance obtained from the discharge curves of Ni(OH)₂ electrodes.

The calculated specific capacitance for Ni(OH)₂ in various electrolytes from the discharging curves is presented in Figure 4.9(b). As a result, the Ni(OH)₂ electrode measured in 1M NaOH electrolyte shows the highest specific capacitance value of 447.03 F/g at a current density of 1 A/g that is nearly two times higher than in other electrolytes. The calculated specific capacitance in various electrolytes is summarized in Table 4.1. With increasing of the current density, the specific capacitance value decreases. This can be explained by the electrolyte ions have enough time to diffuse into the active sites of the electrode material at the lower current density, providing the higher capacitance value while the diffusion time is limited at the higher current density (Shanmugavani *et al.*, 2015). In a contrary, the lowest specific

capacitance value is found in the mixed solution, which is in good agreement with the coulombic efficiency result as shown in Figure 4.10.

Table 4.1 The summarized specific capacitance value of Ni(OH)₂ electrodes as function of current density in various electrolytes.

Current density (A/g)	Specific capacitance (F/g)			
	1M NaOH	1M KOH	2M KOH	1M KOH + 0.5M Na ₂ SO ₄
1	447.03	373.99	246.59	244.33
2	380.50	238.75	212.12	203.29
3	347.60	182.55	189.18	175.75
4	326.19	145.13	171.45	146.13
5	309.73	115.34	156.69	120.15
10	231.07	14.80	88.94	10.15

Comparing aqueous electrolyte of 1M NaOH with 1M KOH, the hydrated sphere, the ionic conductivity, and the ionic mobility of the cations (Zhang *et al.*, 2012; Xu *et al.*, 2011; Zhu *et al.*, 2015) have no significant influence on the specific capacitance value of the Ni(OH)₂ electrodes, which higher specific capacitance value is expected in the smaller hydrated sphere with higher ionic conductivity and mobility of K⁺ ion. The summarized data of these parameters are listed in Table 4.2. In contrast, the free ionic radius (Na⁺ < K⁺) plays an important role on the specific capacitance value of the Ni(OH)₂ electrodes. This can be explained by the relatively easy intercalation/deintercalation of the smaller free ionic radius of Na⁺ ion (0.95 Å) compared with the K⁺ ion (1.33 Å).

Table 4.2 Bare ion size, radius of hydration sphere, ionic mobility and molar ionic conductivity of Na^+ and K^+ ions (Zhong *et al.*, 2015).

Ion	Bare ion size (Å)	Hydrated sphere radius (Å)	Ionic mobility ($10^{-8} \text{ m}^2 \text{ s}^{-1} \text{ V}^{-1}$)	Molar ionic conductivity ($\text{mS m}^2 \text{ mol}^{-1}$)
Na^+	0.95	3.58	5.19	5.01
K^+	1.33	3.31	7.62	7.35

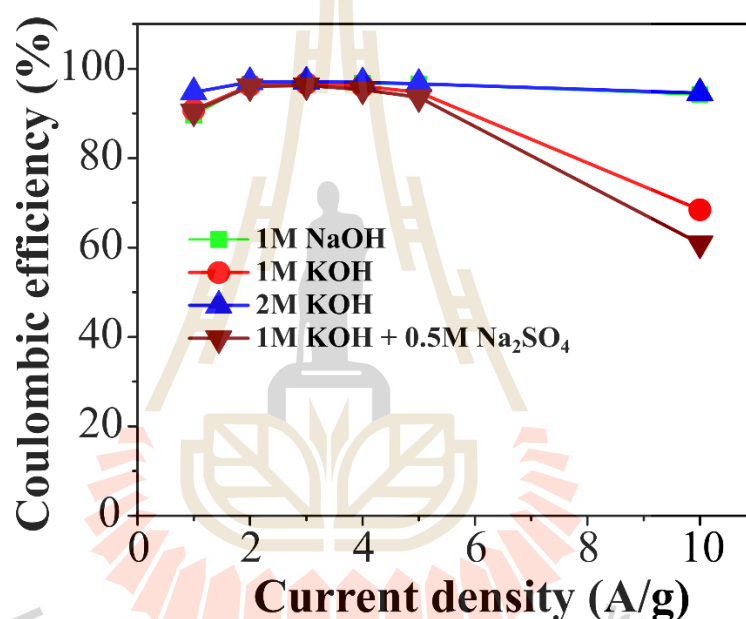


Figure 4.10 The calculated coulombic efficiency of $\text{Ni}(\text{OH})_2$ electrodes in various electrolytes.

The coulombic efficiency (η) was calculated by the following equation of $\eta = t_d/t_c$ where t_d (s) and t_c (s) are discharging and charging times, respectively (He *et al.*, 2012). Generally, the coulombic efficiency is higher than 95%, indicating an ideal capacitive behavior (Ferrero *et al.*, 2015; Laheäär *et al.*, 2015). Based on these results, it is confirmed that the highest capacitance value is found in the 1M NaOH electrolyte due to the highest coulombic efficiency of about 94% at a current density of

10 A/g while the mixed solution shows the lowest coulombic efficiency of about 60% at the same current density.

4.1.3.3 Electrochemical impedance spectroscopy

To further understand the electrochemical performance of the $\text{Ni}(\text{OH})_2$ electrode in different electrolytes, EIS was carried out in the frequency range of 0.1 Hz to 100 kHz at an amplitude of 0.1 V. In general, EIS data are presented as a Nyquist plot or the plot between the imaginary part ($-Z''$) against the real part (Z').

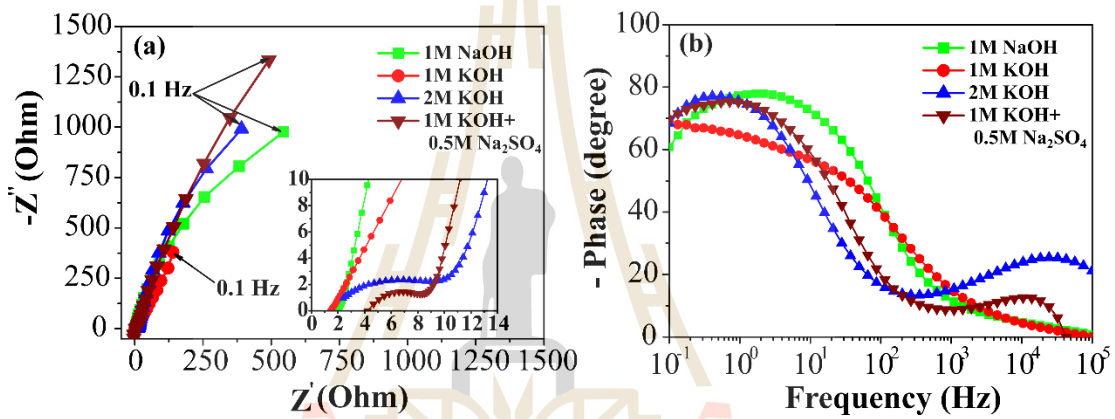


Figure 4.11 (a) Nyquist plots and (b) Bode plots of $\text{Ni}(\text{OH})_2$ electrodes measured at the frequency range of 0.1 Hz to 100 kHz.

As shown in Figure 4.11(a), a Nyquist plot can be divided into three regions. In high frequency region, the intercept of the real axis indicates the bulk resistance (R_s), which is a combination of pore electrolyte resistance, bulk resistance, and a contact resistance between the current collector and electroactive material (Li *et al.*, 2015). The R_s values are estimated to be 1.80, 1.48, 1.38, and 2.42 Ohm in 1M NaOH, 1M KOH, 2M KOH, and 1M KOH + 0.5M Na_2SO_4 , respectively. Moreover, the semicircle curves are observed at the middle frequency. The diameter of the semicircle corresponds to the charge transfer resistance (R_{ct}) caused by Faradic reactions (Qu *et al.*, 2010). It can be seen that the smallest diameter of the semicircle is

found in 2M KOH electrolyte, indicating that it offers a faster charge transfer, ensuring a high capacitive performance (Zhao *et al.*, 2013). In low frequency region, nearly straight lines with an angle along the real axis of about 65° are observed. The slope of the curve shows the Warburg impedance (Z_w), which represents the electrolytes diffusion in the host materials that is observed in all electrolytes (Kumar *et al.*, 2015).

Figure 4.11(b) shows a bode plots of Ni(OH)_2 electrodes in different electrolytes. A bode plot is used to determine the maximum phase angle and frequency response time (Hwang *et al.*, 2017). It is observed that the Ni(OH)_2 electrode measured in 1M NaOH shows the maximum phase angle of about -78° , which is close to the ideal capacitive behavior (-90°). According to the equation $\tau_o = 1/f_o$ where τ_o is relaxation time and f_o is frequency (Yu *et al.*, 2014), the higher the frequency the faster of ion response time (Xu *et al.*, 2014). The Bode plots also present peaks in a high frequency region in both 2M KOH and 1M KOH mixed with 0.5M Na_2SO_4 electrolytes, demonstrating a pseudo charge transfer resistance in the system (Song *et al.*, 2013). To the best of our knowledge, the presence of a charge transfer resistance in 2M KOH and 1M KOH mixed with 0.5M Na_2SO_4 electrolytes is attributed to a decrease in the electrochemical performance.

4.1.3.4 Cyclic stability

The long-term stability of the Ni(OH)_2 electrode in different electrolytes was investigated by repeating the GCD test at a current density of 5 A/g for 1000 cycles. Interestingly, the Ni(OH)_2 electrode performed in 1M NaOH electrolyte shows the greatest cycle stability with increasing capacitance from the initial capacitance and retains about 100% after 1000 cycles as shown in Figure 4.12.

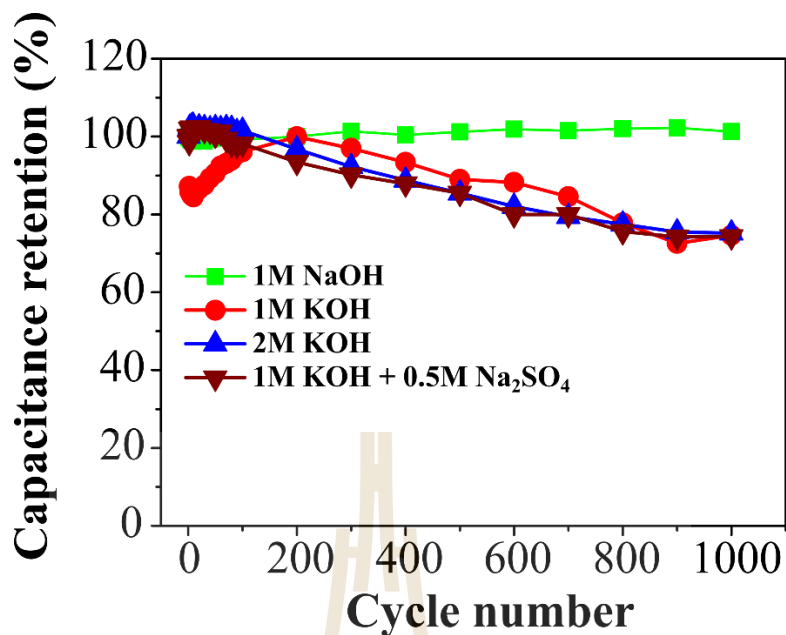


Figure 4.12 Comparison of capacitance retention of Ni(OH)₂ electrodes measured in different electrolytes at 5 A/g for 1000 cycles.

Turning to the synthesis of Ni(OH)₂ nanostructures process, the NaOH solution plays an important role as a precipitating agent that is associated with the creation of mesopores on the surface of the hexagonal Ni(OH)₂ nanostructures as clearly seen in the TEM image. Moreover, NaOH is frequently used in a chemical activation process in order to provide a very high surface area of carbon materials (Raymundo-Piñero *et al.*, 2005; Lillo-Ródenas *et al.*, 2003). Therefore, the increase in the capacitance retention in 1M NaOH electrolyte upon charging and discharging for 1000 cycles may be come from to the enhancement or development of the pores on the Ni(OH)₂ surface that were created in the 1M NaOH electrolyte. Another reason is due to the increasing active species exposed to the electrolyte upon repetitive charge/discharge cycling (Shao *et al.*, 2012). However, Ni(OH)₂ electrode measured in 1M KOH, 2M KOH, and 1M KOH + 0.5M Na₂SO₄ electrolytes exhibit poor cyclic stability with loss of about 25% after 1000 cycles. This might be induced by the

adhesion loss between the electro-active material and the current collector (Yan *et al.*, 2012) or due to the phase transformations and/or the dissolution of active materials (Lu *et al.*, 2017).

To further understand the cyclic stability of the Ni(OH)_2 electrodes in different aqueous electrolytes, the morphology of Ni(OH)_2 electrodes with corresponding EDS result before and after 1000 charging/discharging cycles in 1M NaOH, 1M KOH, and 1M KOH + 0.5M Na_2SO_4 electrolytes were carried out. According to the FE-SEM images, the closely packed of hexagonal Ni(OH)_2 nanoplates with providing a porosity on the surface before the electrochemical test is observed as presented in Figure 4.13(a), which the elemental compositions of electrode materials including active material Ni(OH)_2 , polymer binder (PVDF), and carbon black are confirmed as shown in the EDS results of Figure 4.13(a) (right). After 1000 GCD cycles test, the FE-SEM image of 1M KOH shows the cracks on the surface of the Ni(OH)_2 electrode without the detected of the polymer binder (F) element as seen in Figure 4.13(b). Besides that, the decrease of the interconnected pore size between the agglomerated nanoplates is observed in the mixed electrolyte (Figure 4.13(c)). Therefore, the decrease of the cyclic stability in 1M KOH, 2M KOH, and 1M KOH + 0.5M Na_2SO_4 electrolyte may be explained from the above results.

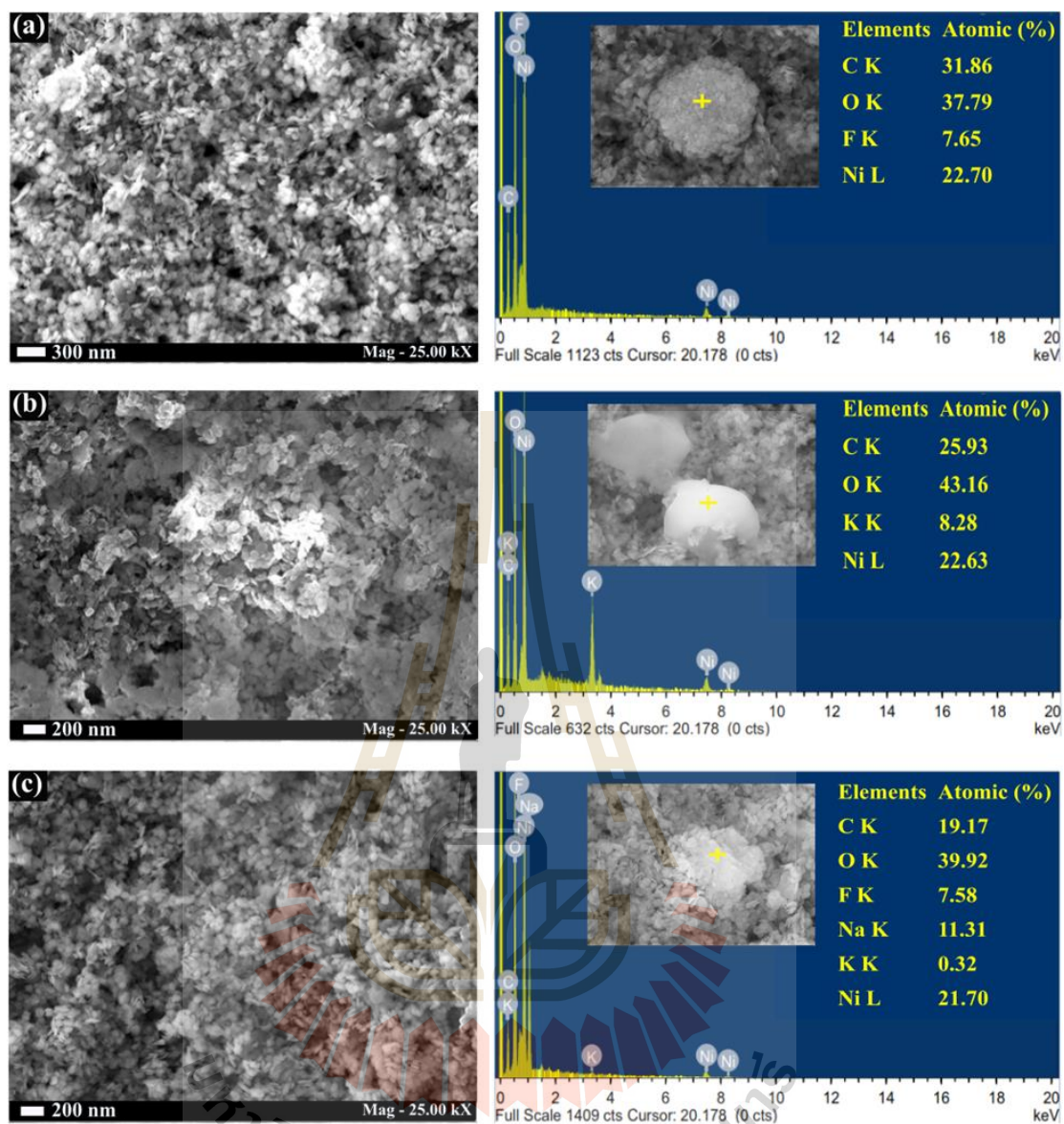


Figure 4.13 FE-SEM images and their corresponding EDS results of the Ni(OH)_2 electrodes (a) before the electrochemical measurements and (b) after GCD test for 1000 cycles in 1M KOH and (c) 1M KOH + 0.5M Na_2SO_4 electrolytes.

More importantly, the structural instability from repeating intercalation/deintercalation of Na^+ ion into the Ni(OH)_2 electrode causes a seriously agglomerated of the Ni(OH)_2 nanoplates as clearly seen in the FE-SEM image of 1M NaOH electrolyte after 1000 GCD cycles measurement as shown in Figure 4.14(a).

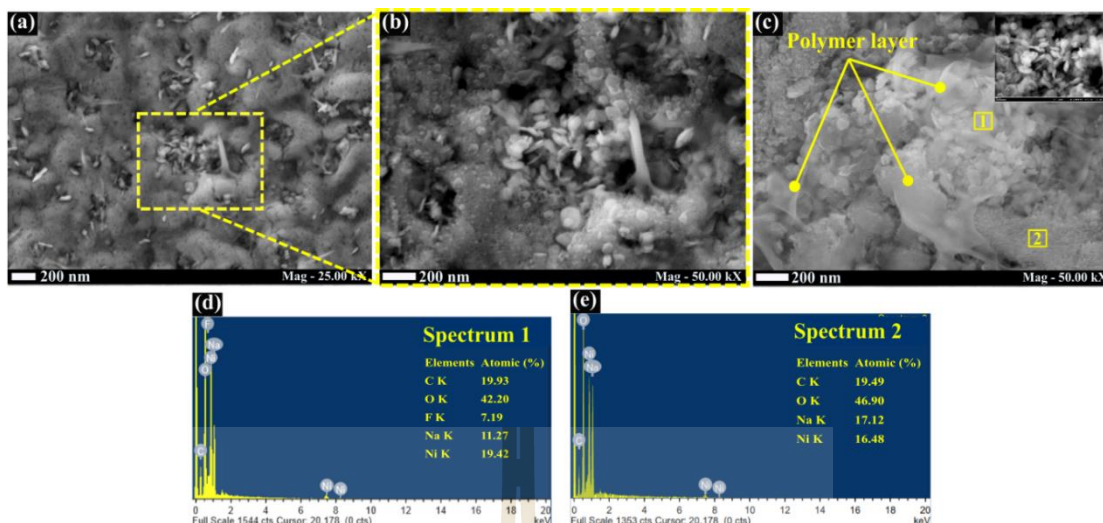


Figure 4.14 (a-c) FE-SEM images with different magnifications of the Ni(OH)_2 electrodes after 1000 GCD cycles test at current density of 5 A/g in 1M NaOH electrolytes and (d-e) the corresponding EDS results of the Ni(OH)_2 electrodes in different detected areas.

Furthermore, the pores producing by PVDF with the located of Ni(OH)_2 nanoplates inside the pore are observed in Figure 4.14(b) and some of the agglomerated nanoplates are covered with thin polymer layer of PVDF (Figure 4.14(c)). The thin polymer layer found here is very important for the long-term cyclic stability for the Ni(OH)_2 electrode that it acts as a glue to connect the electrode materials, including Ni(OH)_2 nanoplates and carbon black together, resulting in an adhesion between electrode materials and current collector. The forming of polymer layer was reported to limit the mobility of ions (Liu *et al.*, 2011). However, due to the higher content of active material of Ni(OH)_2 (80 wt. %) there is insufficient PVDF to form a thin layer, which wraps around both Ni(OH)_2 nanoplates and carbon black as evidence in the lack of the detected F element in EDS result of Figure 4.14(e). Therefore, the carbon black tends

to form as the ionic conducting network (Wagner *et al.*, 2016) that promotes the intercalation/deintercalation of Na^+ ions into the active sites of the electrode material.

From the above results, we can conclude that the presence of thin polymer layer on the surface of the $\text{Ni}(\text{OH})_2$ electrode is very important for the long-term cyclic stability. Therefore, the decrease of the cyclic stability in 1M KOH, 2M KOH, and 1M KOH + 0.5M Na_2SO_4 aqueous electrolytes may be concluded by the absence of polymer layer or the adhesion loss between electrode materials and current collector after the measurement of GCD for 1000 cycles.

4.1.3.5 Energy density and power density

The electrochemical performance of $\text{Ni}(\text{OH})_2$ electrode was also determined by the well-known Ragone plot or the plot between energy density and power density. Figure 4.15 shows the Ragone plots of $\text{Ni}(\text{OH})_2$ electrodes in different electrolytes. The energy density and power density of $\text{Ni}(\text{OH})_2$ electrodes were calculated by using equation 3.35 and 3.36, respectively. The maximum energy density is found to be 16.28 Wh/kg at a power density of 256 W/kg in 1M NaOH electrolyte, suggesting that the $\text{Ni}(\text{OH})_2$ electrodes are promising candidates for supercapacitor applications.

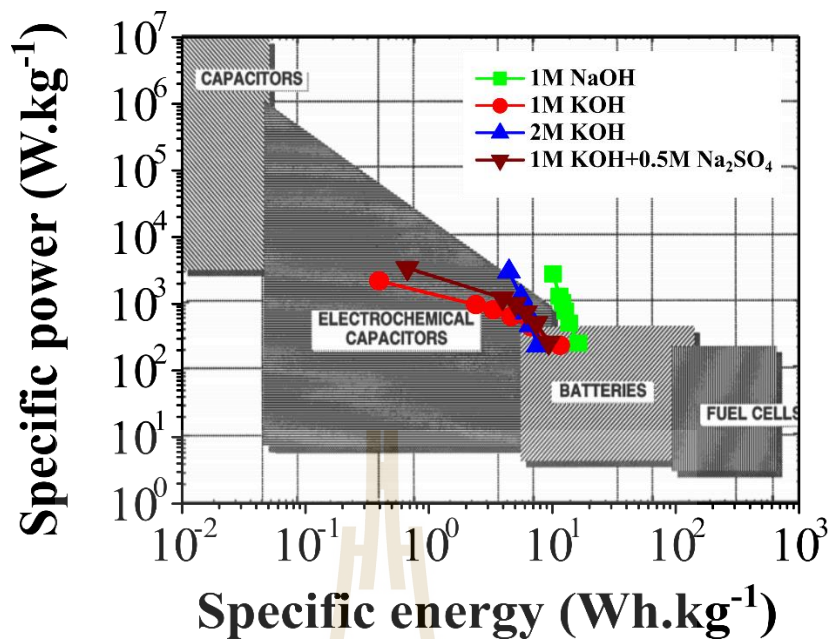


Figure 4.15 Ragone plots of $\text{Ni}(\text{OH})_2$ electrodes compared in various electrolytes.

4.2 Electrochemical studies of $\text{Ni}(\text{OH})_2$ on GDL substrate

Electrochemical capacitors are one of the energy storage devices which generally consists of the following four main parts of active material, electrolyte, separator, and current collector. One of these parts which decides the electrochemical performance is current collector. The current collector, also known as substrate, plays an significant roles in electrochemical capacitors including (Huang *et al.*, 2018): (i) collecting and conducting electricity from the electrode to power source and (ii) supporting the active materials or serving as a holder of the active materials. Therefore, the physical and chemical properties of current collector can impact the performance of electrochemical capacitors which different current collectors result in different electrochemical performances.

Ni foam is a widely used current collector in laboratory research due to its cheap, mechanical strength, inertness, and relatively low toxicity (Grdeń *et al.*, 2012). Generally, opened-pore Ni-foam is produced by coating Ni metal on a polymer type matrix of polyurethane using chemical vapor deposition (CVD) or electrochemical deposition technique (Chaudhari *et al.*, 2017). Therefore, the surface oxide layer can easily form by exposing Ni foam in air. This layer gives rise to an overpotential that reduced the power output (Grdeń *et al.*, 2012). Also, an errors in specific capacitance value due to the presence of nickel oxide/hydroxide on the surface of Ni foam especially the used small amount of active materials in electrochemical measurement was reported (Xing *et al.*, 2011). To overcome this problem, carbon paper namely gas diffusion layer (GDL) is used as a current collector in this study.

GDL is a carbon-based current collector which is generally used in several studies, especially in fuel cell (Gao *et al.*, 2010; Gurau *et al.*, 2006; Bapat and Thynell, 2008; El-Kharouf *et al.*, 2012; Lim and Wang, 2004) and Li-ions batteries (Arbizzani *et al.*, 2005). GDL is made up of interconnected carbon-based electrically conductive material with providing a porous structure. This structure allows GDL to immobilize active materials for the charge transfer. The properties of GDLs such as low sheet resistance, large surface area, good physical strength, biocompatibility and lightweight architecture enable them to be employed as current collectors for supercapacitor applications (Zhang and Gong, 2015).

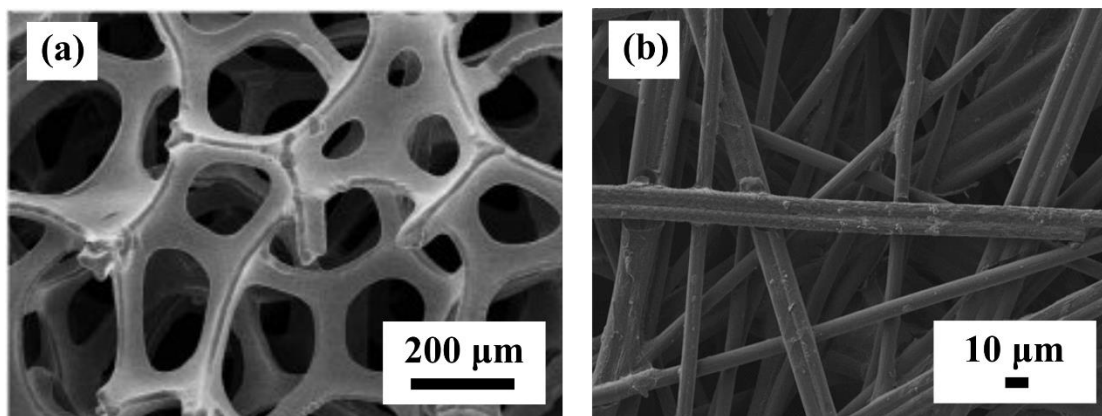


Figure 4.16 Schematic overview of (a) typical Ni-foam substrate adapted from (Li *et al.*, 2014) and (b) GDL substrate of non-woven straight carbon fibers type.

Generally, GDL can be classified into two main groups of woven and non-woven. Carbon cloth group is defined as a woven GDL and carbon paper group is non-woven GDL. According to the carbon fibers arrangement, the non-woven group can be divided into straight and spaghetti fibers types (El-Kharouf *et al.*, 2012). FE-SEM images of two well-known current collectors of Ni foam and straight fiber type of GDL are shown in Figure 4.16.

In this work, non-woven straight carbon fibers type of GDL was used as current collector. The electrochemical studies of $\text{Ni}(\text{OH})_2$ on this type of substrate including the electrode preparation are reported.

4.2.1 Electrode preparation of $\text{Ni}(\text{OH})_2$ on GDL substrate

In the preparation of working electrode, an active material of $\text{Ni}(\text{OH})_2$, conducting agent of carbon black (CB), and binder of polyvinylidene difluoride (PVDF) in the mass ratio of 80:10:10 were hand-mixed using aggregate mortar and pastel. N-methyl pyrrolidone (NMP) solution of 200 μL was directly added to the mixed powder and it was then shaken for 6 h by using mini-shaker in order to obtain a

homogeneous slurry. The slurry of 1 μL was dropped onto GDL substrate, which was placed on the hotplate with temperature of $\sim 90^\circ\text{C}$, within the active area of $1 \times 1 \text{ cm}^2$. The obtained mass loading of $\text{Ni}(\text{OH})_2$ with subtraction of the substrate was about 2-3 mg. The preparation process is illustrated in Figure 4.17.

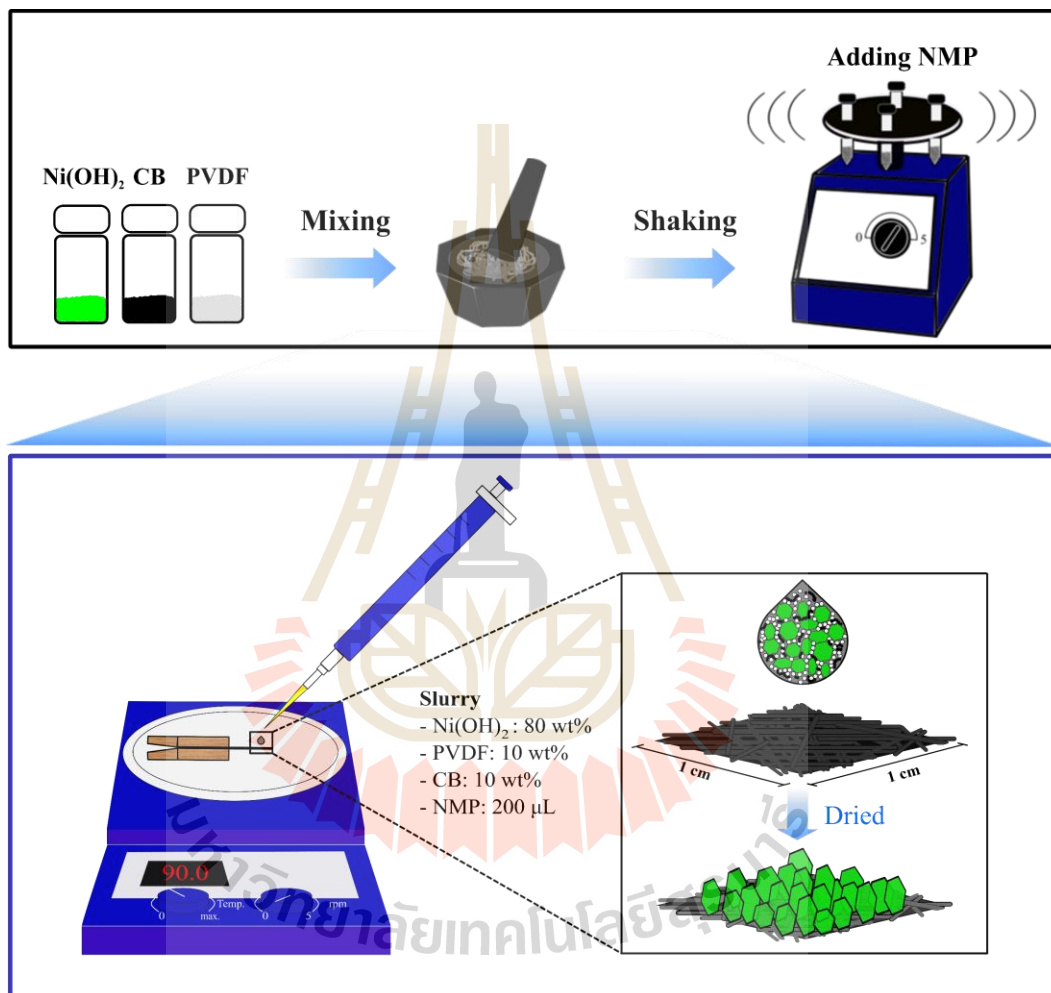


Figure 4.17 Schematic representation for the electrode preparation of $\text{Ni}(\text{OH})_2$ on GDL substrate.

4.2.2 Structural analysis of the prepared $\text{Ni}(\text{OH})_2$ working electrode

Figure 4.18 shows the XRD patterns of XRD holder, bare GDL substrate, the synthesized $\text{Ni}(\text{OH})_2$ powder, and the prepared working electrode. As seen in Figure 4.18(d), XRD pattern of the prepared working electrode shows a series

of sharp peaks within a 2θ ranging from 10 – 80° . The diffracted peaks locate at $2\theta \sim 19.3, 33.0, 38.5, 52.2, 59.0, 62.6, 69.3, 70.5$, and 72.7° corresponding to the lattice planes of (001), (100), (101), (102), (110), (111), (200), (103), and (201) of $\beta\text{-Ni(OH)}_2$ (JCPDS file no. 14-0117), respectively. Owing to the fact that diffracted beams are arisen from different lattice planes, resulting in the observed series of peak. Moreover, the diffracted peaks locate at the $2\theta \sim 26^\circ$ and 55° are also observed in the XRD pattern of the prepared working electrode which are the characteristic peaks of (002) and (004) lattice planes of graphite structure, respectively. (Gao *et al.*, 2010; Li *et al.*, 2007; Jiang *et al.*, 2017). It should be noted that all graphite peaks are originated from the GDL substrate. Comparing the prepared working electrode with GDL substrate, we can conclude that the working electrode was successfully prepared.

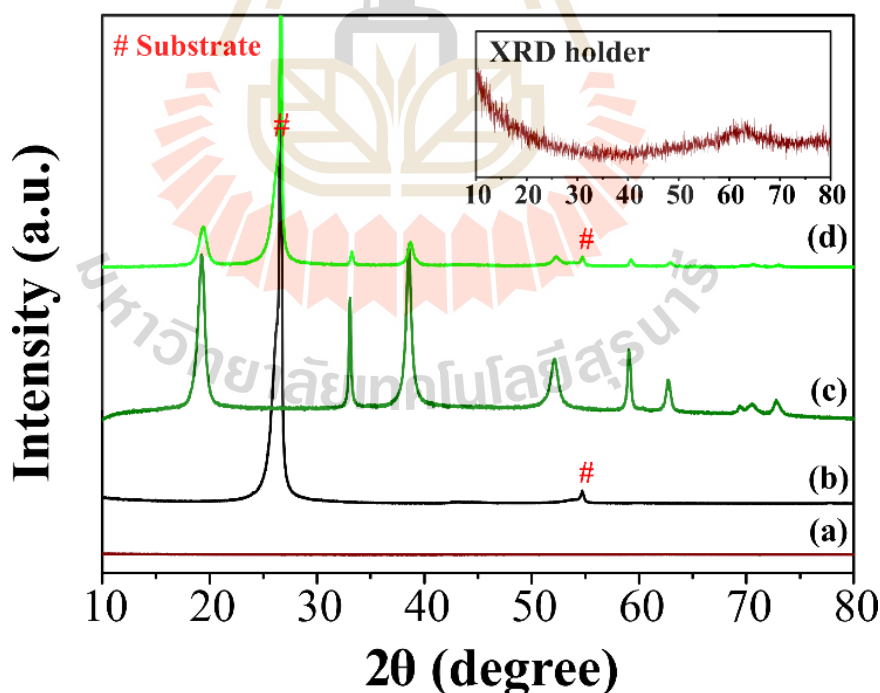


Figure 4.18 XRD patterns of (a) XRD holder, (b) bare GDL substrate, (c) powder Ni(OH)_2 , and (d) the prepared working electrode.

4.2.3 Microstructure and surface morphologies

The surface morphologies and the microstructure of bare GDL substrate and the prepared working electrode are revealed as shown in FE-SEM images of Figure 4.19. It is clearly seen in FE-SEM image that GDL substrate composes of a randomly arrangement of straight carbon fibers in which the interconnected fibers provide a large space between them. These spaces are beneficial for electrolyte ions in order to migrate through the fibers and inner pores, resulting in a decrease of ions transport distance and transport resistance (Liu *et al.*, 2015).

After dropping the slurry on GDL substrate and dried it at $\sim 90\text{ }^{\circ}\text{C}$, the FE-SEM images show that the slurry entirely covered on GDL substrate. As seen in Figure 4.19(b), the presence of a small cracks due to the solvent (NMP) evaporation are also observed on the surface of the prepared working electrode. The high magnificant FE-SEM image (Figure 4.19(d)) shows the aggregation of $\text{Ni}(\text{OH})_2$ plates with providing pores on the surface of the prepared working electrode. As mentioned before, these pores are beneficial for ions diffusion in electrochemical application as they can reduce the diffusion pathway of electrolyte ions resulting in high specific capacitance value.

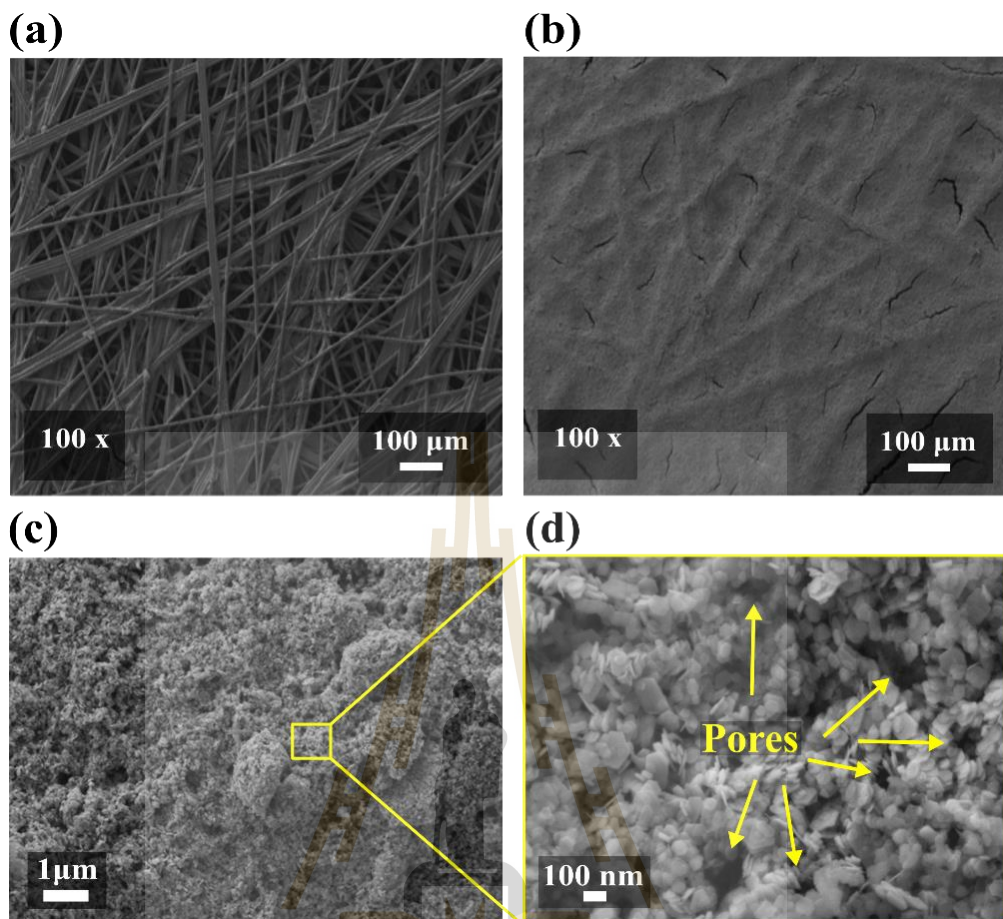


Figure 4.19 FE-SEM images of (a) bare GDL substrate and (b-d) the prepared working electrode with different magnifications.

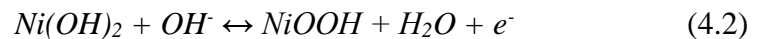
4.2.4 Electrochemical study

The electrochemical performances of $\text{Ni}(\text{OH})_2$ on GDL substrate were evaluated by using three-electrode system. The reference electrode was Ag/AgCl saturated in 3M KCl aqueous electrolyte. The counter electrode was a Pt. plate and the working electrode was the prepared $\text{Ni}(\text{OH})_2$ on GDL substrate.

4.2.4.1 Cyclic voltammetry

At the beginning, two different types of substrates were investigated by cyclic voltammetry (CV) technique. Figure 4.20(a) shows the comparison CV curves of bare Ni foam and GDL substrates which were measured in 1M NaOH aqueous

electrolyte at scan rate of 2 mV/s. The CV curves show remarkable difference between GDL and Ni foam substrates. The CV curve of Ni foam presents redox peak in which the oxidation and reduction peaks are related to Faradaic reaction of Ni(OH)_2 as described by the following well-accepted reaction (Hu *et al.*, 2010).



The oxidation peak at ~ 0.43 V is ascribed to the phase change from β - Ni(OH)_2 to β - NiOOH and the reduction peak at ~ 0.33 V is attributed to the phase transformation from γ - NiOOH or β - NiOOH to β - Ni(OH)_2 (Xing *et al.*, 2011). Therefore, the CV curve in Figure 4.20(a) demonstrates the existence of redox peak on bare Ni foam substrate without adding of any active materials. The presence of this redox peak was reported to generate pseudocapacitance which could bring about an error in the specific capacitance evaluation (Xing *et al.*, 2011). Therefore, GDL substrate was further used for electrochemical studies of Ni(OH)_2 .

Figure 4.20(b) presents the CV curves of Ni(OH)_2 on GDL substrate at different scan rates of 1, 2, 3, 4, 5, and 10 mV/s. A pair of redox peaks is observed, which is attributed to the redox reaction of $\text{Ni}^{2+} \rightleftharpoons \text{Ni}^{3+} + e^-$ (Li *et al.*, 2018). The observed oxidation peak at 0.43 V and reduction peak at 0.36 V were indicated to be due to β - $\text{Ni(OH)}_2/\beta$ - NiOOH redox couple (Xing *et al.*, 2011). With increasing scan rates, the shifts of oxidation peaks to higher potential and reduction peaks to lower potential are observed. The shift of these redox peaks with increasing scan rates ranging from 1 to 10 mV/s was used to identify the charge storage mechanism of Ni(OH)_2 on GDL substrate.

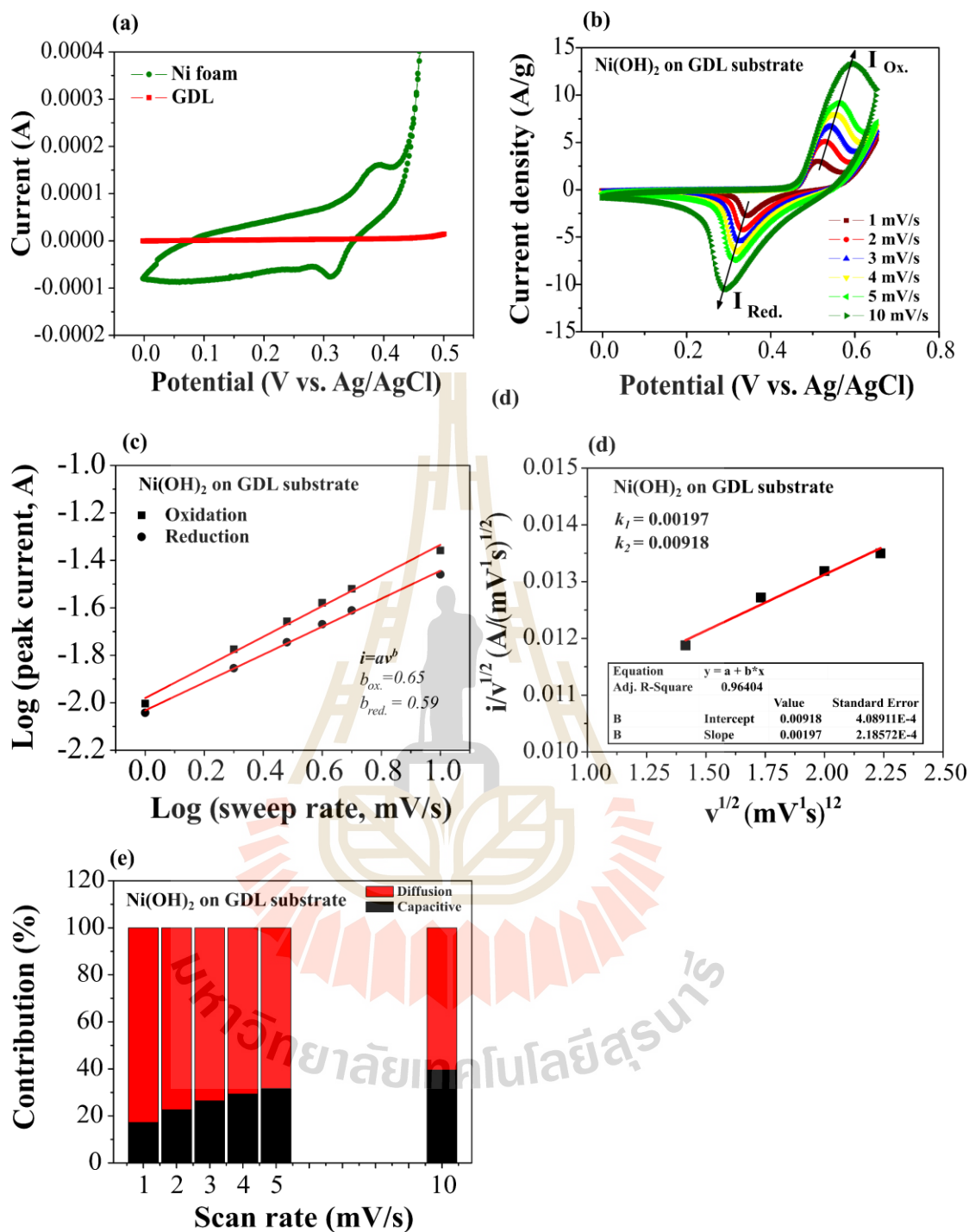


Figure 4.20 (a) Comparison CV curves of Ni foam and GDL substrate, (b) CV curves at different scan rates, (c) the scan rate dependent of peaks current, plots of $i/v^{1/2}$ versus $v^{1/2}$ used to calculate the constants k_1 and k_2 , and (d) the contribution of capacitive and diffusion-controlled mechanism of Ni(OH)₂ on GDL substrate.

4.2.4.2 Kinetic analysis for charge storage mechanism

In general, the dependence of current response with increasing scan rates in a CV measurement can be expressed following the power law of $i = av^b$ where i is the peak current (A), a and b are the adjustable parameters, and v is the scan rate (mV/s). The value of b can be obtained from the slope of the plot between $\log(i)$ versus $\log(v)$. In general, a b -value = 1 indicates that the obtained CV current is due to a capacitive mechanism whereas a b -value = 0.5 indicates that the current is affected by intercalation/deintercalation or diffusion-controlled mechanism.

As shown in Figure 4.20(c), the slopes or the b -values of oxidation and reduction processes are 0.65 and 0.59, respectively. These values are close to 0.5. Hence, it may be concluded that the charge storage of Ni(OH)₂ on GDL substrate originates from intercalation/deintercalation or diffusion-controlled mechanism. Figure 4.20(d) shows the capacitive and diffusion-controlled contribution at different scan rates which obtained from the plot between $i_p/v^{1/2}$ and $v^{1/2}$. It is clearly seen that the capacitive contribution increases with increasing of scan rates, while the diffusion-controlled decreases. This can be explained by the electrolyte ions have enough time to diffuse into the electrode matrix as scan rates decrease, but the diffusion time is limited as scan rates increase. The capacitive and intercalation/deintercalation or diffusion-controlled contributions are summarized in Table 4.3.

Table 4.3 The dependency of the capacitive and diffusion-controlled mechanisms at different scan rates.

Scan rate (mV/s)	Contribution (%)	
	Capacitive	Diffusion-controlled
1	17.148	82.852
2	22.645	77.355
3	26.389	73.611
4	29.276	70.724
5	31.639	68.361
10	39.561	60.439

4.2.4.3 Galvanostatic charge/discharge

Figure 4.21(a) shows the charging and discharging curves of Ni(OH)_2 electrodes measured at a current density of 1, 2, 3, 4, 5, 6, 7, 8, 9, and 10 A/g within the potential window of 0.55 V. As shown in Figure 4.21(a), GCD curves compose of two different curve profiles. The linear profile indicates that the electrode stores charge based on adsorption/desorption of electrolyte ions at the electrode surface, while the plateau profile or battery-type behavior profile implies that the electrode store the charge based on the redox reaction or intercalation/deintercalation mechanism (Senthilkumar *et al.*, 2014). The calculated specific capacitance of Ni(OH)_2 on GDL substrate by using equation 3.34 is presented in Figure 4.2(b). The Ni(OH)_2 electrode shows the highest specific capacitance value of 418.11 F/g at a current density of 1 A/g. With increasing current density from 1 to 10 A/g, the specific capacitance values decrease. This can be explained by the electrolyte ions have enough time to diffuse into the active sites of the electrode material at the lower current density, providing the

higher capacitance value while the diffusion time is limited at the higher current density (Shanmugavani *et al.*, 2015).

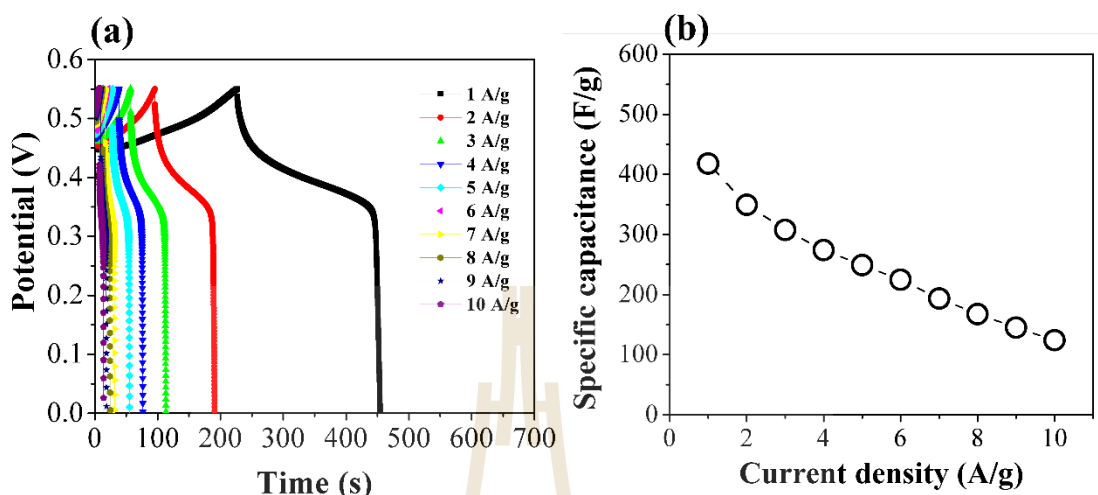


Figure 4.21 (a) Charging and discharging curves of Ni(OH)₂ on GDL substrate at different current densities and (b) the calculated specific capacitance obtained from the discharging curves.

4.2.4.4 Electrochemical impedance spectroscopy

In order to understand electrochemical performance of Ni(OH)₂ on GDL substrate, EIS was carried out in the frequency range of 0.1 Hz to 100 kHz at an amplitude of 0.1 V. As mentioned before, a Nyquist plot or the plot between the imaginary part ($-Z''$) against the real part (Z') can be divided into three regions depending on the frequency range. In high frequency region, the intercept of the real axis indicates the solution resistance (R_s). In mid-to low-frequency region, the charge transfer resistance (R_{ct}) is referred. The diffusion of the electrolyte ions in an electrochemical reaction is defined as a Warburg impedance (Z_w) in low frequency region. As seen in Figure 4.22(a), the R_s values of bare GDL substrate and Ni(OH)₂ on GDL substrate are estimated to be 1.85 and 4.28 Ohm, respectively. Owing to the fact that R_s value is mainly related to the resistance of the substrate and the thickness of the

layer of active material on the substrate (Pardo *et al.*, 2016). The lower R_s value is expected in the thinner electrode following the relation (Meráz *et al.*, 2005).

$$R_s = \frac{L}{\sigma A} \quad (4.3)$$

where L is the thickness of the electrode, σ is the solution conductivity and A is the geometric area of the electrode.

Moreover, the larger charge transfer resistance (R_{ct}) is also observed in bare GDL substrate than in the prepared $\text{Ni}(\text{OH})_2$ on GDL substrate. In generally, the charge transfer resistance associates with heterogeneous electron exchanged involving the redox couple at the electrolyte/electrode interface which is typically given for the equilibrium potential following the Butler-Volmer equation (Wang *et al.*, 2005).

$$R_{ct} = \frac{RT}{nF} \frac{1}{i^0} \quad (4.4)$$

Where R is the molar gas constant, T is temperature, F is Faraday's constant and i^0 is exchange current density of the reaction. According to the equation 4.4, the larger R_{ct} value of GDL substrate is due to the lack of active material $\text{Ni}(\text{OH})_2$ which limited the exchange current density in this process.

At low frequency region, a vertical lines perpendicular to the real axis (Z') are estimated to be about 82.5° and 77.4° in bare GDL substrate and the $\text{Ni}(\text{OH})_2$ on GDL substrate, respectively. A straight line with an angle of 90° indicates the pure capacitive behavior and low diffusion resistance of ions in the structure of the electrode (Wang *et al.*, 2011).

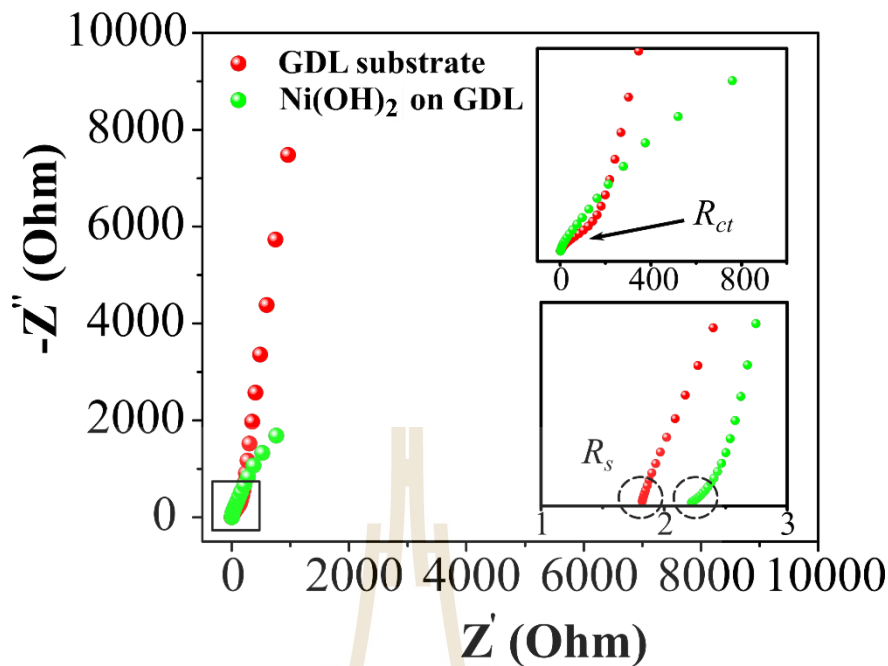


Figure 4.22 Nyquist plots of bare GDL and Ni(OH)₂ on GDL substrate measured at the frequency range of 0.1 Hz to 100 kHz.

4.2.4.5 Cyclic stability

The long-term stability of Ni(OH)₂ on GDL substrate was investigated by repeating the GCD measurement at a current density of 5 A/g for 1000 cycles. As a result, the capacitance retention of Ni(OH)₂ on GDL substrate retains about 81% after 1000 cycles. The decay of the specific capacitance may be due to the loose of electrical contact between the active material and current collector (Tao Li *et al.*, 2019). The calculated coulombic efficiency (η), by using the equation of $\eta = t_d/t_c$ where t_d (s) is discharging time and t_c (s) is charging time (He *et al.*, 2012), is also followed the same trend as the capacitance retention which is found to be about 80% after 1000 cycles as shown in Figure 4.23.

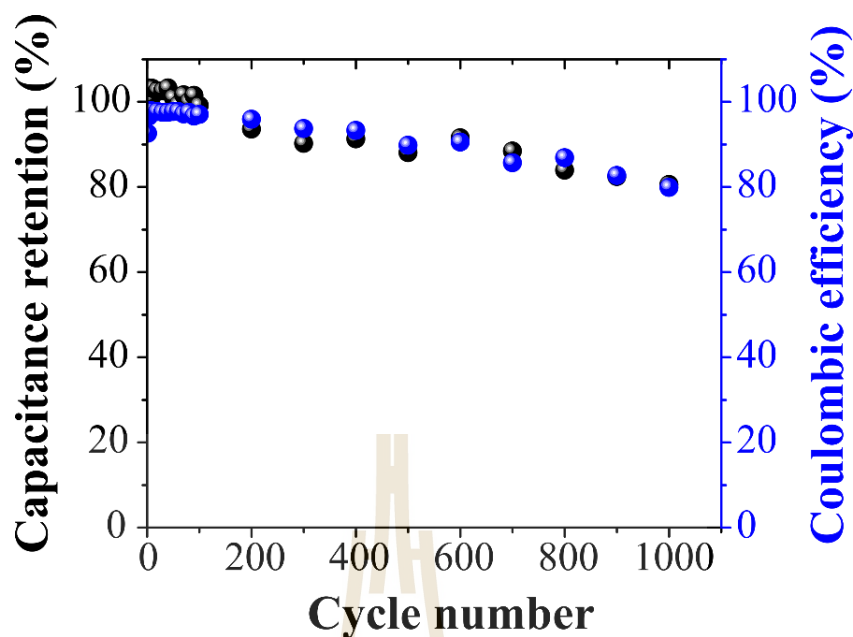


Figure 4.23 The capacitance retention and coulombic efficiency of $\text{Ni}(\text{OH})_2$ on GDL substrate measured in 1M NaOH at current density of 5 A/g for 1000 cycles.

To further understand the long term cyclic stability of $\text{Ni}(\text{OH})_2$ on GDL substrate, the FE-SEM images of $\text{Ni}(\text{OH})_2$ on GDL substrate and the corresponding EDS results before and after GCD measurement for 1000 cycles were revealed. The difference of electrode surface before (see Figure 4.19(b)) and after GCD measurement (Figure 4.24(a)) is observed. It can be noticed in Figure 4.24(a) that the electrode surface consists of two different areas denoted as area 1 (black color) and area 2 (white color). In addition, the high magnificant FE-SEM images reveal the separation between these two areas with the severe cracks on the electrode surface as seen in Figure 4.24(b-c).

In general, cracks are generated from the elastic mismatch between two attached surfaces and are commonly considered as a defects (Lee *et al.*, 2016). The existence of cracks on the electrode surface was reported due to the large volume change, leading to the loss of the electrical contact between individual particles which

results in capacity fading in Lithium-ion battery (Ghosh *et al.*, 2019). On the other hand, the stable mechanical structure and excellent long-term stability were reported by introducing cracks into NiO nanosponge due to NiO is capable expanding/ contracting freely during charge/discharge process (Zhang *et al.*, 2016). Moreover, the densely packed of Ni(OH)₂ plates in the area of active material is clearly observed in Figure 4.24(d). The EDS spectrum of the cycled GCD of the area of substrate denoted as the detected area number 1 shows a very small amount of nickel (Ni) (Figure 4.24(e)). Unlike the EDS spectrum of the active materials denoted as detected area number 2, the amount of this element is high. Interesting result is that the high amount of sodium (Na) is detected in area number 1 when compared with the detected area number 2 as shown in the EDS spectra of Figure 4.24(e-f). Hence, this result suggests the occurrence of new phase after cyclic stability test.

As presented above, the decay of specific capacitance from its initial value may be attributed to the presence of the new phase as evidenced in the EDS result after long cyclic stability test together with the presence of crack on the surface of the prepared working electrode. With further increase of the cycle number, the peeling off or falling down of active materials from the GDL substrate is expected.

The schematic diagram for an explanation effect of cracks on the capacitance decay is proposed as shown in Figure 4.25. Based on the intercalation/deintercalation charge storage mechanism of Ni(OH)₂, the existence of cracks on the electrode surface is helpful for the diffusion of electrolyte ions (Na⁺ ions) into the electrode due to the shorter of the diffusion pathway (see Figure 4.25(b)) when comparing with the uncrack surface as shown in Figure 4.25(a). However, upon repeating charge and discharge or intercalation/deintercalation for many cycles ($c^{th} \rightarrow$

∞), the poor interconnected between the active materials and substrate resulting in the serve cracks on the electrode surface or the separation between active materials and current collector will be observed as shown in Figure 4.2(c).

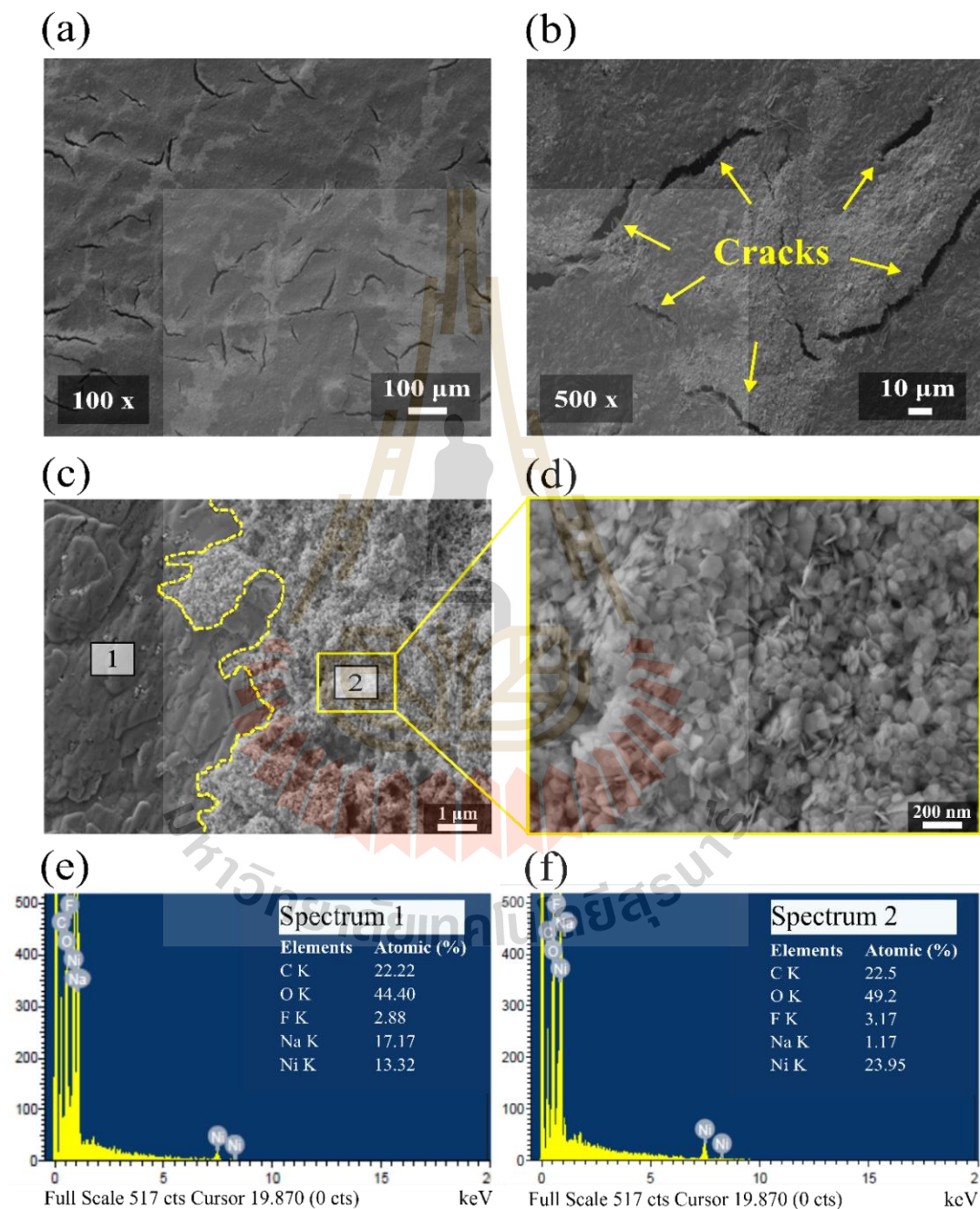


Figure 4.24 (a-d) Surface morphologies and (e-f) the corresponding EDS spectra of $\text{Ni}(\text{OH})_2$ on GDL substrate after repeating GCD measurements for 1000 cycles.

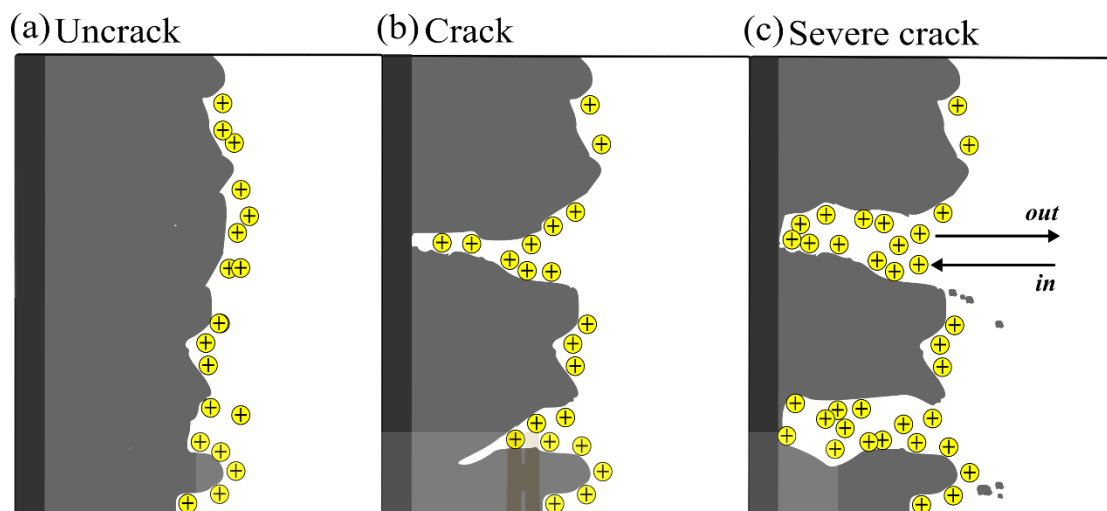


Figure 4.25 The schematic representation of (a) uncrack, (b) crack, and (c) severe crack on the electrode surface of Ni(OH)_2 on GDL substrate.

4.2.4.6 Energy density and power density

Figure 4.26 shows the Ragone plots of Ni(OH)_2 on GDL substrate. The calculated energy density and power density at current density of 1 A/g by using equation 3.35 and 3.36 are 17.25 Wh/kg and 272.50 W/kg, respectively. It is well-known that the Ragone plot is used to compare the performance of energy storage devices (Mei *et al.*, 2019). According to the well-known Ragone plot, the electrochemical capacitors cover a wide range of specific energy (0.05-15 Wh/kg) and specific power (10 - 10^6 W/kg) (Kötz and Carlen, 2000). Therefore, Ni(OH)_2 on GDL substrate is suitable for both electrochemical capacitor and battery applications when comparing with the well-known Ragone plot as presented in Figure 4.26.

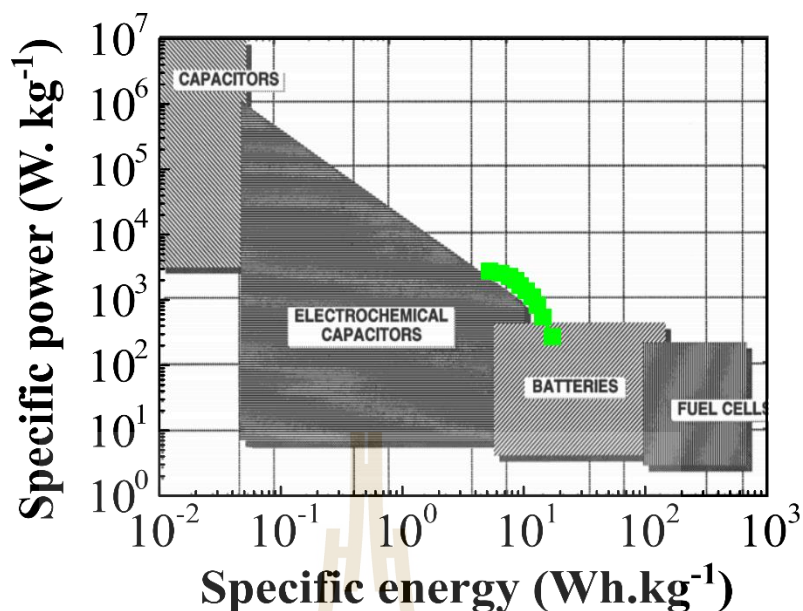


Figure 4.26 The compared Ragone plot of Ni(OH)₂ with the well-known Ragone plot of Kötz (Adapted from (Kötz and Carlen, 2000)).

4.3 Effect of Mg-doped Ni(OH)₂ on structure and electrochemical properties

To enhance the electrochemical performance of electrode materials, the structural design which is based on the turning of structural characteristics like crystallinity, surface area, and morphology is frequently used (Zhang *et al.*, 2016). In this work, the interlayer distance of β -Ni(OH)₂ was modified by the substitution of Ni²⁺ ions with Mg²⁺ ions in order to promote the intercalation/deintercalation of the electrolyte ions. Not only the change of interlayer distance affects the electrochemical performance of Ni(OH)₂, but also the change of charge transfer resistance. Therefore, the effect of Mg doping on structure and electrochemical properties of Ni(OH)₂ is reported in this work.

4.3.1 Structural and morphology analysis

As already mentioned before, X-ray diffraction (XRD) technique is mainly used for crystalline materials characterization. The information about crystal structure of lattice parameters including phase composition can be determined from this technique.

Figure 4.27 shows the XRD patterns of Mg-doped $\text{Ni}(\text{OH})_2$ with different Mg contents of 0.00, 0.05, 0.10, and 0.15, respectively. As seen in Figure 4.27, the diffraction peaks at the diffraction angle (2θ) of about 19.4, 33.0, 38.5, 52.1, 59.0, 62.7, 69.3, 70.4, and 72.6° within the diffraction angle ranging from 10-80 degrees are observed. The overall diffraction peaks well-matched with the standard powder diffraction of hexagonal $\beta\text{-Ni}(\text{OH})_2$ (JCPDS file no. 14-0117) with space group of $P\bar{3}m1$. The observed peaks in XRD patterns, from low - to high - diffraction angle (2θ), can be indexed as (001), (100), (101), (102), (110), (111), (200), (103), and (201) lattice planes, respectively. In addition, no diffraction peaks relate to the second phase or the impurities are observed from the XRD patterns of Mg-doped $\text{Ni}(\text{OH})_2$. This may be concluded that Mg^{2+} ions can completely substitute the Ni^{2+} sites in $\text{Ni}(\text{OH})_2$ crystal lattice. Additionally, it can be noticed that the diffraction peaks of $x = 0.15$ shift to lower 2θ . The possible reason is due to the substitution of smaller ionic radius of Ni^{2+} (0.69 Å) with larger ionic radius of Mg^{2+} (0.72 Å) (Shannon, 1976). Whereas the shift of XRD peaks to higher 2θ is also observed in sample of $x = 0.10$. The shift of these diffraction peaks with Mg^{2+} doping suggests the change in lattice parameters.

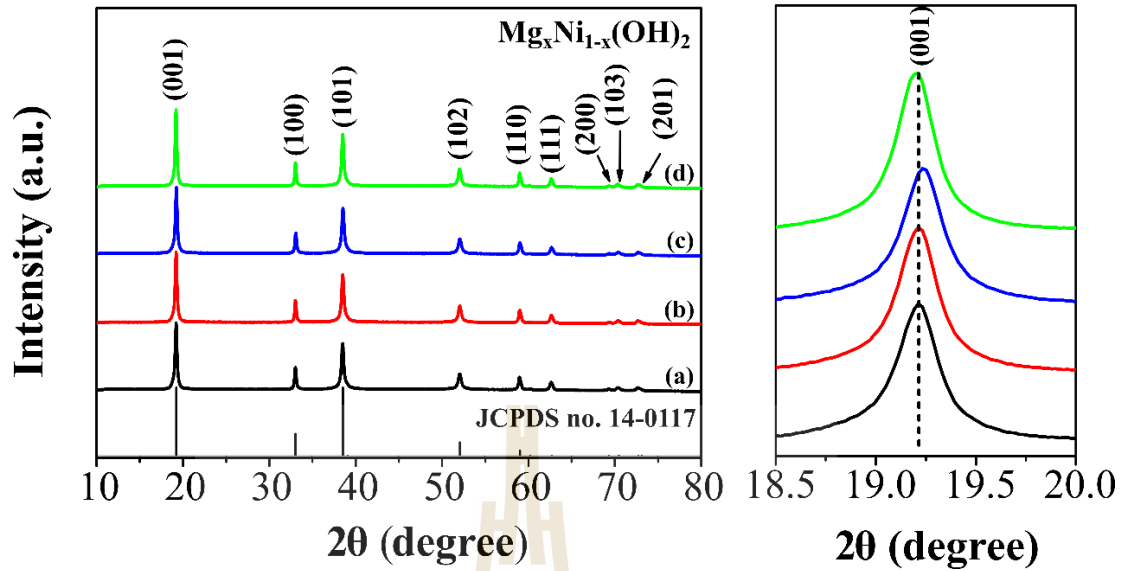


Figure 4.27 XRD patterns of $\text{Mg}_x\text{Ni}_{1-x}(\text{OH})_2$ samples with (a) $x = 0.00$, (b) $x = 0.05$, (c) $x = 0.10$, and (d) $x = 0.15$ and their corresponding enlarged view of the diffraction peaks in 2θ ranging from 18.5 to 20.0 degree.

One can also see in Figure 4.27 that the (001) peaks in $\text{Mg}_x\text{Ni}_{1-x}(\text{OH})_2$ samples show the strongest peaks intensities implying that the crystal growth are related to the stacking of $\text{Ni}(\text{OH})_2$ along the [001] direction (Wang *et al.*, 2018). In the standard powder diffraction data (JCPDS file no. 14-0117), the intensity ratio between (001) and (101) is equal to 1. As seen in Figure 4.27, the observed diffraction intensity of (001) planes is higher than (101) planes meaning that there exists the preferred orientation of the $\text{Ni}(\text{OH})_2$ crystal along the [001] planes which can influence the height of the XRD peak (Li *et al.*, 2018). To explore the structural change affected by the Mg doping, the Rietveld refinement was performed by using JANA2006 software. The Pseudo-Voigt was used as the profile function. The refinement was performed in the 2θ range of 10 - 80° based on the hexagonal crystal structure with space group of $P\bar{3}m1$. The lattice parameters $a = 3.13 \text{ \AA}$ and $c = 4.63 \text{ \AA}$ of $\beta\text{-Ni}(\text{OH})_2$ were used for the lattice parameters

refinement. The values of profile factor (R_p), weighted profile residual (R_{wp}), and goodness of fit (GOF) were used to assess the quality of the refinement. Note that the preferred orientation was also included in the refinement by using March-Dollase function (Zolotoyabko, 2009).

As seen in Figure 4.28, the difference between the observed and calculated profiles is shown at the bottom of each figure. The Bragg positions are indicated by small vertical lines. The refinement results of all $Mg_xNi_{1-x}(OH)_2$ samples are in good agreement between the observed and the calculated XRD pattern. The refined lattice parameters, unit cell volume, and crystal density are given in Table 4.4 in which the values of R_p , R_{wp} , and GOF of $Mg_xNi_{1-x}(OH)_2$ samples are under 10% meaning that the Rietveld refinement results are reliable (Huang *et al.*, 2015; Li *et al.*, 2017). As presented in Figure 4.29, the lattice parameter c values are found to be increased with increasing Mg contents. Whereas the variations of lattice parameters a are observed with increasing Mg contents. The increase of lattice parameter c value indicates the increase of c/a ratio and the unit cell volume with increasing Mg contents. The expansion of unit cell is possibly due to the substitute of the larger ionic radius of Mg^{2+} ions. The average crystallite size from (001), (100), and (101) planes was calculated by using Scherer's equation. Figure 4.29(d) shows that the average crystallite size increases as the Mg content increases. Furthermore, the calculated d -spacing of (001), (100), and (101) planes by using equation 3.3 are summarized in Table 4.4. It was reported that the increase in the interlayer distance which is related to the lattice parameter c of β -Ni(OH)₂ delivered better electrochemical performance (Huang *et al.*, 2013). As clearly seen in Figure 4.30, the lattice parameters c values of the Mg doping samples are higher than the undoped sample meaning that Mg^{2+} ions doping caused the

increase of interlayer spacing which is beneficial to promote the protons diffusion. Therefore, the electrochemical performance is expected to be enhanced with increasing Mg contents.

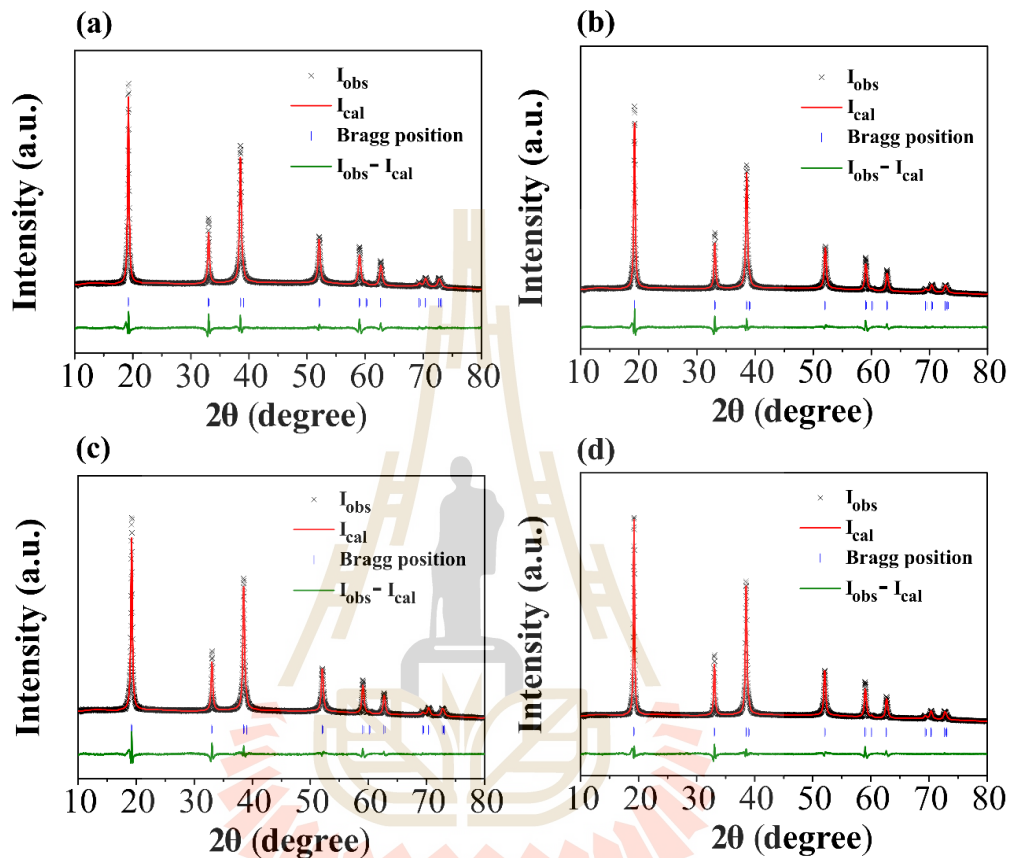


Figure 4.28 Rietveld refinement of $\text{Mg}_x\text{Ni}_{1-x}(\text{OH})_2$ samples with $x = 0.00, 0.05, 0.10$, and 0.15 .

In addition, the decrease in d_{100} value which is associated with Ni-Ni distance within the layers was reported to increase the electronic conductivity due to better orbital overlapping and thus result in a lower polarization in the sample (Oliva *et al.*, 1982). Based on this assumption, the better electrochemical performance is expected in samples of $x = 0.05$ and 0.15 . The electrochemical performance of $\text{Mg}_x\text{Ni}_{1-x}(\text{OH})_2$ samples will be discussed in section 4.3.4.

Table 4.4 The details of lattice parameter a and c , profile factor (R_p), weighted profile residual (R_{wp}), goodness of fit (GOF), unit cell volume, and crystal density obtained from the Rietveld refinement. The calculated d -spacing of (001), (100), and (101) planes and the calculated crystallite size from Scherrer's equation of $Mg_xNi_{1-x}(OH)_2$ samples with $x = 0.00, 0.05, 0.10$, and 0.15 .

Parameters	$x = 0.00$	$x = 0.05$	$x = 0.10$	$x = 0.15$
Lattice parameter (\AA)				
$a = b$	3.128735	3.127884	3.128277	3.127969
c	4.611137	4.611951	4.614351	4.614708
c/a	1.473800	1.474560	1.475150	1.475300
d-spacing (\AA)				
(001)	4.6111	4.6120	4.6144	4.6147
(100)	2.7096	2.7088	2.7092	2.7089
(101)	2.3361	2.3357	2.3363	2.3361
R_p (%)	2.86	2.65	2.69	2.44
R_{wp} (%)	4.37	3.99	3.94	3.70
GOF (%)	2.91	2.67	2.59	2.47
Volume (\AA^3)	39.09095	39.07658	39.10674	39.10207
Density (g/cm^3)	3.937953	3.939401	3.936363	3.936833
D (nm)	41.69 \pm 0.53	42.16 \pm 1.02	44.85 \pm 0.77	45.11 \pm 1.00

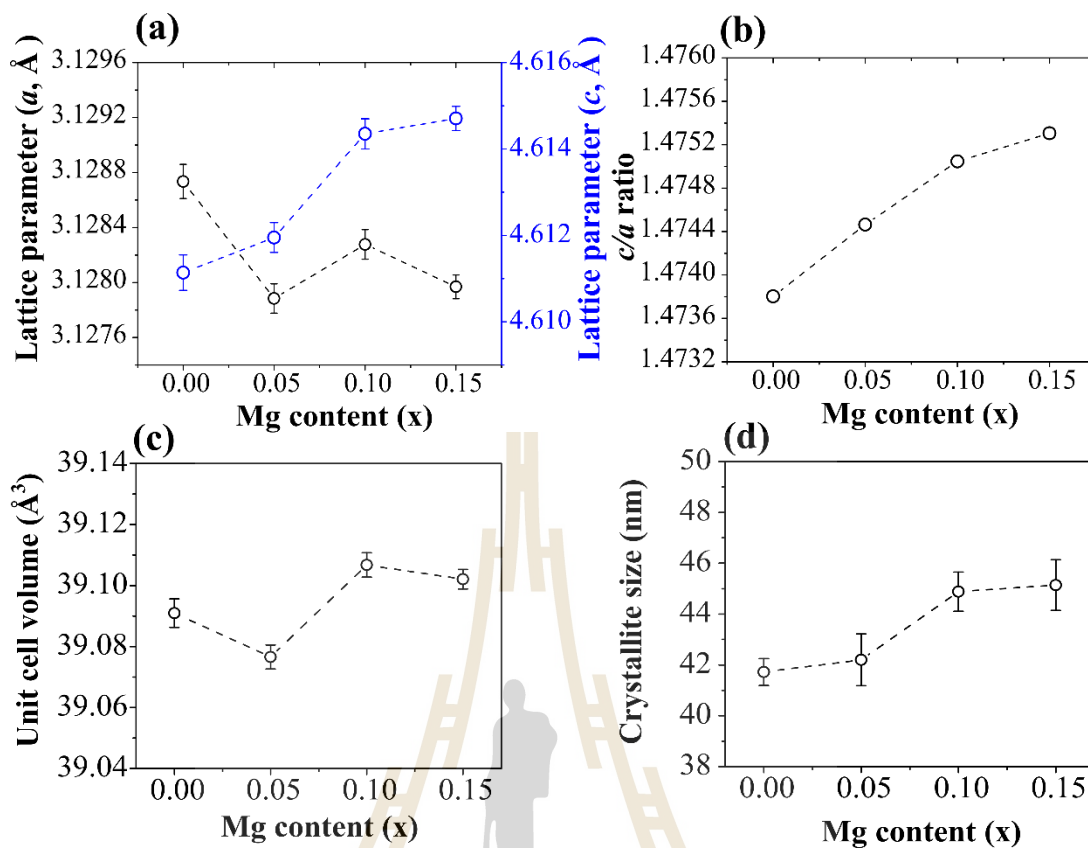


Figure 4.29 (a) Lattice parameters a and c , (b) c/a ratio, (c) unit cell volume, and (d) crystallite size as function of Mg content (x) obtained from Rietveld refinement.

The morphologies with the corresponding selected area electron diffraction (SAED) patterns of $\text{Mg}_x\text{Ni}_{1-x}(\text{OH})_2$ samples with different Mg contents of 0.00, 0.05, 0.10, and 0.15 are revealed as shown in Figure 4.30. It is seen in those TEM bright field images that Mg^{2+} doping is found to have an effect on the particle size of $\text{Ni}(\text{OH})_2$. With increasing Mg contents, the particle sizes seem to be increased except for sample of $x = 0.10$ as clearly seen in Figure 4.32. The average particle sizes of hexagonal shape are estimated to be 41.96 ± 2.57 , 48.88 ± 3.11 , 38.48 ± 2.13 , and 59.48 ± 5.53 nm in sample of $x = 0.00, 0.05, 0.10$, and 0.15 , respectively. The average particle sizes found here have a great impact on the electrochemical performance of

$\text{Mg}_x\text{Ni}_{1-x}(\text{OH})_2$ samples. The effect of particle size on electrochemical performance of $\text{Ni}(\text{OH})_2$ will be discussed in section 4.3.4.

In addition, the difference in morphologies of hexagonal and bar-like shapes of $\text{Ni}(\text{OH})_2$ are also observed in which some of these shapes are stacking together. The observed difference in morphologies of $\text{Ni}(\text{OH})_2$ may be explained by the placing of $\text{Ni}(\text{OH})_2$ nanoplates in different directions. The plate-like morphology is related to an upward (100) facet and the bar-like shape is related to an upward (001) facet (Wang *et al.*, 2015). According to $\beta\text{-Ni}(\text{OH})_2$ structure, the (001) facet is polar and the (100) and (010) facets are non-polar. Therefore, the polar surfaces with potentially high activity diminish easily along the crystal growth because of the surface energy minimization (Zhang *et al.*, 2011). The lattice fringes from high resolution-TEM images with the detected d -spacing of 0.464, 0.477, 0.484, and 0.493 nm are observed in sample of $x = 0.00, 0.05, 0.10$, and 0.15 corresponding to the d -spacing of (001) plane as shown in Figure 4.31(a-d). These results are also in good agreement with the refinement result of the lattice parameters c . Therefore, this result confirms that the bar-like shape of $\text{Ni}(\text{OH})_2$ is due to an upward (001) facet which is consistent with the literature (Li *et al.*, 2018). Additionally, the exposure of (100) planes or rod-like shape was reported to enhance the electrochemical activities of $\beta\text{-Ni}(\text{OH})_2$ due to the easier electron hopping along the [100] direction than that along the [001] direction (Lv *et al.*, 2013). Furthermore, the selected area electron diffraction (SAED) patterns of the $\text{Mg}_x\text{Ni}_{1-x}(\text{OH})_2$ samples show a spotty ring patterns as seen in Figure 4.30. Comparing with the standard diffraction data, the spotty rings show the characteristic of polycrystalline $\beta\text{-Ni}(\text{OH})_2$ (JCPDS file no. 14-0117) which are in good agreement with XRD results.

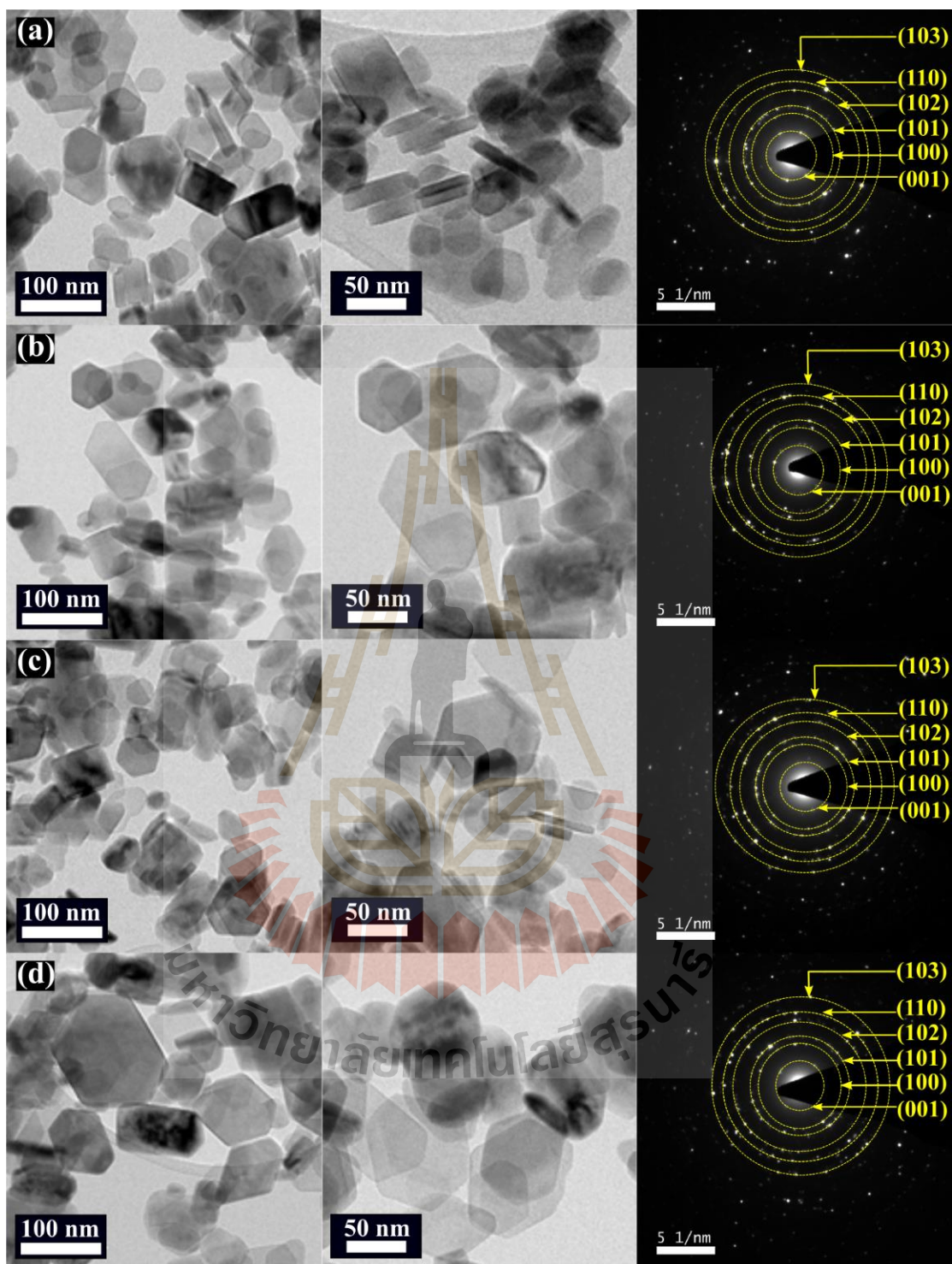


Figure 4.30 TEM bright field images and their corresponding SAED patterns of $\text{Mg}_x\text{Ni}_{1-x}(\text{OH})_2$ samples with (a) $x = 0.00$, (b) $x = 0.05$, (c) $x = 0.10$, and (d) $x = 0.15$, respectively.

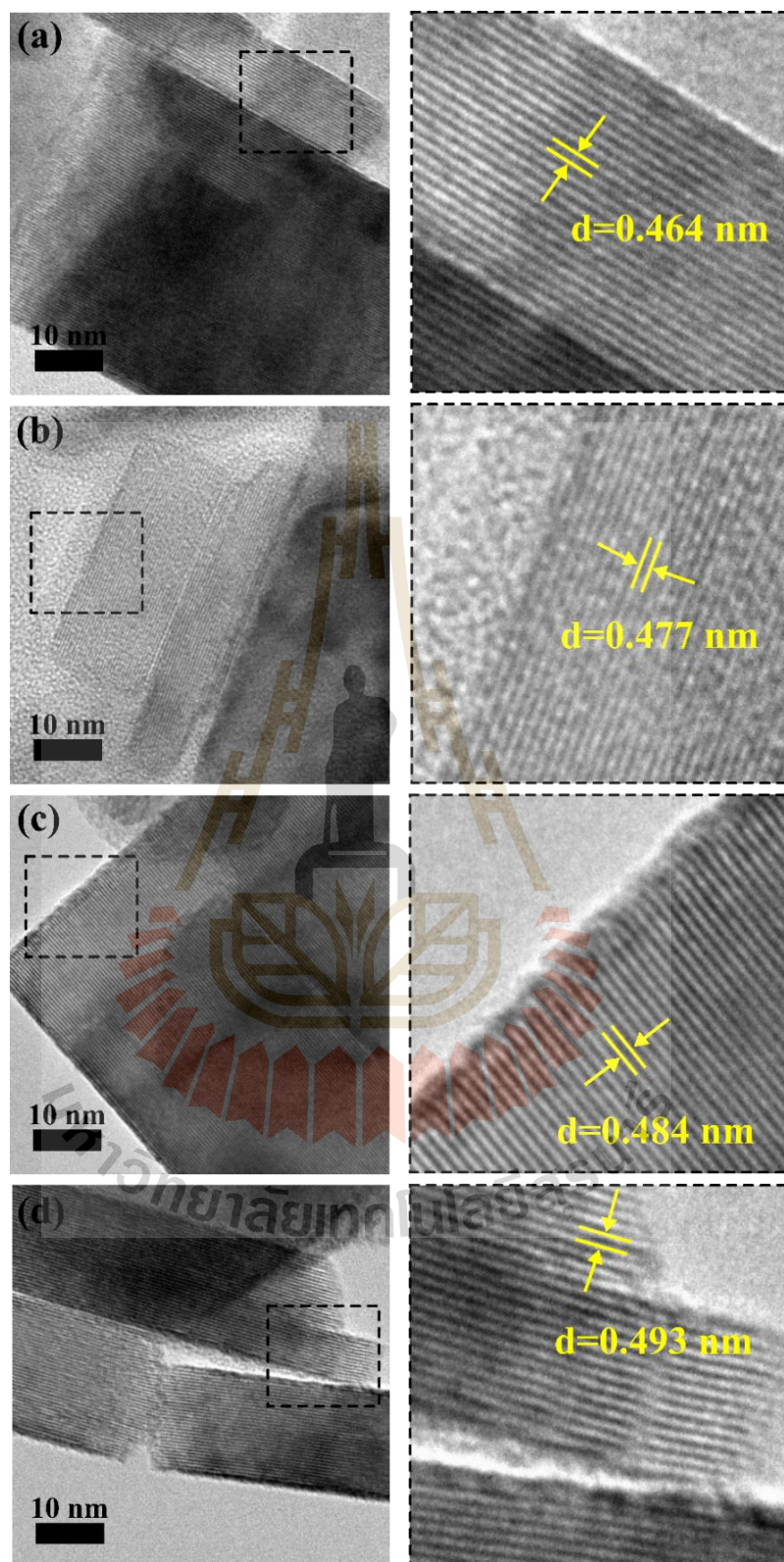


Figure 4.31 Lattice fringes from HRTEM of $\text{Mg}_x\text{Ni}_{1-x}(\text{OH})_2$ samples with (a) $x = 0.00$, $x = 0.05$, $x = 0.10$, and $x = 0.15$, respectively.

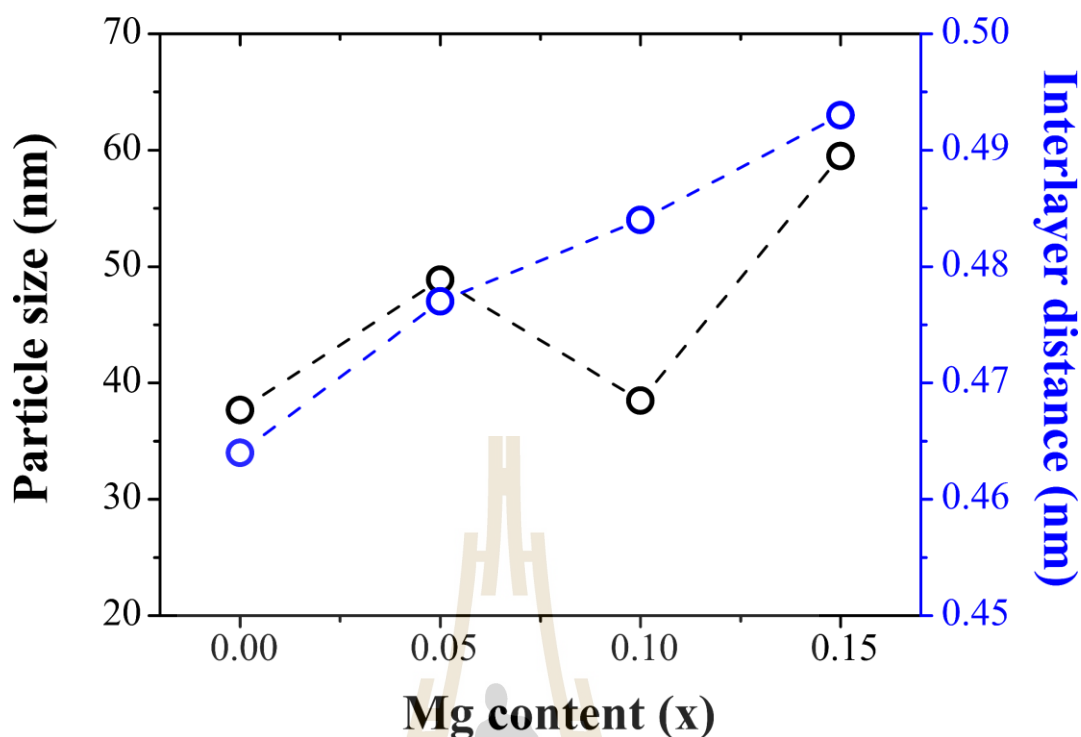


Figure 4.32 The average particle size and the obtained interlayer distance of (001) plane from TEM images of $\text{Mg}_x\text{Ni}_{1-x}(\text{OH})_2$ samples with $x = 0.00, 0.05, 0.10$, and 0.15 .

4.3.2 Chemical compositions and oxidation state analysis

To investigate the change of Mg contents on the chemical environment of $\text{Mg}_x\text{Ni}_{1-x}(\text{OH})_2$ samples, XPS technique is used. Owing to the fact that XPS technique is used for measurement an emitted photoelectron by exciting a samples surface with known energy of X-rays photon. Hence, the binding energy is calculated which is characteristic of chemical bonds in material. From the binding energy and intensity of the photoelectron peak, the chemical compositions and chemical state can be determined. As shown in Figure 4.33(a), the survey spectra confirm the presence of C 1s, O 1s, Ni 2p on the sample surface of all $\text{Mg}_x\text{Ni}_{1-x}(\text{OH})_2$ samples. Due to the fact that XPS is the surface analysis technique and small amounts of Mg^{2+} ions ($x = 0.05, 0.10$, and $x = 0.15$) are substituted in Ni^{2+} sites, thus the characteristic peaks in Mg 2s

region are not clearly observed in all survey spectra of Mg doping as shown in Figure 4.33(a).

The high resolution XPS spectra in Mg 2s region of all Mg doping are shown in Figure 4.33(b). By using Gaussian curve fitting, those three peaks are centered at binding energy of about 88.7- 89 eV which are similar to MgO indicating that the oxidation state of Mg is 2+ (Brown *et al.*, 2011). The slightly shift of Mg 2s peak to higher binding energy of $x = 0.15$ is attributed to more chemical interaction of nickel with magnesium. These results confirm the presence of Mg^{2+} in all $\text{Mg}_x\text{Ni}_{1-x}(\text{OH})_2$ samples.

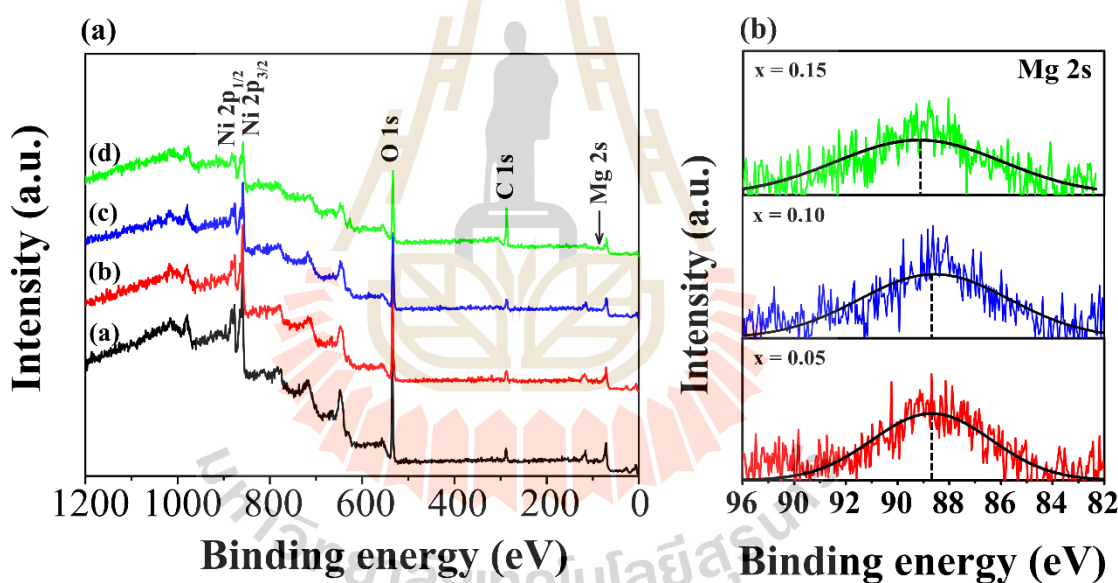


Figure 4.33 (a) The survey XPS spectra and (b) the high resolution XPS spectra in Mg 2s region of $\text{Mg}_x\text{Ni}_{1-x}(\text{OH})_2$ samples with $x = 0.00, 0.05, 0.10,$ and 0.15 .

4.3.3 Specific surface area and porosity analysis

It is well known that the electrochemical performance of the materials largely depends on the specific surface area and pore size distribution, especially for carbon-based materials. The higher specific surface area suggested that to provide a

larger contact area between electrode and electrolyte which is beneficial to a charge accumulation at the electrode/electrolyte interface resulting in a high capacitance (Gao *et al.*, 2019).

To study the porous structure of $\text{Mg}_x\text{Ni}_{1-x}(\text{OH})_2$ samples, the N_2 adsorption/desorption isotherm and pore size distribution were investigated. The specific surface area and pore structure of $\text{Mg}_x\text{Ni}_{1-x}(\text{OH})_2$ samples were determined via Brunauer-Emmett-Teller (BET) (Brunauer *et al.*, 1938) and Barrett-Joyner-Halenda (BJH) (Barrett *et al.*, 1951) methods, respectively. As shown in Figure 4.34(a), the N_2 isotherms of $\text{Mg}_x\text{Ni}_{1-x}(\text{OH})_2$ samples can be classified as type IV according to IUPAC classifications. As clearly seen in the inset of Figure 4.34(a), the presence of hysteresis loops at the relative pressures P/P_0 ranging from 0.8 to 1.0 indicates the characteristic of mesoporous materials.

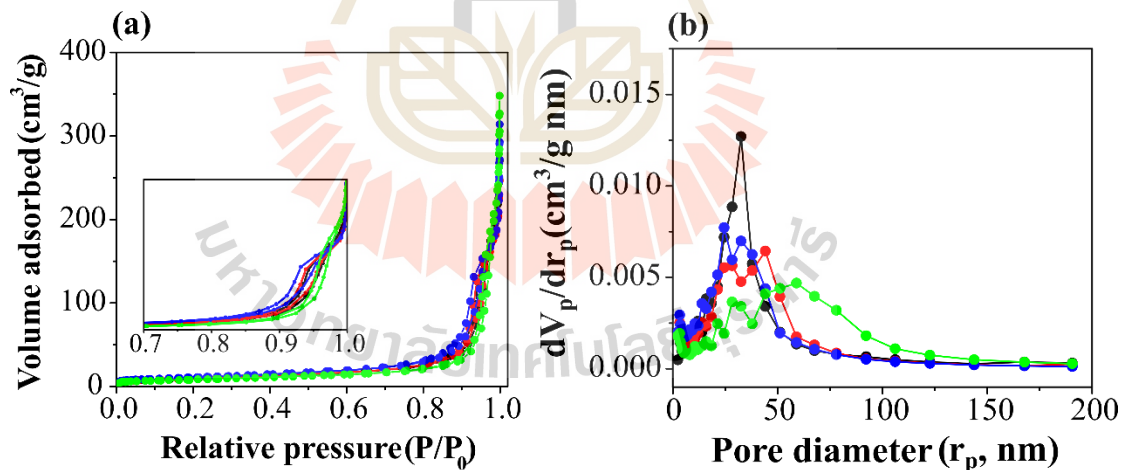


Figure 4.34 (a) N_2 adsorption/desorption isotherms and (b) pore size distribution of $\text{Mg}_x\text{Ni}_{1-x}(\text{OH})_2$ samples with $x = 0.00, 0.05, 0.10$, and 0.15 , respectively.

The BET specific surface areas from the N_2 isotherms were found to be increased from $33.026 \text{ m}^2/\text{g}$ to $38.531 \text{ m}^2/\text{g}$ with increasing Mg contents from 0.00 to 0.10. With further increase of Mg content up to 0.15, the specific surface area was found

to be decreased to 29.428 m²/g. By assuming the nanoparticle to be spherical shape, the particle size (d_{BET}) can be estimated from the specific surface area following the relation (Wang *et al.*, 2007).

$$d_{BET} = \frac{6}{\rho S_{BET}} \quad (4.5)$$

Where ρ is the density (g/cm³) of Mg_xNi_{1-x}(OH)₂ nanoparticles obtained from the refinement and S_{BET} is the specific surface area (m²/g). As a result, the calculated particle size values from BET technique correlate well with the observed particle size by TEM. The summarized data of the specific surface area (S_{BET}), mean pore diameter (D_{MP}), total pore volume (V_T), mesopore diameter (D_{BJH}), mesopore volume (V_{BJH}), and the calculated particle size from BET method (d_{BET}) of Mg_xNi_{1-x}(OH)₂ samples with $x = 0.00, 0.05, 0.10$, and 0.15 are listed in Table 4.5.

Table 4.5 Specific surface area (S_{BET}), mean pore diameter (D_{MP}), total pore volume (V_T), mesopore diameter (D_{BJH}), mesopore volume (V_{BJH}), and BET particle size (d_{BET}), of Mg_xNi_{1-x}(OH)₂ samples.

x	S_{BET} (m ² /g)	D_{MP} (nm)	V_T (cm ³ /g)	D_{BJH} (nm)	V_{BJH} (cm ³ /g)	d_{BET} (nm)
0.00	33.026	36.932	0.305	32.57	0.317	46.13
0.05	33.747	33.818	0.285	44.14	0.287	45.13
0.10	38.531	29.766	0.287	24.49	0.288	39.56
0.15	29.428	45.663	0.336	59.00	0.336	51.79

One can also see in Table 4.5 is that the decrease of particle size causes the increase of BET surface area. This result can be simply explained by the increase of surface-to-volume ratio as particle size decreases. As mentioned before that porous $\text{Ni}(\text{OH})_2$ results from the interconnected of nanoparticles, so the gap or space between individual nanoparticles depends on the particle size. Larger particle size should provide larger gap or space, leading to larger pore diameter in sample of $x = 0.15$. Figure 4.34(b) shows the pore size distributions obtained from BJH method. As seen in Figure 4.34(b), a narrower pore size distribution with a peak centering at 32.57 nm is observed in the undoped sample ($x = 0.00$). After Mg doping, the pore size distributions become wider especially in sample of $x = 0.15$ and those peaks are centered at 44.14, 24.49, and 59.00 nm in samples of $x = 0.05, 0.10$, and 0.15 , respectively. These results indicate that Mg^{2+} doping has a profound influence on the pore size distributions of $\text{Mg}_x\text{Ni}_{1-x}(\text{OH})_2$ samples and these results are also confirmed the existence of mesopore in the materials.

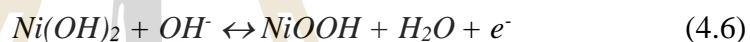
4.3.4 Electrochemical study

The electrochemical performances of $\text{Mg}_x\text{Ni}_{1-x}(\text{OH})_2$ samples were evaluated using three-electrode system. The reference electrode was Ag/AgCl saturated in 3M KCl aqueous electrolyte. The counter electrode was a Pt. plate and the working electrode was the prepared $\text{Mg}_x\text{Ni}_{1-x}(\text{OH})_2$ with $x = 0.00, 0.05, 0.10$, and 0.15 on GDL substrate. Three well-known electrochemical techniques of cyclic voltammetry (CV), galvanostatic charge/discharge (GCD), and electrochemical impedance spectroscopy (EIS) were carried out for electrochemical study.

4.3.4.1 Cyclic voltammetry

As presented in section 4.2, using Ni foam as current collector could bring about an error in a specific capacitance evaluation due to the presence of redox peaks in CV curve of Ni foam substrate. To overcome this problem, the electrochemical properties of Mg-doped Ni(OH)₂ were studied on carbon-type, namely GDL substrate. The preparation of Mg_xNi_{1-x}(OH)₂ electrodes on GDL substrates is described in section 4.2.1. The electrochemical performances of these electrodes were performed in 1M NaOH aqueous electrolyte within the potential window of 0.65 V.

As shown in Figure 4.35, a pair of redox peaks are observed in Mg_xNi_{1-x}(OH)₂ samples, indicating a Faradaic redox reaction. The redox peaks in CV curves are attributed to the following reversible reactions (Nagaraju *et al.*, 2017).



Taking a closer look to the CV curves where the area under CV curve indicates how much charge can store in the materials, larger area under CV curve means higher charge storage (Jia *et al.*, 2018; Singh and Chandra, 2016). It can be noticed that the undoped sample ($x = 0.00$) possess the larger area under CV curves than those of Mg-doped Ni(OH)₂ samples, implying the higher specific capacitance in this sample.

The comparison CV curves of Mg_xNi_{1-x}(OH)₂ samples at scan rate of 2 mV/s are shown in Figure 4.36. It is clearly seen that after Mg doping the area under CV curves decrease with a slight shift of oxidation and reduction peaks toward the higher potential. The potential separation ($\Delta E = E_a - E_c$) between oxidation (E_a) and reduction peaks (E_c) shows the increase of the potential values after Mg doping as shown in the (table) inset of Figure 4.36. As the potential separation decreases, the reversible and charge-discharge efficiency can be enhanced (Yue *et al.*, 2012).

Therefore, this result indicates the worse reversibility after Mg doping. Note that the oxygen evolution reaction (OER), which is occurred during the charging process, is also observed at the potential above 0.5 V in all $\text{Mg}_x\text{Ni}_{1-x}(\text{OH})_2$ samples.

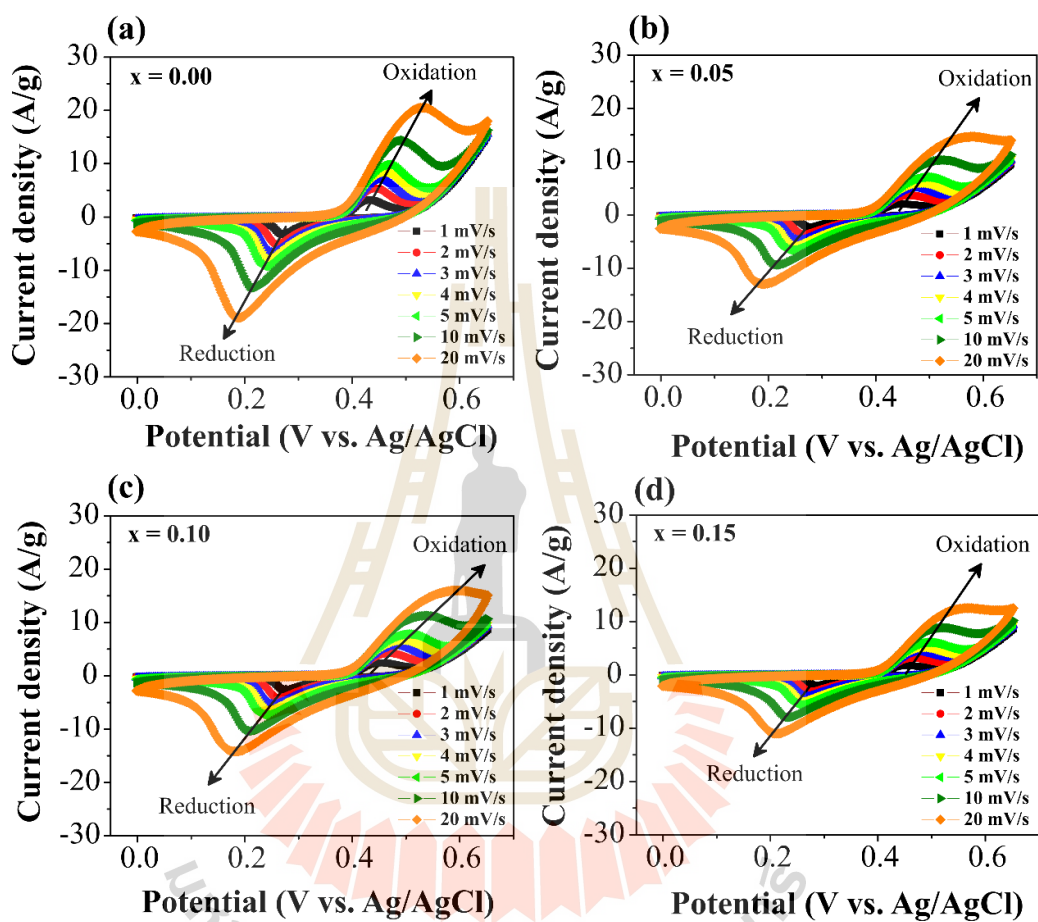


Figure 4.35 CV curves of $\text{Mg}_x\text{Ni}_{1-x}(\text{OH})_2$ samples with (a) $x = 0.00$, (b) $x = 0.05$, (c) $x = 0.10$, and (d) $x = 0.15$ at different scan rates of 1, 2, 3, 4, 5, 10, and 20 mV/s.

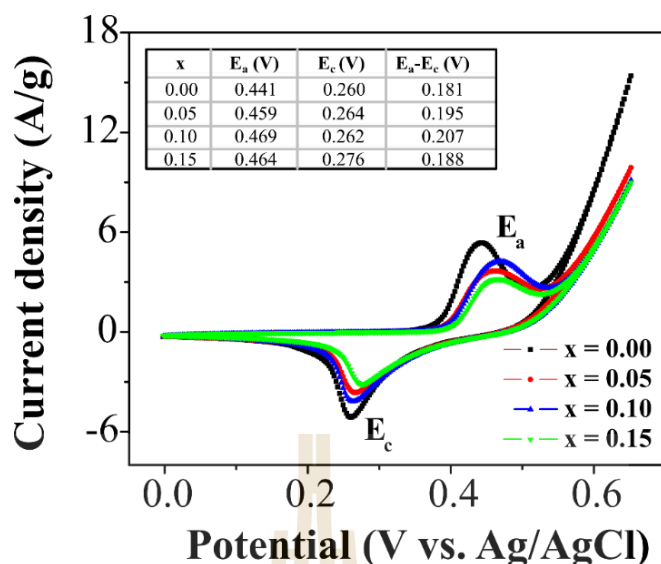


Figure 4.36 Comparison CV curves of $\text{Mg}_x\text{Ni}_{1-x}(\text{OH})_2$ samples at scan rates of 2 mV/s.

4.3.4.2 Kinetic analysis of charge storage mechanism

To further understand the charge storage mechanism, it is necessary to perform a kinetic analysis. The relationship between a scan rate and the peak current response observed in CV measurement can be expressed following the equation 3.28. The obtained b -value from slope of the plot between $\log(i)$ versus $\log(v)$ is generally used to distinguish the charge storage mechanism of the materials. The b -value = 0.5 implies that the current is affected by intercalation/deintercalation or ion diffusion-controlled mechanism and b -value = 1 indicates that the obtained CV current is due to a capacitive mechanism. As seen in Figure 4.37, the obtained b -values from oxidation and reduction peaks in $\text{Mg}_x\text{Ni}_{1-x}(\text{OH})_2$ samples are close to 0.5. Therefore, it can be concluded that the total charge storage in $\text{Mg}_x\text{Ni}_{1-x}(\text{OH})_2$ samples originates from intercalation/deintercalation or diffusion-controlled mechanism. By comparing the obtained b -values from oxidation process with Mg content (x) (Figure 4.38), it is clearly seen that the b -values become more prominent in samples of $x = 0.05$ and 0.15 indicating that the more capacitive processes are governing.

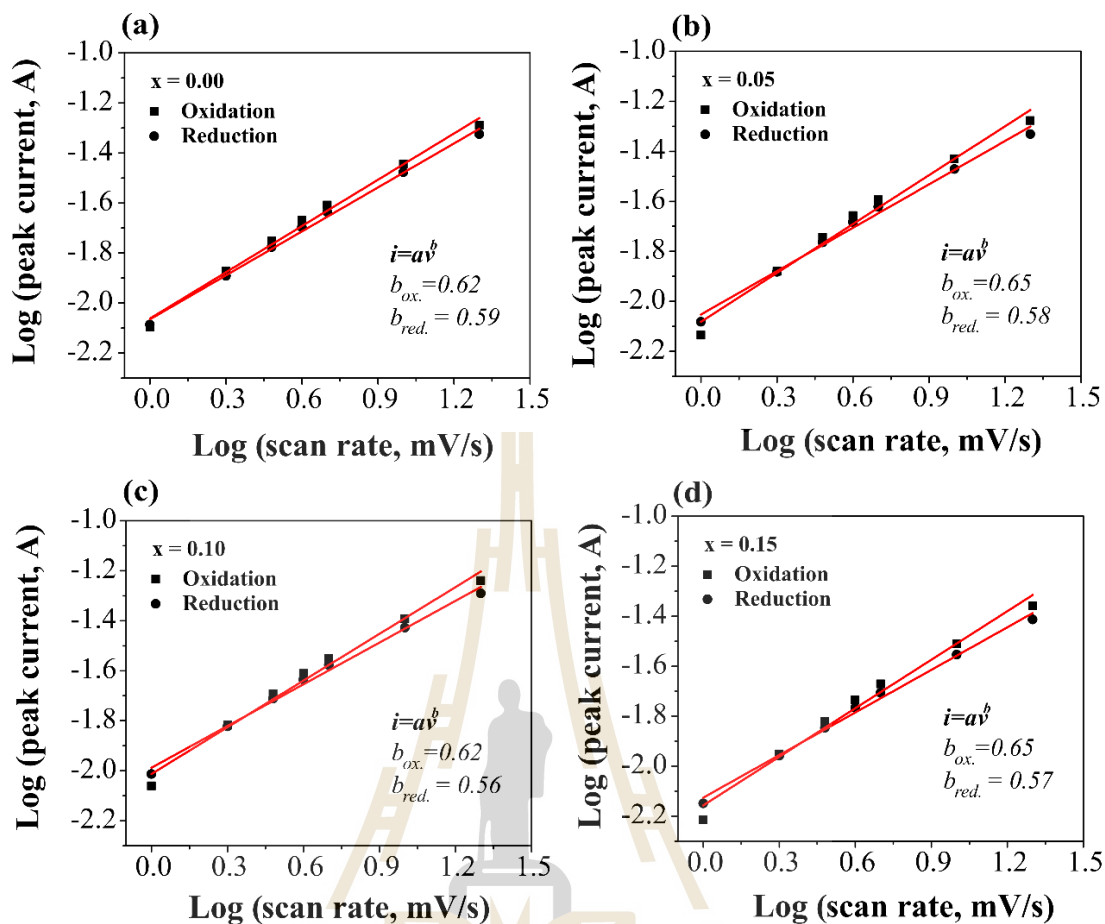


Figure 4.37 The scan rate dependence of peaks current of $\text{Mg}_x\text{Ni}_{1-x}(\text{OH})_2$ samples at different scan rates of 1, 2, 3, 4, 5, 10, and 20 mV/s.

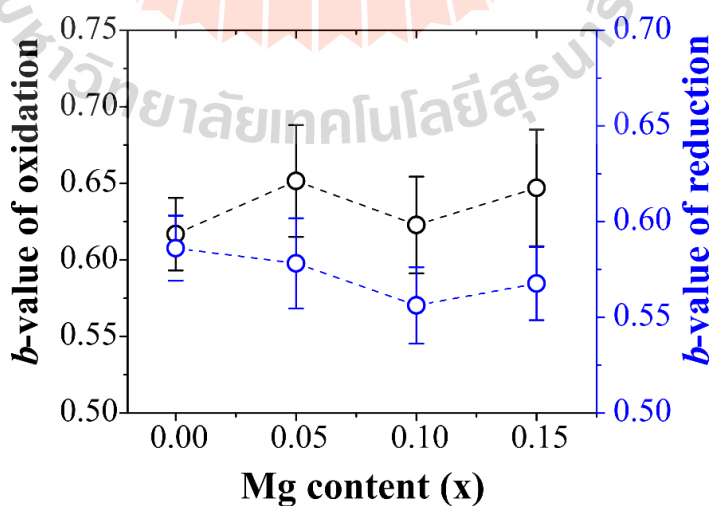


Figure 4.38 Dependence of b -values obtained from oxidation and reduction process as function of Mg content (x).

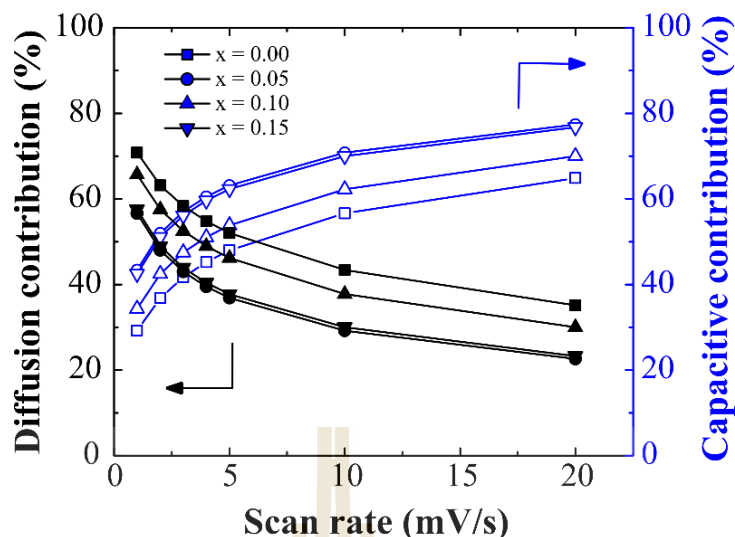


Figure 4.39 The contributions from capacitive and diffusion process varying with scan rates in $\text{Mg}_x\text{Ni}_{1-x}(\text{OH})_2$ samples.

From kinetic analysis, the total charge storage in electrode has been assumed to be the combination of the capacitive and diffusion-controlled mechanisms. The contribution from these two charge storage mechanisms can be distinguished according to equation 3.32. Figure 4.39 shows the plot between the contribution (%) obtained from capacitive and diffusion-controlled process as function of scan rate. It is clearly seen that the capacitive contributions increase with increasing scan rates, while the diffusion contributions decrease as scan rates increase. Trasatti *et al.* (Ardizzone *et al.*, 1990) proposed the relationship between the voltammetry charge and scan rate in order to identify the behavior of electrode materials during charge and discharge with different scan rates. The charge storage in the electrode materials with different scan rates is related to the diffusion of protons at the inner and outer active surface of the electrodes in which the total voltammetry charge (q_T) is the sum of voltammetry charge

at outer electrode surface (q_o) and inner electrode surface (q_i) following the relation (Ardizzone *et al.*, 1990).

$$q_T = q_o + q_i \quad (4.7)$$

They explained that the volumetric charge of the inner surface, such as pores and cracks becomes less accessible of protons diffusion, decreased with a rate of $v^{-1/2}$ as increasing scan rate ($v \rightarrow \infty$) which can be expressed as follows (Forghani and Donne, 2018):

$$q(v) = q_o + C_1 v^{-1/2} \quad (4.8)$$

where $q(v)$ is the measured voltammetric charge and C_1 is a numerical constant. They also assumed that the voltammetric charge should increase with $v^{1/2}$ as decreasing scan rate. Therefore, the total voltammetric charge at very low scan rates ($v \rightarrow 0$) which is composed of outer and inner voltammetric charges can be expressed as follows (Forghani and Donne, 2018):

$$\frac{1}{q(v)} = \frac{1}{q_T} + C_2 v^{1/2} \quad (4.9)$$

where $q(v)$ is the measured voltammetric charge and C_2 is a numerical constant.

Based on the above assumption, the voltammetric charge storage dependence of scan rate can be explained by the charges will store only at the electrode surface as scan rates increase ($v \rightarrow \infty$), resulting in higher capacitive than diffusion contribution. As scan rates decrease ($v \rightarrow 0$), the diffusion contribution becomes prominent due to the electrolyte ions have enough time to diffuse into electrode matrix resulting in higher intercalation/deintercalation or diffusion-controlled than capacitive contribution (Wang *et al.*, 2007; Forghani and Donne, 2018). It can be also noticed that

the diffusion-controlled mechanism dominates in sample of $x = 0.00$ and $x = 0.10$, while the capacitive process is dominant in samples of $x = 0.05$ and 0.15 for all scan rates. The summarized data obtained from the capacitive and diffusion-controlled contributions of $\text{Mg}_x\text{Ni}_{1-x}(\text{OH})_2$ samples are listed in Table 4.6.

Table 4.6 The capacitive and diffusion contributions of $\text{Mg}_x\text{Ni}_{1-x}(\text{OH})_2$ samples determined from the oxidation peaks at different scan rates.

Scan rate (mV/s)	Capacitive contribution (%)				Diffusion contribution (%)			
	$x = 0.00$	$x = 0.05$	$x = 0.10$	$x = 0.15$	$x = 0.00$	$x = 0.05$	$x = 0.10$	$x = 0.15$
1	29.21	43.38	34.29	42.48	70.79	56.62	65.71	57.52
2	36.85	52.01	42.46	51.09	63.15	47.99	57.54	48.91
3	41.68	57.03	47.47	56.12	58.32	42.97	52.53	43.88
4	45.22	60.51	51.06	59.63	54.78	39.49	48.94	40.37
5	47.99	63.14	53.85	62.28	52.01	36.86	46.15	37.72
10	56.62	70.79	62.26	70.02	43.38	29.21	37.74	29.98
20	64.86	77.41	70.00	76.76	35.14	22.59	30.00	23.24

The relative contributions from both capacitive and diffusion processes versus Mg content (x) at scan rate of 1 mV/s in all $\text{Mg}_x\text{Ni}_{1-x}(\text{OH})_2$ samples are shown in Figure 4.40. The contributions from diffusion-controlled process account for 70.79, 56.62, 65.71, and 57.52% in samples of $x = 0.00$, 0.05, 0.10, and 0.15, respectively. A remarkable observation is that the diffusion-controlled processes dominate in samples of $x = 0.00$ and 0.10. While the capacitive processes are prominent in sample of $x = 0.05$ and 0.15. In generally, the higher diffusion-controlled contribution suggests that

the higher intercalation/deintercalation of electrolyte ions (i.g. Na^+ , K^+) in the materials (Du *et al.*, 2017). Therefore, the higher specific capacitance value due to the higher intercalation/deintercalation contribution is expected in the undoped sample ($x = 0.00$).

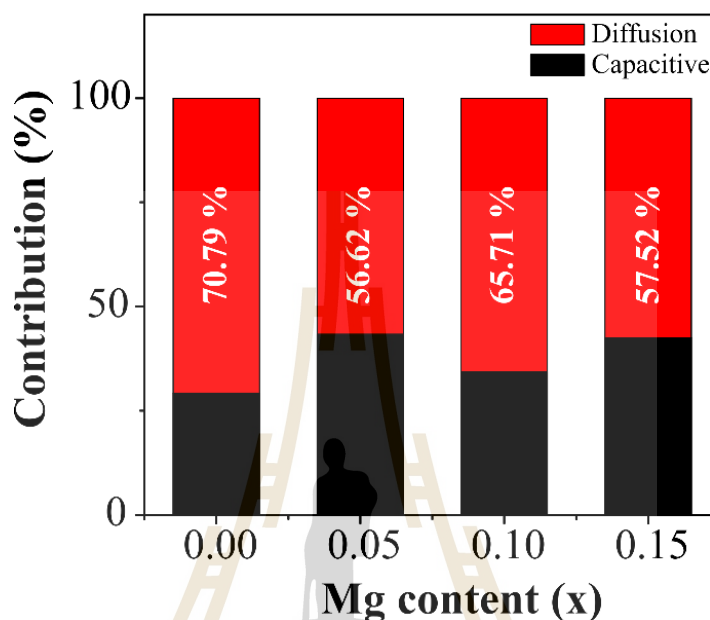


Figure 4.40 The relative contributions of capacitive and diffusion-controlled mechanisms at scan rate of 1 mV/s of $\text{Mg}_x\text{Ni}_{1-x}(\text{OH})_2$ samples.

4.3.4.3 Galvanostatic charge/discharge

Figure 4.41 shows the charge and discharge curves of $\text{Mg}_x\text{Ni}_{1-x}(\text{OH})_2$ samples at various current densities within the potential window of 0.51 V. As seen in Figure 4.41, a non-linear curves are observed implying that the electrodes store the charge base on redox or intercalation/deintercalation mechanism (Senthilkumar *et al.*, 2014). Moreover, the higher discharge times are observed at lower current densities in all $\text{Mg}_x\text{Ni}_{1-x}(\text{OH})_2$ samples. According to equation 3.34, the higher discharge time means that the higher specific capacitance value in these samples (Nithya *et al.*, 2013).

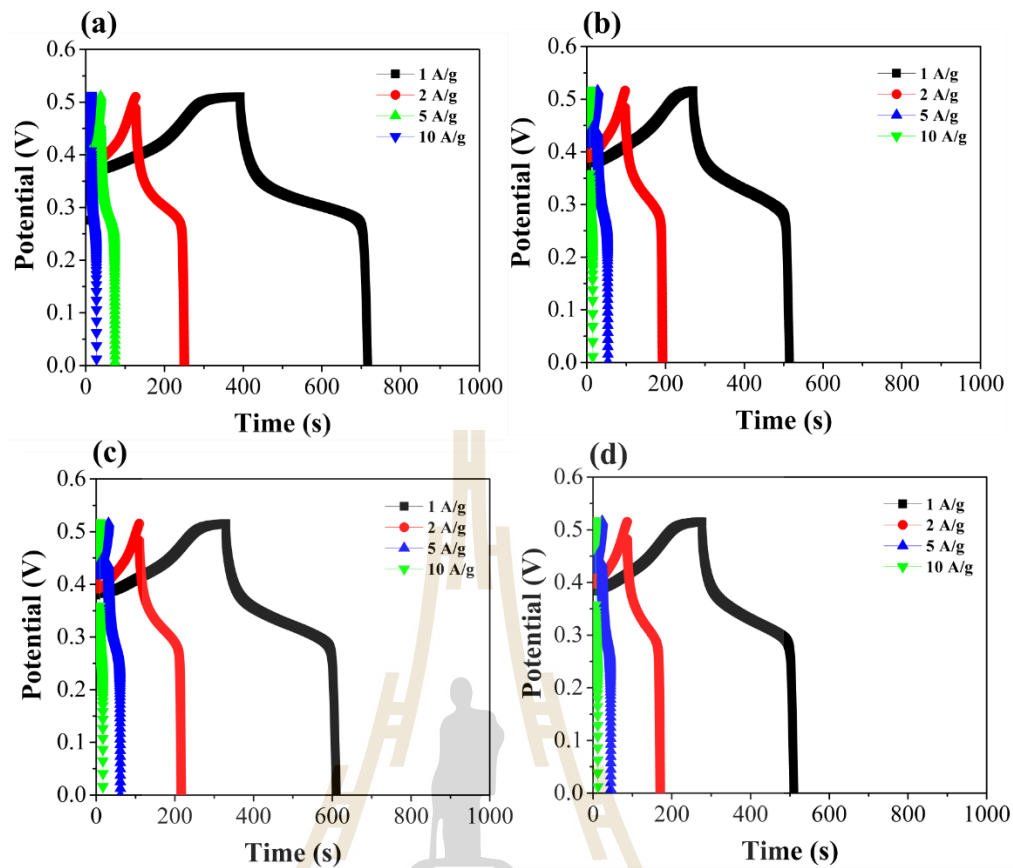


Figure 4.41 GCD curves at different current densities of $\text{Mg}_x\text{Ni}_{1-x}(\text{OH})_2$ with (a) $x = 0.00$, (b) $x = 0.05$, (c) $x = 0.10$, and (d) $x = 0.15$.

The comparison GCD curves of $\text{Mg}_x\text{Ni}_{1-x}(\text{OH})_2$ samples at current density of 1 A/g are shown in Figure 4.42. Each GCD curve composes of two different curve profiles. The linear profile indicates that the electrode store charges based on adsorption/desorption of the electrolyte ions at the electrode surface while the plateau profile or battery-type behavior implies that the electrode store the charges based on redox reaction or intercalation/deintercalation mechanism (Senthilkumar *et al.*, 2014). As seen in Figure 4.42, the longer discharge time is observed in the undoped sample ($x = 0.00$) indicating that it offers higher specific capacitance value. Besides, the internal resistance (IR) drops at the beginning of each discharge curve in all $\text{Mg}_x\text{Ni}_{1-x}(\text{OH})_2$

samples are also observed. The IR drop values in samples of $x = 0.00, 0.05, 0.10$, and 0.15 are estimated to be $0.013, 0.019, 0.018$, and 0.020 V, respectively. The lower IR drop correlates well with the higher specific capacitance value in the undoped sample.

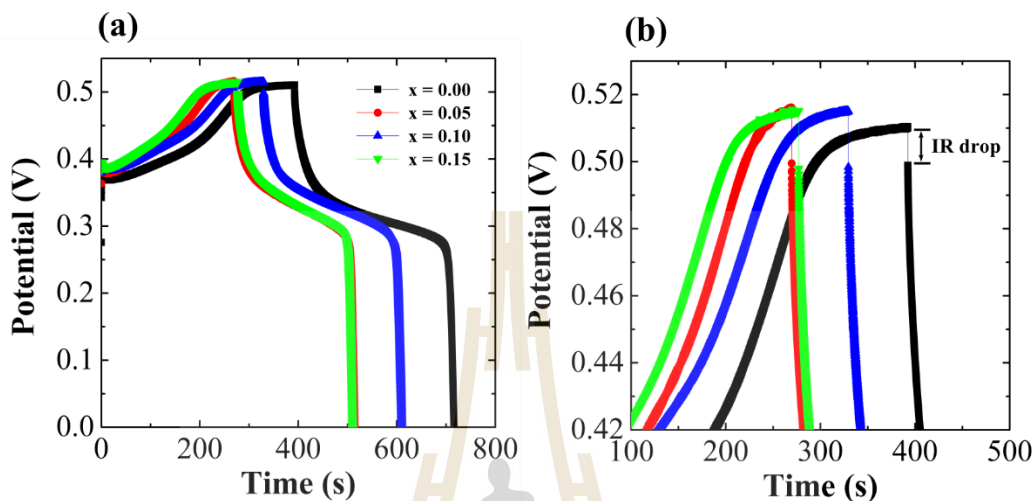


Figure 4.42 (a) The comparison of GCD curves and (b) their corresponding IR drop at current density of 1 A/g in $\text{Mg}_x\text{Ni}_{1-x}(\text{OH})_2$ samples.

The specific capacitance values of $\text{Mg}_x\text{Ni}_{1-x}(\text{OH})_2$ samples were calculated from the discharging curves by using equation 3.34 and are presented in Figure 4.43. As a result, the undoped sample shows the highest specific capacitance value of 641.25 F/g at current density of 1 A/g . Among all Mg doping samples, the sample of $x = 0.10$ shows the higher specific capacitance value of 555.81 F/g at current density of 1 A/g . According to the experimental results, it can be concluded that the Mg^{2+} doping does not improve the specific capacitance value of $\beta\text{-Ni}(\text{OH})_2$. Based on these results, the higher specific capacitance value can be explained due to the better reversibility in pure $\text{Ni}(\text{OH})_2$ sample. Furthermore, the specific capacitance value is found to be consistent with the d -spacing of (100) plane or lattice parameter a . As the d_{100} increases, the increase of specific capacitance value is observed. Oliva *et al.* (Oliva

et al., 1982) reported on the decreased in d_{001} value, which is associated with Ni-Ni distance within the layers, increased the electronic conductivity of β -Ni(OH)₂ due to better orbital overlapping and thus result in a lower polarization in the sample. Therefore, the opposite trend is observed in this work.

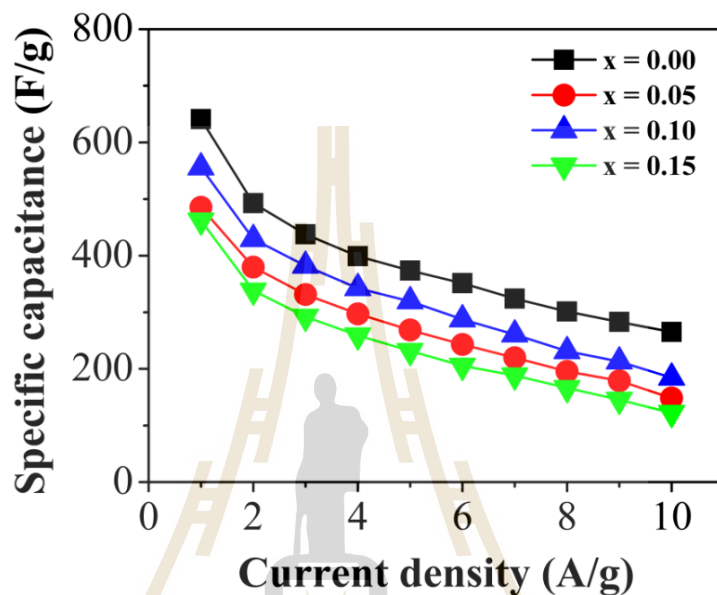


Figure 4.43 The calculated specific capacitance as function of current density in $\text{Mg}_x\text{Ni}_{1-x}(\text{OH})_2$ samples.

Based on the non-linear GCD curves, the specific capacity values (mAh/g) were also calculated by using the following equation (Wang *et al.*, 2019).

$$C = \frac{I \Delta t}{3.6m} \quad (4.10)$$

where I is current density (A), m is mass of active materials (g), and Δt is discharge time (h). The highest specific capacity value of 90.00 mAh/g is found in sample of $x = 0.00$ at current density of 1 A/g. This value is much lower than the theoretical specific capacity value of β -Ni(OH)₂ (Wang *et al.*, 2011). The summarized data obtained from the specific capacitance and specific capacity calculations are listed in Table 4.7.

Table 4.7 The summarized data obtained from the specific capacitance (F/g) and specific capacity (mAh/g) calculations.

Current density (A/g)	Specific capacitance (F/g)				Specific capacity (mAh/g)			
	x = 0.00	x = 0.05	x = 0.10	x = 0.15	x = 0.00	x = 0.05	x = 0.10	x = 0.15
1	641.25	485.42	555.81	462.01	90.00	68.06	78.00	64.76
2	492.65	379.59	429.14	338.26	68.75	52.83	59.28	46.75
3	437.71	331.23	382.08	291.95	60.71	45.88	51.92	39.88
4	399.01	297.08	342.40	259.06	55.44	40.83	46.67	34.89
5	373.49	268.57	319.28	231.46	51.25	36.74	42.22	30.90
6	351.23	243.16	287.26	205.31	47.83	33.08	38.33	27.50
7	323.89	219.72	260.65	188.39	44.92	29.65	34.61	24.21
8	301.35	195.58	231.06	166.06	42.22	26.44	30.89	21.33
9	282.69	179.02	212.94	145.16	39.62	23.13	27.12	18.50
10	265.11	148.22	184.37	122.17	37.50	20.00	23.47	15.69

4.3.4.4 Electrochemical impedance spectroscopy

To further understand the electrochemical performance of Mg-doped $\text{Ni}(\text{OH})_2$ with different contents of $x = 0.00, 0.05, 0.10$, and 0.15 , electrochemical impedance spectroscopy (EIS) was carried out in the frequency range of 0.1 Hz to 100 kHz at an amplitude of 0.1 V .

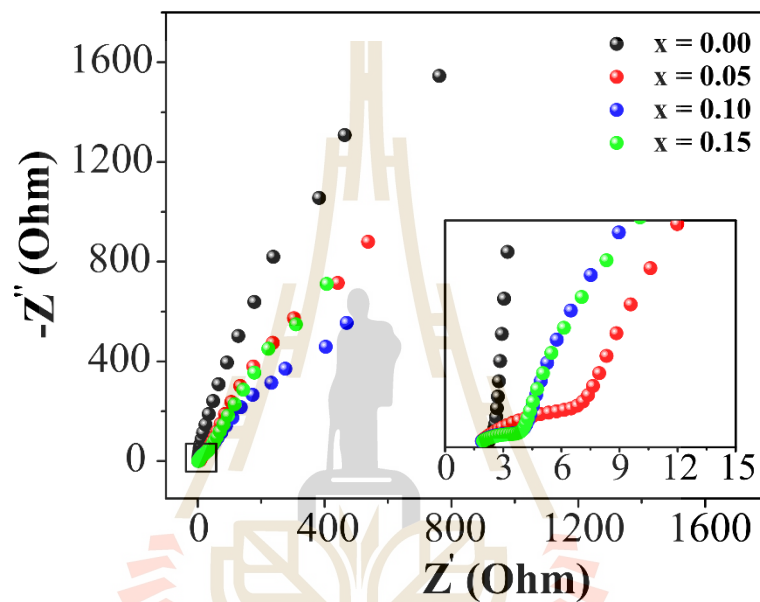


Figure 4.44 Nyquist plots of $\text{Mg}_x\text{Ni}_{1-x}(\text{OH})_2$ samples measured at the frequency range of 0.1 Hz to 100 kHz . Inset shows an enlarged view of Nyquist plots.

As clearly seen in Figure 4.44, the Nyquist plots represent the semicircle in all Mg-doped $\text{Ni}(\text{OH})_2$ samples indicating that the charge transfer resistance (R_{ct}) at the electrode/electrolyte interface of Mg-doped $\text{Ni}(\text{OH})_2$ samples is larger than in the undoped $\text{Ni}(\text{OH})_2$ sample. The estimated R_{ct} values in samples of $x = 0.00, 0.05, 0.10$, and 0.15 are $0.35, 8.55, 3.94$, and 3.80 Ohm , respectively. The lower R_{ct} values indicate the easier and more rapid charge transfer in the undoped $\text{Ni}(\text{OH})_2$ sample (Du *et al.*, 2017). Moreover, it was reported that the R_{ct} value is closely related to the particle size of the materials (Son *et al.*, 2014). The reduction of particle size until it reached the

critical size (~ 8 nm) of Ni(OH)_2 led to the decrease of R_{ct} value (Wang *et al.*, 2015). Therefore, it may be concluded that Mg^{2+} doping causes the increase of charge transferred resistance due to the increase of particle size. Moreover, the observed vertical lines in low frequency region which associated with Na ion diffusivity in the electrode pores and in the host materials (Yang *et al.*, 2016) are estimated to be 67.18, 55.77, and 42.95, and 55.51 degree in samples of $x = 0.00$, 0.05, 0.10, and 0.15, respectively. The more vertical line (close to 90 degree) suggested that a higher Na ion diffusivity in the active materials (Wang *et al.*, 2018). Based on the above results, it may be concluded that the higher specific capacitance value in the undoped Ni(OH)_2 sample is due to the lower charge transfer resistance and higher Na ions diffusivity.

4.3.4.5 Cyclic stability

It is well-known that the cyclic stability is an important factor for energy storage applications. Therefore, the cyclic stability of $\text{Mg}_x\text{Ni}_{1-x}(\text{OH})_2$ samples was evaluated by repeating GCD measurement at current density of 5 A/g for 1000 cycles. As shown in Figure 4.45, the sample of $x = 0.05$ shows the excellent cyclic stability of 101.16% after 1000 cycles. Additionally, it is clearly seen that the specific capacitance value of this sample slightly decreases initially and then increases and stays almost constant as an extended cycle number. The increase of capacitance retention from 98.08 to 106.53% during the 50 - 400th cycle in this sample could be attributed to the gradual activation of the electrode surface resulting in the better electrolyte ions accessible into the electrode (Zequine *et al.*, 2016). It should be noted that the greatest cyclic stability is observed in the sample with the capacitive contribution becoming more prominent. Therefore, the cyclic stability of Ni(OH)_2 is significant improved after adding small amount of Mg ($x = 0.05$). Figure 4.45(b) shows the coulombic efficiency of

$\text{Mg}_x\text{Ni}_{1-x}(\text{OH})_2$ samples. A higher coulombic efficiency values ($> 95\%$) are observed in samples of $x = 0.00$, 0.05 , and 0.15 . Moreover, the slight decrease of coulombic efficiency values ($<95\%$) is observed in sample of $x = 0.10$ which is accordance with the observed lower capacitance retention in this sample. The summarized data obtained from EIS measurement including cyclic stability and coulombic efficiency are listed in Table 4.8.

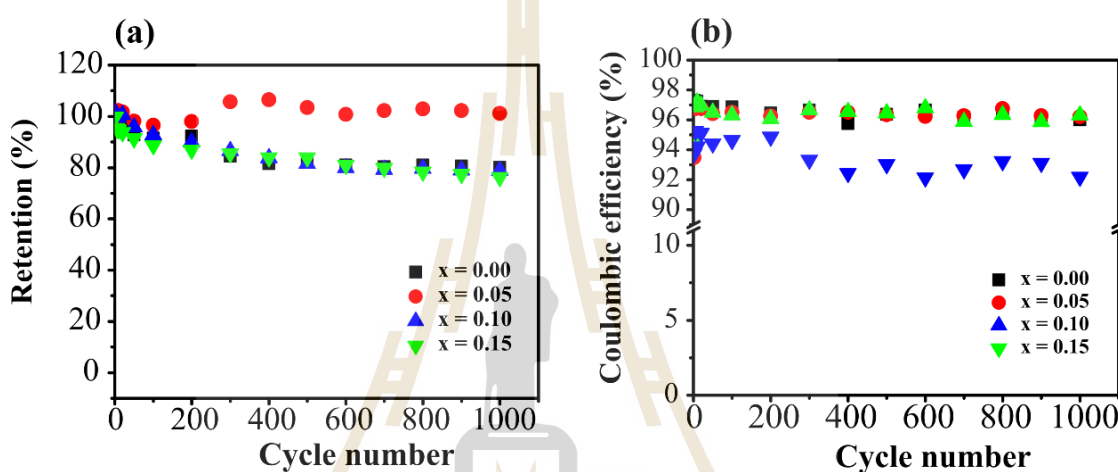


Figure 4.45 Comparison of (a) capacitance retention and (b) coulombic efficiency as function of cycle number of $\text{Mg}_x\text{Ni}_{1-x}(\text{OH})_2$ samples measured at current density of 5 A/g for 1000 cycles.

Table 4.8 The details of solution resistance (R_s), charge transferred resistance (R_{ct}), and the angle of vertical line with x -axis obtained from EIS measurement and cyclic stability and coulombic efficiency obtained from repeating GCD measurement at current density of 5 A/g for 1000 cycles in $Mg_xNi_{1-x}(OH)_2$ samples.

x	R_s (Ohm)	R_{ct} (Ohm)	Angle (°)	Cyclic stability (%)	Coulombic efficiency (%)
0.00	2.01	0.35	67.18	80.02	96.00
0.05	1.57	8.55	55.77	101.16	96.21
0.10	1.47	3.94	42.95	78.90	96.31
0.15	1.51	3.80	55.51	76.17	92.17

To better understand the excellent cyclic stability in sample of $x = 0.05$, EIS was performed after GCD measurement for 1000 cycles and it was compared with the EIS data before the GCD measurement. As shown in Figure 4.46, the decrease of charge transfer resistance (R_{ct}) was clearly observed after repeating GCD measurement for 1000 cycles. According to the equation 4.44, the lower R_{ct} value means the higher exchanged current density at the electrode/electrolyte interface providing a better performance in sample of $x = 0.05$. Comparing with the cyclic stability of $x = 0.15$, EIS result after repeating GCD measurement for 1000 cycles shows the presence of additional semicircle in high frequency region as seen in Figure 4.47. Based on these results, it may be concluded that the better cyclic stability comes from the lower charge transfer resistance (R_{ct}) with no observation of additional semicircle after repeating GCD measurement for 1000 cycles.

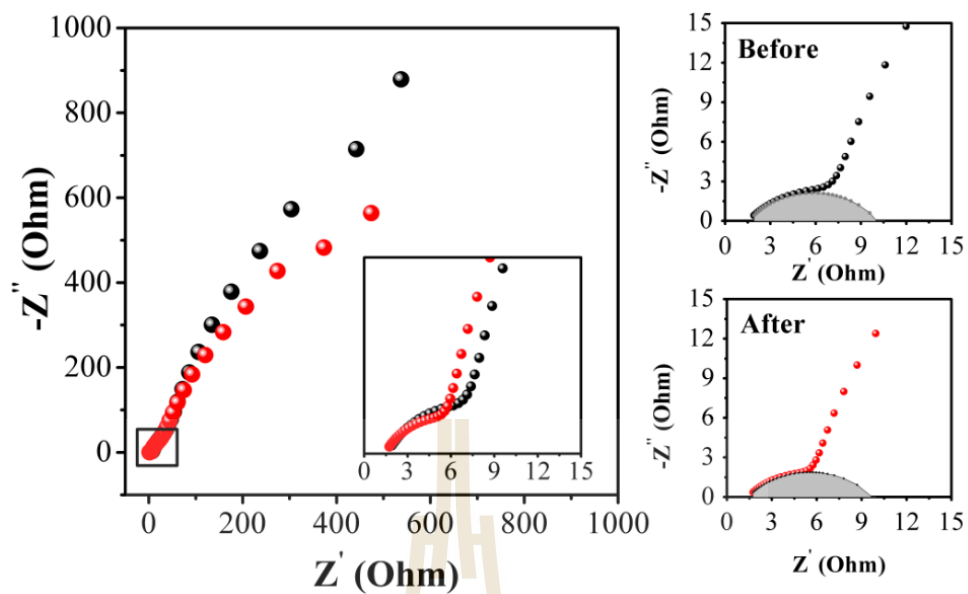


Figure 4.46 Comparison of Nyquist plot before and after the GCD measurement at current density of 5 A/g for 1000 cycles in sample of $x = 0.05$.

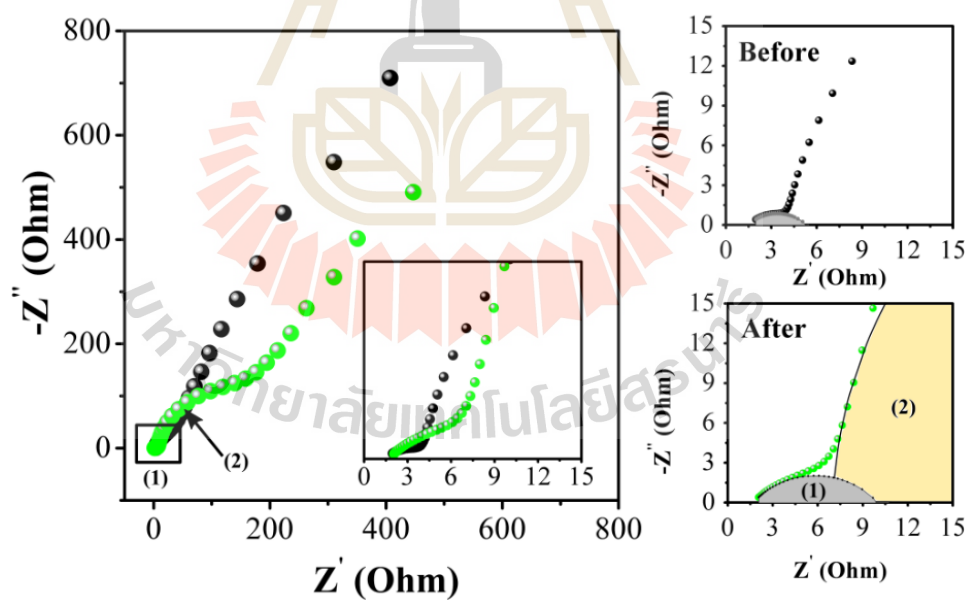


Figure 4.47 Comparison of Nyquist plot before and after the GCD measurement at current density of 5 A/g for 1000 cycles in sample of $x = 0.15$. Number 1 and 2 indicate the presence of two semicircles in the sample.

4.3.4.6 Energy density and power density

It is well-known that the performance of energy storage devices is determined by the Ragone plot or the plot between specific power and specific energy. As shown in Figure 4.48(a), the specific energies at different current densities ranging from 1-10 A/g seem to be decreased with increasing of Mg contents. Whereas the specific power increases with increasing current density as summarized in Table 4.9. Among all $\text{Mg}_x\text{Ni}_{1-x}(\text{OH})_2$ samples, the undoped sample shows the highest specific energy of 22.74 Wh/kg with specific energy of 252.60 W/kg at current density of 1 A/g. According to the Ragone plot, $\text{Mg}_x\text{Ni}_{1-x}(\text{OH})_2$ samples are suitable for both electrochemical capacitor and battery applications when comparing with the well-known Ragone plot as shown in Figure 4.48(b).

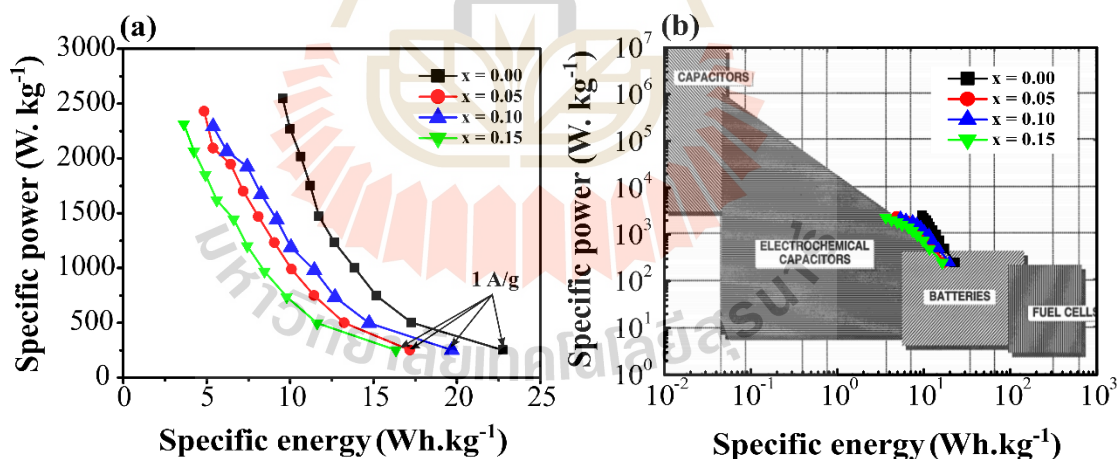


Figure 4.48 (a) The Ragone plot of $\text{Mg}_x\text{Ni}_{1-x}(\text{OH})_2$ samples and (b) the comparison of Ragone plot of $\text{Mg}_x\text{Ni}_{1-x}(\text{OH})_2$ samples with a well-known Ragone plot of Kötz (Kotz and Carlen, 2000).

Table 4.9 The specific energies (E) and the specific power (P) of $\text{Mg}_x\text{Ni}_{1-x}(\text{OH})_2$ samples at various current densities.

Current density (A/g)	E (Wh/kg)				P (W/kg)			
	x = 0.00	x = 0.05	x = 0.10	x = 0.15	x = 0.00	x = 0.05	x = 0.10	x = 0.15
1	22.74	17.17	19.70	16.34	252.60	252.40	252.60	252.30
2	17.27	13.24	14.74	11.63	502.40	501.10	497.30	497.50
3	15.16	11.44	12.70	9.80	748.90	747.90	733.70	737.50
4	13.87	10.10	11.45	8.46	1000.50	989.60	981.30	969.70
5	12.66	9.05	10.05	7.43	1235.00	1231.10	1190.20	1201.60
6	11.73	8.10	9.21	6.63	1470.80	1469.40	1441.20	1446.60
7	11.21	7.20	8.27	5.60	1747.30	1700.40	1673.10	1619.20
8	10.65	6.44	7.43	4.93	2017.60	1947.00	1925.00	1850.00
9	10.00	5.38	6.22	4.24	2270.70	2092.60	2063.60	2064.60
10	9.55	4.86	5.38	3.63	2546.10	2428.90	2291.60	2312.30

4.4 Effects of transition metals (Mn, Cu, and Zn) doped Ni(OH)₂ on structure and electrochemical properties

4.4.1 Structural and morphology analysis

XRD patterns of Mn, Cu, and Zn-doped Ni(OH)₂ with different contents (x) of 0.00, 0.05, 0.10, and 0.15 are shown in Figure 4.49, 4.50, and 4.51, respectively. As seen in those Figures, the diffraction peaks at the diffraction angle (2θ) of about 19.4, 33.0, 38.5, 52.1, 59.0, 62.7, 69.3, 70.4, and 72.6° within the diffraction angle ranging from 10-80 degrees are observed in the undoped Ni(OH)₂. The overall diffraction peaks well-matched with the standard powder diffraction of hexagonal β-Ni(OH)₂ (JCPDS file no. 14-0117) with space group of $P\bar{3}m1$. The observed peaks in the XRD patterns from low - to high - diffraction angle (2θ) can be indexed as (001), (100), (101), (102), (110), (111), (200), (103), and (201) lattice planes, respectively. In addition, no diffraction peaks relate to the second phase or the impurities are observed from the XRD patterns of all Mn, Cu, and Zn doping samples. This may be conclude that Mn²⁺, Cu²⁺, and Zn²⁺ can completely substitute the Ni²⁺ sites in Ni(OH)₂ crystal lattice.

As clearly seen in the enlarged view of (001) plane in Figure 4.49 of Mn-doped Ni(OH)₂ samples, the observed diffraction peaks shift towards higher diffraction angle implying the change of lattice parameters. Owing to the fact that ionic radius of Mn²⁺(0.83 Å) is larger than Ni²⁺(0.69 Å) (Shannon, 1976) , the shift of diffraction peaks to higher 2θ is possibly due to the larger Mn²⁺ ions could not substitute in smaller Ni²⁺ sites completely and instead the shrinking of the octahedra takes place resulting in the shift of diffraction peaks towards higher 2θ. For Cu²⁺ and Zn²⁺ doping

(Figure 4.50 and 4.51), no significant changes in diffraction peaks are observed. This is possibly due to that the ionic radius of Cu (0.73 Å) and Zn (0.74 Å) are nearly the same as the ionic radius of Ni^{2+} (0.69 Å) (Shannon, 1976).

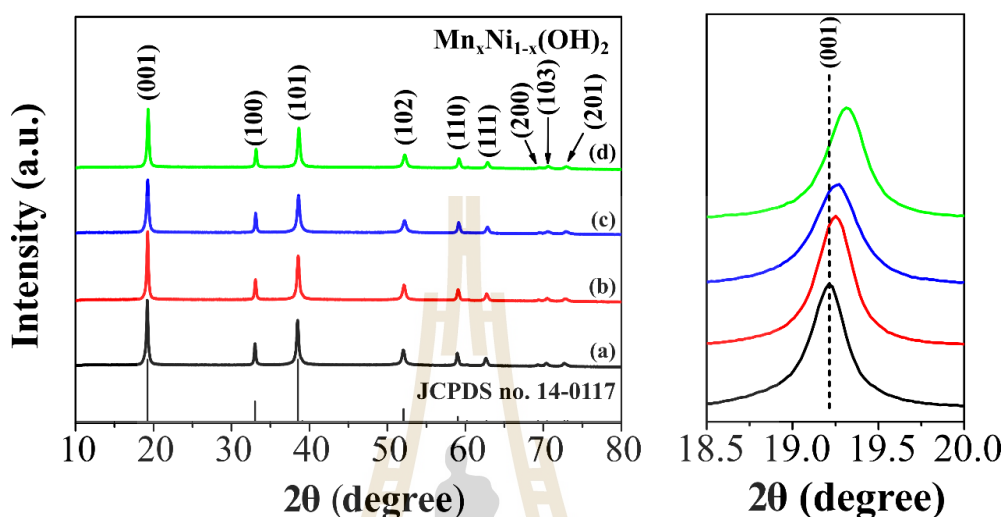


Figure 4.49 XRD patterns of $\text{Mn}_x\text{Ni}_{1-x}(\text{OH})_2$ samples with (a) $x = 0.00$, (b) $x = 0.05$, (c) $x = 0.10$, and (d) $x = 0.15$ and their corresponding enlarged view of the diffraction peaks in 2θ ranging from 18.5 to 20.0 degree.

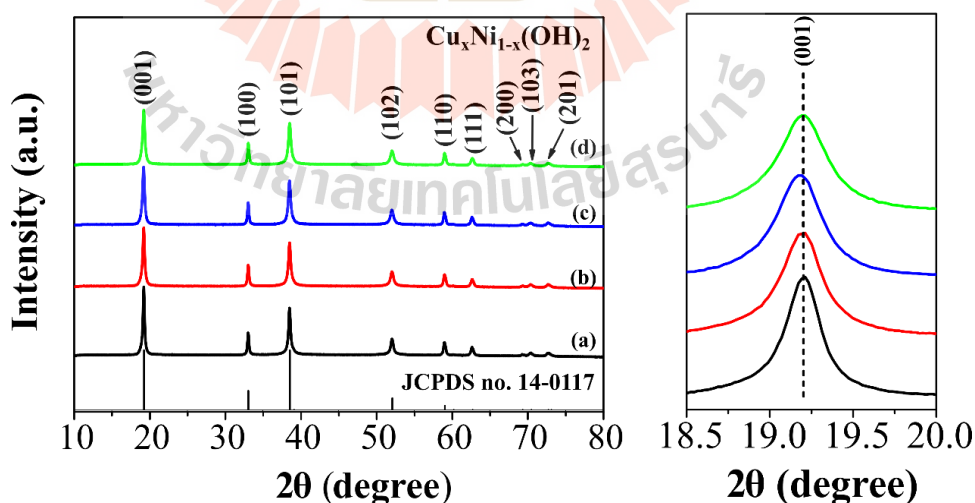


Figure 4.50 XRD patterns of $\text{Cu}_x\text{Ni}_{1-x}(\text{OH})_2$ samples with (a) $x = 0.00$, (b) $x = 0.05$, (c) $x = 0.10$, and (d) $x = 0.15$ and their corresponding enlarged view of the diffraction peaks in 2θ ranging from 18.5 to 20.0 degree.

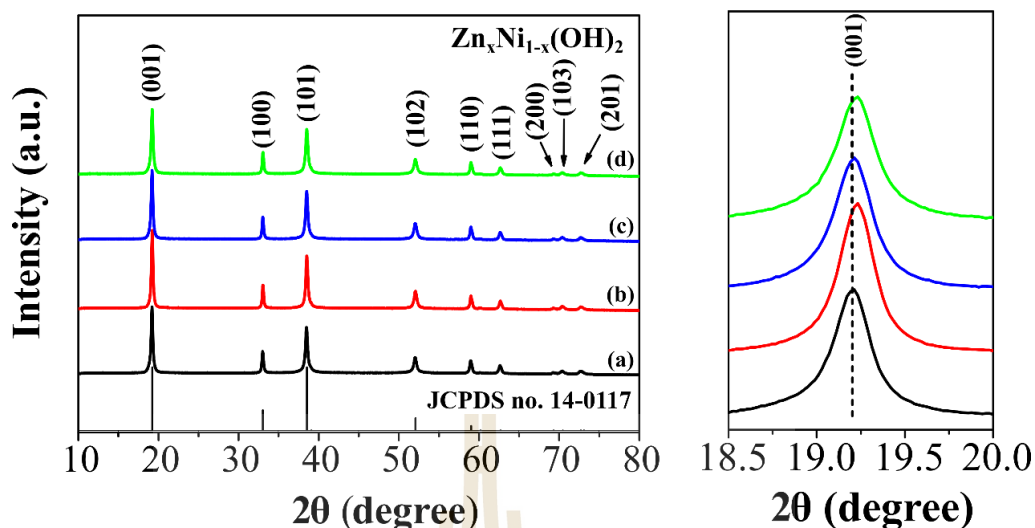


Figure 4.51 XRD patterns of $\text{Zn}_x\text{Ni}_{1-x}(\text{OH})_2$ samples with (a) $x = 0.00$, (b) $x = 0.05$, (c) $x = 0.10$, and (d) $x = 0.15$ and their corresponding enlarged view of the diffraction peaks in 2θ ranging from 18.5 to 20.0 degree.

To explore the structural change affected by Mn, Cu, and Zn doping, the Rietveld refinement was performed by using JANA2006 software. The Pseudo-Voigt was used as the profile function. The refinement was performed in the 2θ range of 10 - 80° based on the hexagonal crystal structure with space group of $P\bar{3}m1$. The lattice parameter $a = 3.13 \text{ \AA}$ and $c = 4.63 \text{ \AA}$ of $\beta\text{-Ni}(\text{OH})_2$ were used for the lattice parameters refinement. As seen in Figure 4.52, 4.53, and 4.54, the difference between the observed and calculated profiles is shown at the bottom of each figure. The Bragg positions are indicated by small vertical lines. As a result, the refinement of $\text{Mn}_x\text{Ni}_{1-x}(\text{OH})_2$, $\text{Cu}_x\text{Ni}_{1-x}(\text{OH})_2$, and $\text{Zn}_x\text{Ni}_{1-x}(\text{OH})_2$ samples are in good agreement between the observed and the calculated XRD patterns. The data obtained from the refinement of $\text{Mn}_x\text{Ni}_{1-x}(\text{OH})_2$, $\text{Cu}_x\text{Ni}_{1-x}(\text{OH})_2$, and $\text{Zn}_x\text{Ni}_{1-x}(\text{OH})_2$ samples are summarized in Table 4.10, 4.11, and 4.12, respectively. As seen in those tables, the values of R_p , R_{wp} , and

GOF of $\text{Mn}_x\text{Ni}_{1-x}(\text{OH})_2$, $\text{Cu}_x\text{Ni}_{1-x}(\text{OH})_2$, and $\text{Zn}_x\text{Ni}_{1-x}(\text{OH})_2$ samples are under 10% meaning that the Rietveld refinement results are reliable (Huang *et al.*, 2015; Li *et al.*, 2017).

Figure 4.45(a-b) shows the plots between lattice parameters a and c as function of Mn, Cu, and Zn contents. A remarkable observation is that the decrease of lattice parameters a and c after Mn^{2+} doping resulting in the decrease of unit cell volume as seen in Figure 4.55(d). On the other hand, the decrease of lattice parameter a with rising of lattice parameter c is observed for Cu and Zn doping. The calculated c/a ratio shows the higher values in Cu than Mn and Zn-doped $\text{Ni}(\text{OH})_2$. In contrast, the lower c/a values present in Mn-doped $\text{Ni}(\text{OH})_2$. Sun *et al.* (Sun *et al.*, 2018) pointed out that the change of c/a ratio directly induces lattice strain in crystal structure. Also, Mancini *et al.* (Mancini *et al.*, 2016) stated that the increase of c/a ratio would indicate lattice distortion and structure stress in the materials. In addition, the change of c/a ratio was reported to affect the electrochemical performance of materials (Lee *et al.*, 2012; Mancini *et al.*, 2016). Based on the above results, it may be concluded that Mn, Cu, and Zn doping caused the changed in lattice parameters due to the difference of ionic radius between the dopants and Ni^{2+} ions. Furthermore, the average crystallite size (D) of $\text{Mn}_x\text{Ni}_{1-x}(\text{OH})_2$, $\text{Cu}_x\text{Ni}_{1-x}(\text{OH})_2$, and $\text{Zn}_x\text{Ni}_{1-x}(\text{OH})_2$ samples was calculated from the most intense peaks of (001), (100), and (101) planes by using equation 3.2. For Mn^{2+} doping, the calculated crystallite size increases with increasing Mn contents. In case of Cu^{2+} and Zn^{2+} doping, the average crystallite size tends to decrease with increasing Cu and Zn contents. In general, the crystal growth results from the formation of supersaturation and followed by nucleation (Harding *et al.*, 2014; Thanh *et al.*, 2014). Therefore, the size of crystal or crystallite size depends on the nucleation and growth

rate. If the nucleation rate is rapid relative to growth rate, a small crystal is obtained. In contrast, large crystallite size is due to the slow nucleation rate relative to growth rate. This implies that the nucleation rate plays an important in Mn, Cu, and Zn doping. The larger crystallite size in $\text{Mn}_x\text{Ni}_{1-x}(\text{OH})_2$ samples prefers to the slow nucleation rate, whereas the rapid rate is presented in Cu and Zn doping. One can also see in Figure 4.55(c) is that the decrease of c/a ratio in Mn-doped $\text{Ni}(\text{OH})_2$ caused the increase of crystallite size as shown in Figure 4.55(e). The decrease of crystallite size was referred to an increase of crystal lattice distortion $\langle \varepsilon^2 \rangle^{1/2}$ at the same diffraction angle following the relation (Gaber *et al.*, 2014; Song *et al.*, 2016).

$$\langle \varepsilon^2 \rangle^{1/2} = \frac{1}{D} \frac{1}{\sin \theta} \frac{\lambda}{K} \sqrt{\frac{\pi^2 K^2 - 4}{32}} \quad (4.11)$$

Where D is average crystallite size obtained from Scherrer's equation. K is the shape factor equals to 0.89 and θ is the Bragg diffraction angle. According to equation 4.11, lower crystallite size means higher crystal lattice distortion.

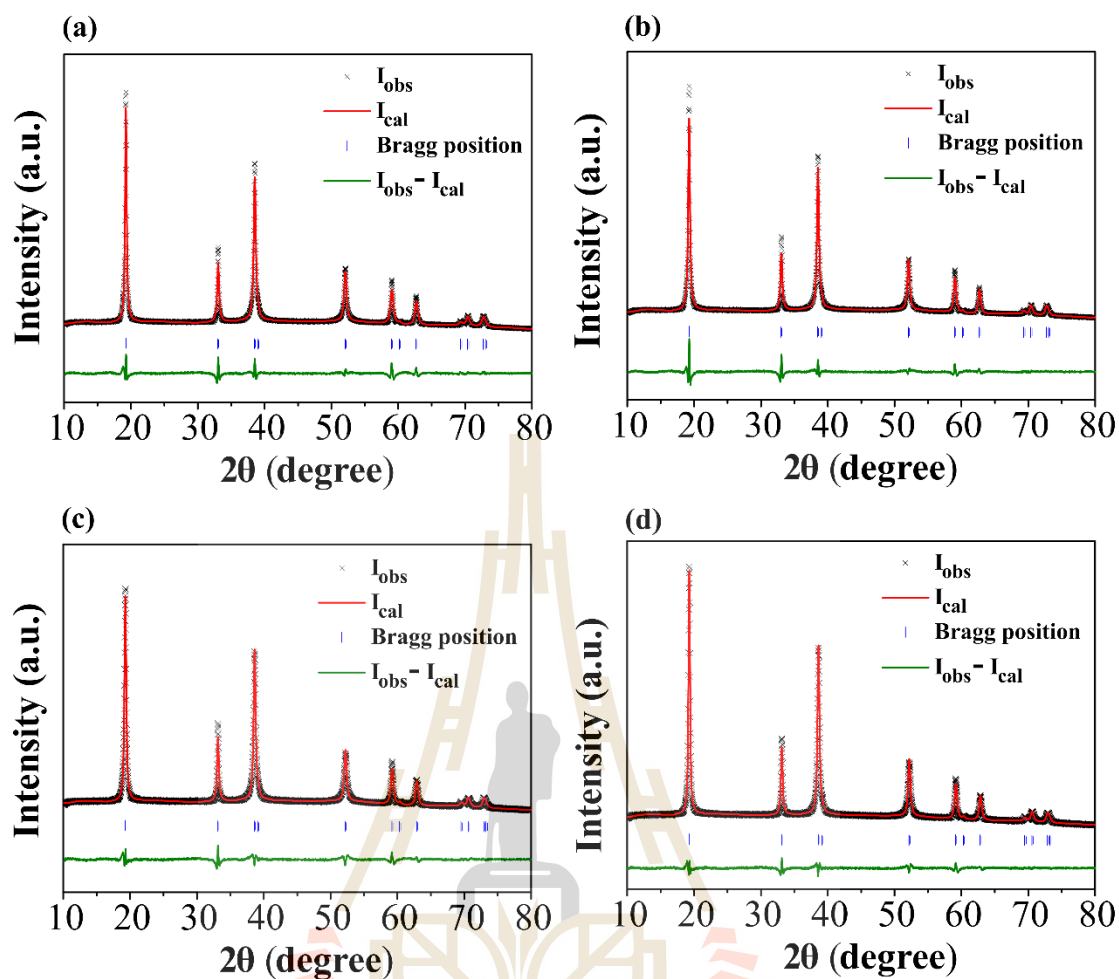


Figure 4.52 Rietveld refinement of $\text{Mn}_x\text{Ni}_{1-x}(\text{OH})_2$ samples with $x = 0.00, 0.05, 0.10,$ and 0.15 .

Table 4.10 The details of lattice parameter a and c , profile factor (R_p), weighted profile residual (R_{wp}), goodness of fit (GOF), unit cell volume, and density obtained from the Rietveld refinement including the calculated d -spacing of (001), (100), and (101) planes and the calculated crystallite size from Scherrer's equation of $Mn_xNi_{1-x}(OH)_2$ samples with $x = 0.00, 0.05, 0.10$, and 0.15 .

Parameters	$x = 0.00$	$x = 0.05$	$x = 0.10$	$x = 0.15$
Lattice parameter (\AA)				
$a = b$	3.128735	3.128810	3.120279	3.122076
c	4.611137	4.610646	4.598770	4.600843
c/a	1.473802	1.473610	1.473833	1.473649
d-spacing (\AA)				
(001)	4.6111	4.6106	4.5988	4.6008
(100)	2.7096	2.7096	2.7022	2.7038
(101)	2.3361	2.3361	2.3298	2.3311
R_p (%)	2.86	2.91	2.58	2.25
R_{wp} (%)	4.36	4.42	3.73	3.11
GOF (%)	2.90	2.96	2.45	1.96
Volume (\AA^3)	39.09095	39.08866	38.77566	38.83783
Density (g/cm^3)	3.937953	3.938184	3.969973	3.963618
D (nm)	41.69 \pm 0.53	42.16 \pm 1.02	44.85 \pm 0.77	45.11 \pm 1.00

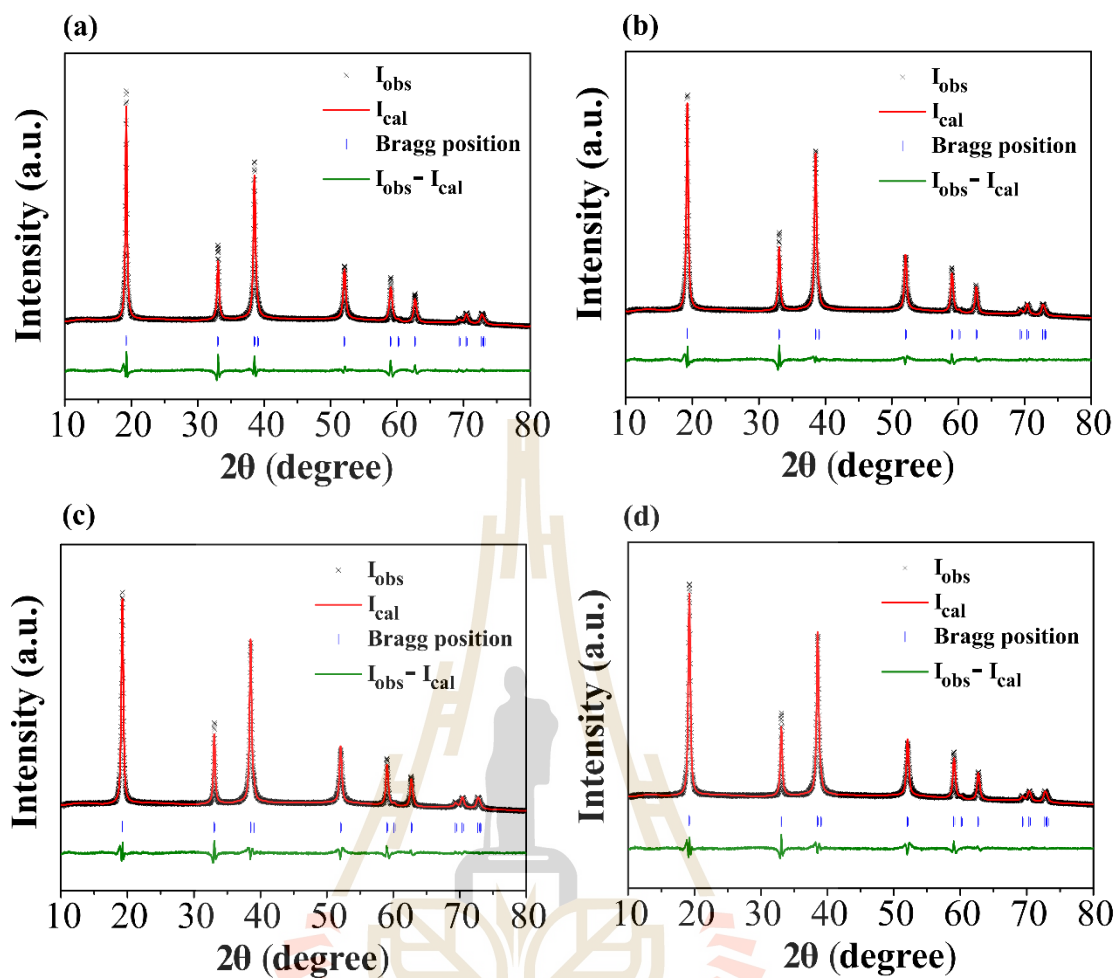


Figure 4.53 Rietveld refinement of $\text{Cu}_x\text{Ni}_{1-x}(\text{OH})_2$ samples with $x = 0.00, 0.05, 0.10,$ and 0.15 .

Table 4.11 The details of lattice parameter a and c , profile factor (R_p), weighted profile residual (R_{wp}), goodness of fit (GOF), unit cell volume, and density obtained from the Rietveld refinement including the calculated d -spacing of (001), (100), and (101) planes and the calculated crystallite size from Scherrer's equation of $\text{Cu}_x\text{Ni}_{1-x}(\text{OH})_2$ samples with $x = 0.00, 0.05, 0.10$, and 0.15 .

Parameters	$x = 0.00$	$x = 0.05$	$x = 0.10$	$x = 0.15$
Lattice parameter (\AA)				
$a = b$	3.128735	3.128063	3.127911	3.127899
c	4.611137	4.612585	4.613012	4.614178
c/a	1.473802	1.474582	1.474790	1.475168
d-spacing (\AA)				
(001)	4.6111	4.6126	4.6130	4.6142
(100)	2.7096	2.7090	2.7089	2.7088
(101)	2.3361	2.3359	2.3359	2.3360
R_p (%)	2.86	2.54	2.67	2.61
R_{wp} (%)	4.36	3.73	3.85	3.78
GOF (%)	2.90	2.49	2.57	2.52
Volume (\AA^3)	39.090950	39.086440	39.086250	39.095830
Density (g/cm^3)	3.937953	3.938407	3.938426	3.937462
D (nm)	41.68 \pm 0.53	38.22 \pm 0.87	36.99 \pm 0.80	36.21 \pm 1.04

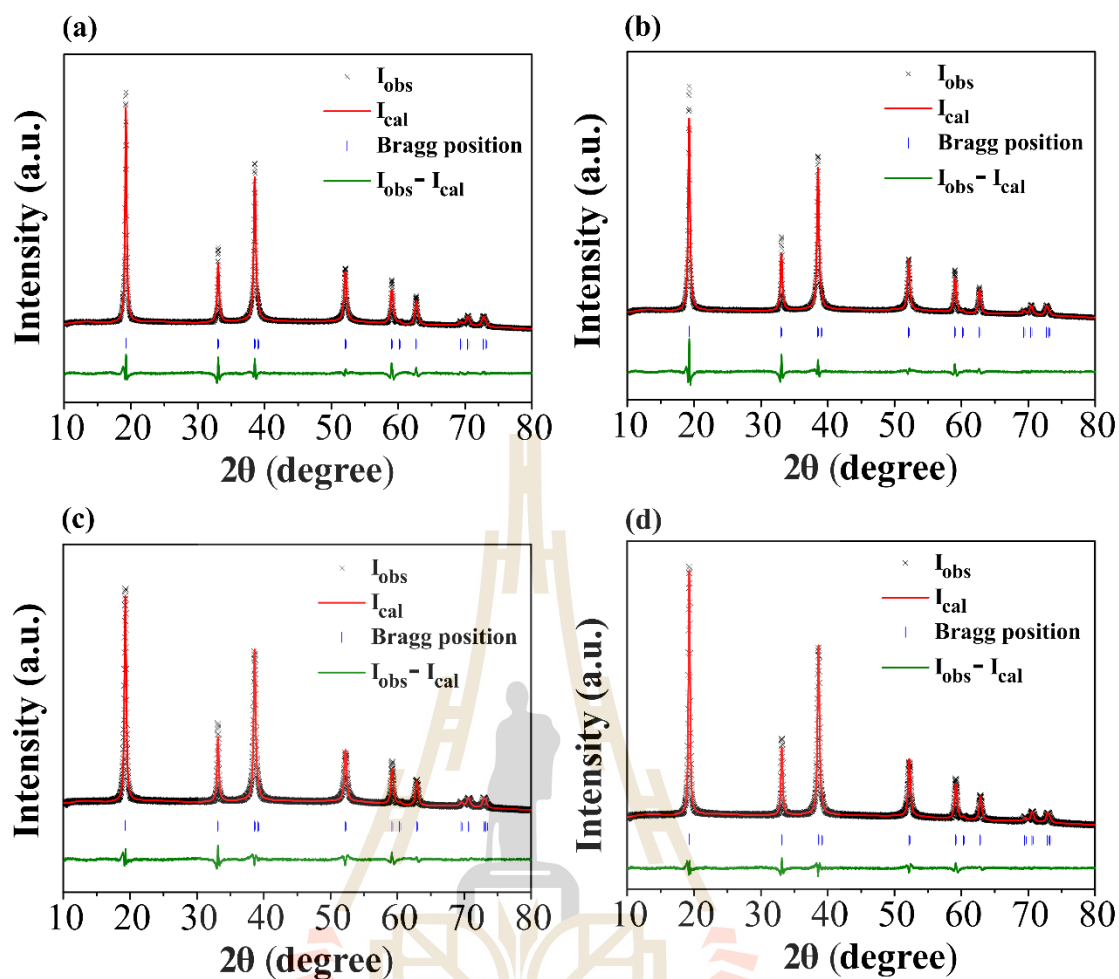


Figure 4.54 Rietveld refinement of $\text{Zn}_x\text{Ni}_{1-x}(\text{OH})_2$ samples with $x = 0.00, 0.05, 0.10,$ and 0.15 .

Table 4.12 The details of lattice parameter a and c , profile factor (R_p), weighted profile residual (R_{wp}), goodness of fit (GOF), unit cell volume, and density obtained from the Rietveld refinement including the calculated d -spacing of (001), (100), and (101) planes and the calculated crystallite size from Scherrer's equation of $Zn_xNi_{1-x}(OH)_2$ samples with $x = 0.00, 0.05, 0.10$, and 0.15 .

Parameters	$x = 0.00$	$x = 0.05$	$x = 0.10$	$x = 0.15$
Lattice parameter (\AA)				
$a = b$	3.128735	3.128089	3.127635	3.12781
c	4.611137	4.610414	4.610921	4.611841
c/a	1.473802	1.473876	1.474252	1.474463
d-spacing (\AA)				
(001)	4.6111	4.6104	4.6109	4.6118
(100)	2.7096	2.7090	2.7086	2.7088
(101)	2.3361	2.3356	2.3355	2.3357
R_p (%)	2.86	2.34	2.45	2.57
R_{wp} (%)	4.36	3.27	3.43	3.87
GOF (%)	2.90	2.15	2.28	2.56
Volume (\AA^3)	39.09095	39.06868	39.06164	39.07380
Density (g/cm^3)	3.93795	3.94020	3.94091	3.93968
D (nm)	41.68 \pm 0.53	43.23 \pm 0.68	42.16 \pm 1.02	41.26 \pm 1.33

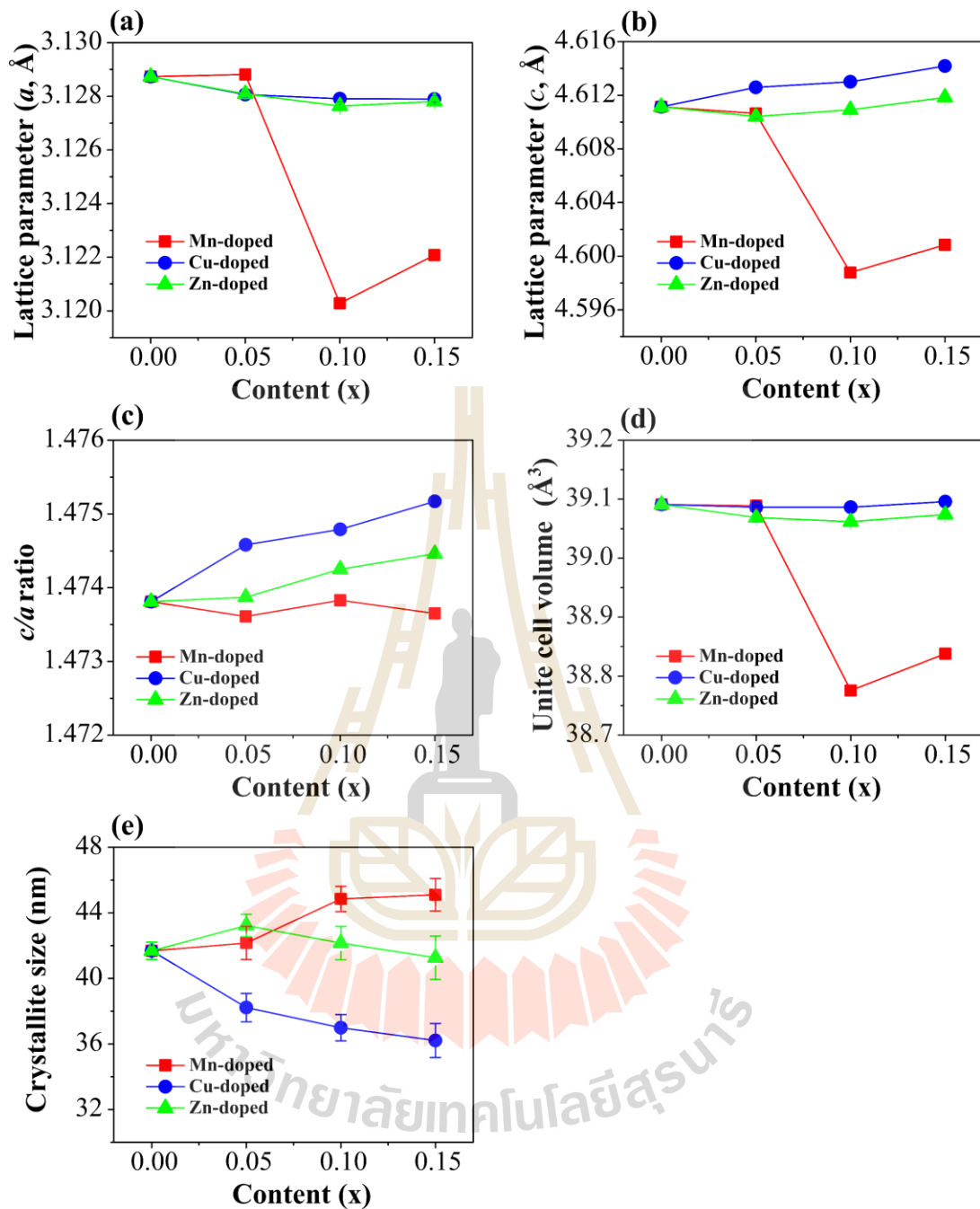


Figure 4.55 (a) Lattice parameter a , (b) Lattice parameter c , (c) c/a ratio, and unit cell volume obtained from the Rietveld refinement. (e) The calculated crystallite size as function of Mn, Cu, and Zn content (x) obtained from Scherer's equation.

Effects of Mn, Cu, and Zn-doped Ni(OH)₂ on size, shape, and surface morphologies were further characterized by using TEM technique. The morphologies with their corresponding selected area electron diffraction (SAED) patterns of Mn_xNi_{1-x}(OH)₂, Cu_xNi_{1-x}(OH)₂, and Zn_xNi_{1-x}(OH)₂ samples with different contents (x) of 0.00, 0.05, 0.10, and 0.15 are revealed as shown in Figure 4.56, 4.57, and 4.58, respectively. It is clearly seen in those TEM bright field images that Mn²⁺, Cu²⁺, and Zn²⁺ doping have a significant effect on the particle size, shape, and surface morphologies of Ni(OH)₂.

For Mn doping, the plate-like structure of hexagonal shape is clearly observed. Furthermore, Mn doping also found to have a great impact on surface evolution of hexagonal Ni(OH)₂. A remarkable observation is that the increase of the surface roughness with increasing Mn contents. The increase of roughness surface is possibly due to the developing of pores within the nanoplate. As previously presented in section 4.1.1 (Figure 4.3) that the formation of pores within the nanoplate is achieved through an aggregation of Ni(OH)₂ nanoparticles. The loss of water molecule under hydrothermal conditions creates the formation of nickel-oxygen bond at the interface of these aggregations, resulting in the formation of porous plate-like structure (Singh *et al.*, 2014). Therefore, this formation implies that the substitution of Mn may affect the bond of nickel-oxygen at the interface resulting in the change of surface morphologies. This observation could be advantages for electrochemical applications in order to promote the adsorption/desorption of electrolyte ions with providing a shorter diffusion pathway. The average particle size of hexagonal shape from TEM images are estimated to be 41.96±2.57, 43.00±2.02, 39.62±2.65, and 43.33±2.24 nm in samples of x = 0.00, 0.05, 0.10, and 0.15, respectively. The reduction of particle size

after Mn doping may be attributed to the lattice strain due to the size mismatch between Mn^{2+} ions and Ni^{2+} ions. In comparison, the crystallite size calculated by Scherer's equation is nearly the same as the particle size observed from TEM. One can also observe from TEM images is the difference in morphologies of hexagonal and bar-like shapes. The difference in morphologies can be explained by placing of the nanoplates in different directions as previously mentioned in Mg-doped $\text{Ni}(\text{OH})_2$ section. The selected area electron diffraction (SAED) patterns of $\text{Mn}_x\text{Ni}_{1-x}(\text{OH})_2$ samples reveal a spotty ring patterns as seen in Figure 4.56. Comparing with the standard diffraction data, the spotty rings show the characteristic of polycrystalline $\beta\text{-Ni}(\text{OH})_2$ (JCPDS file no. 14-0117) which are in good agreement with XRD results.

For Cu and Zn doping, the difference in morphologies between plate-like and bar-like shapes due to the placing of particle in difference directions are clearly observed as shown in Figure 4.57 and 4.58. The estimated particle size of hexagonal shape increases from 41.96 ± 2.57 to 46.96 ± 3.26 nm with increasing Cu contents from 0.00 to 0.10. With further increase Cu content up to 0.15, the decrease of particle size is observed. In case of Zn doping, the estimated particle size of hexagonal shape increases from 35.56 ± 1.87 to 39.64 ± 2.04 nm with increasing Zn contents from 0.05 to 0.15 whereas these values are still lower than the particle size of the undoped $\text{Ni}(\text{OH})_2$ sample ($x = 0.00$). The summarized data of the estimated particle size obtained from TEM images of $\text{Mn}_x\text{Ni}_{1-x}(\text{OH})_2$, $\text{Cu}_x\text{Ni}_{1-x}(\text{OH})_2$, and $\text{Zn}_x\text{Ni}_{1-x}(\text{OH})_2$ samples are listed in Table 4.13.

One can also see from TEM images of Cu-doped $\text{Ni}(\text{OH})_2$ in Figure 4.57 is that the lattice fringes are detected with the estimated d -spacing of 0.464, 0.4720, 0.476, and 0.481 nm in samples of $x = 0.00, 0.05, 0.10$, and 0.15, respectively. The

increase of these d -spacing values is consistent with the calculated d -spacing from XRD technique. These detected lattice fringes are also confirmed the placing of the particles in different directions. Moreover, the selected area electron diffraction (SAED) patterns of Cu and Zn doping reveal a spotty ring patterns as seen in Figure 4.57 and 4.58, respectively. Comparing with the standard diffraction data, these spotty rings show the characteristic of polycrystalline β -Ni(OH)₂ (JCPDS file no. 14-0117) which are in good agreement with XRD results.

In conclusion of the morphology analysis, it is found from the experimental results that Mn, Cu, and Zn doping have a great impact on the morphology and size of the materials, especially for Mn doping. A remarkable observation is that the developing of pores within the nanoplates resulting in the increase of roughness surface after Mn doping. This observation would be beneficial for electrochemical applications in order to provide a shorter diffusion pathway of electrolyte ions. In contrast, the significant change of particle size was clearly observed after Cu and Zn doping. Therefore, these observations are expected to associate with the electrochemical performances of the materials, which will be discussed in the electrochemical section.

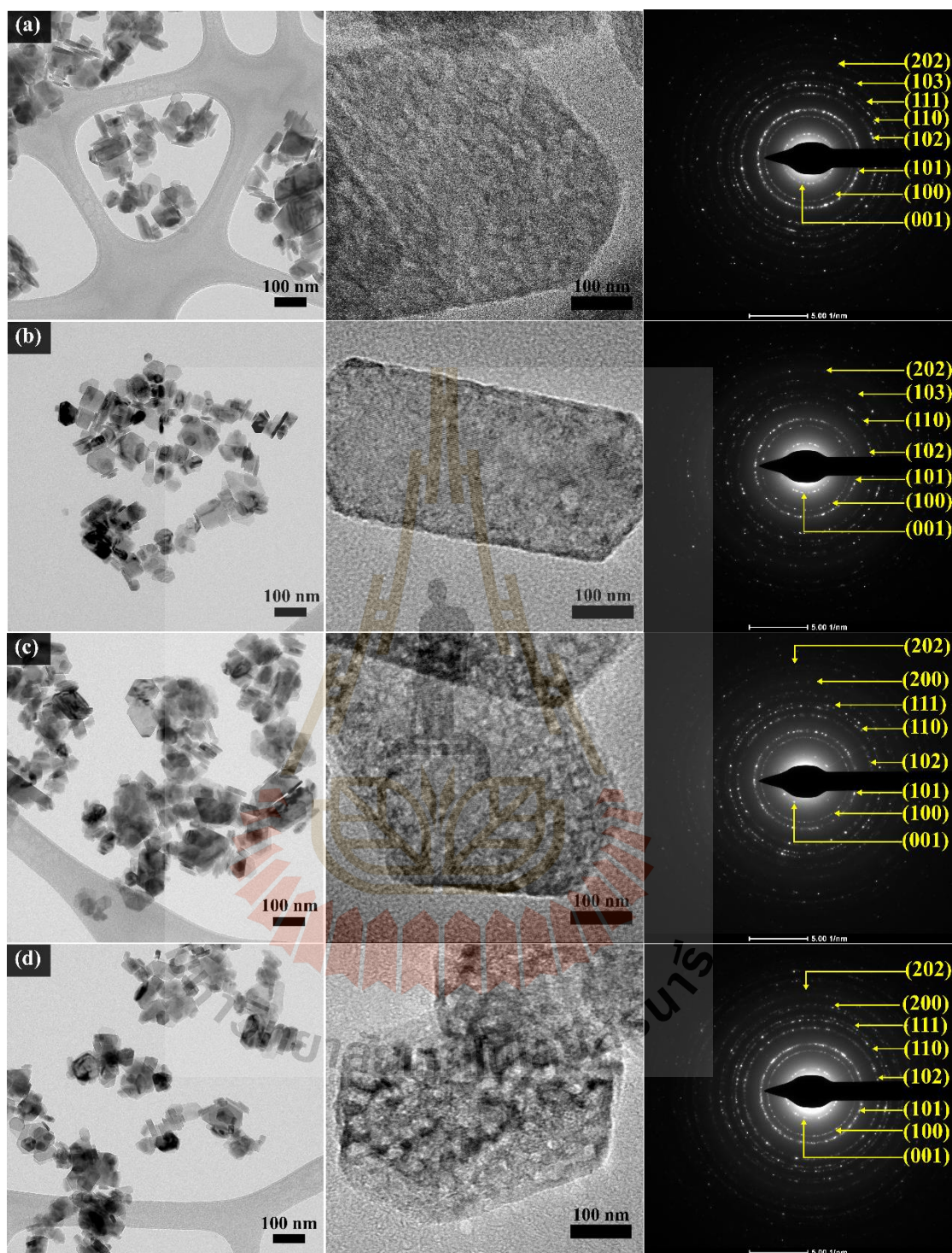


Figure 4.56 TEM bright field images and their corresponding SAED patterns of $\text{Mn}_x\text{Ni}_{1-x}(\text{OH})_2$ samples with (a) $x = 0.00$, (b) $x = 0.05$, (c) $x = 0.10$, and (d) $x = 0.15$, respectively.

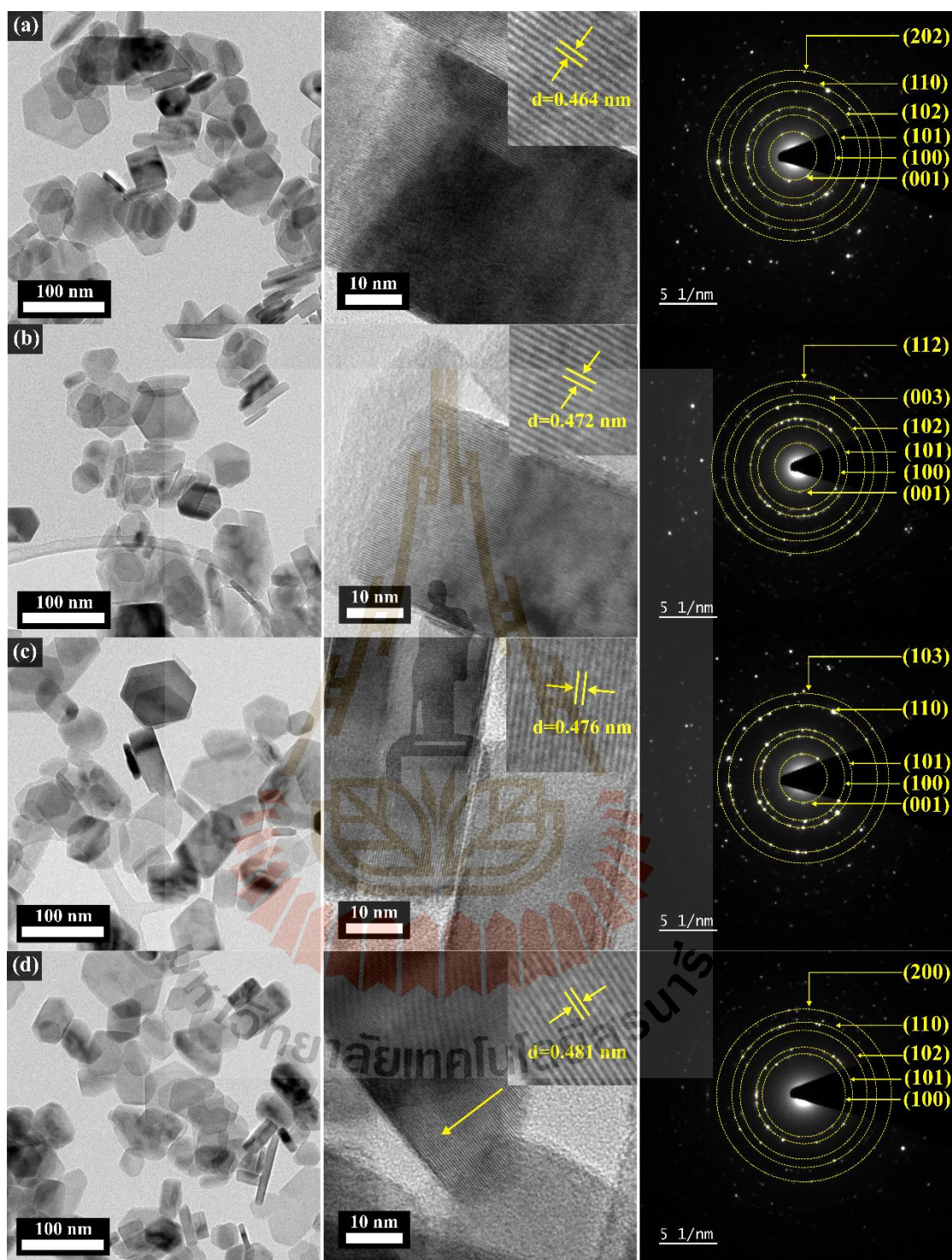


Figure 4.57 TEM bright field images, lattice fringes and their corresponding SAED patterns of $\text{Cu}_x\text{Ni}_{1-x}(\text{OH})_2$ samples with (a) $x = 0.00$, (b) $x = 0.05$, (c) $x = 0.10$, and (d) $x = 0.15$, respectively.

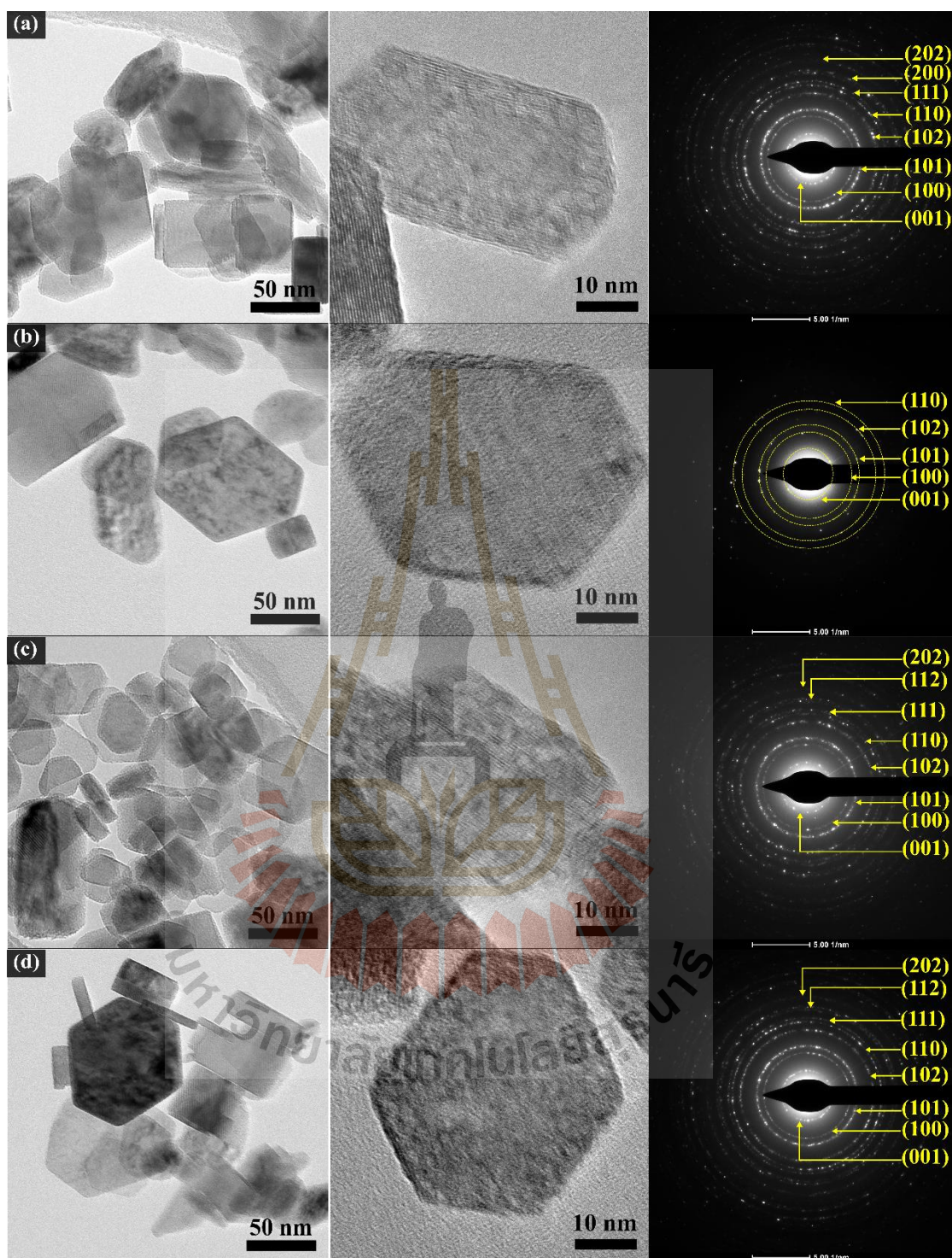


Figure 4.58 TEM bright field images and their corresponding SAED patterns of $\text{Zn}_x\text{Ni}_{1-x}(\text{OH})_2$ samples with (a) $x = 0.00$, (b) $x = 0.05$, (c) $x = 0.10$, and (d) $x = 0.15$, respectively.

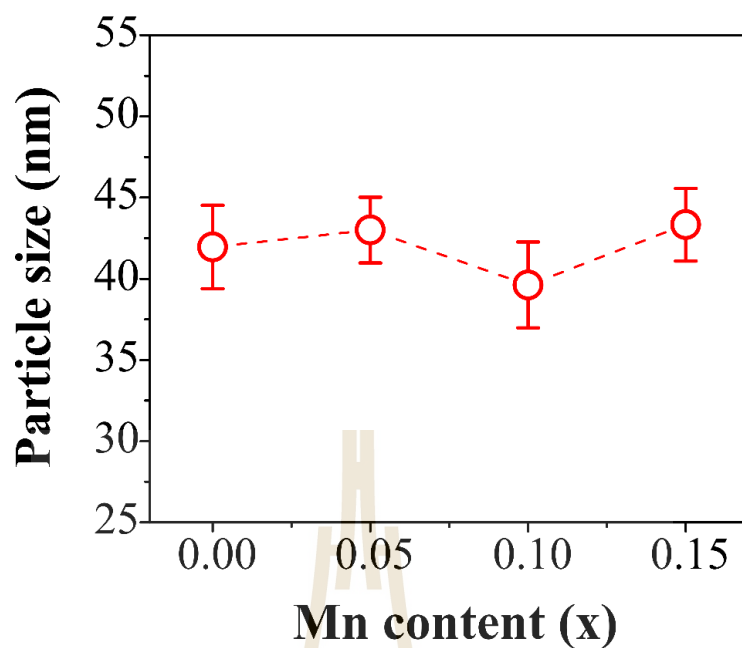


Figure 4.59 The average particle size of $\text{Mn}_x\text{Ni}_{1-x}(\text{OH})_2$ samples as function of Mn content (x).

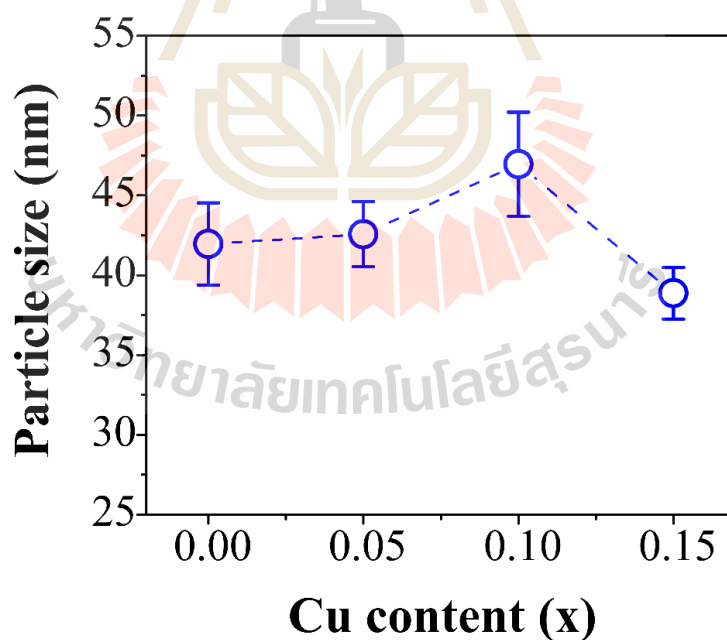


Figure 4.60 The average particle size of $\text{Cu}_x\text{Ni}_{1-x}(\text{OH})_2$ samples as function of Cu content (x).

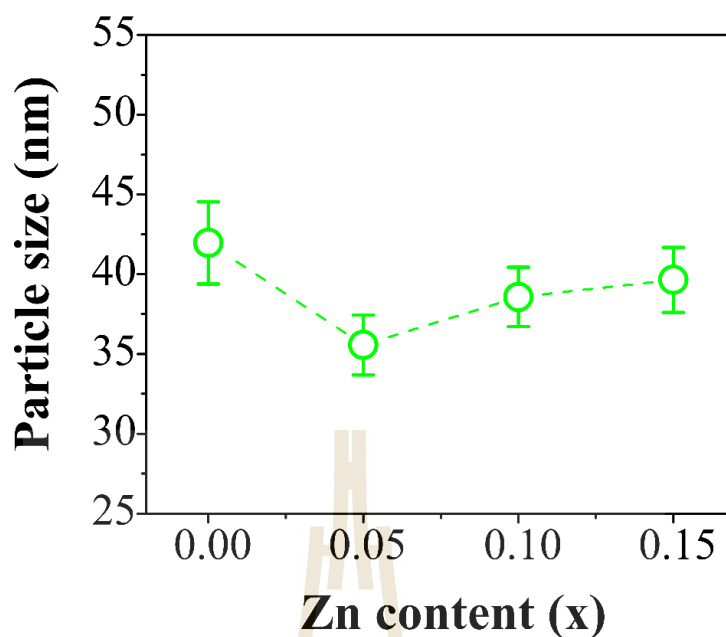


Figure 4.61 The average particle size for $\text{Zn}_x\text{Ni}_{1-x}(\text{OH})_2$ samples as function of Zn content (x).

Table 4.13 The summary of the average particle size for $\text{Mn}_x\text{Ni}_{1-x}(\text{OH})_2$, $\text{Cu}_x\text{Ni}_{1-x}(\text{OH})_2$, and $\text{Zn}_x\text{Ni}_{1-x}(\text{OH})_2$ samples with different Mn, Cu, and Zn doping contents.

Content (x)	Particle size (nm)		
	Mn-doped	Cu-doped	Zn-doped
0.00	41.96±2.57	41.96±2.57	41.96±2.57
0.05	43.00±2.02	42.76±2.04	35.56±1.87
0.10	39.62±2.65	46.96±3.26	38.57±1.86
0.15	43.33±2.24	38.87±1.62	39.64±2.04

4.4.2 Chemical compositions and oxidation states analysis

To investigate the change of Mn, Cu, and Zn contents on the chemical environment in $\text{Mn}_x\text{Ni}_{1-x}(\text{OH})_2$, $\text{Cu}_x\text{Ni}_{1-x}(\text{OH})_2$, and $\text{Zn}_x\text{Ni}_{1-x}(\text{OH})_2$ samples, XPS technique is used. Owing to the fact that XPS technique is used for measurement an emitted photoelectron by exciting a samples surface with known energy of X-rays phonon. Hence, the binding energy is calculated which is characteristic of chemical bonds in material. From the binding energy and intensity of the photoelectron peak, the elemental identity, chemical state, and quantity of the detected element can be determined. Figure 4.62, 4.63, 4.64 shows the survey XPS spectra of $\text{Mn}_x\text{Ni}_{1-x}(\text{OH})_2$, $\text{Cu}_x\text{Ni}_{1-x}(\text{OH})_2$, and $\text{Zn}_x\text{Ni}_{1-x}(\text{OH})_2$ samples, respectively. Those XPS survey spectra confirm the presence of C 1s, O 1s, and Ni 2p on the samples surface. It should be noted that the characteristic peaks of Mn 2p₃, Cu 2p, and Zn 2p region are not clearly observed in the doping samples due to the small amounts of Mn^{2+} , Cu^{2+} , and Zn^{2+} ions ($x = 0.05, 0.10$, and $x = 0.15$) were substituted in Ni^{2+} sites.

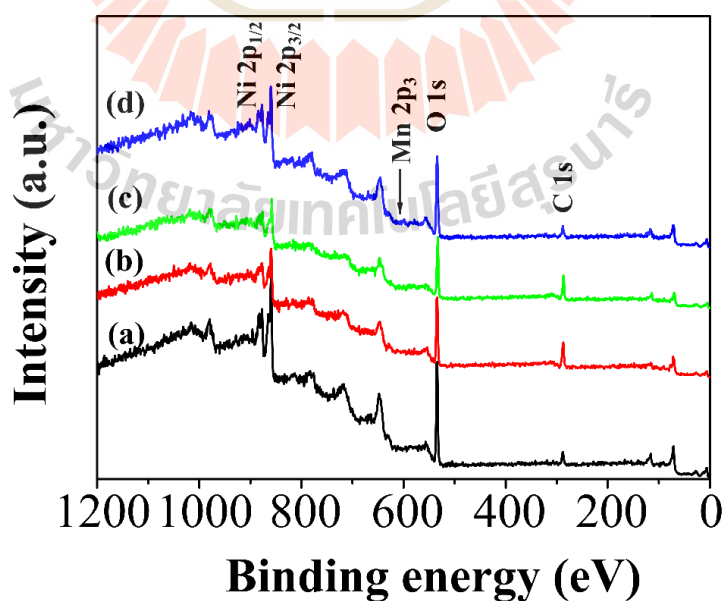


Figure 4.62 The survey XPS spectrum of $\text{Mn}_x\text{Ni}_{1-x}(\text{OH})_2$ samples with (a) $x = 0.00$, (b) $x = 0.05$, (c) $x = 0.10$, and (d) $x = 0.15$.

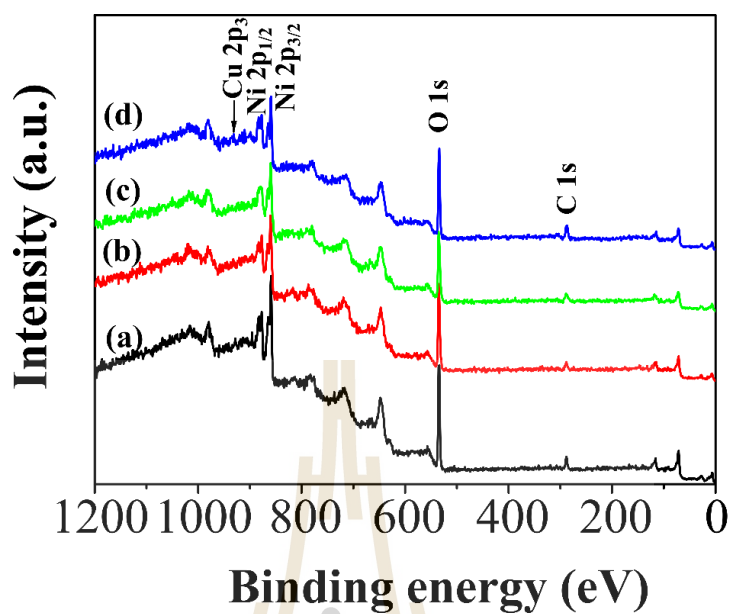


Figure 4.63 The survey XPS spectrum of $\text{Cu}_x\text{Ni}_{1-x}(\text{OH})_2$ samples with (a) $x = 0.00$, (b) $x = 0.05$, (c) $x = 0.10$, and (d) $x = 0.15$.

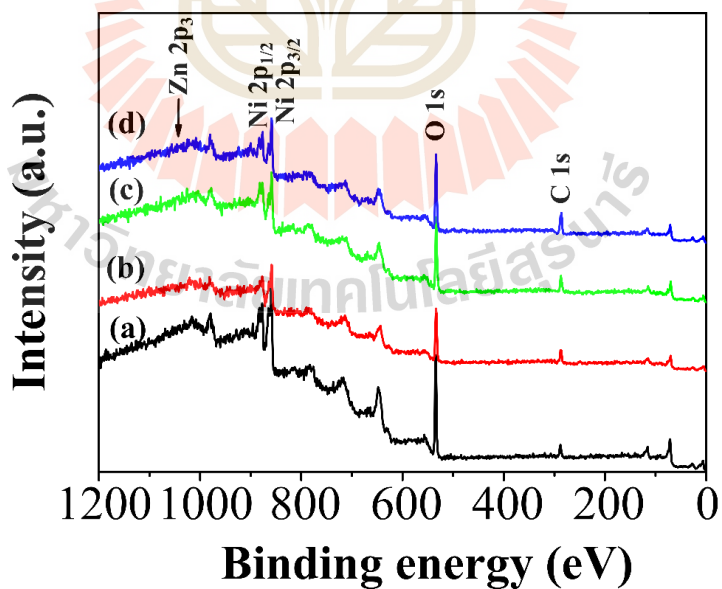


Figure 4.64 The survey XPS spectrum of $\text{Zn}_x\text{Ni}_{1-x}(\text{OH})_2$ samples with (a) $x = 0.00$, (b) $x = 0.05$, (c) $x = 0.10$, and (d) $x = 0.15$.

As previously mentioned before, XAS measurements are used to study the local structure of the material. It is a technique which probes the core-shell electrons of an atom by the beam of X-ray photons. In general, XAS spectrum consists of two main regions of XANES and EXAFS. XANES gives an information about the oxidation number and atomic coordination of added impurity ions (Tsuzuki *et al.*, 2019). In this work, XANES measurements of Zn-doped Ni(OH)₂ were collected at SLRI (BL 5.2). All spectra at Ni (8333 eV) and Zn (9656 eV) *K*-edge were carried out in transmission mode, and fluorescent mode, respectively. Nickel and zinc foils were used for the calibration of the edge energy. The XANES spectra of the samples were compared to those of the reference standard metals and compounds of Ni foil, NiO, Zn foil, ZnO, and Zn(CH₃COO)₂·2H₂O standard samples to indicate the oxidation state of an absorbing atom of the samples.

Generally, the oxidation state of an absorbing atom can be determined by the energy position of pre-edge features or from the absorption edge of XANES spectrum (Berghöfer *et al.*, 1993). Figure 4.65 shows the normalized Ni *K*-edge XANES spectra of Zn-doped Ni(OH)₂. It is clearly seen that the spectra show three main features in all Zn-doped Ni(OH)₂ samples. In region I, the presence of pre-edge absorption in all Zn-doped Ni(OH)₂ samples at energy about 8333.6±0.2 eV can be explained due to the transition from a 1s state to an unoccupied 3d state (Farges *et al.*, 2001). The change of pre-edge positions at different energies indicates the change of Ni-coordination (Landers *et al.*, 2011). Therefore, this result suggests the change of Ni-coordination after Zn doping. In region II, the positions of the Ni *K*-edge in all samples are close to that of the NiO standard sample indicating that the oxidation state of Ni is 2+ which is also confirmed by the first derivative plots as shown in Figure 4.66. For

region III, the white-line intensity and width slight increase with increasing Zn contents. A reduction of a white-line width is related to a reduction of the distortion on MO_6 octahedral (Cuartero *et al.*, 2016). As seen in Figure 4.65, the more distortion due to the wider white line width is observed after Zn doping. The distortion is associated with structural instability of the materials (Sharma *et al.*, 2017). This structural instability can lead to the poor cycle performance in the materials (Wei *et al.*, 2018).

The normalized XANES spectra of Zn *K*-edge of Zn-doped $\text{Ni}(\text{OH})_2$ samples are shown in Figure 4.67. As seen in the Figure, the positions of the Zn *K*-edge in all samples are close to that of the ZnO standard sample indicating that the oxidation state of Zn is 2+ which is also confirmed by the first derivative plots of Zn *K*-edge as shown in Figure 4.68.

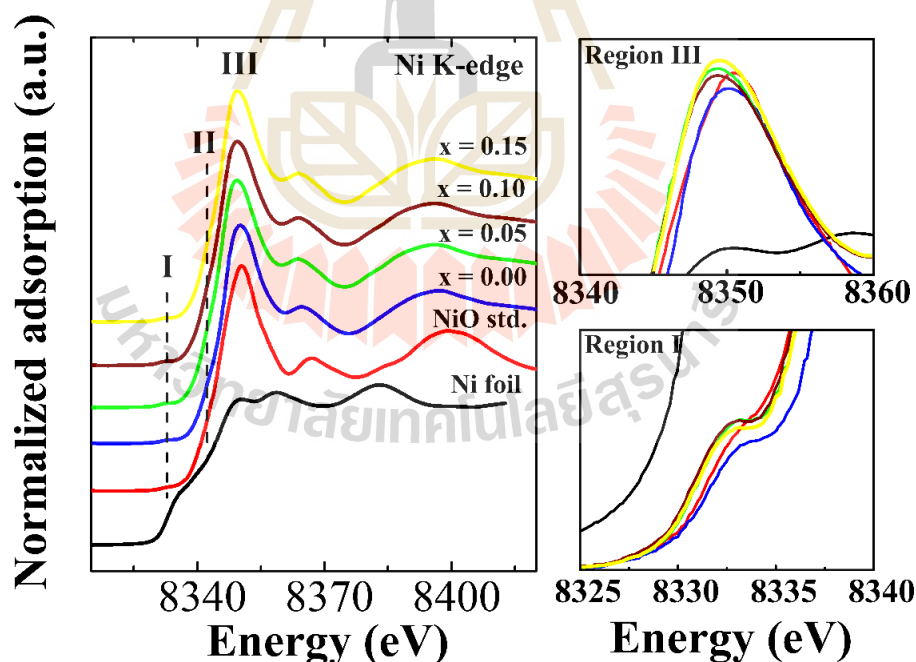


Figure 4.65 XANES spectra including pre-edge (region I) and white line region (region III) of Zn-doped $\text{Ni}(\text{OH})_2$ at Ni *K*-edge measured in transmission mode.

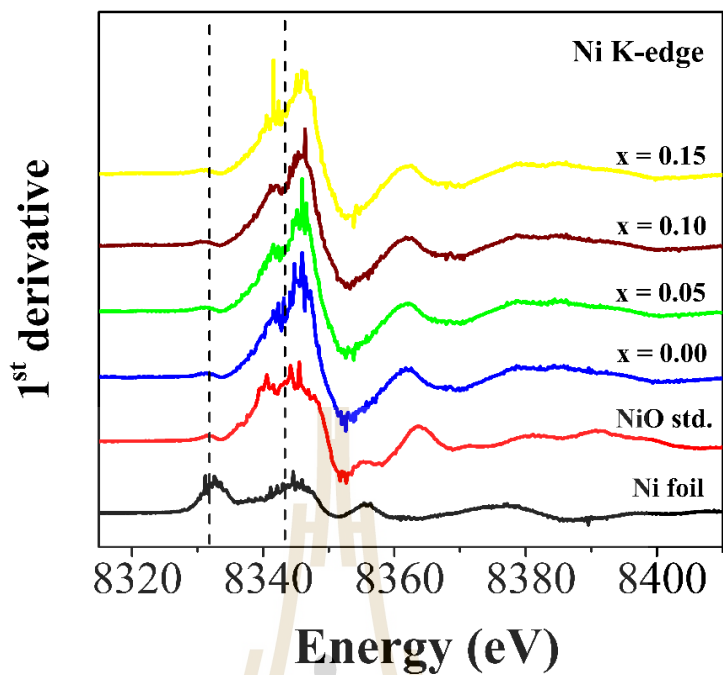


Figure 4.66 The first derivative plots of Zn-doped $\text{Ni}(\text{OH})_2$ at Ni K-edge measured in transmission mode.

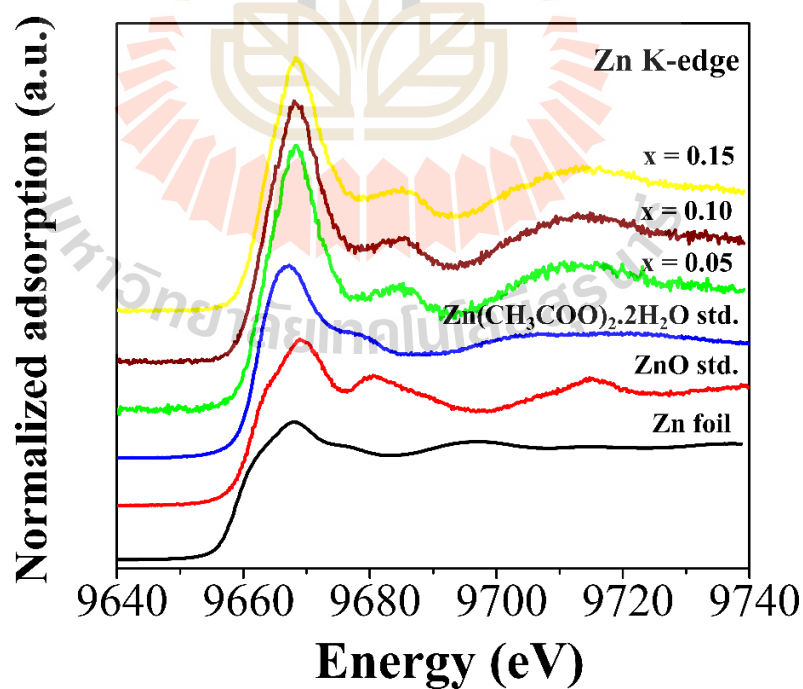


Figure 4.67 XANES spectra of Zn-doped $\text{Ni}(\text{OH})_2$ samples at Zn K-edge measured in fluorescence mode.

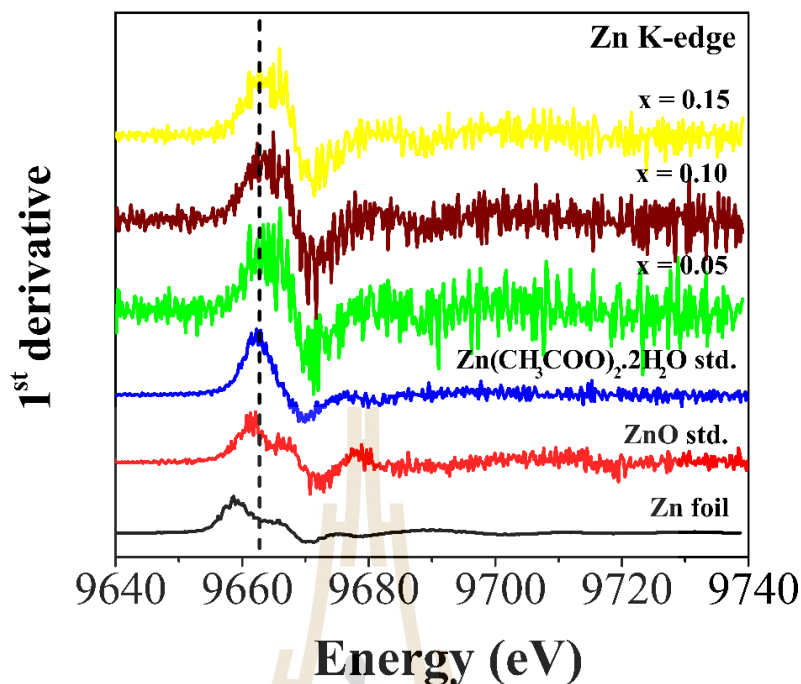


Figure 4.68 The first derivative plots of Zn-doped $\text{Ni}(\text{OH})_2$ at Zn K-edge measured in transmission mode.

4.4.3 Specific surface area and porosity analysis

As mentioned before, the specific surface area and porosity of materials play significant roles in an electrochemical performance, especially for carbon-based materials. Figure 4.69 shows the N_2 adsorption/desorption isotherms and their corresponding pore size distributions of $\text{Mn}_x\text{Ni}_{1-x}(\text{OH})_2$, $\text{Cu}_x\text{Ni}_{1-x}(\text{OH})_2$, and $\text{Zn}_x\text{Ni}_{1-x}(\text{OH})_2$ samples, respectively. As seen in those Figures, the N_2 sorption isotherm curves present the hysteresis loop at the relative pressure ranging from 0.4 to 0.9 after Mn and Zn doping which can be classified as type IV with H3 hysteresis loops according to IUPAC classifications (Nagaraju *et al.*, 2017). It is also noticed in Figure 4.69(c) that the adsorbed volume in the isotherms after Cu doping is lower than the undoped sample. The summarized data obtained from N_2 sorption and pore size

distribution of $\text{Mn}_x\text{Ni}_{1-x}(\text{OH})_2$, $\text{Cu}_x\text{Ni}_{1-x}(\text{OH})_2$, $\text{Zn}_x\text{Ni}_{1-x}(\text{OH})_2$ samples are given in Table 4.14, 4.15, and 4.16, respectively.

For Mn doping, the calculated BET specific surface area from the N_2 isotherm was found to be increased with increasing Mn content from 0.05 to 0.15. It was reported that the higher specific surface area of the materials suggested that to provide a larger contact area with the electrolyte, which is highly beneficial for the delivery of higher capacitance value (Sun *et al.*, 2015). In contrast, the total pore volume (V_T) was found to be increased with increasing Mn contents from 0.00 to 0.15. This result is consistent with the observed developing of pores in TEM images as clearly seen in Figure 4.56 in which the developing of pores increases with increasing Mn contents resulting in an increase of total pore volume (V_T). Additionally, mean pore diameter was found to be increased after Mn doping and it was decreased with increasing Mn contents. The size of pores was reported to have an important effect for the transportation of an electrolyte ions (Chuan-xiang *et al.*, 2010). The mesopore diameter and mesopore volume are also followed the same trend as mean pore diameter and total pore volume. One can also see from Table 4.14 is that the specific surface area increases as the particle size decreases. As seen in Figure 4.69(b), the calculated pore size distribution from the adsorption branch of the nitrogen isotherm by using the Barrett-Joyner-Halenda (BJH) method (Barrett *et al.*, 1951) shows the wider pore size distribution after Mn doping. The peaks centering in those Mn-doped $\text{Ni}(\text{OH})_2$ samples are found to be in the range of 51-59 nm. Therefore, this result confirms the mesoporous structure in all Mn-doped $\text{Ni}(\text{OH})_2$ samples. The difference in pore size distribution is expected for the difference in electrochemical behaviors of $\text{Mn}_x\text{Ni}_{1-x}(\text{OH})_2$ samples.

For Cu doping, mean pore diameter and total pore volume decrease significantly after Cu doping (see Table 4.15). This may be explained by that the copper has penetrated into the multiple pore structure and filled the mesoporous of the materials (Zhao *et al.*, 2017), resulting in the decrease of both mean pore diameter and total pore volume. As seen in Figure 4.69(d), the calculated pore size distributions from both BJH and MP methods show the narrower pore size distributions after Cu doping. The peaks centering in those Cu-doped Ni(OH)₂ samples are found to be the same value (0.7 nm) in all samples. This result clearly indicates the existence of microporous structure after Cu doping. In carbon-based materials, the existence of micropore is very useful for the enhanced capacitance value. Chmiola *et al.* (Chmiola *et al.*, 2006) reported on the improved capacitance value due to the solvated shell of electrolyte ions was partially removed in order to enter into small pores (<1nm). The schematic representation for the decrease of mean pore diameter and total pore volume after Cu doping is proposed as shown in Figure 4.70.

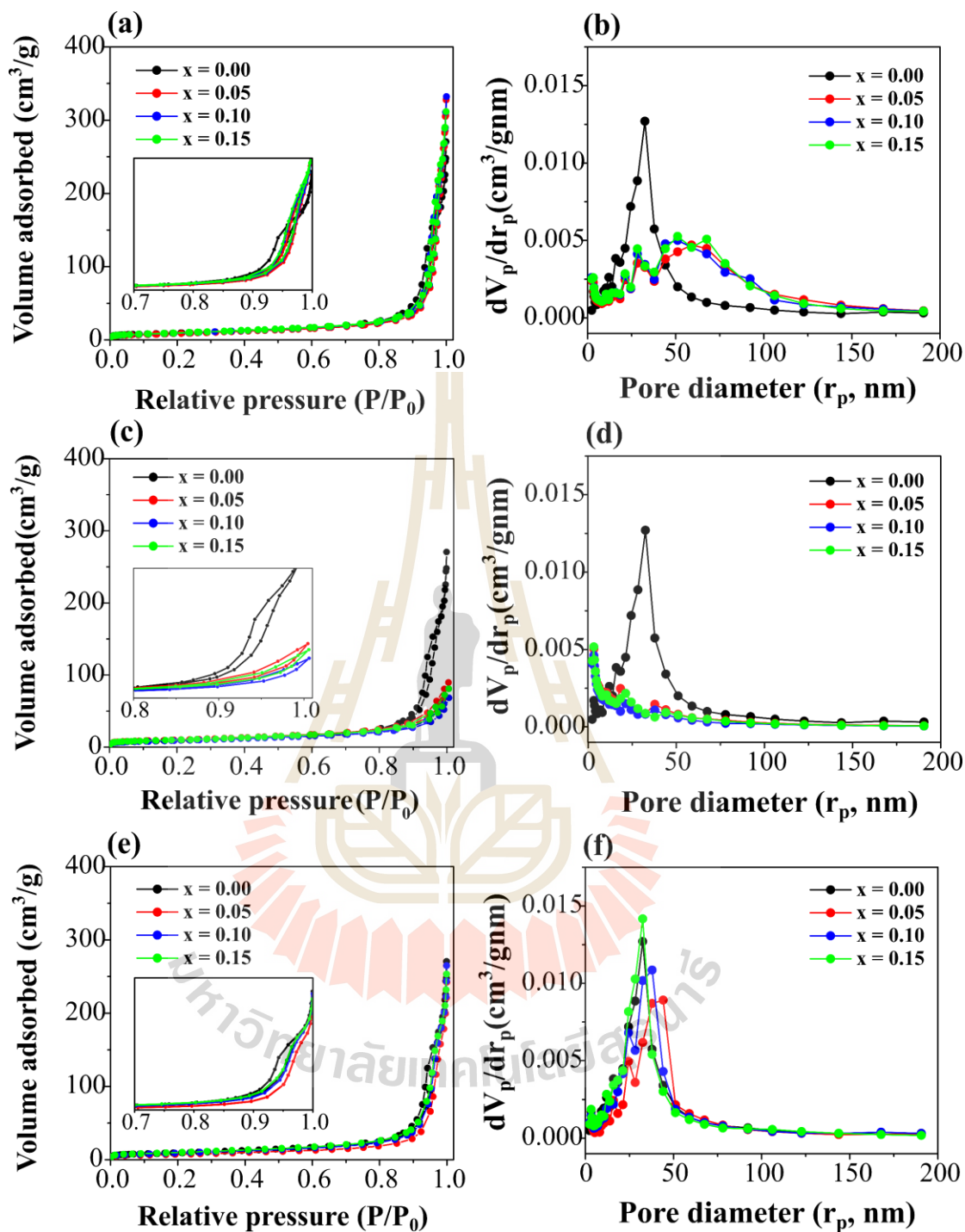


Figure 4.69 (a, c, e) N_2 adsorption/desorption isotherm and (b, d, f) the pore size distribution of $Mn_xNi_{1-x}(OH)_2$, $Cu_xNi_{1-x}(OH)_2$, and $Zn_xNi_{1-x}(OH)_2$ samples calculated from BET and BJH methods, respectively. The inset indicates the presence of hysteresis loops and micropore distributions.

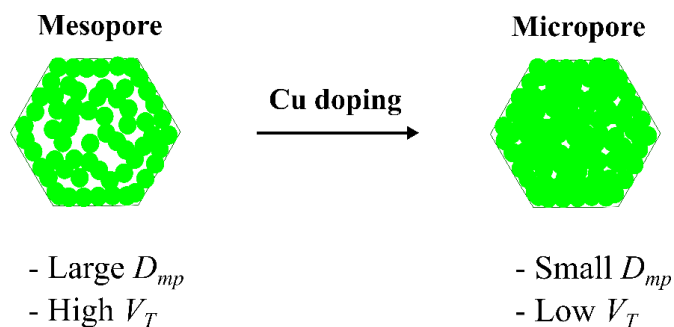


Figure 4.70 Schematic representation of the decrease of mean pore diameter (D_{mp}) and total pore volume (V_T) after Cu doping.

In case of Zn doping (Figure 4.69(e, f)), the decrease of mean pore diameters accounting for the higher specific surface area and total pore volume is clearly observed. The calculated pore size distributions from BJH method demonstrate that the pore size distributions are centered at 32.57, 44.14, 37.87, and 32.57 nm in samples for $x = 0.00, 0.05, 0.10$, and 0.15 , respectively. These results confirm the presence of mesopores in all Zn-doped $\text{Ni}(\text{OH})_2$ samples.

In conclusion of specific surface area and porosity analysis, it is found from the experimental results that Mn, Cu, and Zn doping have great effects on the specific surface area, pore diameter, and pore volume of the materials. A significant observation is the increase of pore diameter and pore volume due to the developing of pores after Mn doping which affected the surface morphology as clearly seen in the TEM images. The specific surface area correlates well with the particle size (d_{BET}) in which the specific surface area increases as particle size decreases. This can be simply explained by the higher surface-to-volume ratio in smaller particle size. The difference in these results is expected in the different electrochemical performances of Mn, Cu, and Zn-doped $\text{Ni}(\text{OH})_2$.

Table 4.14 Specific surface area (S_{BET}), mean pore diameter (D_{MP}), total pore volume (V_{T}), mesopore diameter (D_{BJH}), mesopore volume (V_{BJH}), and BET particle size (d_{BET}) of $\text{Mn}_x\text{Ni}_{1-x}(\text{OH})_2$ samples.

Sample	S_{BET} (m^2/g)	D_{MP} (nm)	V_{T} (cm^3/g)	D_{BJH} (nm)	V_{BJH} (cm^3/g)	d_{BET} (nm)
$x = 0.00$	33.026	36.932	0.305	32.57	0.317	46.13
$x = 0.05$	31.719	47.096	0.374	59.00	0.374	48.03
$x = 0.10$	33.887	44.523	0.377	51.10	0.378	44.60
$x = 0.15$	34.452	45.010	0.389	51.10	0.389	43.94

Table 4.15 Specific surface area (S_{BET}), mean pore diameter (D_{MP}), total pore volume (V_{T}), mesopore diameter (D_{BJH}), mesopore volume (V_{BJH}), micropore diameter (D_{Micro}), and BET particle size (d_{BET}) of $\text{Cu}_x\text{Ni}_{1-x}(\text{OH})_2$ samples.

Sample	S_{BET} (m^2/g)	D_{MP} (nm)	V_{T} (cm^3/g)	D_{BJH} (nm)	V_{BJH} (cm^3/g)	D_{Micro} (nm)	d_{BET} (nm)
$x = 0.00$	33.026	36.932	0.305	32.57	0.317	-	46.13
$x = 0.05$	35.412	11.921	0.106	3.28	0.119	0.70	43.02
$x = 0.10$	31.026	10.185	0.079	3.28	0.088	0.70	49.10
$x = 0.15$	34.418	11.126	0.096	3.28	0.016	0.70	44.27

Table 4.16 Specific surface area (S_{BET}), mean pore diameter (D_{MP}), total pore volume (V_{T}), mesopore diameter (D_{BJH}), mesopore volume (V_{BJH}), and BET particle size (d_{BET}) of $\text{Zn}_x\text{Ni}_{1-x}(\text{OH})_2$ samples.

Sample	S_{BET} (m^2/g)	D_{MP} (nm)	V_{T} (cm^3/g)	D_{BJH} (nm)	V_{BJH} (nm)	d_{BET} (nm)
$x = 0.00$	33.026	36.932	0.305	32.57	0.317	46.13
$x = 0.05$	26.130	41.776	0.273	44.14	0.283	58.28
$x = 0.10$	32.460	37.349	0.303	37.87	0.316	46.90
$x = 0.15$	35.531	34.605	0.307	32.57	0.317	42.86

4.4.4 Electrochemical study

The electrochemical performance of the Mn, Cu, and Zn doping was evaluated using three-electrode system. The reference electrode was Ag/AgCl saturated in 3M KCl aqueous electrolyte. The counter electrode was a Pt. plate and the working electrode was the prepared $\text{Mn}_x\text{Ni}_{1-x}(\text{OH})_2$, $\text{Cu}_x\text{Ni}_{1-x}(\text{OH})_2$, and $\text{Zn}_x\text{Ni}_{1-x}(\text{OH})_2$ samples with $x = 0.00, 0.05, 0.10$, and 0.15 on GDL substrate. Three well-known electrochemical techniques including cyclic voltammetry (CV), galvanostatic charge/discharge (GCD), and electrochemical impedance spectroscopy (EIS) were carried out for electrochemical study.

4.4.4.1 Cyclic voltammetry

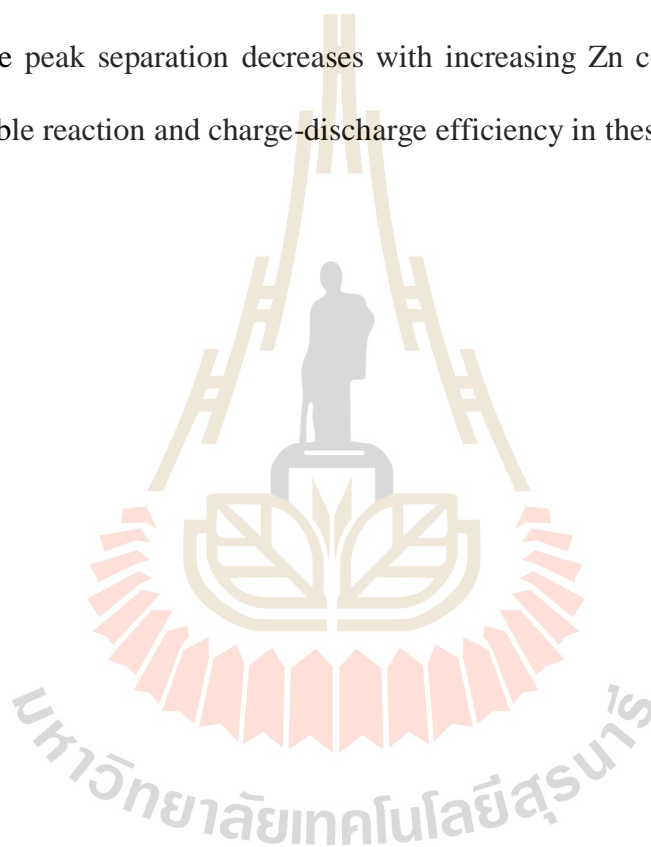
The effect of Mn, Cu, and Zn doping on electrochemical performance was evaluated by CV analysis. The CV curves at different scan rates of 1, 2, 3, 4, 5, and 10 mV/s of $\text{Mn}_x\text{Ni}_{1-x}(\text{OH})_2$, $\text{Cu}_x\text{Ni}_{1-x}(\text{OH})_2$, and $\text{Zn}_x\text{Ni}_{1-x}(\text{OH})_2$ samples are shown in

Figure 4.71, 4.72, and 4.73, respectively. As seen in those figures, a pair of redox peaks is clearly observed in all Mn, Cu, and Zn-doped Ni(OH)_2 samples, indicating a Faradaic redox reaction. The redox peaks in CV curves are attributed to the reversible reaction between Ni(OH)_2 to NiOOH following the equation 4.6. Taking a closer look to the CV curves in all $\text{Mn}_x\text{Ni}_{1-x}(\text{OH})_2$, $\text{Cu}_x\text{Ni}_{1-x}(\text{OH})_2$, and $\text{Zn}_x\text{Ni}_{1-x}(\text{OH})_2$ samples, the shifts of oxidation and reduction peaks toward higher and lower potentials are clearly observed with increasing scan rates. These results are attributed to the increase of electric polarization and irreversible reactions at higher scan rates (Wang *et al.*, 2017).

The comparison of CV curves for $\text{Mn}_x\text{Ni}_{1-x}(\text{OH})_2$ samples at scan rate of 2 mV/s are shown in Figure 4.74. It is clearly seen that after Mn doping the area under CV curves of $x = 0.05$ and $x = 0.10$ become smaller, while the area under CV curve of $x = 0.15$ is a little bit larger than the undoped sample ($x = 0.00$). Taking into account that the area under CV curve is directly related to the amount of charge storage in the materials. As a result, a larger area under CV curve means a higher charge storage (Singh and Chandra, 2016; Jia *et al.*, 2018). Therefore, this result suggests the higher specific capacitance value in sample of $x = 0.15$. Furthermore, the potential separation ($\Delta E = E_a - E_c$) between oxidation peak (E_a) and reduction peak (E_c) increases with increasing Mn contents. The decrease of the potential separation value is attributed to the enhancement of the reversible and charge-discharge efficiency (Yue *et al.*, 2012). The increase of potential separation ΔE , as shown in the (table) inset of Figure 4.74, after Mn doping indicates the worse reversibility in all Mn-doped Ni(OH)_2 samples.

For Cu doping (Figure 4.75), a remarkable observation is that the redox peak shifts toward lower potential in sample of $x = 0.05$. This shift was caused by adding small amount of Cu ions to the Ni(OH)_2 . Moreover, the potential peak separation

seems to be increased with increasing Cu contents except for sample of $x = 0.10$. In addition, the sample of $x = 0.05$ exhibits much higher oxygen evolution reaction (OER) than those of the other samples. The higher OER is attributed to the increase of specific surface area which is consistent with the literature (Zhou *et al.*, 2017). For Zn doping (Figure 4.76), it can be noticed that the larger area under CV curves are observed in all Zn-doped $\text{Ni}(\text{OH})_2$ samples, implying the higher specific capacitance in these samples. Moreover, the peak separation decreases with increasing Zn contents indicating the better reversible reaction and charge-discharge efficiency in these samples (Yue *et al.*, 2012).



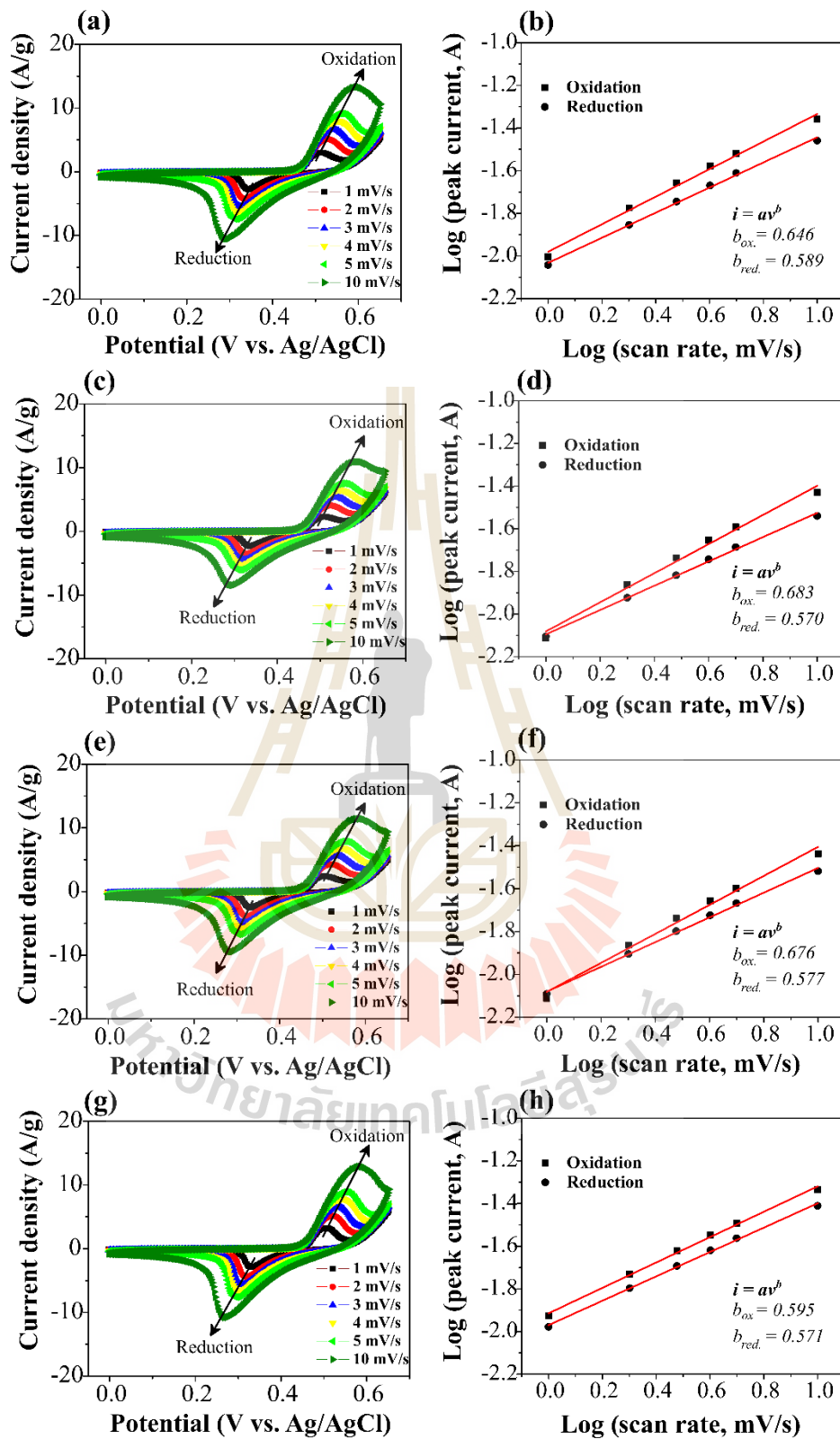


Figure 4.71 (a, c, e, g) CV curves and (b, d, f, h) their scan rate dependent of peaks current of $\text{Mn}_x\text{Ni}_{1-x}(\text{OH})_2$ samples with $x = 0.00, 0.05, 0.10,$ and 0.15 , respectively.

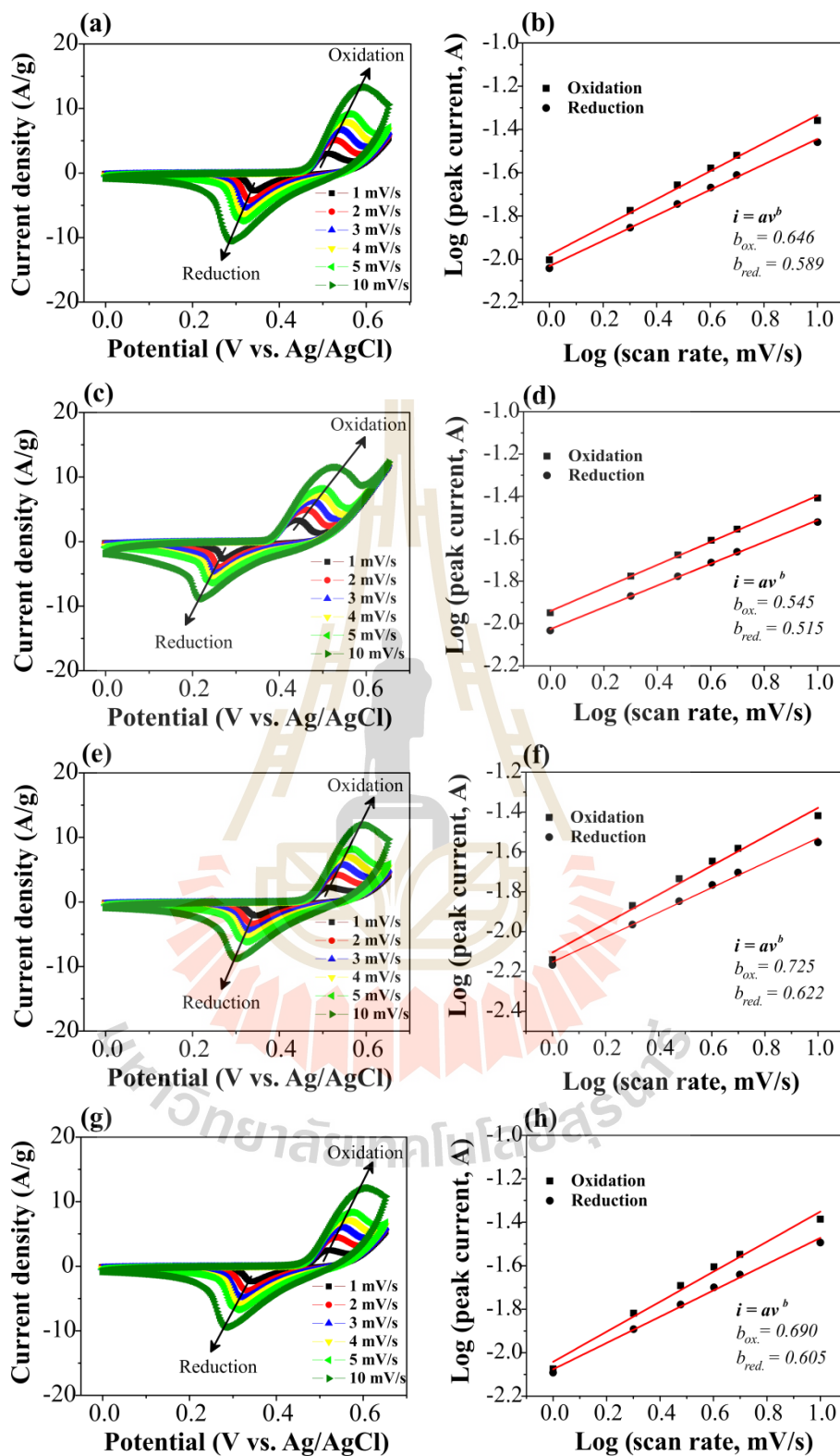


Figure 4.72 (a, c, e, g) CV curves and (b, d, f, h) their scan rate dependent of peaks current of $\text{Cu}_x\text{Ni}_{1-x}(\text{OH})_2$ samples with $x = 0.00, 0.05, 0.10,$ and 0.15 , respectively.

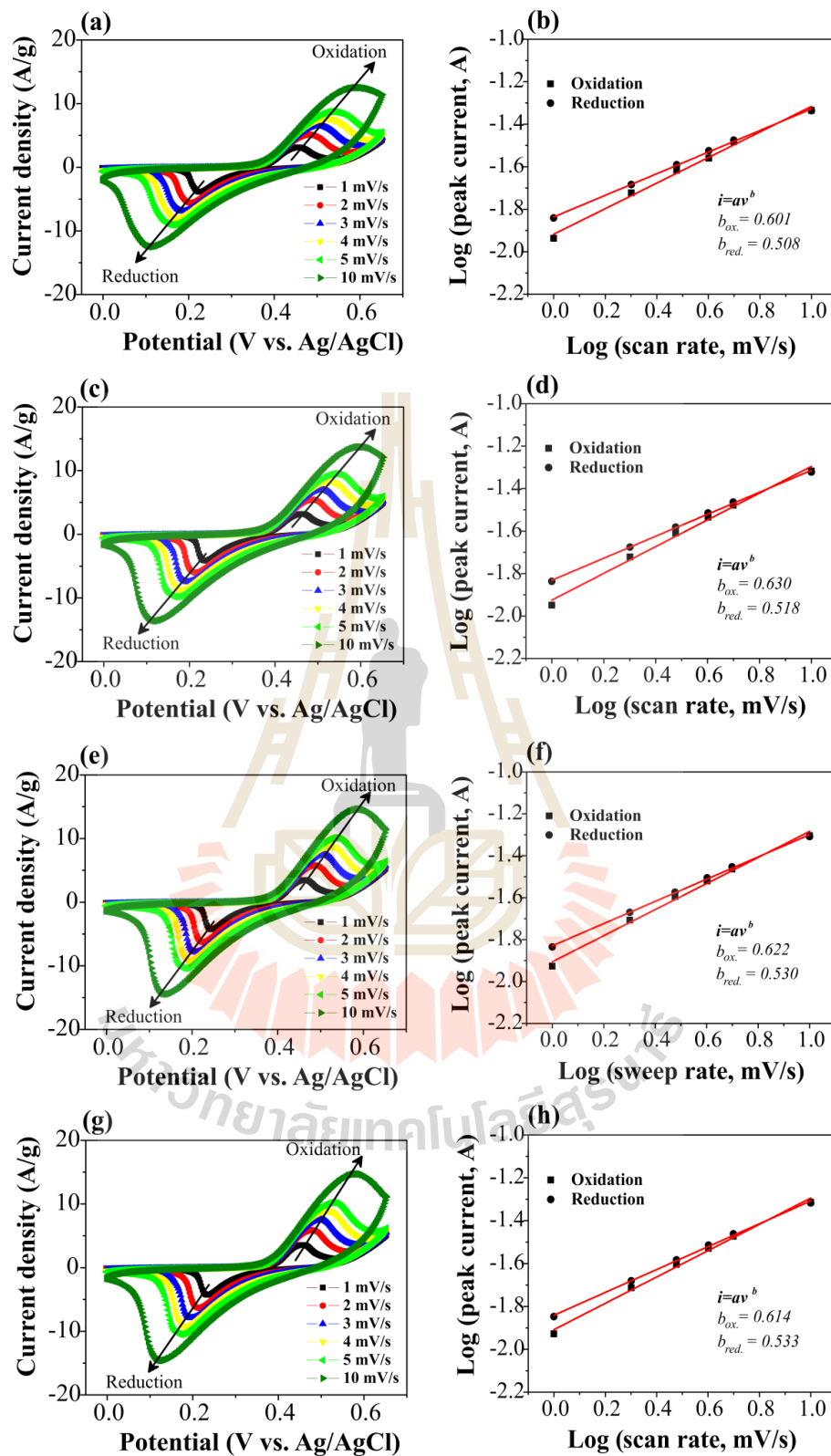


Figure 4.73 (a, c, e, g) CV curves and (b, d, f, h) their scan rate dependent of peaks current of $\text{Zn}_x\text{Ni}_{1-x}(\text{OH})_2$ samples with $x = 0.00, 0.05, 0.10,$ and 0.15 , respectively.

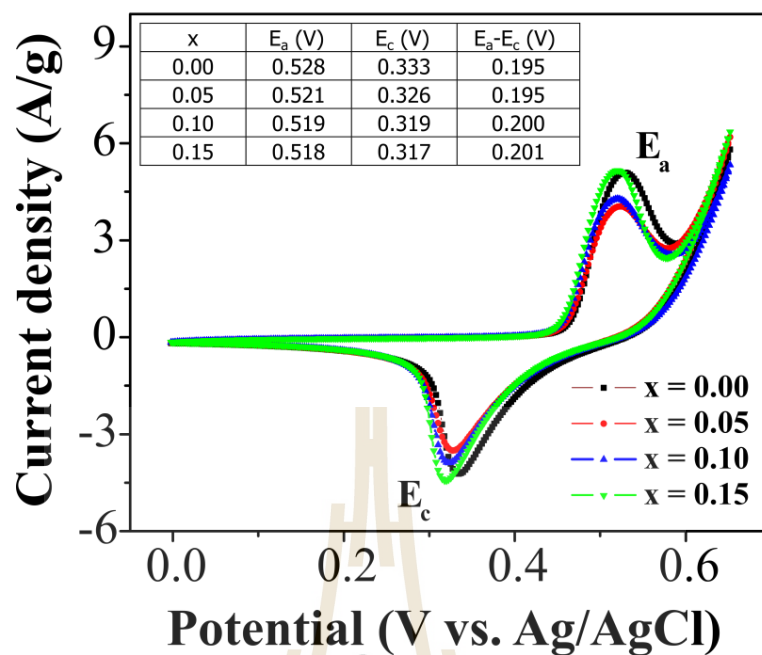


Figure 4.74 Comparison CV curves of $Mn_xNi_{1-x}(OH)_2$ samples at scan rates of 2 mV/s.

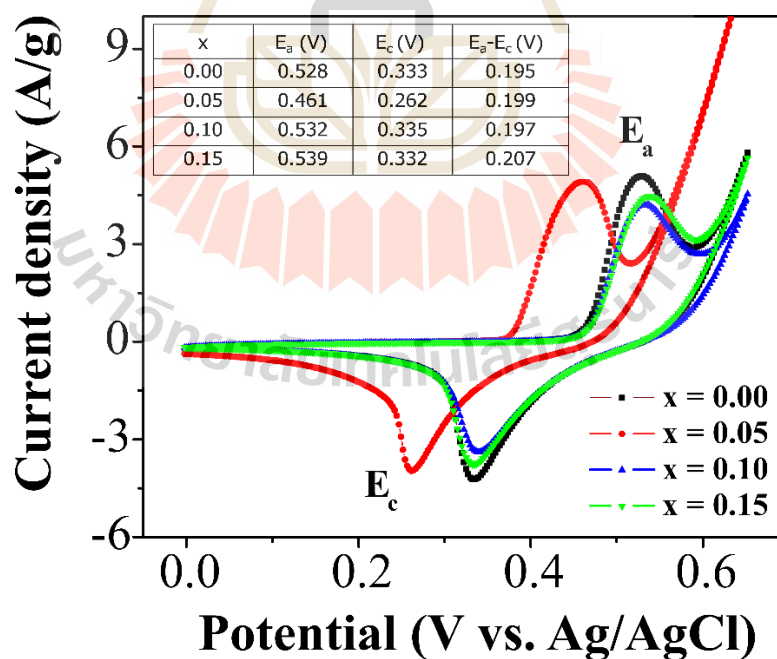


Figure 4.75 Comparison CV curves of $Cu_xNi_{1-x}(OH)_2$ samples at scan rates of 2 mV/s.

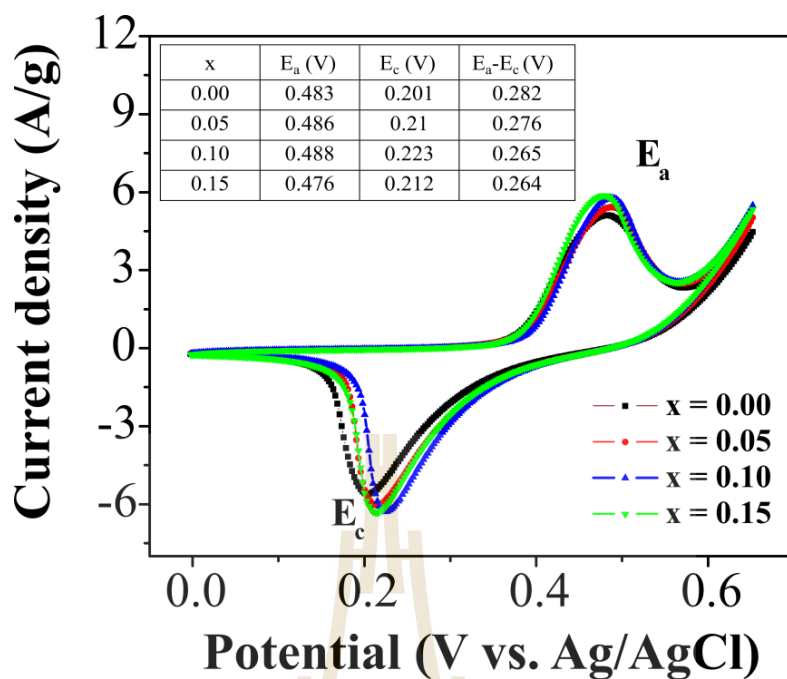


Figure 4.76 Comparison CV curves of $\text{Zn}_x\text{Ni}_{1-x}(\text{OH})_2$ samples at scan rates of 2 mV/s.

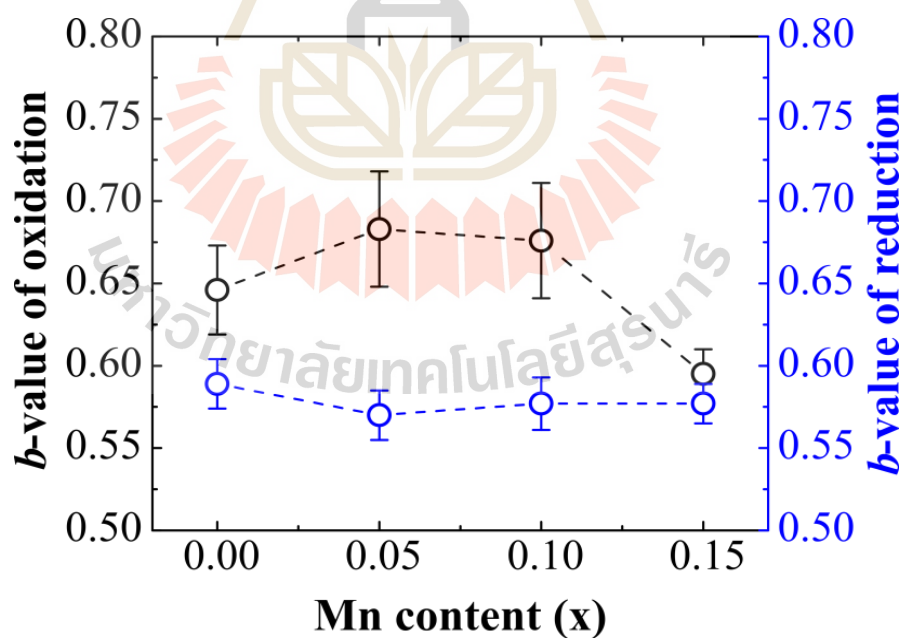


Figure 4.77 Dependence of b -values obtained from oxidation and reduction process as function of Mn content (x).

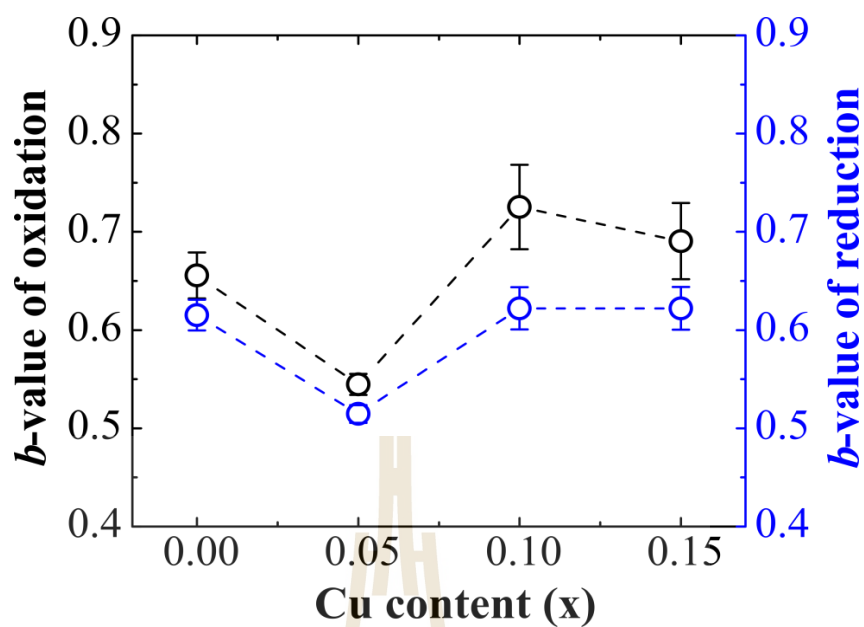


Figure 4.78 Dependence of b -values obtained from oxidation and reduction process as function of Cu content (x).

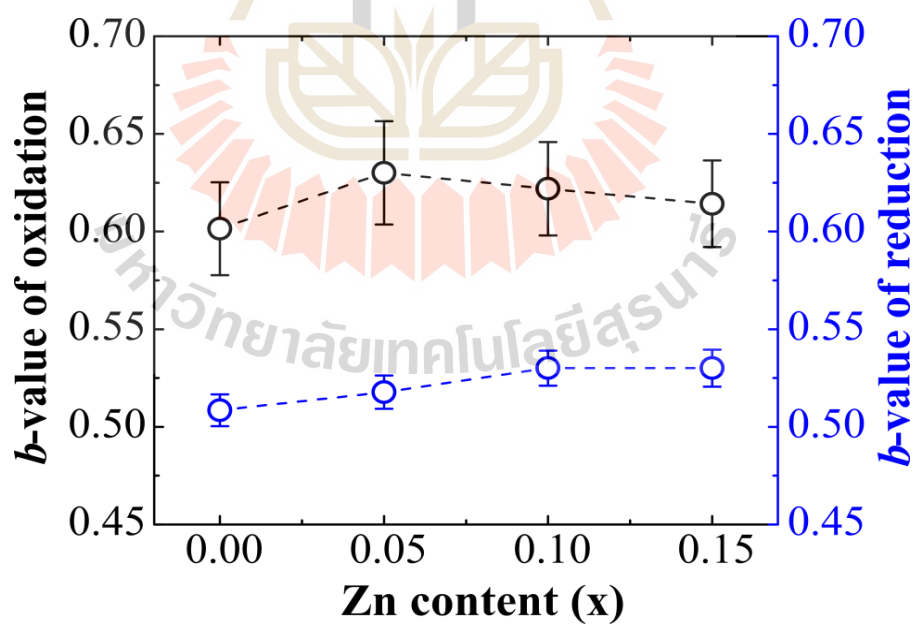


Figure 4.79 Dependence of b -values obtained from oxidation and reduction process as function of Zn content (x).

4.4.4.2 Kinetic analysis of charge storage mechanism

To further understand the charge storage mechanism, it is necessary to perform a kinetic analysis. The relationship between a scan rate and the peak current response observed in CV measurement can be expressed following the equation 3.28. For a redox reaction, the peak current i varies with $v^{1/2}$. Whereas the peak current (i) of capacitive process varies with v (Dong *et al.*, 2016). Based on this relationship, the obtained b -value from the slope of the plot between $\log(i)$ versus $\log(v)$ is used to distinguish the charge storage mechanism of the materials. The b -value = 0.5 implies that the current is affected by intercalation/deintercalation or ion diffusion-controlled mechanism and b -value = 1 indicates that the obtained CV current is due to a capacitive mechanism. As seen in Figure 4.71, 4.72, and 4.73(b, d, f, h), the obtained b -values from oxidation and reduction peaks in these samples are between 0.50-0.73. Based on these results, it may be concluded that the charge storage mechanisms are prominent by intercalation/deintercalation or diffusion-controlled mechanism. By comparing the b -values of oxidation peaks with Mn contents (x) as shown in Figure 4.77, it is clearly seen that lower b -values of 0.595 is found in sample of $x = 0.15$. For Cu doping (Figure 4.78), the lower b -value of 0.545 is found in sample of $x = 0.05$. In case of Zn doping (Figure 4.79), the lower b -value of 0.601 is found in sample of $x = 0.00$.

From the kinetic analysis, the total charge storage in electrode has been assumed to be the combination of the capacitive and intercalation/deintercalation or diffusion-controlled mechanism. The contribution from these two charge storage mechanisms can be distinguished according to equation 3.32. The relative contributions from both capacitive and diffusion-controlled processes versus Mn, Cu, and Zn content (x) at scan rate of 1 mV/s are shown in Figure 4.80, 4.81, and 4.82, respectively. For

Mn doping, the higher diffusion-controlled contribution accounts for 87.92% in samples of $x = 0.15$. In case of Cu doping, the sample of $x = 0.05$ possesses the highest diffusion-controlled contribution of 93.48%. The increase of diffusion-controlled contribution values from 79.13 to 87.24% is found with increasing Zn contents from 0.00 to 0.15. In general, the higher diffusion-controlled contribution suggests that the higher intercalation/deintercalation of electrolyte ions (i.g. Na^+ , K^+) in the materials (Du *et al.*, 2017). Therefore, the higher specific capacitance values due to the higher intercalation/deintercalation or diffusion-controlled contribution are expected in these samples.

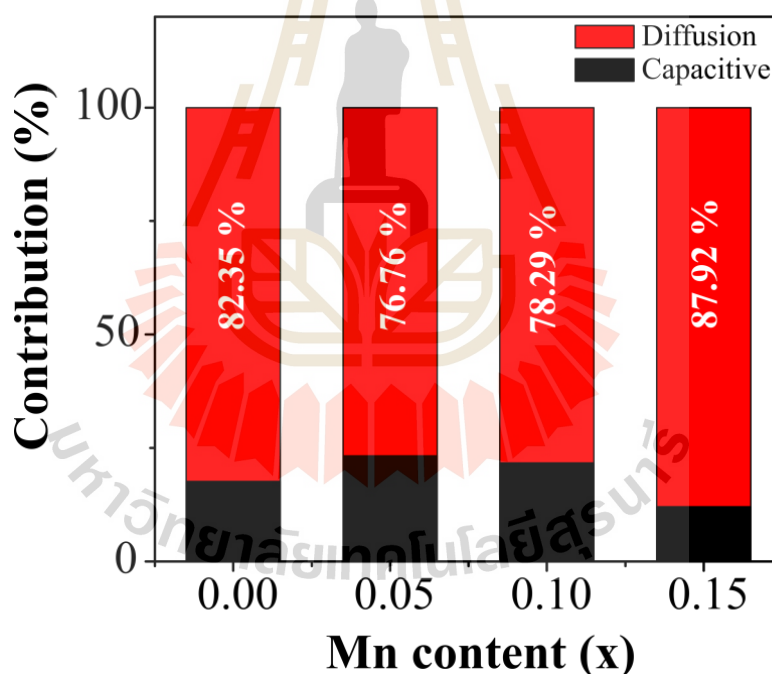


Figure 4.80 The relative contributions of capacitive and diffusion-controlled mechanisms at scan rate of 1 mV/s in $\text{Mn}_x\text{Ni}_{1-x}(\text{OH})_2$ samples.

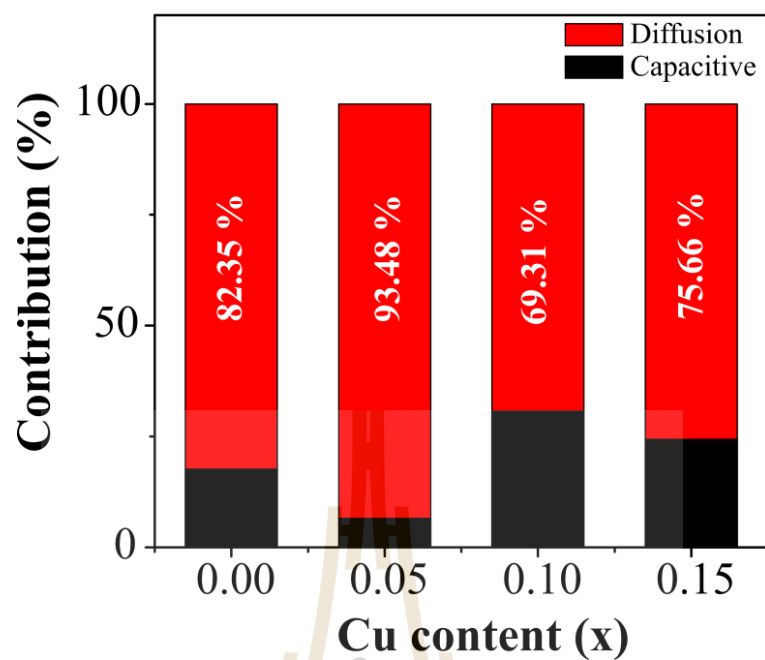


Figure 4.81 The relative contributions of capacitive and diffusion-controlled mechanisms at scan rate of 1 mV/s in $\text{Cu}_x\text{Ni}_{1-x}(\text{OH})_2$ samples.

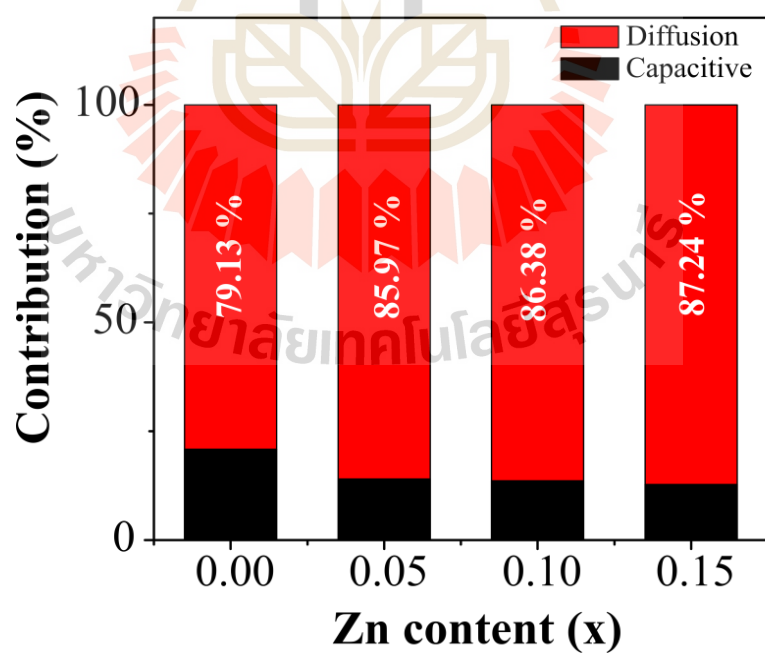


Figure 4.82 The relative contributions of capacitive and diffusion-controlled mechanisms at scan rate of 1 mV/s in $\text{Zn}_x\text{Ni}_{1-x}(\text{OH})_2$ samples.

4.4.4.3 Galvanostatic charge/discharge

As previous presented in section 4.3.3, the charging and discharging times decrease with increasing current density from 1 to 10 A/g. Figure 4.83, 4.84, and 4.85 shows the comparison of GCD curves at current density of 1 A/g for $\text{Mn}_x\text{Ni}_{1-x}(\text{OH})_2$, $\text{Cu}_x\text{Ni}_{1-x}(\text{OH})_2$, and $\text{Zn}_x\text{Ni}_{1-x}(\text{OH})_2$ samples, respectively. As seen in those Figures, a non-linear curves are clearly observed implying that the electrodes store the charge based on redox or intercalation/deintercalation mechanism (Senthilkumar *et al.*, 2014). For Mn doping, the longer discharging time is observed in the sample of $x = 0.00$ which is nearly the same as sample of $x = 0.15$. According to equation 3.34, the higher discharge time means the higher specific capacitance value in samples of $x = 0.00$ and $x = 0.15$. Moreover, the internal resistance (IR) drops at the beginning of each discharging curve in all $\text{Mn}_x\text{Ni}_{1-x}(\text{OH})_2$ samples are observed. The values of IR drop are estimated to be 0.013, 0.019, 0.018, and 0.020 V in samples of $x = 0.00, 0.05, 0.10$, and 0.15 , respectively. For Cu doping, the longer discharge time is observed in sample of $x = 0.05$ within the narrower potential window of 0.51 V. According to the comparison of CV curves in Figure 4.75 of Cu-doped $\text{Ni}(\text{OH})_2$ samples, the actual potential window of $x = 0.05$ excluding the oxygen evolution reaction (OER) is lower than those of the other samples. Therefore, this sample could not reach the cut-off potential window of 0.55 V. According to equation 3.35, the higher cut-off potential window is beneficial for higher energy density, whereas the capacitance value is lower. This result suggests the higher specific capacitance value in sample of $x = 0.05$. For Zn doping, the increase of discharging times is observed. Therefore, the result indicates the improved specific capacitance values after the substitution of Ni^{2+} with Zn^{2+} ions.

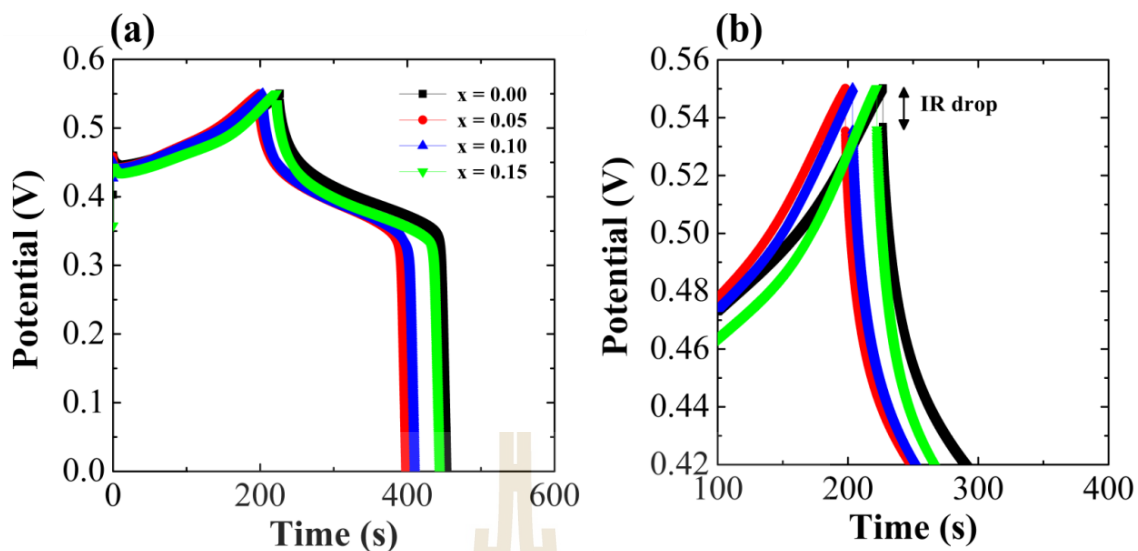


Figure 4.83 (a) Comparison of GCD curves at current density of 1 A/g and (b) their corresponding IR drop of $\text{Mn}_x\text{Ni}_{1-x}(\text{OH})_2$ samples.

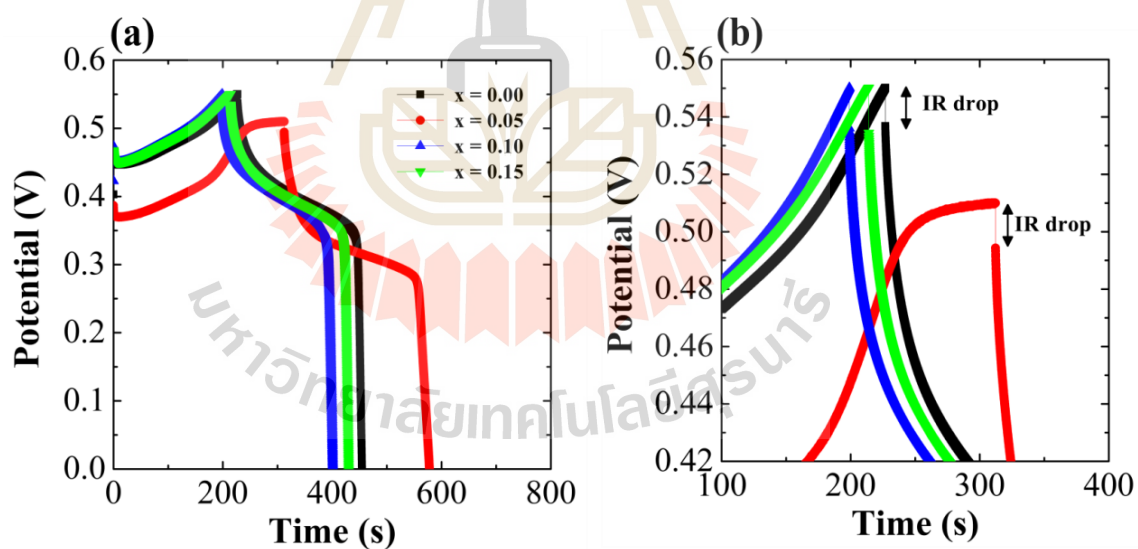


Figure 4.84 (a) Comparison of GCD curves at current density of 1 A/g and (b) their corresponding IR drop of $\text{Cu}_x\text{Ni}_{1-x}(\text{OH})_2$ samples.

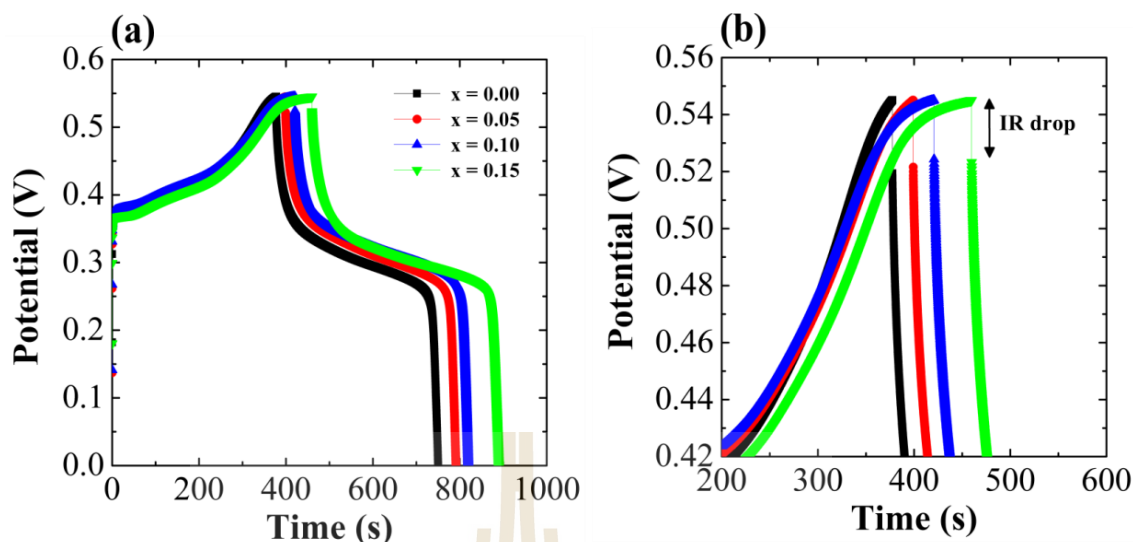


Figure 4.85 (a) Comparison of GCD curves at current density of 1 A/g and (b) their corresponding IR drop of $\text{Zn}_x\text{Ni}_{1-x}(\text{OH})_2$ samples.

In conclusion of GCD analysis, Mn, Cu, and Zn-doped $\text{Ni}(\text{OH})_2$ have a great influence on charging and discharging times. The longer discharging time is directly related to the higher specific capacitance value. For Mn doping, the longer discharging time together with the lower IR drop are observed in the undoped $\text{Ni}(\text{OH})_2$ sample and sample of $x = 0.15$. In contrast, the narrower potential window together with longer discharging time is observed after smaller amount ($x = 0.05$) of Cu doping. In addition, the increase of discharging time is observed in all Zn doping samples. Therefore, these results suggest the improved specific capacitance value of the Zn-doped $\text{Ni}(\text{OH})_2$ samples. This may be related to the smaller particle size as observed in the TEM images after Zn doping when comparing with those in Mn and Cu-doped $\text{Ni}(\text{OH})_2$ samples. In addition, the longer discharging time is attributed in the smaller particle size due to the presence of higher number active sites in the materials (Jahromia *et al.*, 2015).

The calculated specific capacitance values from discharging curves of Mn, Cu, and Zn doping are presented in Figure 4.86, 4.87, and 4.88, respectively. The summarized data obtained from the calculated capacitance value of $\text{Mn}_x\text{Ni}_{1-x}(\text{OH})_2$, $\text{Cu}_x\text{Ni}_{1-x}(\text{OH})_2$, and $\text{Zn}_x\text{Ni}_{1-x}(\text{OH})_2$ samples are listed in Table 4.17, 4.18, and 4.19, respectively. As seen in those figures and tables, the specific capacitance value is improved after Zn doping. Based on the experimental results, the improved capacitance value is related to the higher intercalation/deintercalation or diffusion-controlled contribution. This higher contribution may be explained due to the better reversibility of Zn-doped $\text{Ni}(\text{OH})_2$. According to the structural analysis, the interlayer spacing which is associated with lattice parameter c is increased after Cu and Zn doping. However, the specific capacitance value does not improve in all Cu-doped $\text{Ni}(\text{OH})_2$ samples. Therefore, the increased interlayer spacing could not clearly explain the enhancement of the capacitance value in transition metals-doped $\text{Ni}(\text{OH})_2$. Instead, the particle size greatly affects the electrochemical performance of the materials. The reduction of particle size allows higher reversibility due to the shortened diffusion pathway of electrolyte ions. The relationship between the diffusion length (L) and diffusion time (τ) can be expressed as follows (Gao *et al.*, 2015):

$$\tau = \frac{L^2}{2D} \quad (4.12)$$

where D is diffusion coefficient. This relationship indicates that the shorter diffusion pathway can reduce the diffusion time of electrolyte ions and thus improve the kinetic performance of the materials.

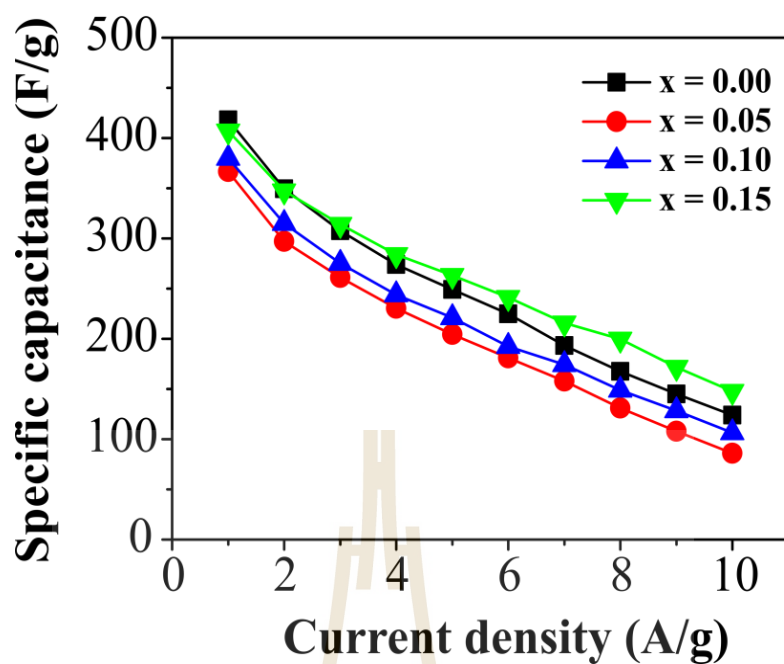


Figure 4.86 The calculated specific capacitance as function of current density in $\text{Mn}_x\text{Ni}_{1-x}(\text{OH})_2$ samples.

Table 4.17 The specific capacitance of $\text{Mn}_x\text{Ni}_{1-x}(\text{OH})_2$ samples with various current densities.

Current density (A/g)	Specific capacitance (F/g)			
	x = 0.00	x = 0.05	x = 0.10	x = 0.15
1	418.11	366.62	379.71	407.04
2	349.43	297.02	314.9	347.25
3	307.64	261.14	275.12	314.15
4	274.10	230.33	243.98	283.77
5	249.14	204.27	221.02	263.08
6	224.78	181.04	192.3	241.26
7	193.36	157.95	174.32	215.87
8	167.59	130.92	148.84	199.62
9	145.1	107.93	128.46	171.72
10	124.11	86.07	106.31	147.79

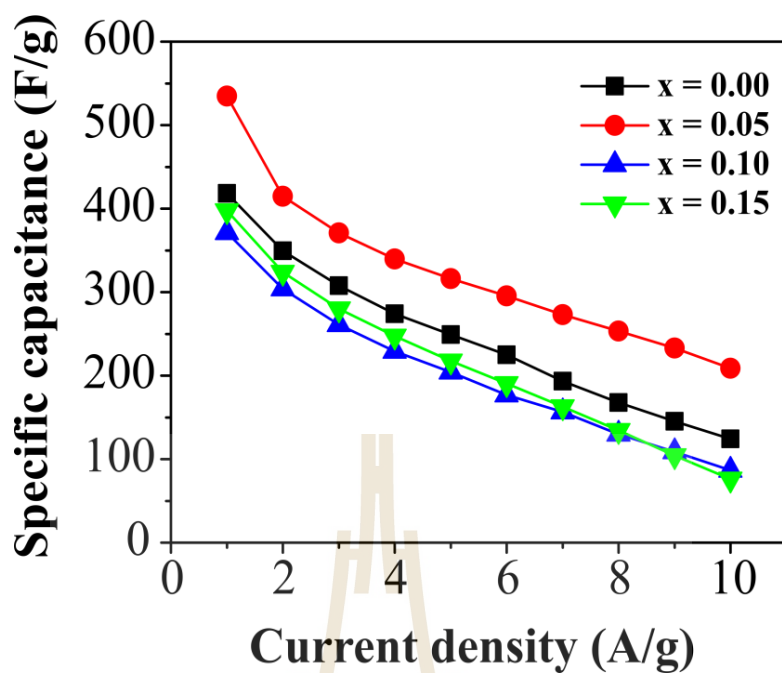


Figure 4.87 The calculated specific capacitance as function of current density in $\text{Cu}_x\text{Ni}_{1-x}(\text{OH})_2$ samples.

Table 4.18 The specific capacitance of $\text{Cu}_x\text{Ni}_{1-x}(\text{OH})_2$ samples with various current densities.

Current density (A/g)	Specific capacitance (F/g)			
	x = 0.00	x = 0.05	x = 0.10	x = 0.15
1	418.11	534.87	371.09	397.62
2	349.43	414.83	304.01	323.94
3	307.64	370.89	260.93	280.03
4	274.10	339.68	229.01	247.26
5	249.14	316.13	204.12	217.47
6	224.78	295.52	177.01	190.36
7	193.36	273.04	156.50	162.77
8	167.59	253.16	130.00	134.50
9	145.10	233.11	108.70	104.15
10	124.11	208.88	86.67	76.24

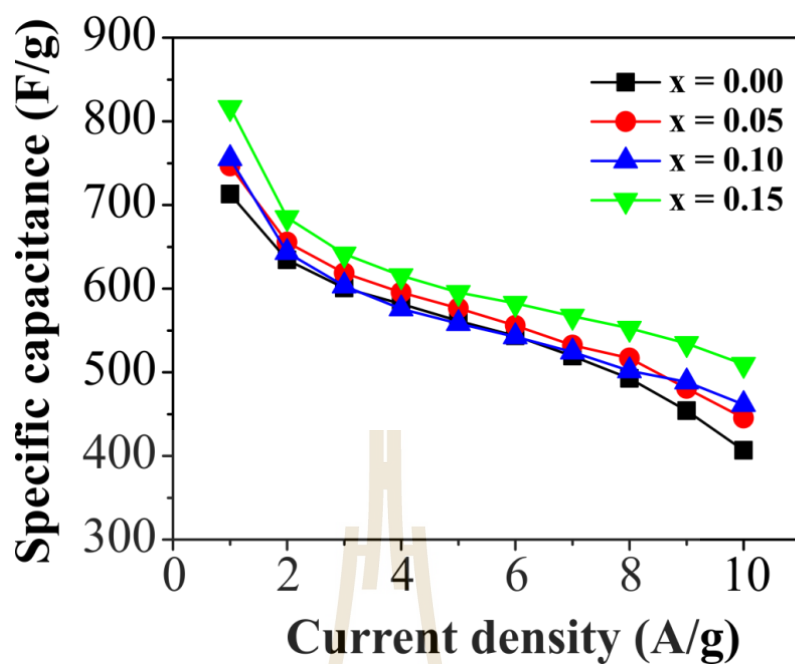


Figure 4.88 The calculated specific capacitance as function of current density in $\text{Zn}_x\text{Ni}_{1-x}(\text{OH})_2$ samples.

Table 4.19 The specific capacitance of $\text{Zn}_x\text{Ni}_{1-x}(\text{OH})_2$ samples with various current densities.

Current density (A/g)	Specific capacitance (F/g)			
	x = 0.00	x = 0.05	x = 0.10	x = 0.15
1	713.04	746.58	755.43	816.48
2	634.26	655.29	643.33	684.76
3	600.69	618.77	603.28	641.56
4	581.64	595.52	575.84	615.45
5	561.36	576.51	558.28	595.32
6	543.37	555.77	542.41	582.39
7	519.22	532.33	524.06	566.96
8	492.50	516.82	501.72	552.74
9	454.07	480.58	488.27	534.38
10	406.82	445.12	461.49	509.48

4.4.4.4 Electrochemical impedance spectroscopy

To further understand the electrochemical performance of Mn, Cu, and Zn-doped Ni(OH)_2 with different contents of $x = 0.00, 0.05, 0.10$, and 0.15 , electrochemical impedance spectroscopy (EIS) was carried out in the frequency range of 0.1 Hz to 100 kHz at an amplitude of 0.1 V . Nyquist plots of $\text{Mn}_x\text{Ni}_{1-x}(\text{OH})_2$, $\text{Cu}_x\text{Ni}_{1-x}(\text{OH})_2$, and $\text{Zn}_x\text{Ni}_{1-x}(\text{OH})_2$ samples are presented in Figure 4.89, 4.90, and 4.91, respectively. As seen in those Figures, there consists of three main features. One is the intercept of the real axis (Z') which indicates the solution resistance (R_s) as seen in the enlarged view of the Nyquist plots. Another one is the charge transfer resistance (R_{ct}) or the semicircle part. The last one is the inclined line of Warburg impedance (Z_w).

It can be seen from those figures that the pure Ni(OH)_2 in all Mn, Cu, and Zn-doped Ni(OH)_2 shows a small charge transfer resistance (R_{ct}). A remarkable observation after Mn, Cu, and Zn doping is that the decrease of charge transfer resistance especially after Zn doping. Lie *et al.* (Liu *et al.*, 2013) reported on the improvement of specific capacitance value of Co-doped Ni(OH)_2 due to the lower charge transfer resistance in which the lower R_{ct} values indicate the easier charge transfer in the materials. Moreover, the observed inclined lines in low frequency region which associated with Na ion diffusivity in the electrode pores and in the host materials are closer to the ideal capacitive (close to 90°) after Mn and Cu doping. Based on these results, it may be concluded that the higher specific capacitance values are due to the lower charge transfer resistance and higher Na ion diffusivity. The summarized data obtained from EIS measurement of $\text{Mn}_x\text{Ni}_{1-x}(\text{OH})_2$, $\text{Cu}_x\text{Ni}_{1-x}(\text{OH})_2$, and $\text{Zn}_x\text{Ni}_{1-x}(\text{OH})_2$ samples are given in Table 4.20, 4.21, and 4.22, respectively.

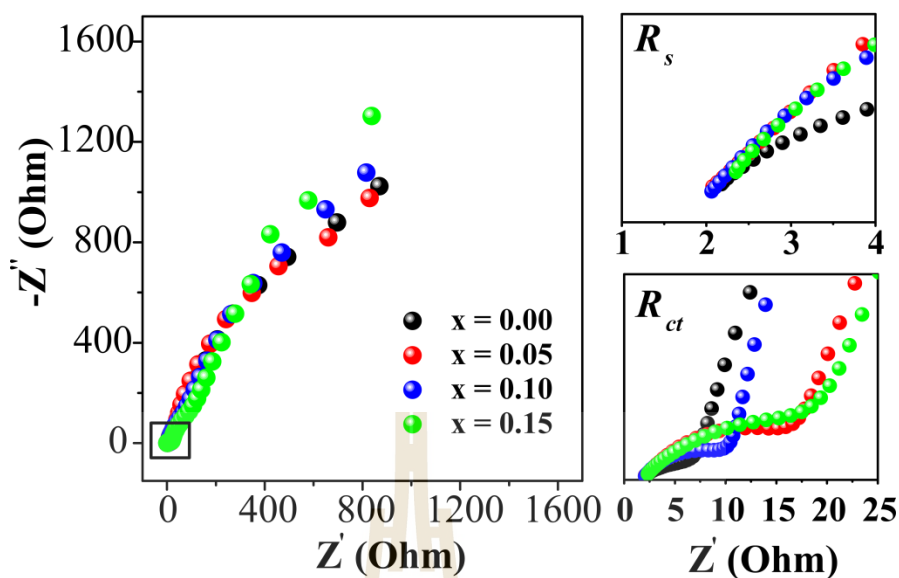


Figure 4.89 Nyquist plots of $\text{Mn}_x\text{Ni}_{1-x}(\text{OH})_2$ samples measured at the frequency range of 0.1 Hz to 100 kHz. Enlarged views of Nyquist plot showing the solution resistance (R_s) and charge transfer resistance (R_{ct}).

Table 4.20 The details of solution resistance (R_s), charge transferred resistance (R_{ct}), and the angle of inclined line with x -axis obtained from EIS measurement and the cyclic stability obtained from repeating GCD measurement at current density of 5 A/g for 1000 cycles in $\text{Mn}_x\text{Ni}_{1-x}(\text{OH})_2$ samples.

x	R_s (Ohm)	R_{ct} (Ohm)	Angle ($^\circ$)	Cyclic stability (%)
0.00	1.65	8.53	48.55	80.61
0.05	1.81	22.42	48.27	96.28
0.10	1.82	11.91	52.22	89.16
0.15	1.75	28.85	57.29	81.06

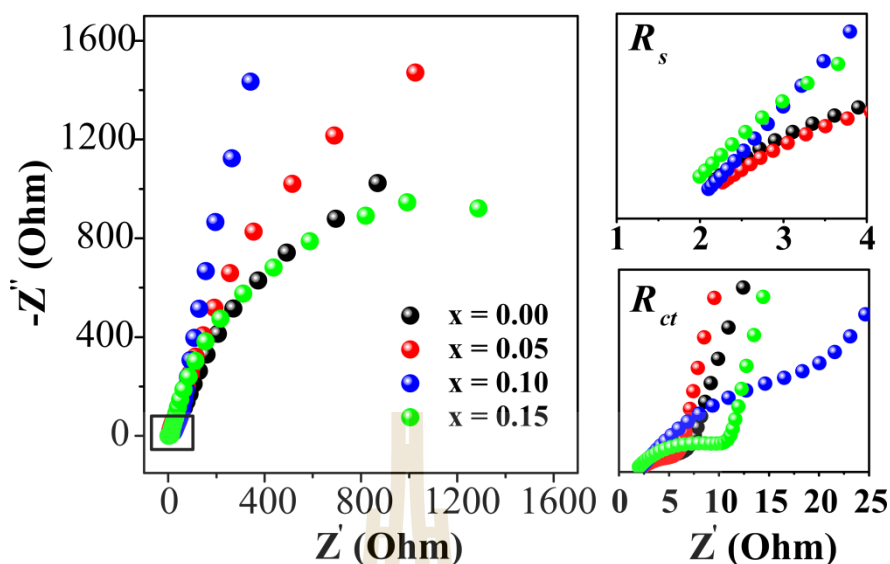


Figure 4.90 Nyquist plots of $\text{Cu}_x\text{Ni}_{1-x}(\text{OH})_2$ samples measured at the frequency range of 0.1 Hz to 100 kHz. Enlarged views of Nyquist plot showing the solution resistance (R_s) and charge transfer resistance (R_{ct}).

Table 4.21 The details of solution resistance (R_s), charge transferred resistance (R_{ct}), and the angle of inclined line with x -axis obtained from EIS measurement and the cyclic stability obtained from repeating GCD measurement at current density of 5 A/g for 1000 cycles in $\text{Cu}_x\text{Ni}_{1-x}(\text{OH})_2$ samples.

x	R_s (Ohm)	R_{ct} (Ohm)	Angle ($^\circ$)	Cyclic stability (%)
0.00	1.65	8.53	48.97	80.61
0.05	1.77	7.53	55.52	98.72
0.10	1.88	43.70	80.63	109.08
0.15	1.54	13.53	41.62	106.96

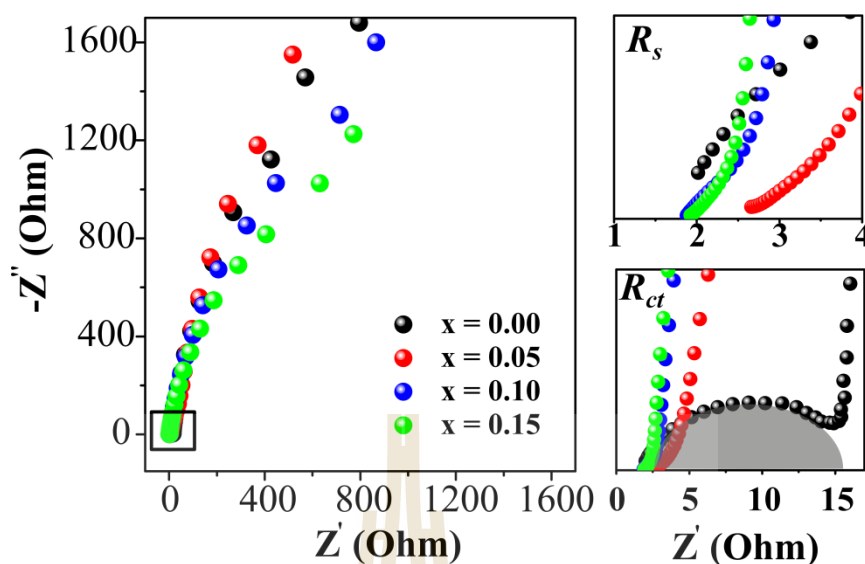


Figure 4.91 Nyquist plots of $\text{Zn}_x\text{Ni}_{1-x}(\text{OH})_2$ samples measured at the frequency range of 0.1 Hz to 100 kHz. Enlarged views of Nyquist plot showing the solution resistance (R_s) and charge transfer resistance (R_{ct}).

Table 4.22 The details of solution resistance (R_s), charge transferred resistance (R_{ct}), and the angle of inclined line with x -axis obtained from EIS measurement and the cyclic stability obtained from repeating GCD measurement at current density of 5 A/g for 1000 cycles in $\text{Zn}_x\text{Ni}_{1-x}(\text{OH})_2$ samples.

x	R_s (Ohm)	R_{ct} (Ohm)	Angle ($^\circ$)	Cyclic stability (%)
0.00	1.68	15.91	67.14	93.45
0.05	2.66	-	71.21	103.07
0.10	1.88	-	61.91	71.38
0.15	1.92	-	55.42	67.91

4.4.4.5 Cyclic stability

Long cycle life of electrochemical capacitors is the crucial parameter for their practical applications. The cyclic stability of Mn, Cu, and Zn-doped Ni(OH)₂ was evaluated by repeating GCD measurements at current density of 5 A/g for 1000 cycles. As seen in Figure 4.92, 4.93, and 4.94, the specific capacitance values of pure Ni(OH)₂ retain about 80-93% of its initial specific capacitance values after repeating GCD for 1000 cycles. For Mn doping, the capacitance retention of all Mn-doped Ni(OH)₂ samples slight decreases from 100 - 500th cycle and stays almost constant as an extended cycle except for $x = 0.05$. The increase of capacitance value from 500 - 800th cycle is observed in sample of $x = 0.05$, which may be explained due to the gradual activation of the electrode surface resulting in the better electrolyte ion accessible into the electrode (Zequine *et al.*, 2016). For Cu doping, the improved cyclic stability is observed in all Cu-doped Ni(OH)₂ samples. In case of Zn doping, the cyclic stability was improved in a small amount of Zn doping ($x = 0.05$) to the maximum value of 103.7% after 1000 cycles. To sum up, the cyclic stability was improved due to the existence of micropore in Cu-doped Ni(OH)₂ samples. The improved cyclic stability can be explained due to the confining electrolyte ions in micropore (Wang *et al.*, 2008). Moreover, the poor cyclic stability in Zn-doped Ni(OH)₂ samples may be related to the distortion of NiO₆ octahedral after Zn doping as presented in the XAS result. This distortion would associate the more structural instability as extended cyclic.

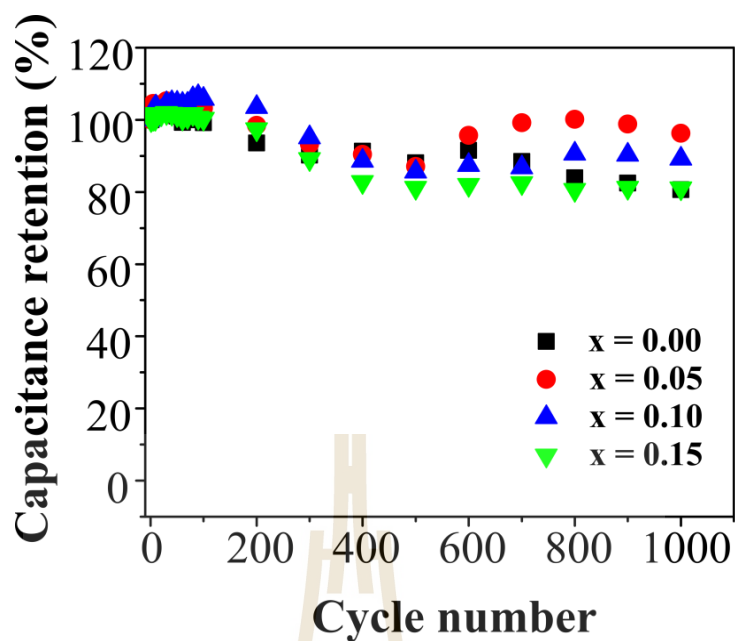


Figure 4.92 Comparison of capacitance retention as function of cycle number for $\text{Mn}_x\text{Ni}_{1-x}(\text{OH})_2$ samples measured at current density of 5 A/g for 1000 cycles.

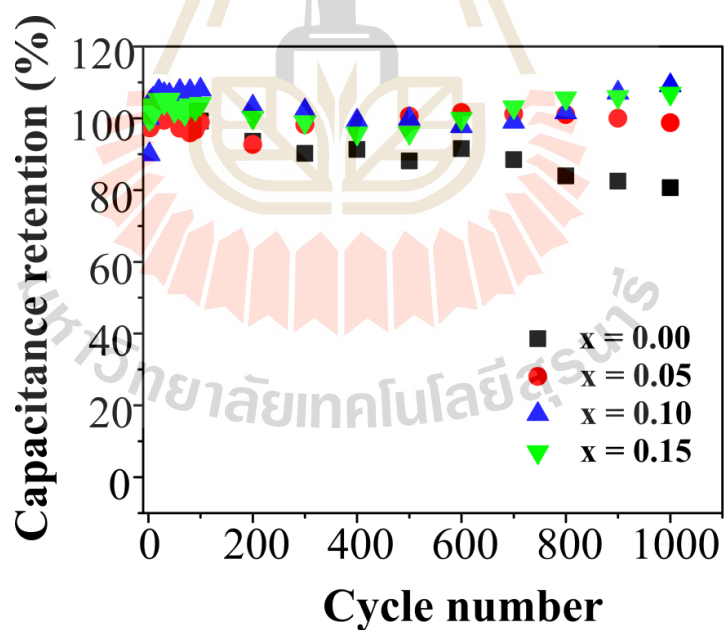


Figure 4.93 Comparison of capacitance retention as function of cycle number for $\text{Cu}_x\text{Ni}_{1-x}(\text{OH})_2$ samples measured at current density of 5 A/g for 1000 cycles.

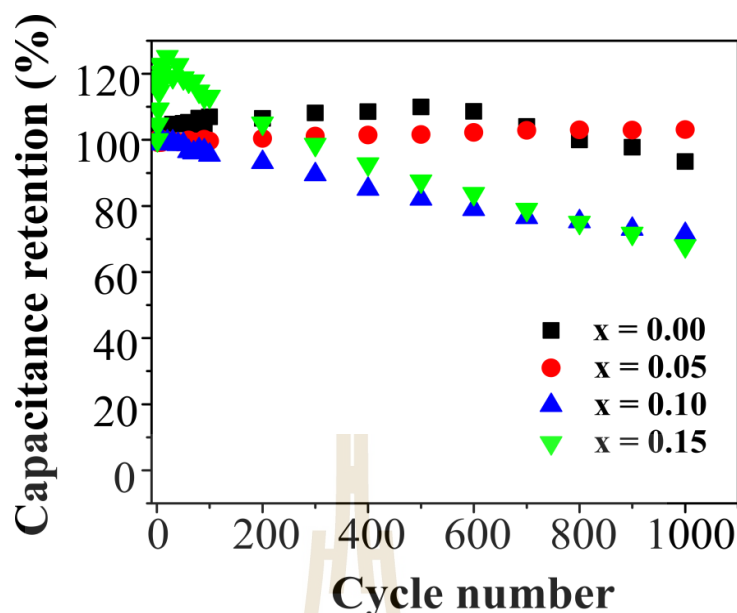


Figure 4.94 Comparison of capacitance retention as function of cycle number for $\text{Zn}_x\text{Ni}_{1-x}(\text{OH})_2$ samples measured at current density of 5 A/g for 1000 cycles.

4.4.4.6 Energy density and power density

It is well-known that the performance of energy storage devices is determined by the Ragone plot or the plot between specific power and specific energy. The Ragone plots of Mn, Cu, and Zn-doped $\text{Ni}(\text{OH})_2$ are shown in Figure 4.95, 4.96, and 4.97, respectively. Among those Ragone plots, the Zn-doped $\text{Ni}(\text{OH})_2$ samples dominate the highest specific energy and specific power indicating the improved of the performance. For Cu doping, the specific energy and specific power are not improved due to the lower specific capacitance value after Cu doping. One can also see in Figure 4.96(a) is that the lower specific power results from the lower potential window of $x = 0.05$ after Cu doping. Comparing those Ragone plots with a well-known Ragone plots, it can conclude that $\text{Mn}_x\text{Ni}_{1-x}(\text{OH})_2$, $\text{Cu}_x\text{Ni}_{1-x}(\text{OH})_2$, and $\text{Zn}_x\text{Ni}_{1-x}(\text{OH})_2$ samples are suitable for both electrochemical capacitor and batterie applications.

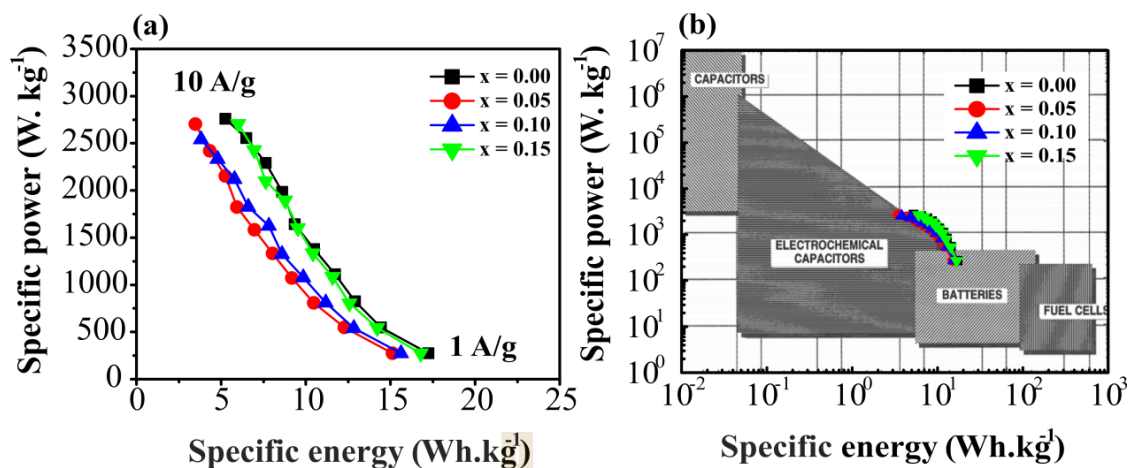


Figure 4.95 (a) The Ragone plot of $\text{Mn}_x\text{Ni}_{1-x}(\text{OH})_2$ samples and (b) the comparison of Ragone plot of $\text{Mn}_x\text{Ni}_{1-x}(\text{OH})_2$ samples with a well-known Ragone plot of Kötz (Kötz and Carlen, 2000).

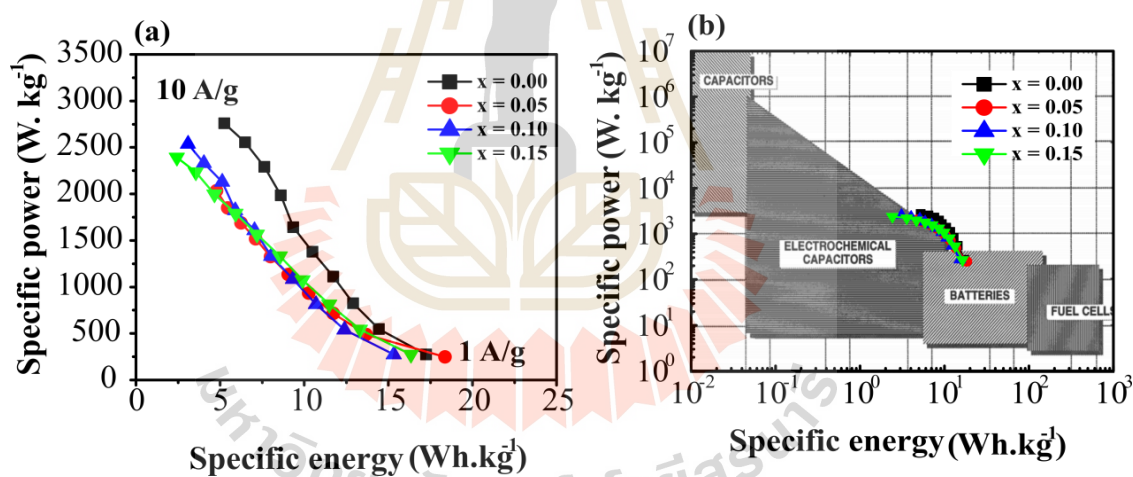


Figure 4.96 (a) The Ragone plot of $\text{Cu}_x\text{Ni}_{1-x}(\text{OH})_2$ samples and (b) the comparison of Ragone plot of $\text{Cu}_x\text{Ni}_{1-x}(\text{OH})_2$ samples with a well-known Ragone plot of Kötz (Kötz and Carlen, 2000).

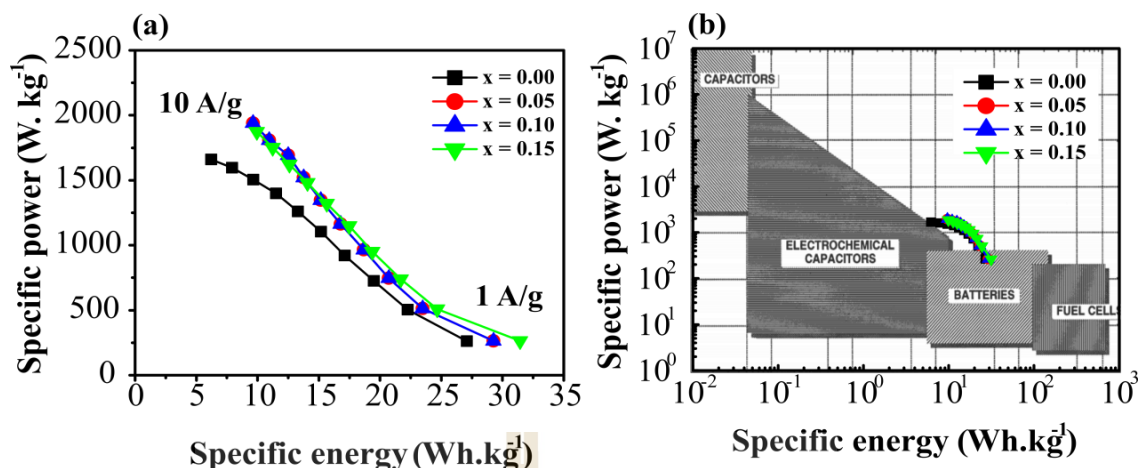


Figure 4.97 (a) The Ragone plot of $\text{Zn}_x\text{Ni}_{1-x}(\text{OH})_2$ samples and (b) the comparison of Ragone plot of $\text{Zn}_x\text{Ni}_{1-x}(\text{OH})_2$ samples with a well-known Ragone plot of Kötz (Kötz and Carlen, 2000).

4.5 Effects of Bi-doped $\text{Ni}(\text{OH})_2$ on structure and electrochemical properties

4.5.1 Structural and morphology analysis

XRD patterns of Bi-doped $\text{Ni}(\text{OH})_2$ with different contents of $x = 0.00$, 0.05, 0.10, and 0.15 are shown in Figure 4.98. As seen in Figure 4.98, the diffraction peaks at the diffraction angle (2θ) of about 19.3, 33.0, 38.5, 52.2, 59.0, 62.6, 69.3, 70.5, and 72.7° within the diffraction angle ranging from 10-80 degrees are observed in the undoped $\text{Ni}(\text{OH})_2$. The overall diffraction peaks well-matched with the standard powder diffraction of hexagonal $\beta\text{-Ni}(\text{OH})_2$ (JCPDS file no. 14-0117) with space group of $P\bar{3}m1$. The observed peaks in XRD patterns, from low - to high - diffraction angle (2θ), can be indexed as (001), (100), (101), (102), (110), (111), (200), (103), and (201) lattice planes, respectively. In addition, no diffraction peaks relate to the second phase

or the impurities are observed from the XRD patterns of $\text{Bi}_x\text{Ni}_{1-x}(\text{OH})_2$ samples. This may be concluded that Bi^{3+} ions can completely substitute the Ni^{2+} sites in $\text{Ni}(\text{OH})_2$ crystal lattice.

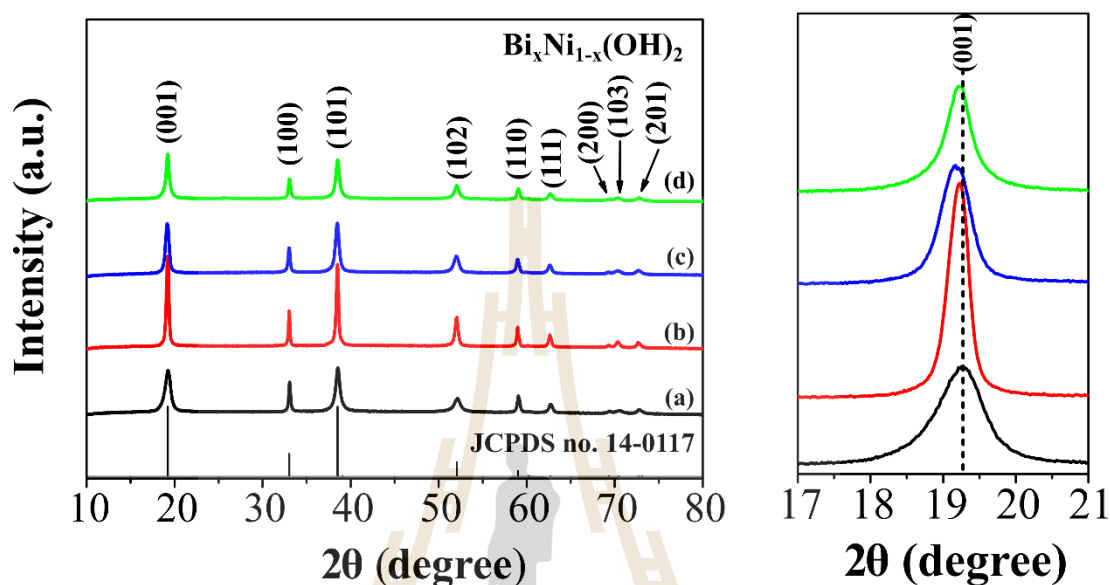


Figure 4.98 XRD patterns of $\text{Bi}_x\text{Ni}_{1-x}(\text{OH})_2$ samples with (a) $x = 0.00$, (b) $x = 0.05$, (c) $x = 0.10$, and (d) $x = 0.15$ and their corresponding enlarged view of the diffraction peaks in 2θ ranging from 17 to 21 degree.

As clearly seen in the enlarged view of (001) planes in Figure 4.98, the observed diffraction peaks shift toward lower diffraction angles implying the change of lattice parameters. Owing to the fact that ionic radius of Bi^{3+} (1.03 Å) (Gore *et al.*, 2015) is larger than Ni^{2+} (0.69 Å) (Shannon, 1976), the shift of diffraction peaks to lower diffraction angles is possibly caused by the relative larger Bi^{3+} ions than Ni^{2+} ions. Furthermore, the higher crystallinity due to the narrower and sharper of the reflection peak is also observed in sample of $x = 0.05$. Zheng *et al.* (Zheng *et al.*, 2017) reported that the higher crystallinity of the materials promoted the ions diffusion rate, the reversible phase transition, and the accommodation of the structural strain, thus

significantly enhanced the cyclic stability of the materials. Based on this report, the better cyclic stability is expected in sample with higher crystallinity of $x = 0.05$.

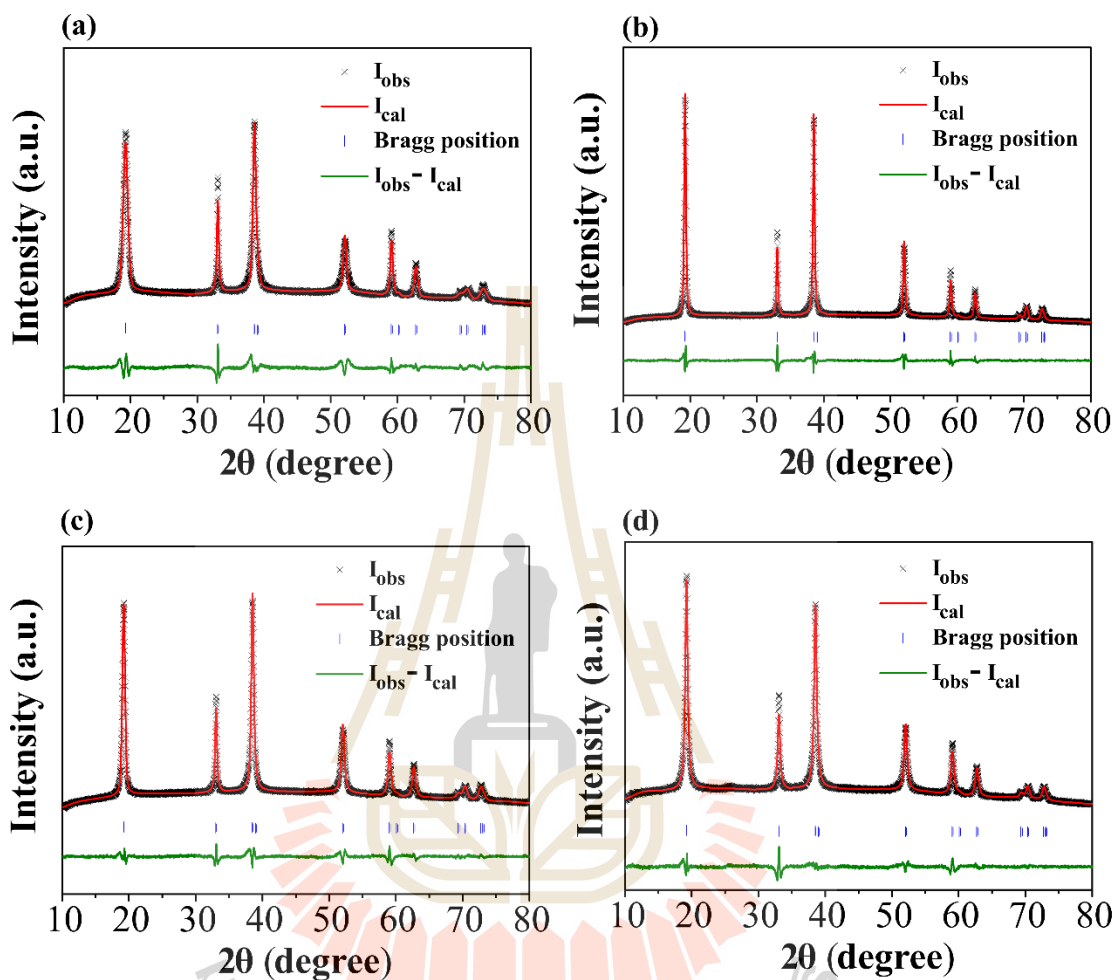


Figure 4.99 Rietveld refinement of $\text{Bi}_x\text{Ni}_{1-x}(\text{OH})_2$ samples with $x = 0.00, 0.05, 0.10$, and 0.15 .

To explore the structural change affected by Bi doping, the Rietveld refinement was performed by using JANA2006 software. The Pseudo-Voigt was used as the profile function. The refinement was performed in the 2θ range of $10 - 80^\circ$ based on the hexagonal crystal structure with space group of $P\bar{3}m1$. The lattice parameter $a = 3.13 \text{ \AA}$ and $c = 4.63 \text{ \AA}$ of $\beta\text{-Ni}(\text{OH})_2$ were used for the lattice parameters refinement. As seen in Figure 4.99, the difference between the observed and calculated profiles is

shown at the bottom of each figure. The Bragg positions are indicated by small vertical lines. As a result, the refinement of $\text{Bi}_x\text{Ni}_{1-x}(\text{OH})_2$ samples are in good agreement between the observed and the calculated XRD patterns. The data obtained from the refinement of $\text{Bi}_x\text{Ni}_{1-x}(\text{OH})_2$ samples are summarized in Table 4.23. As seen in the table, the values of R_p , R_{wp} , and GOF of $\text{Bi}_x\text{Ni}_{1-x}(\text{OH})_2$ samples are under 10% meaning that the Rietveld refinement results are reliable (Huang *et al.*, 2015; Li *et al.*, 2017).

Figure 4.100 (a) shows the plots between lattice parameters a and c as function of Bi content (x). As seen in this Figure, the values of lattice parameter c increase with increasing Bi content. Whereas the lattice parameter a values increase first and then decrease with further increasing Bi content. Based on these results, it may be concluded that the Bi doping caused the expansion of unit cell which is clearly observed in Figure 4.100(b) due to the substitution of larger Bi^{3+} ions in smaller Ni^{2+} sites. Furthermore, the increase of lattice parameter c indicates the increase of c/a ratio. The calculated crystallite size values from the most intense peaks of (001), (100), and (101) planes by using Scherer's equation are found to be 36.10 ± 1.74 , 37.22 ± 2.31 , 33.09 ± 1.51 , 33.72 ± 0.37 nm for $x = 0.00, 0.05, 0.10$, and 0.15 , respectively.

Table 4.23 The details of lattice parameter a and c , profile factor (R_p), weighted profile residual (R_{wp}), goodness of fit (GOF), unit cell volume, and crystal density obtained from the Rietveld refinement including the calculated d -spacing of (001), (100), and (101) planes and the calculated crystallite size from Scherrer's equation of $\text{Bi}_x\text{Ni}_{1-x}(\text{OH})_2$ samples with $x = 0.00, 0.05, 0.10$, and 0.15 .

Parameters	$x = 0.00$	$x = 0.05$	$x = 0.10$	$x = 0.15$
Lattice parameter (\AA)				
$a = b$	3.125604	3.129443	3.128314	3.127287
c	4.610133	4.612962	4.615070	4.615835
c/a	1.474957	1.474052	1.475258	1.475987
d-spacing (\AA)				
(001)	4.6101	4.6130	4.6151	4.6158
(100)	2.1471	2.1478	2.1483	2.1484
(101)	1.4653	1.4655	1.4657	1.4658
R_p (%)	3.16	2.72	2.42	2.25
R_{wp} (%)	4.59	4.14	3.46	3.39
GOF (%)	3.08	2.71	2.24	2.14
Volume (\AA^3)	39.00426	39.12412	39.11376	39.09456
Density (g/cm^3)	3.94671	3.93461	3.93566	3.93759
D (nm)	36.10 \pm 1.74	37.22 \pm 2.31	33.09 \pm 1.51	33.72 \pm 0.37

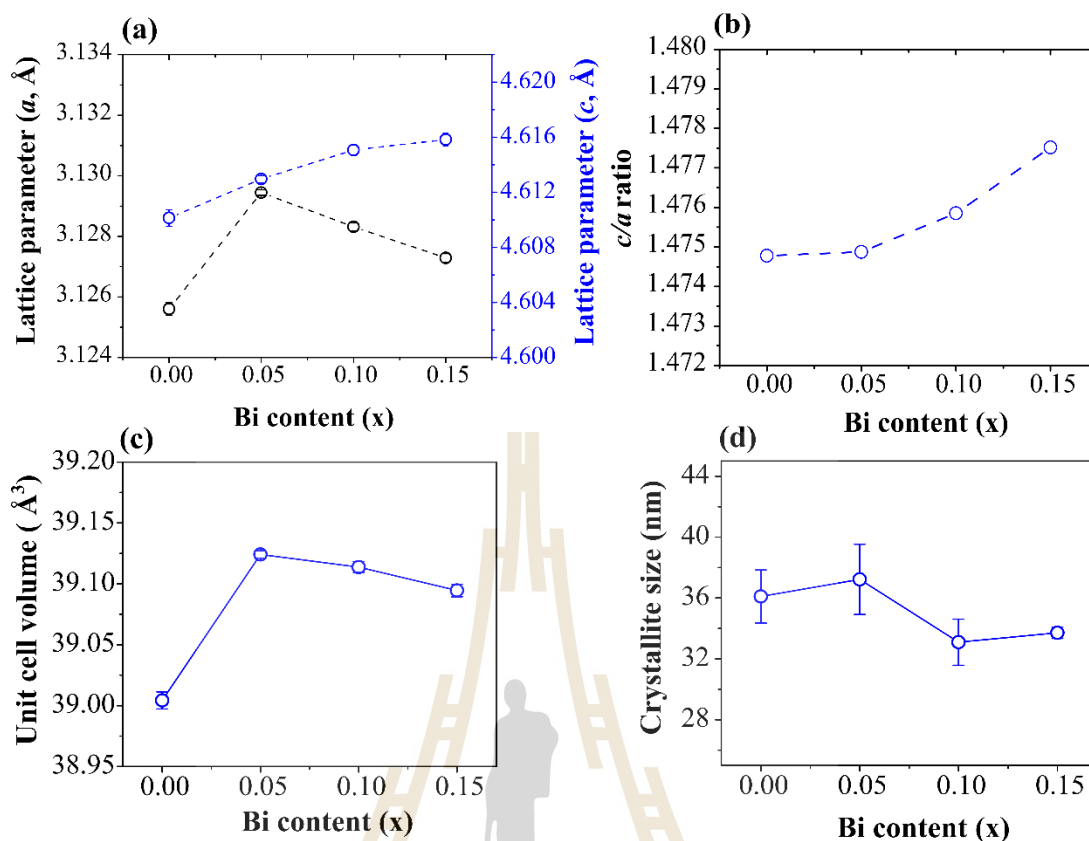


Figure 4.100 (a) Lattice parameters a and c , (b) c/a ratio, (c) unit cell volume, and (d) crystallite size as function of Bi content (x).

Effects of Bi doping on size, shape, thickness, and morphologies of Ni(OH)₂ were further characterized using TEM technique. As seen in Figure 4.101, TEM images show a plate-like morphology in all Bi-doped Ni(OH)₂ samples. The TEM images also reveal that the nanoplates are stacking together. Furthermore, TEM images show that Bi³⁺ doping has a significant effect on the particle size. With increasing Bi content, the particle size increases first and then decreases after further increasing Bi content from 0.05 to 0.15. These results are in good agreement with the calculated crystallite size by Scherer's equation. Moreover, the difference in morphologies of plate and rod-like shapes are clearly observed especially in $x = 0.05$. This is due to the placing of the nanoplates in different directions. The rod-like morphology is related to an

upward (001) facet and the plate-like morphology is related to an upward (100) facet (Wang *et al.*, 2015). According to the crystal structure of β -Ni(OH)₂, two Ni²⁺ ions along the [001] direction are separated by two OH⁻ layers and two Ni²⁺ ions along the [100] direction are linked by one OH⁻ group. Zhang *et al.* (Zhang *et al.*, 2011) reported on the higher electrochemical activity in rod-like shape rather than in plate or slice-like shape due to the easier electron hopping along the (100) direction than that along (001) direction. However, the electrochemical performance also depends on the thickness of rod-like shape. The thinner rod could facilitate the better electrolyte ions diffusion, resulting in higher specific capacitance value. In this work, the thickness of rod-like shape is estimated to be 10.87 ± 1.29 , 34.70 ± 0.92 , 16.91 ± 0.83 , and 15.30 ± 2.02 nm for $x = 0.00$, 0.05 , 0.10 , and 0.15 , respectively. As shown in Figure 4.102, the thickness is also followed the same trend as particle size. This observation clearly indicates that the Bi doping induced the changes of morphology. The selected area electron diffraction (SAED) patterns of Bi_xNi_{1-x}(OH)₂ samples reveal a spotty ring patterns as clearly seen in Figure 4.101. Comparing with the standard diffraction data, the spotty rings show the characteristic of polycrystalline β -Ni(OH)₂ (JCPDS file no. 14-0117) which are in good agreement with XRD results.

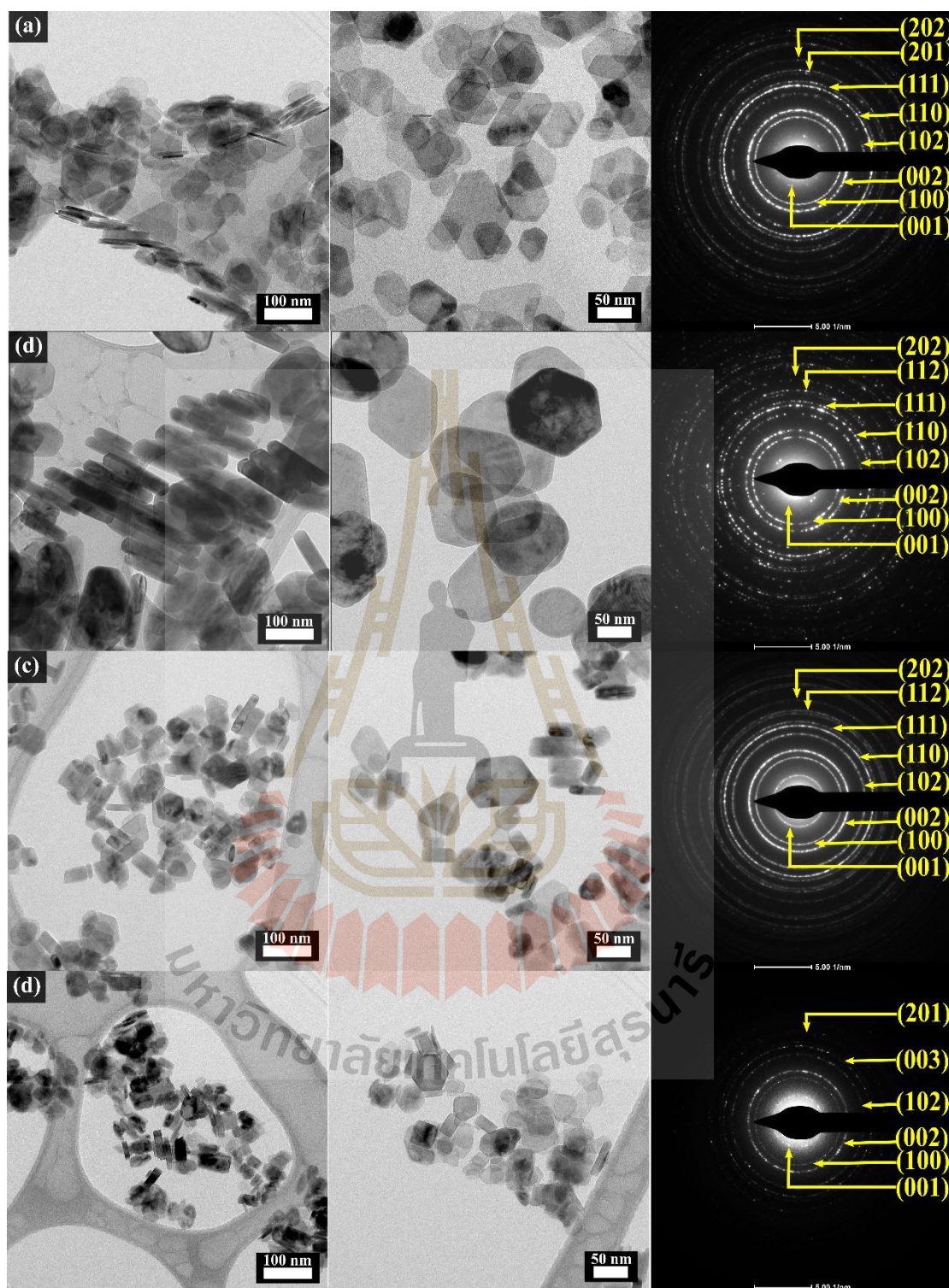


Figure 4.101 TEM bright field images and their corresponding SAED patterns of $\text{Bi}_x\text{Ni}_{1-x}(\text{OH})_2$ samples with (a) $x = 0.00$, (b) $x = 0.05$, (c) $x = 0.10$, and (d) $x = 0.15$, respectively.

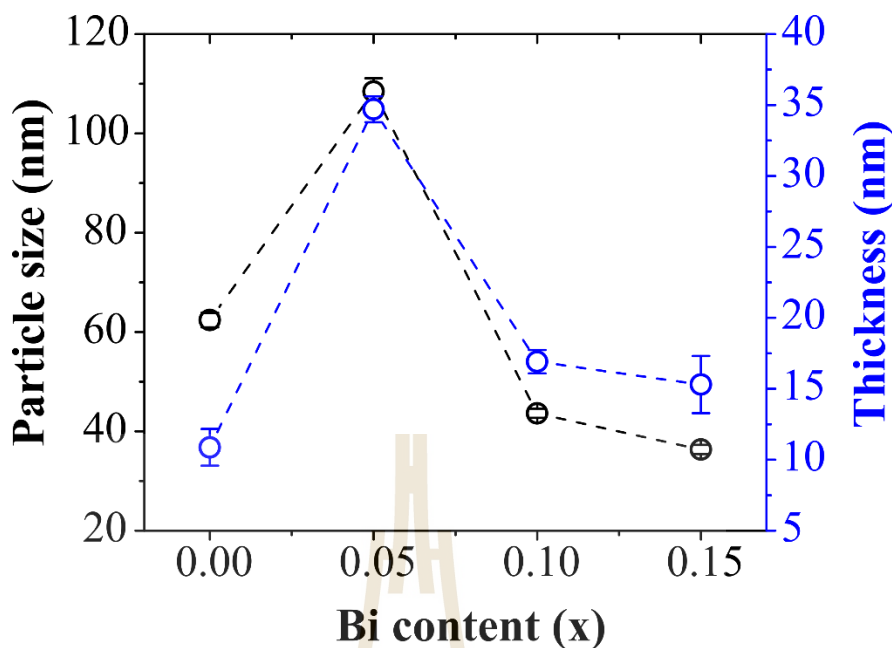


Figure 4.102 The average particles size of $\text{Bi}_x\text{Ni}_{1-x}(\text{OH})_2$ samples as a function of Bi content (x).

4.5.2 Chemical compositions and oxidation state analysis

To investigate the change of Bi contents on the chemical environment in $\text{Bi}_x\text{Ni}_{1-x}(\text{OH})_2$ samples, XPS technique is used. Owing to the fact that XPS technique is used for measurement an emitted photoelectron by exciting a samples surface with known energy of X-rays photon. Hence, the binding energy is calculated which is characteristic of chemical bonds in material. From the binding energy and intensity of the photoelectron peak, the elemental identity, chemical state, and quantity of the detected element can be determined. Figure 4.103 shows the survey XPS spectra of $\text{Bi}_x\text{Ni}_{1-x}(\text{OH})_2$ samples. Those XPS survey spectra confirm the presence of C 1s, O 1s, Ni 2p, and Bi 4f on the samples surface. A remarkable observation after Bi doping is that the increase of the Bi 4f intensity with increasing Bi content.

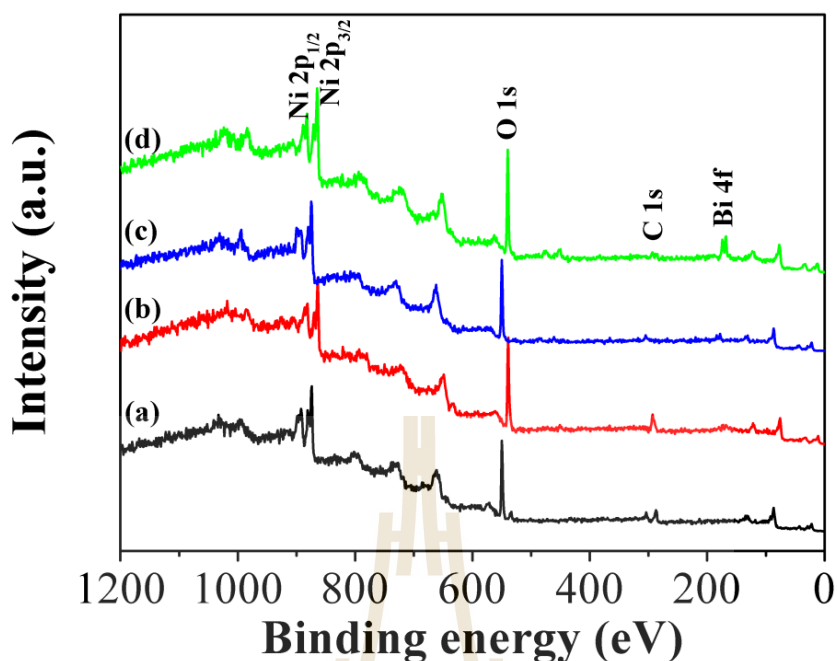


Figure 4.103 The survey XPS spectrum of $\text{Bi}_x\text{Ni}_{1-x}(\text{OH})_2$ samples with different Bi content of $x = 0.00$, (b) $x = 0.05$, (c) $x = 0.10$, and (d) $x = 0.15$.

As previously mentioned before, XAS measurements are used to study the local structure of the material. It is a technique which probes the core-shell electrons of an atom by the beam of X-ray photons. According to two main regions of XAS spectrum, XANES gives an information about the oxidation number and atomic coordination of added impurity ions (Tsuzuki *et al.*, 2019). In this work, XANES measurements were collected at SLRI (BL 5.2). All spectra at Ni K -edge (8333 eV) and Bi M_5 -edge (2580 eV) were carried out in transmission mode, and fluorescent mode, respectively. The XANES spectra of the samples were compared to those of the reference standard metals and compounds of Ni foil, NiO, Bi_2O_3 , NaBiO_3 standard samples to indicate the oxidation state of an absorbing atoms. In general, the oxidation state of an absorbing atom can be determined by the energy position of pre-edge features or from the absorption edge of XANES spectrum (Berghöfer *et al.*, 1993).

Figure 4.104 shows the normalized Ni *K*-edge XANES spectra of Bi-doped Ni(OH)₂. It is clearly seen that the spectra show three main features in all Bi-doped Ni(OH)₂ samples. In region I, the presence of pre-edge absorption at energy about 8333.6 ± 0.2 eV is similar to that of NiO standard sample. Therefore, it can be concluded that the oxidation state of Ni is 2+. This pre-edge occurs due to the transition of $1s \rightarrow 3d$ state in which the change of pre-edge positions at different energies indicates the change of Ni-coordination (Landers *et al.*, 2011). Therefore, this result suggests no change of Ni-coordination after Bi doping. In region II, the edge positions of the Ni *K*-edge in all samples are close to that of the NiO standard sample indicating that the oxidation state of Ni is 2+ which is also confirmed by the first derivative plots as shown in Figure 4.105. For region III, the increase of white-line intensity after Bi doping is observed indicating the more distortion on NiO₆ octahedral (Cuartero *et al.*, 2016).

The normalized XANES spectra of Bi *M*₅-edge of all Bi-doped Ni(OH)₂ samples are presented in Figure 4.106. Similar to Ni *K*-edge spectra, the spectra of Bi *M*₅-edge show three main features in all Bi-doped Ni(OH)₂ samples. In region I, the presence of pre-edge absorption at energy about 2582 eV is similar to that of Bi₂O₃ standard sample indicating that the oxidation state of Bi is 3+. In general, the pre-edge at *M*₅-edge region indicates the transition of $3d \rightarrow 6p$ state (Ozkendir and Bozgeyik, 2010). In region II, the edge positions of Bi *M*₅-edge in all samples are close to that of the Bi₂O₃ standard sample which also indicate that the oxidation state of Bi is 3+. This result is in good agreement with the first derivative plots as shown in Figure 4.107. For region III, the increase of white line intensities with increasing Bi content from 0.05 to 0.10 is observed in which the change of a white-line intensity is related to the symmetry.

Therefore, this result indicates the change of symmetry due to the change of white-line intensity in the crystal when increasing Bi contents.

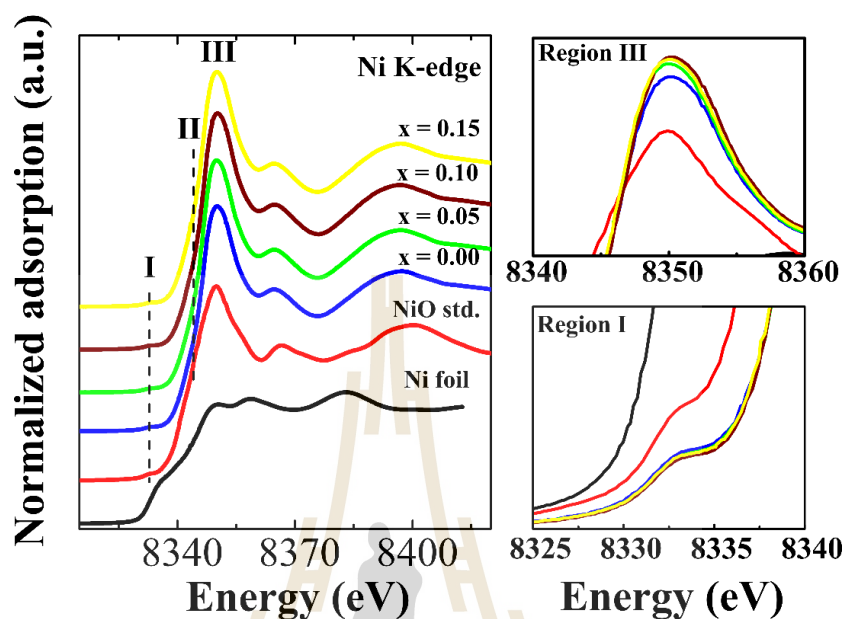


Figure 4.104 The normalized XANES spectra including pre-edge (region I) and white line region (region III) of Bi-doped $\text{Ni}(\text{OH})_2$ at Ni K-edge measured in transmission mode.

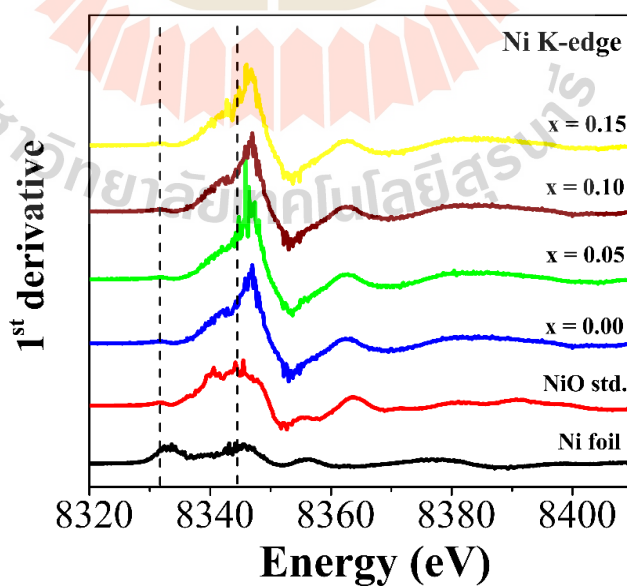


Figure 4.105 The first derivative plots of Bi-doped $\text{Ni}(\text{OH})_2$ at Ni K-edge measured in transmission mode.

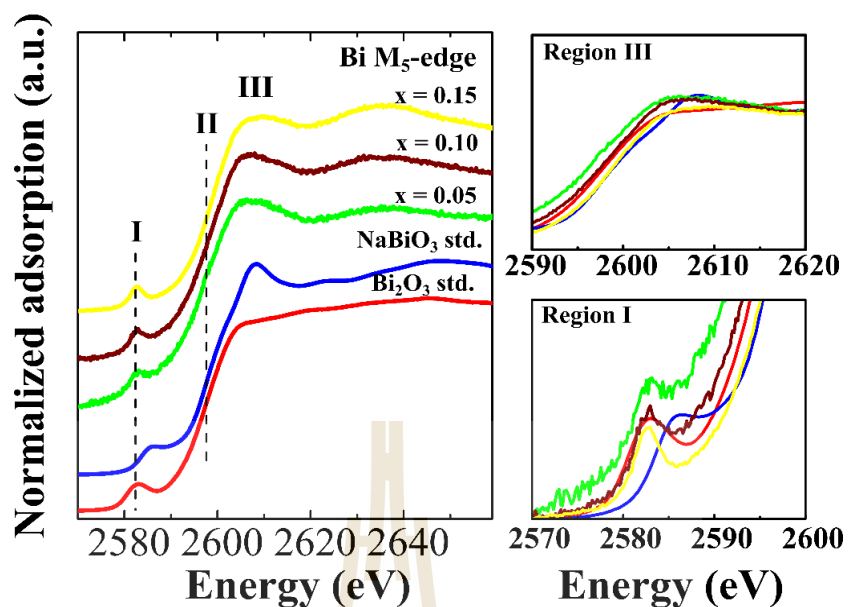


Figure 4.106 The normalized XANES spectra including pre-edge (region I) and white line region (region III) of Bi-doped $\text{Ni}(\text{OH})_2$ samples at Bi M_5 -edge measured in fluorescence mode.

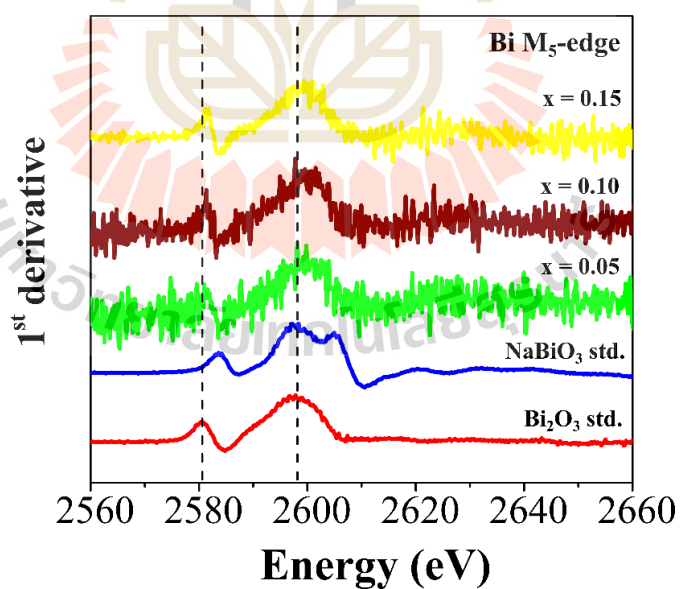


Figure 4.107 The first derivative plots of Bi-doped $\text{Ni}(\text{OH})_2$ at Bi M_5 -edge measured in transmission mode.

4.5.3 Specific surface area and porosity analysis

As mentioned before, the specific surface area and porosity plays significant roles in an electrochemical performance, especially for carbon-based materials. Figure 4.108 (a) shows the N₂ adsorption/desorption isotherms and their corresponding pore size distribution of Bi_xNi_{1-x}(OH)₂ samples. As seen in Figure 4.108, the N₂ isotherm curves present the hysteresis loop at the relative pressure ranging from 0.4 to 1.0 which can be classified as type IV with H3 hysteresis loop according to IUPAC classifications (Nagaraju *et al.*, 2017). The specific surface area (S_{BET}), mean pore diameter (D_{MP}), total pore volume (V_{T}), mesopore diameter (D_{BJH}), mesopore volume (V_{BJH}), and BET particle size (d_{BET}) are given in Table 4.24.

As seen in Table 4.24, the calculated BET specific surface area from the N₂ isotherm was found to be decreased after Bi doping. The higher specific surface area correlates well with the smaller BET particle size (d_{BET}) as calculated by using equation 4.5. One can also see in Table 4.24 is the increase of mean pore diameter (D_{MP}) and the decrease of total pore volume (V_{T}) after Bi doping. The calculated pore size distribution by BJH method in Figure 4.108 (b) shows the wider pore size distribution after Bi doping with the centering of peaks at about 24.49, 51.10, 32.57, and 24.49 nm in samples of $x = 0.00, 0.05, 0.10$, and 0.15 , respectively. This results clearly indicate the decrease of mesopore diameter with increasing Bi contents from 0.05 to 0.15. The difference in the above results is expected for the difference in electrochemical behaviors of Bi_xNi_{1-x}(OH)₂ samples.

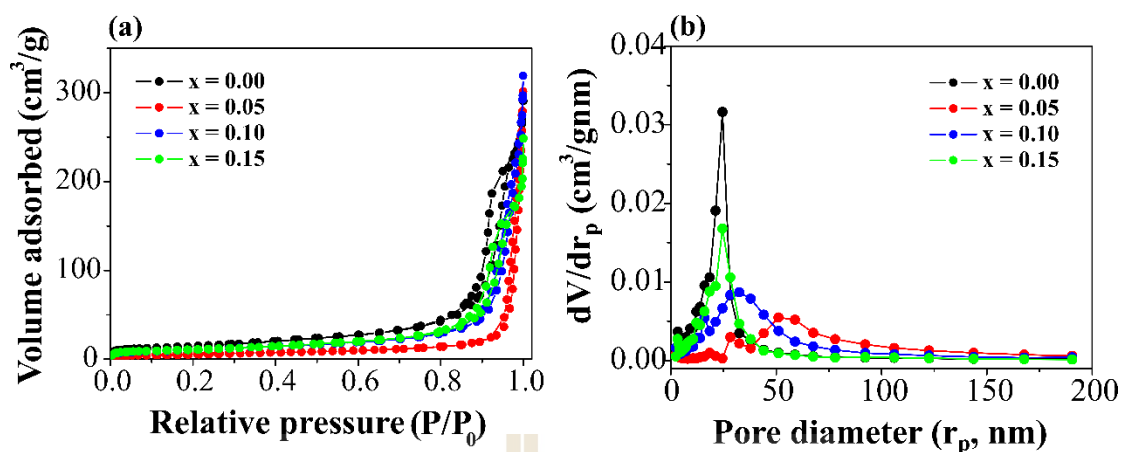


Figure 4.108 (a) N_2 adsorption/desorption isotherm and (b) the pore size distribution of $Bi_xNi_{1-x}(OH)_2$ samples calculated from BET and BJH methods, respectively.

Table 4.24 Specific surface area (S_{BET}), mean pore diameter (D_{MP}), total pore volume (V_T), mesopore diameter (D_{BJH}), mesopore volume (V_{BJH}), and BET particle size (d_{BET}) of $Bi_xNi_{1-x}(OH)_2$ samples.

Sample	S_{BET} (m^2/g)	D_{MP} (nm)	V_T (cm^3/g)	D_{BJH} (nm)	V_{BJH} (cm^3/g)	d_{BET} (nm)
$x = 0.00$	59.799	28.601	0.378	24.49	0.390	25.42
$x = 0.05$	19.879	59.473	0.296	51.10	0.342	76.71
$x = 0.10$	38.939	37.717	0.367	32.57	0.386	39.15
$x = 0.15$	38.346	29.518	0.283	24.49	0.294	39.74

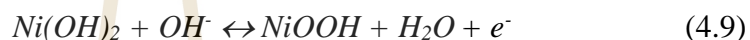
4.5.4 Electrochemical study

Electrochemical performance of the $Bi_xNi_{1-x}(OH)_2$ samples were evaluated in 1M NaOH electrolyte by using three-electrode system. The reference electrode was Ag/AgCl saturated in 3M KCl aqueous electrolyte. The counter electrode was a Pt. plate and the working electrode was the prepared $Bi_xNi_{1-x}(OH)_2$ with $x = 0.00$,

0.05, 0.10, and 0.15 on GDL substrate. Three well-known electrochemical techniques consisting cyclic voltammetry (CV), galvanostatic charge/discharge (GCD), and electrochemical impedance spectroscopy (EIS) were carried out for electrochemical study.

4.5.4.1 Cyclic voltammetry

As shown in Figure 4.109, a pair of redox peaks are observed in $\text{Bi}_x\text{Ni}_{1-x}(\text{OH})_2$ samples, indicating a Faradaic redox reaction. The redox peaks in CV curves are attributed to the following reversible reaction (Nagaraju *et al.*, 2017):



Taking a closer look to the CV curves where the area under CV curve indicates how much charge can store in the materials, larger area under CV curve means higher charge storage (Jia *et al.*, 2018; Singh and Chandra, 2016). Among those samples, it can be noticed that the samples of $x = 0.10$ and $x = 0.15$ possess the larger area under CV curves. These results imply the higher specific capacitance in the samples. The comparison CV curves of $\text{Bi}_x\text{Ni}_{1-x}(\text{OH})_2$ samples at scan rate of 2 mV/s are shown in Figure 4.110. It is clearly seen that after Bi doping the area under CV curves increase and the reduction peaks shift to higher potentials. In general, the potential difference ($\Delta E = E_a - E_c$) between oxidation (E_a) and reduction peaks (E_c) is the measurement of the redox reaction reversibility (Ravikumar *et al.*, 2018). The small is this value, the more reversible is the electrode reaction (Chen, 1999). Due to the substitution of Bi, the potential peak separation is found to be decreased as shown in the (table) inset of Figure 4.110. This behavior suggests that the Bi doping causes a significant development in the oxidation and reduction states reversibility. Note that the oxygen evolution reaction (OER), which is occurred during the charging process, is

also observed at the potential above 0.5 V in all $\text{Bi}_x\text{Ni}_{1-x}(\text{OH})_2$ samples with the actual charge and discharge potential range of 0.0 to 0.55 V.

4.5.4.2 Kinetic analysis of charge storage mechanism

To further understand the charge storage mechanism, it is necessary to perform a kinetic analysis. The relationship between a scan rate and the peak current response observed in CV measurement can be expressed following the equation 3.28. The obtained b -value from the slope of the plot between $\log(i)$ versus $\log(v)$ is generally used to distinguish the charge storage mechanism of the materials. The b -value = 0.5 implies that the current is affected by intercalation/deintercalation or diffusion-controlled mechanism and b -value = 1 indicates that the obtained CV current is due to a capacitive mechanism. As seen in Figure 4.109, the obtained b -values from oxidation and reduction peaks in $\text{Bi}_x\text{Ni}_{1-x}(\text{OH})_2$ samples are between 0.55-0.90. Therefore, it can be concluded that the total charge storage in $\text{Bi}_x\text{Ni}_{1-x}(\text{OH})_2$ samples originates from both capacitive and intercalation/deintercalation or diffusion-controlled mechanisms. By comparing the obtained b -values with Bi content (x) in Figure 4.111, it is clearly seen that the b -values become more prominent in sample of $x = 0.05$ which indicates the more capacitive process is governing.

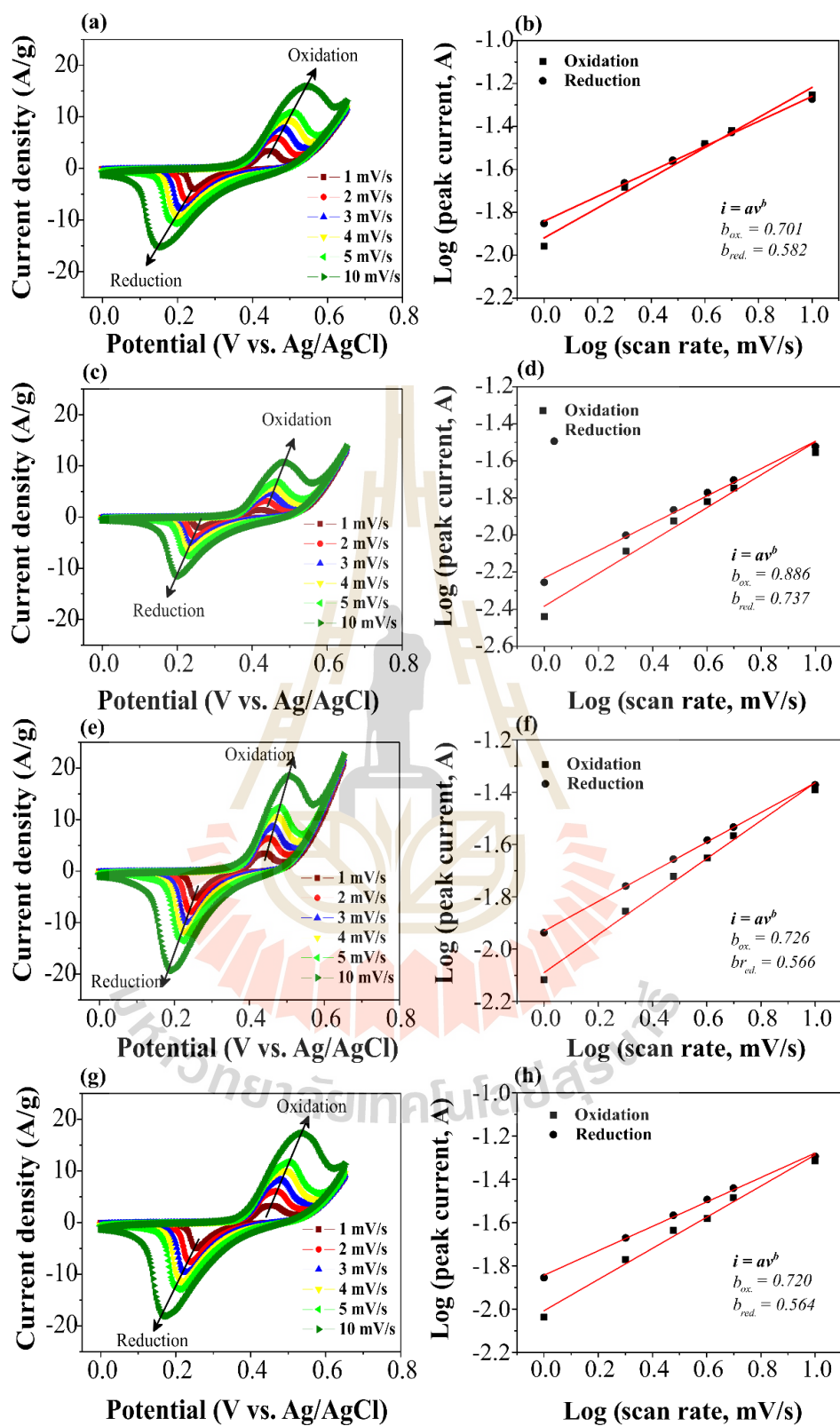


Figure 4.109 (a, c, e, g) CV curves and (b, d, f, h) their scan rate dependent of peaks current of $\text{Bi}_x\text{Ni}_{1-x}(\text{OH})_2$ samples with $x = 0.00, 0.05, 0.10,$ and 0.15 , respectively.

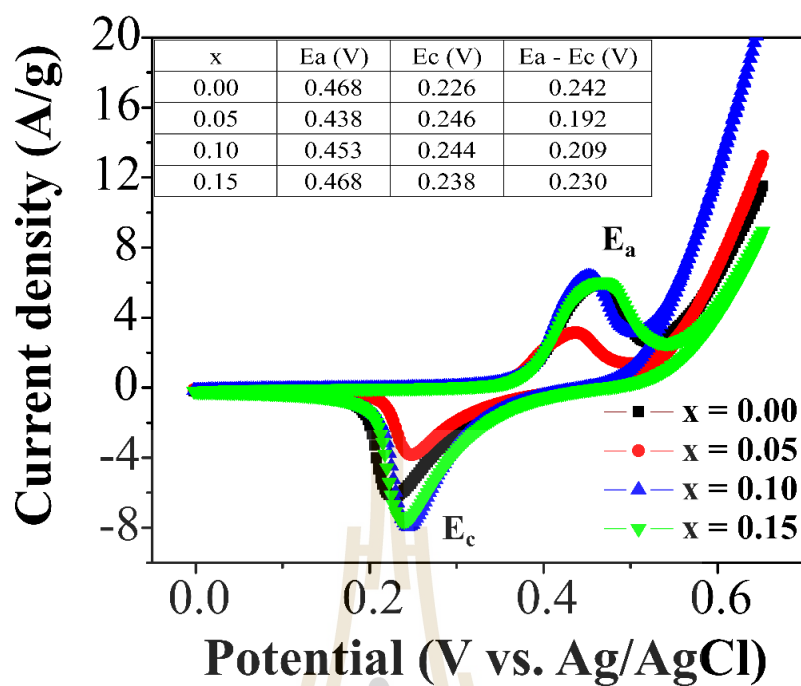


Figure 4.110 Comparison CV curves of $\text{Bi}_x\text{Ni}_{1-x}(\text{OH})_2$ samples at scan rates of 2 mV/s.

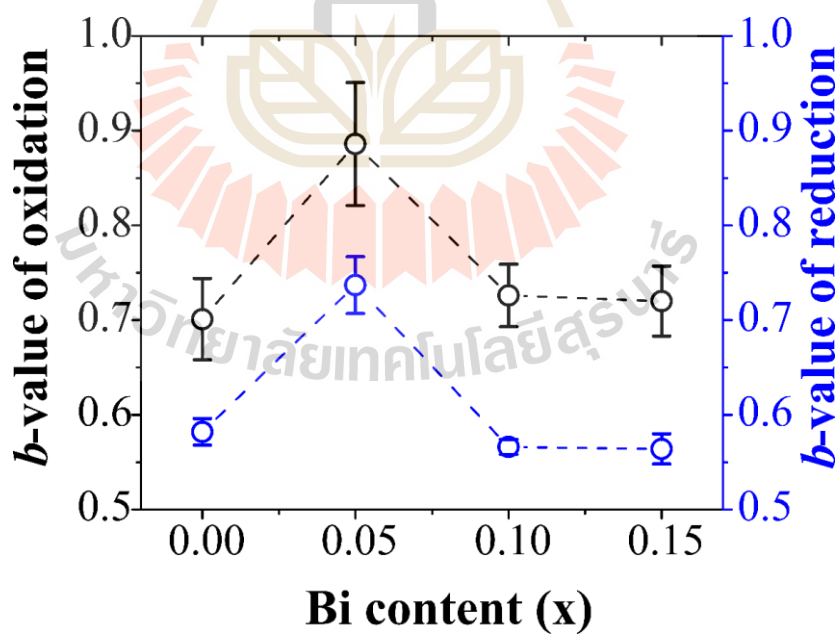


Figure 4.111 Dependence of b-values obtained from oxidation and reduction process as function of Bi content (x).

Furthermore, the total charge storage in electrode from the CV kinetic analysis has been assumed to be the combination of the capacitive and diffusion-controlled mechanism. The contribution from these two charge storage mechanisms can be distinguished according to equation 3.32. As seen in Figure 4.112, it can be also noticed that the intercalation/deintercalation or diffusion-controlled mechanism dominates in sample of $x = 0.10$ and $x = 0.15$ whereas the capacitive mechanism is prominent in samples of $x = 0.00$ and 0.05 . In generally, the higher diffusion-controlled contribution suggests that the higher intercalation/deintercalation of electrolyte ions (i.g. Na^+ , K^+) in the materials (Du *et al.*, 2017). Therefore, the higher specific capacitance value is expected in samples with higher intercalation/deintercalation contribution.

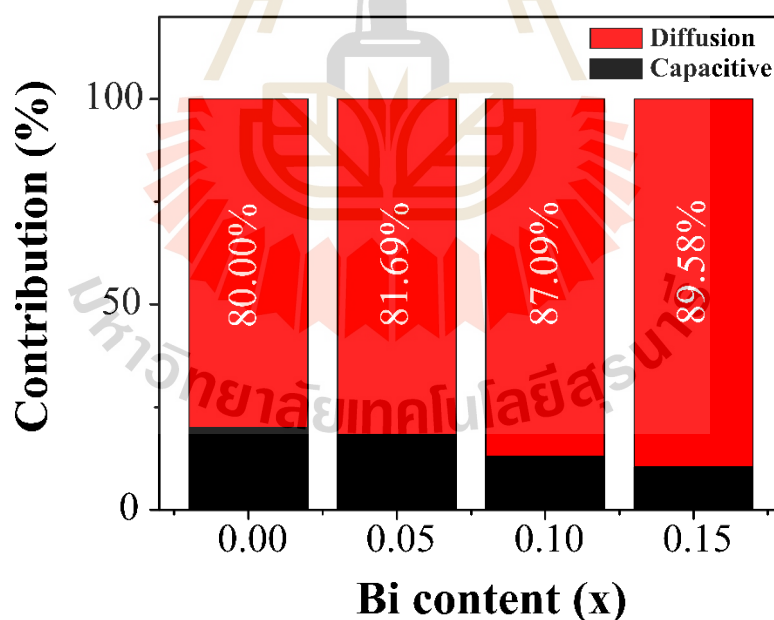


Figure 4.112 The relative contribution of capacitive and diffusion-controlled mechanisms at scan rate of 1 mV/s in $\text{Bi}_x\text{Ni}_{1-x}(\text{OH})_2$ samples.

4.5.4.3 Galvanostatic charge/discharge

As previously presented in section 4.3.3 that the charging and discharging times decrease with increasing current density from 1 to 10 A/g. The comparison GCD curves of $\text{Bi}_x\text{Ni}_{1-x}(\text{OH})_2$ samples at current density of 1 A/g are shown in Figure 4.113. As seen in the Figure, each GCD curve composes of two different curve profiles. The linear profile indicates that the electrode store charge based on adsorption/desorption of the electrolyte ions at the electrode surface while the plateau profile or battery-type behavior implies that the electrode store the charge based on redox reaction or intercalation/deintercalation mechanism (Senthilkumar *et al.*, 2014). As seen in Figure 4.113(a), the longer discharging time is observed after Bi doping indicating that it offers higher specific capacitance value. Besides, GCD curves also represent the voltage drop or IR drop caused by the internal resistance at the beginning of each discharging curve in all Bi-doped $\text{Ni}(\text{OH})_2$ samples. In general, low internal resistance of supercapacitors indicates less energy will be wasted to produce unnecessary heat during charging and discharging processes. As clearly seen in Figure 4.113(b), the higher IR drop values are observed in sample of $x = 0.10$ indicating the higher internal resistance in this sample.

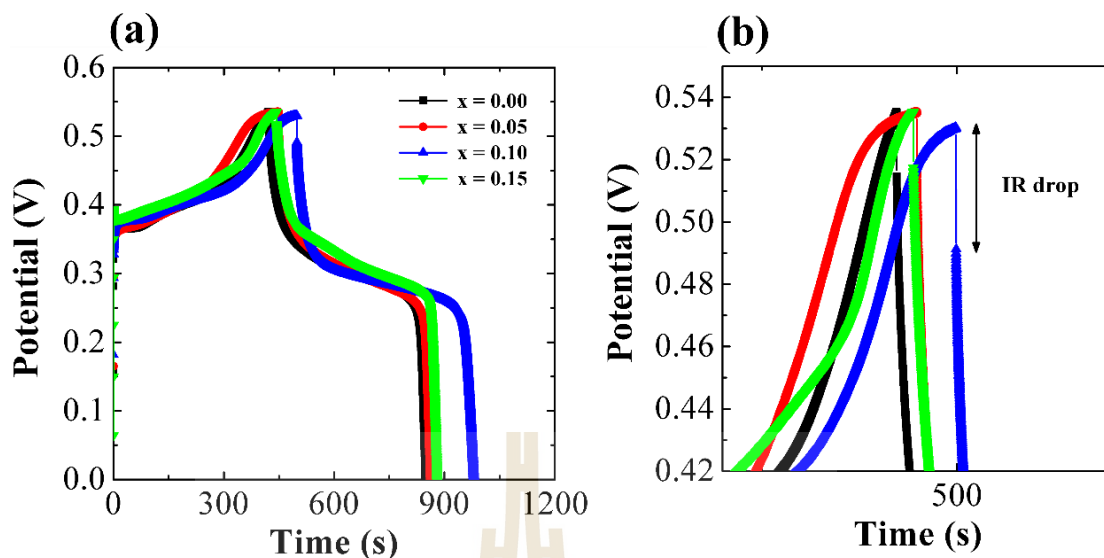


Figure 4.113 (a) Comparison of GCD curves at current density of 1 A/g and (b) their corresponding IR drop of $\text{Bi}_x\text{Ni}_{1-x}(\text{OH})_2$ samples.

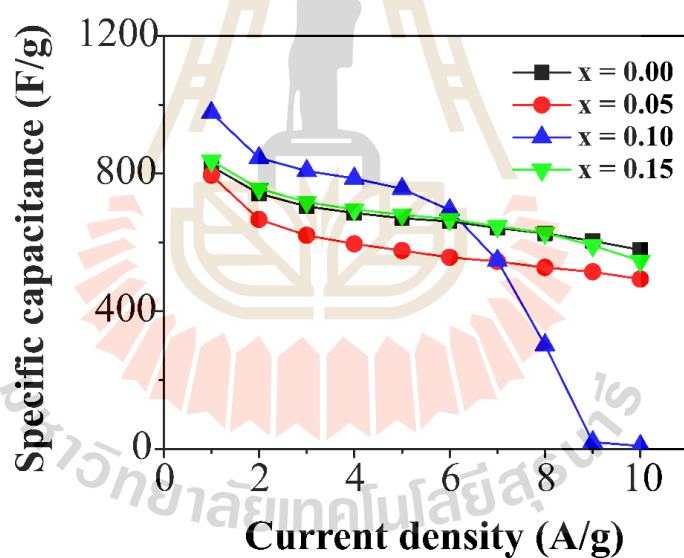


Figure 4.114 The calculated specific capacitance as function of current density in $\text{Bi}_x\text{Ni}_{1-x}(\text{OH})_2$ samples.

The calculated specific capacitance values from the discharging curves of Bi-doped $\text{Ni}(\text{OH})_2$ samples are presented in Figure 4.114. The summarized data obtained from the specific capacitance calculation of $\text{Bi}_x\text{Ni}_{1-x}(\text{OH})_2$ samples are listed in Table 4.25. As seen in the Figure, the highest specific capacitance value at current

density of 1 A/g is observed in sample of $x = 0.10$. One can also see in this sample is that the specific capacitance value sudden decreases at the higher current of 6 A/g. Compared with those of other Bi-doped $\text{Ni}(\text{OH})_2$ samples, the specific capacitance value slightly decrease as the current density increases. The sudden decrease of specific capacitance value might be explained by the larger IR drop in sample of $x = 0.10$ as clearly in Figure 4.113(b). Moreover, the lower specific capacitance values are found to be related to the higher capacitive contributions.

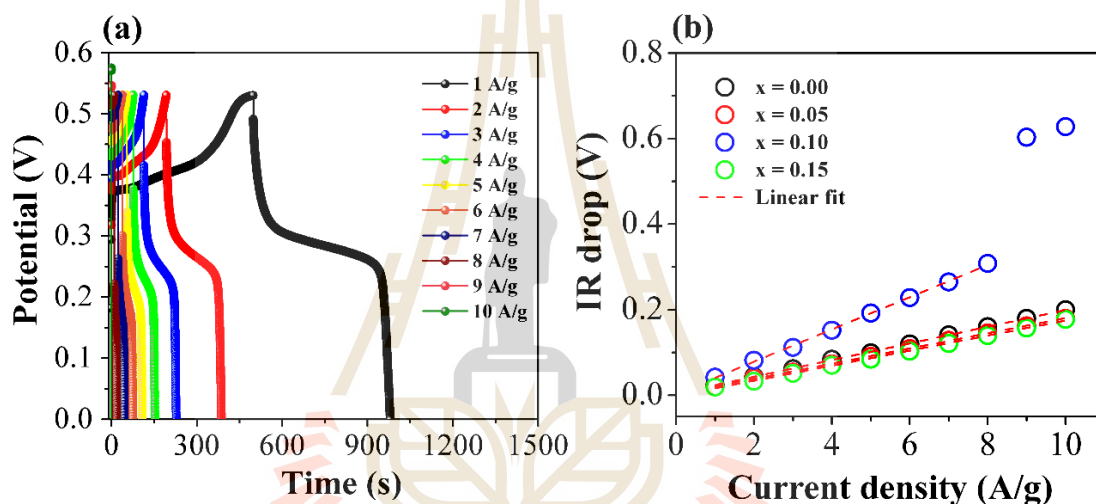


Figure 4.115 (a) The GCD curves of $\text{Bi}_x\text{Ni}_{1-x}(\text{OH})_2$ with $x = 0.10$ at different current densities and (d) the corresponding IR drop of all $\text{Bi}_x\text{Ni}_{1-x}(\text{OH})_2$ samples as function of a current density.

To explore the decrease of specific capacitance value with increasing current density, the plots between IR drop value and current density are presented in Figure 4.115(b). An example GCD plots of Bi-doped $\text{Ni}(\text{OH})_2$ samples with different current densities are presented in Figure 4.115(a). It is clearly seen in Figure 4.115(b) that the IR drop increases with increasing current density indicating the higher internal resistance in the electrodes. Furthermore, the jump of IR drop values at the higher

current density of 8 A/g in sample of $x = 0.10$ leads to the sudden drop of the specific capacitance value from 301.62 F/g (at current density of 8 A/g) to 8.76 F/g (at current density of 10 A/g). Moreover, the slope of the plot between current density and IR drop value has been used to estimate the overall resistance of the capacitors (Stoller and Ruoff, 2010). By using linear fitting, the slope values are found to be 0.020, 0.018, 0.038, 0.018 in samples of $x = 0.00$, 0.05, 0.10, and 0.15, respectively. The higher slope value means the greater the overall resistance of the capacitor. This result suggests that the higher IR drop values can significantly reduce the electrochemical performance of the materials at higher current density.

Table 4.25 The specific capacitance of $\text{Bi}_x\text{Ni}_{1-x}(\text{OH})_2$ samples with various current densities.

Current density (A/g)	Specific capacitance (F/g)			
	$x = 0.00$	$x = 0.05$	$x = 0.10$	$x = 0.15$
1	820.85	795.04	976.83	837.35
2	741.45	666.61	845.69	756.31
3	704.63	620.51	807.51	717.26
4	685.42	596.10	785.74	695.44
5	669.94	576.37	755.99	680.88
6	661.31	556.15	694.02	667.17
7	642.21	544.62	547.03	647.19
8	625.96	526.82	301.62	627.50
9	604.36	514.14	19.57	591.04
10	578.15	493.65	8.76	546.77

4.5.4.4 Electrochemical impedance spectroscopy

To further understand the electrochemical performance of Bi-doped $\text{Ni}(\text{OH})_2$ with different Bi contents of $x = 0.00, 0.05, 0.10$, and 0.15 , electrochemical impedance spectroscopy (EIS) was carried out in the frequency range of 0.1 Hz to 100 kHz at an amplitude of 0.1 V. Nyquist plots of $\text{Bi}_x\text{Ni}_{1-x}(\text{OH})_2$ samples are presented in Figure 4.116. In general, Nyquist plots consist of three main parts of solution resistance (R_s), charge transfer resistance (R_{ct}), and Warburg impedance (Z_w). As seen in Figure 4.116, the decrease of solution resistance (R_s) is clearly observed after Bi doping indicating lower either pore electrolyte or bulk and a contact resistance between the current collector and electroactive material in the electrodes (Li *et al.*, 2015). Furthermore, the observed inclined lines in low frequency region which relate to Na ion diffusivity in the electrode pores and in the host materials (Yang *et al.*, 2016) slight change after Bi doping. Therefore, the above result demonstrates that the addition of Bi reduced the solution resistance.

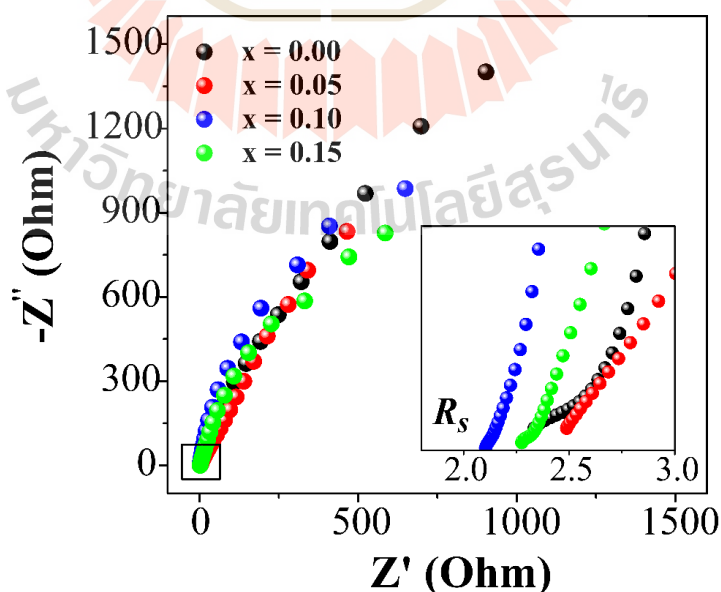


Figure 4.116 Nyquist plots of $\text{Bi}_x\text{Ni}_{1-x}(\text{OH})_2$ samples measured at the frequency range of 0.1 Hz to 100 kHz. Enlarged views showing the solution resistance (R_s).

Table 4.26 The details of solution resistance (R_s), the inclined line angle with x -axis obtained from EIS measurement and the cyclic stability obtained from repeating GCD measurement at current density of 5 A/g for 1000 cycles of $\text{Bi}_x\text{Ni}_{1-x}(\text{OH})_2$ samples.

Sample	R_s (Ohm)	Angle ($^\circ$)	Cyclic stability (%)
$x = 0.00$	2.32	78.38	82.80
$x = 0.05$	2.49	65.55	78.64
$x = 0.10$	2.10	81.02	61.33
$x = 0.15$	2.27	74.77	66.07

4.5.4.5 Cyclic stability

It is well-known that long cycle life of electrochemical capacitors is the crucial parameter for their practical applications. Therefore, the cyclic stability of Bi-doped $\text{Ni}(\text{OH})_2$ was evaluated by repeating GCD measurements at current density of 5 A/g for 1000 cycles. As seen in Figure 4.117, the specific capacitance value retains about 82.80, 78.64, 61.33, and 66.10% of its initial capacitance value after 1000 cycles in sample of $x = 0.00, 0.05, 0.10$, and 0.15 , respectively. The significant observation is that the capacitance value in sample of $x = 0.05$ slight decreases initially from 1st to 100th cycle and then stay almost constant as an extended cycle. Therefore, it might be concluded that the better cyclic stability comes from the higher crystallinity in this sample which is consistent with the literature (Zheng *et al.*, 2017). Whereas the continuously decrease of the capacitance retention due to the lower crystallinity with increasing cycle numbers is observed in sample of $x = 0.10$ and 0.15 . The better cyclic

stability may also be explained by the dominant capacitive mechanism due to the charge storage occurred only at the electrode/electrolyte interface.

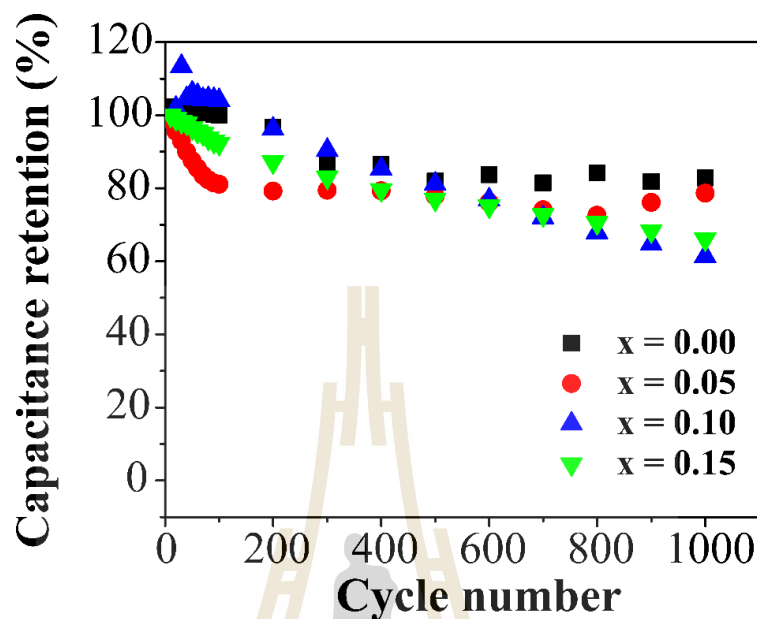


Figure 4.117 The capacitance retention as function of cycle number for $\text{Bi}_x\text{Ni}_{1-x}(\text{OH})_2$ samples measured at current density of 5 A/g for 1000 cycles.

4.5.4.6 Energy density and power density

It is well-known that the performance of energy storage devices is determined by the Ragone plot or the plot between specific power and specific energy. The Ragone plot of Bi doping at current density of 1-8 A/g is shown in Figure 4.118. Among those samples, the sample of $x = 0.15$ dominates both higher specific energy and specific power indicating the improved electrochemical performance. It can be noticed in this figure that the lower specific energy and power are observed in sample of $x = 0.10$ due to the larger IR drop value. Comparing the Ragone plot of Bi doping with the well-known Ragone plot, $\text{Bi}_x\text{Ni}_{1-x}(\text{OH})_2$ samples are suitable for both electrochemical capacitor and battery applications.

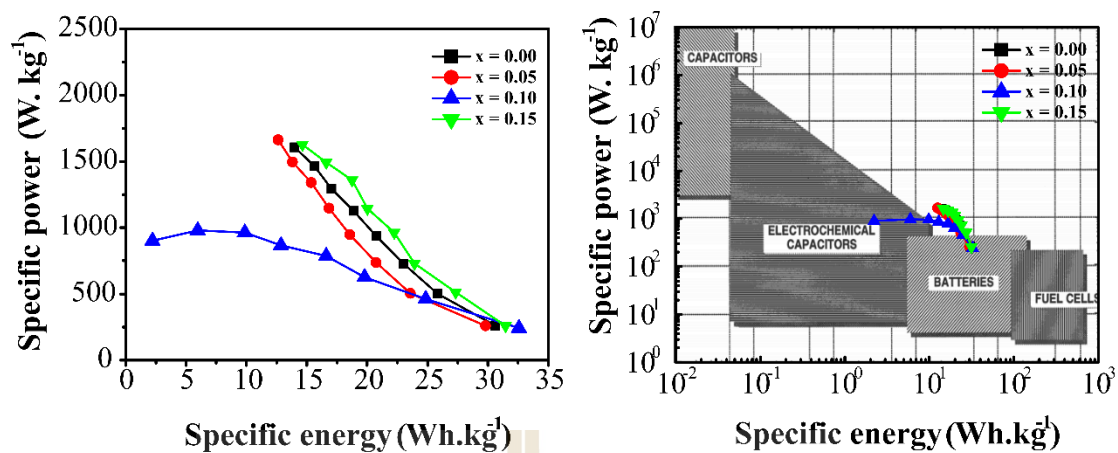


Figure 4.118 (a) The Ragone plot of $\text{Bi}_x\text{Ni}_{1-x}(\text{OH})_2$ samples and (b) the comparison of Ragone plot of $\text{Bi}_x\text{Ni}_{1-x}(\text{OH})_2$ samples with a well-known Ragone plot of Kötz (Kötz and Carlen, 2000).



CHAPTER V

CONCLUSIONS AND SUGGESTIONS

We have successfully synthesized $M_xNi_{1-x}(OH)_2$ (where $M = Mg, Mn, Cu, Zn$, and Bi) nanostructures with $x = 0.00, 0.05, 0.10$, and 0.15 by a hydrothermal method. The crystal structure and morphology were characterized by XRD, SEM, and TEM technique. The chemical compositions and oxidation state were investigated by XPS and XAS. The specific surface area and their porosity were determined by gas absorption technique, comprising BET and BJH methods. The electrochemical studies were investigated by CV, GCD, and EIS techniques. All results are summarized as follows:

5.1 Effect of various electrolytes on electrochemical properties of $Ni(OH)_2$ -based nanostructures

It is well-known that the electrochemical performance of materials is largely dependent on the nature of the electrolyte. Compared the electrochemical performance of $Ni(OH)_2$ in various electrolytes, The results showed that $Ni(OH)_2$ delivered the better electrochemical performance including high specific capacitance, superior cyclic stability, and high energy density in 1M NaOH electrolyte. The possible reasons are summarized as follows: (i) the smaller ionic radius of Na^+ ion the easier intercalated/deintercalated into or out the electrode. (ii) the lower charge transfer

resistance the faster ions transportation. (iii) the presence of thin polymer layers which acted as a glue to hold the electrode materials together.

5.2 Electrochemical studies of $\text{Ni}(\text{OH})_2$ on GDL substrate

In this work, the electrochemical studies of $\text{Ni}(\text{OH})_2$ on GDL substrate are reported owing to the fact that different current collectors resulting in different electrochemical performances. The working electrode of $\text{Ni}(\text{OH})_2$ was successfully prepared by a simple dropping method which was confirmed by XRD and SEM results. Based on the kinetic analysis, the charge storage of $\text{Ni}(\text{OH})_2$ on carbon-type substrate originated from intercalation/deintercalation or diffusion-controlled mechanism. The highest specific capacitance value of $\text{Ni}(\text{OH})_2$ was found to be 418.11 F/g at a current density of 1 A/g within the potential window of 0.55 V. The cyclic stability retained about 81% after 1000 cycles. The separation between the occurrence of new phase and active material of $\text{Ni}(\text{OH})_2$ together with the existence of serve cracks on the electrode surface was proposed to be the main reason for the decrease of the capacitance retention after repeating charge/discharge for 1000 cycles. To improve the long cycle life of $\text{Ni}(\text{OH})_2$ on carbon-type substrate, the electrode preparation need to be optimized in the future work. Therefore, GDL substrate is one of the suitable current collectors for electrochemical studies of Ni-based materials in order to overcome the problem of oxide layer on Ni foam substrate.

5.3 Effects of Mg-doped Ni(OH)₂ on structure and electrochemical properties

In this work, Mg-doped Ni(OH)₂ nanostructures have been successfully prepared by a hydrothermal method. Effects of Mg-doped Ni(OH)₂ on structure and electrochemical properties were studied. The obtained pure phase of hexagonal Ni(OH)₂, the increase in lattice parameter c , and the expansion of unit cell confirm the substitution of smaller ionic radius of Ni²⁺ ions with larger ionic radius of Mg²⁺ ions. The Mg doping was found to have a significant influence on particle size. The reduction of particle size caused the increase of specific surface area. For the electrochemical studies, the increase of interlayer distance which relates to the lattice parameter c after Mg doping does not affect the electrochemical performance of Ni(OH)₂. In contrast, the enhanced electrochemical performance of Ni(OH)₂ may be related to the lattice parameter a which corresponds to the d -spacing of (100) plane. The undoped Ni(OH)₂ delivers the better electrochemical performances including higher specific capacitance value and higher energy density. The possible reasons are (i) the larger d -spacing of (100) plane, (ii) the smaller particle size providing the larger active area, (iii) the better redox reaction reversibility, (iv) the lower charge transferred resistance which promotes the faster ions transportation, and (v) the higher Na ions diffusivity. Owing to the prominent capacitive charge storage mechanism, the small amount of Mg-doping ($x = 0.05$) possess the excellent cyclic stability of about 100% after 1000 cycles. Additionally, Ragone plots of the Mg-doped Ni(OH)₂ samples show the potential applications in electrochemical capacitor and battery.

5.4 Effects of transition metals (Mn, Cu, Zn) doped Ni(OH)₂ on structure and electrochemical properties

In this work, Mn, Cu, Zn-doped Ni(OH)₂ nanostructures have been successfully prepared by a hydrothermal method. Effects of Mn, Cu, and Zn-doped Ni(OH)₂ on structure and electrochemical properties were studied. The obtained pure phase of hexagonal Ni(OH)₂, the change of lattice parameters, and the expansion or shrink of unit cell confirm the substitution of Ni²⁺ ions with various ionic radius of Mn²⁺, Cu²⁺, and Zn²⁺. Based on the experimental results, the Mn, Cu, and Zn doping have a great impact on the morphology and particle size. The smaller particle size is found after Zn doping which is correlated well with the lower charge transfer resistance. In addition, the developing of pores on hexagonal surface created the larger mesopore diameter and total pore volume in the Mn doping which was confirmed by nitrogen gas sorption analysis. On the other hand, the decreased of pore diameter and pore volume indicates the existence of micropore after Cu doping. For the electrochemical studies, the improved capacitance value is related to the higher intercalation/deintercalation or diffusion-controlled contribution. This higher contribution could be explained due to the better reversibility in Zn doping samples. Moreover, the higher capacitance value correlated well with the smaller particle size which provides higher active area. According to the structural analysis, the increased interlayer spacing could not clearly explain the enhancement of the capacitance value in transition metals-doped Ni(OH)₂. Instead, the particle size greatly affects the electrochemical performance of the materials. Interestingly, the existence of microporous structure in the Cu doping improved the cyclic stability which might be explained due to the confining Na ions in

micropores. The Ragone plots of these transition metals-doped $\text{Ni}(\text{OH})_2$ show the potential applications in electrochemical capacitor and battery.

5.5 Effect of Bi-doped $\text{Ni}(\text{OH})_2$ on structure and electrochemical properties

In this work, Bi-doped $\text{Ni}(\text{OH})_2$ nanostructures have been successfully prepared by a hydrothermal method. Effects of Bi-doped $\text{Ni}(\text{OH})_2$ on structure and electrochemical properties were studied. The obtained pure phase of hexagonal $\text{Ni}(\text{OH})_2$, the increase in lattice parameters a and c , and the expansion of unit cell confirm the substitution of smaller ionic radius of Ni^{2+} ions with larger ionic radius of Bi^{3+} ions. TEM images showed that Bi^{3+} doping has a significant effect on the particle size. The smaller particle size related to the higher specific capacitance value. The chemical compositions and oxidation of Bi (3+) were confirmed by XPS and XANES results. Based on the experimental results, the increase of interlayer spacing does not relate to the electrochemical performance of the materials. In contrary, the decrease of particle size and solution resistance plays an important roles in the electrochemical performance of $\text{Ni}(\text{OH})_2$. From the kinetic analysis, it was found that the higher specific capacitance value originated from the higher intercalation/deintercalation or diffusion-controlled contribution. The improved specific capacitance values after Bi doping were observed at the lower current density ($\leq 6 \text{ A/g}$). The increase of specific capacitance value was due to the lower solution resistance. For the cyclic stability, the Bi doping does not improve the long-cycle life because the capacitance retention continuously decreases with extended cycle number. For the applications, the Ragone plots of Bi-

doped Ni(OH)_2 show the potential applications in electrochemical capacitor and battery.

In conclusion of Mg, Mn, Cu, Zn, and Bi-doped Ni(OH)_2 on the structure and electrochemical performances, based on the experimental results, the dopants created the change of lattice parameters and unit cell volume of the host materials because of their dissimilar ionic radius. To promote the intercalation/deintercalation of the electrolyte ions, the interlayer distance was modified by doping with the different ionic radius of Mg^{2+} , Mn^{2+} , Cu^{2+} , Zn^{2+} , and Bi^{3+} ions. The lower ionic radius of Zn^{2+} substitution showed the improvement of specific capacitance value due to the increase of interlayer spacing. Whereas the larger increase of interlayer spacing after substitution with Cu^{2+} does not improve the specific capacitance value. According to the experimental results, there are two approaches to enhance the specific capacitance value of Ni(OH)_2 -based materials. (i) reducing the particle size providing the large active area. (ii) lowering the solution and charge transfer resistance promoting the faster electrolyte ions transportation. Among the various dopants, Cu is regarded as one of the most suitable elements for the improved long-cycle life due to the electrolyte ions confinement in microporous structure. In conclusion, the metals ions-doped Ni(OH)_2 are promising for electrochemical capacitor and battery applications as demonstrated by the Ragone plots.

5.6 Suggestions

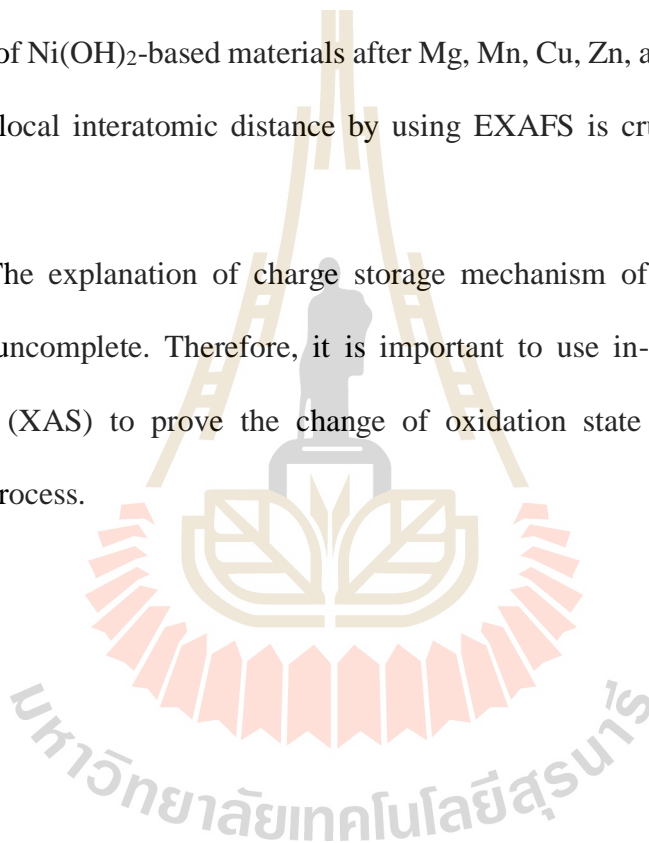
Based on the study of the structure and electrochemical properties of $\text{M}_x\text{Ni}_{1-x}(\text{OH})_2$ (where M = Mg, Mn, Cu, Zn, and Bi) nanostructures with $x = 0.00, 0.05,$

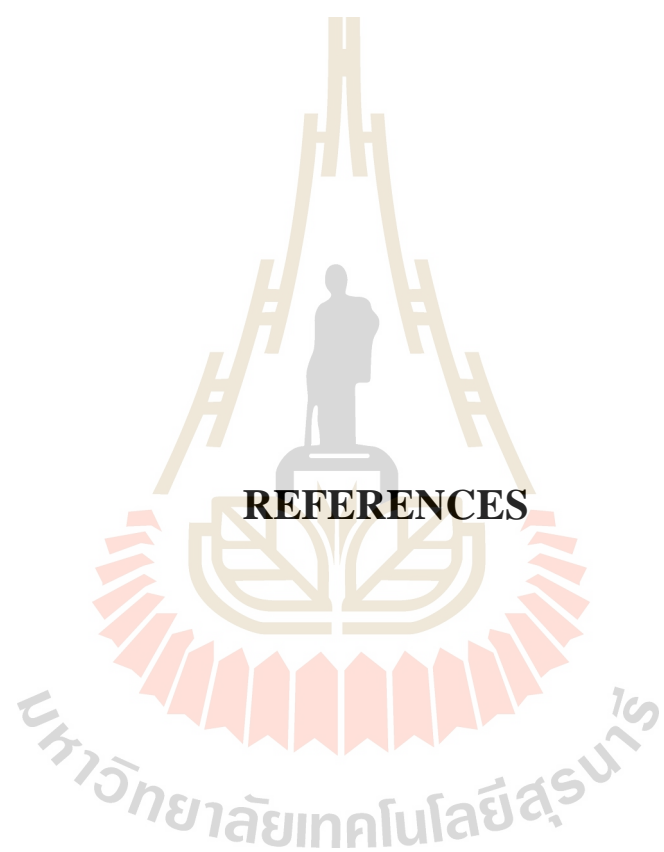
0.10, and 0.15, we have many suggestions for future works to make a clear explanation of the results as list in the followings.

(i) According to the electrochemical studies of pure $\text{Ni}(\text{OH})_2$ on GDL substrate, the electrode preparation on GDL substrate need to be optimized in order to improve the long-cycle life of pure $\text{Ni}(\text{OH})_2$.

(ii) To clearly explain how structural change affected the electrochemical performance of $\text{Ni}(\text{OH})_2$ -based materials after Mg, Mn, Cu, Zn, and Bi substitution, the study of the local interatomic distance by using EXAFS is crucial to have a better understand.

(iii) The explanation of charge storage mechanism of the materials is still unclear and uncomplete. Therefore, it is important to use in-situ X-ray absorption spectroscopy (XAS) to prove the change of oxidation state during charging and discharging process.





REFERENCES

- Arbizzani, C., Beninati, S., Lazzari, M., and Mastragostino, M. (2005). Carbon paper as three-dimensional conducting substrate for tin anodes in lithium-ion batteries. **Journal of Power Sources**. 141: 149-155.
- Ardizzone, S., Fregonara, G., and Trasatti, S. (1990). "Inner" and "outer" active surface of RuO₂ electrodes. **Electrochimica Acta**. 35(1): 263-267.
- Audemmer, A., Delahaye, A., Farhi, R., Sac-Epée, N., and Tarascon, J. M. (1997). Electrochemical and Raman studies of beta-type nickel hydroxides Ni_{1-x}Co_x(OH)₂ electrode materials. **Journal of The Electrochemical Society**. 144(8): 2614-2620.
- Augustyn, V., Simon, P., and Dunn, B. (2014). Pseudocapacitive oxide materials for high-rate electrochemical energy storage. **Energy & Environmental Science**. 7(5): 1597-1614.
- Barrett, E. P., Joyner, L. G., and Halenda, P. P. (1951). The determination of pore volume and area distributions in porous substances. I. computations from nitrogen isotherms. **Journal of the American Chemical Society**. 73: 373-380.
- Becker, H. J. (1957). **Low voltage electrolytic capacitor**. United States Patent Office.
- Béguin, F., Presser, V., Balducci, A., and Frackowiak, E. (2014). Carbons and Electrolytes for Advanced Supercapacitors. **Advanced Materials**. 26: 2219-2251.
- Berghöfer, G., Reinen, D., Akhtar, G., and Hormes, J. (1993). X-ray absorption studies of mixed-valent Bi oxides with perovskite structure. **Modern Physics Letters B**. 7: 1133-1140.

- Bode, H., Dehmelt, K., and Witte, J. (1966). Zur kenntnis der nickelhydroxide electrode-I. Über das nuckel (II)-hydroxidhydrate. **Electrochimica Acta**. 11: 1079-1087.
- Brown, M. A., Fujimori, Y., Ringleb, F., Shao, X., Stavale, F., Sterrer, M., and Freund, H. (2011). Oxidation of Au by surface OH: nucleation and electronic structure of gold on hydroxylated MgO(001). **Journal of the American Chemical Society**. 133(27): 10668-10676.
- Brunauer, S., Emmett, P. H., and Teller, E. (1938). Adsorption of gases in multimolecular layers. **Journal of the American Chemical Society**. 60: 309-319.
- Byrappa, K. (2013). **Handbook of hydrothermal technology A technology for crystal growth and materials Processing**. New York, William Andrew Publishing.
- Chakrabarty, N., and Chakraborty, A. K. (2019). Controlling the electrochemical performance of β -Ni(OH)₂/carbon nanotube hybrid electrodes for supercapacitor applications by La doping: a systematic investigation. **Electrochimica Acta**. 297: 173-187.
- Chapman, D. L. (1913). LI. A contribution to the theory of electrocapillarity. **Philosophical Magazine**. 25(148): 475-481.
- Chaudhari, N. K., Jin, H., Kim, B., and Lee, K. (2017). Nanostructured materials on 3D nickel foam as electrocatalysts for water splitting. **Nanoscale**. 9(34): 12231-12247.
- Chen, J., Bradhurst, D. H., Dou, S. X., and Liu, H. K. (1999). Nickel hydroxide as an active material for the positive electrode in rechargeable alkaline batteries. **Journal of The Electrochemical Society**. 146(10): 3606-3612.

- Chmiola, J., Yushin, G., Gogotsi, Y., Portet, C., Simon, P., and Taberna, P. L. (2006). Anomalous increase in carbon capacitance at pore sizes less than 1 nanometer. **Science**. 313: 1760-1763.
- Chuan-xiang, Z., Rui, Z., Bao-lin, X., Guo, C., and Ying-bo, X. (2010). Effect of pore structure on the electrochemical performance of coal-based activated carbons in non-aqueous electrolyte. **New Carbon Materials**. 25(2): 129-133.
- Conway, B. E. (1999). **Electrochemical supercapacitors scientific fundamental and technological applications**. New York, Kluwer Academic/Plenum Publishers.
- Cuartero, V., Lafuerza, S., Rovezzi, M., Garc, J., Blasco, J., Sub, G., and Jiménez, E. (2016). X-ray absorption and emission spectroscopy study of Mn and Co valence and spin states in $\text{TbMn}_{1-x}\text{Co}_x\text{O}_3$. **Physical Review B**. 94: 1-10.
- Dhillon, S., and Kant, R. (2017). Theory for electrochemical impedance spectroscopy of heterogeneous electrode with distributed capacitance and charge transfer resistance. **Journal of Chemical Sciences**. 129(8): 1277-1292.
- Dinnebier, R. E., and Billinge, S. J. L. (2008). **Powder diffraction theory and practice**. The Royal Society of Chemistry (RSC) Publishing.
- Dong, X., Chen, L., Liu, J., Haller, S., Wang, Y., and Xia, Y. (2016). Environmentally-friendly aqueous Li (or Na)-ion battery with fast electrode kinetics and super-long life. **Science Advances**. 2(1): 1-8.
- Du, D., Lan, R., Xie, K., Wang, H., and Tao, S. (2017). Synthesis of $\text{Li}_2\text{Ni}_2(\text{MoO}_4)_3$ as a high-performance positive electrode for asymmetric supercapacitors. **RSC Advances**. 7(22): 13304-13311.
- Dubal, D. P., Fulari, V. J., and Lokhande, C. D. (2012). Effect of morphology on supercapacitive properties of chemically grown $\beta\text{-Ni}(\text{OH})_2$ thin films.

Microporous and Mesoporous Materials. 151: 511-516.

El-Kharouf, A., Mason, T. J., Brett, D. J. L., and Pollet, B. G. (2012). Ex-situ characterisation of gas diffusion layers for proton exchange membrane fuel cells. **Journal of Power Sources.** 218: 393-404.

Farges, F., Brown, G., Petit, P., and Munoz, M. (2001). Transition elements in water-bearing silicate glasses/melts. Part I. A high-resolution and anharmonic analysis of Ni coordination environments in crystals, glasses, and melts. **Geochimica et Cosmochimica Acta.** 65(10): 1665-1678.

Ferrero, G. A., Fuertes, A. B., and Sevilla, M. (2015). From soybean residue to advanced supercapacitors. **Scientific Reports.** 5(1): 1-13.

Forghani, M., and Donne, S. W. (2018). Method comparison for deconvoluting capacitive and pseudo-capacitive contributions to electrochemical capacitor electrode behavior. **Journal of The Electrochemical Society.** 165(3): A664-A673.

Gaber, A., Abdel- Rahim, M. A., Abdel-Latief, A. Y., and Abdel-Salam, M. N. (2014). Influence of calcination temperature on the structure and porosity of nanocrystalline SnO₂ synthesized by a conventional precipitation method. **International Journal of Electrochemical Science.** 9(1): 81-95.

Gao, J., Shi, S.-Q., and Li, H. (2015). Brief overview of electrochemical potential in lithium ion batteries. **Chinese Physics B.** 25(1): 018210.

Gao, X., Sun, X., Xu, L., Zhang, H., and Liu, G. (2019). Synthesis and electrochemical properties of benzoxazine-based heteroatom-doped carbon materials. **Journal of Materials Research.** 34(07): 1219-1228.

Gao, Y., Sun, G. Q., Wang, S. L., and Zhu, S. (2010). Carbon nanotubes based gas

- diffusion layers in direct methanol fuel cells. **Energy**. 35(3): 1455-1459.
- Ghosh, A., Ghosh, S., Seshadhri, G. M., and Ramaprabhu, S. (2019). Green synthesis of nitrogen- doped self-assembled porous carbon-metal oxide composite towards energy and environmental applications. **Scientific Reports**. 9: 1-13.
- Gore, S. K., Mane, R. S., Naushad, M., Jadhav, S. S., Zate, M. K., Alothman, Z. A., and Hui, B. K. N. (2015). Influence of Bi^{3+} -doping on the magnetic and Mössbauer properties of spinel cobalt ferrite. **Dalton Transactions**. 44(14): 6384-6390.
- Gouy, M. (1910). Constitution of the electric charge at the surface of an electrolyte. **Journal of Physics**. 9: 457-467.
- Grdeń, M., Alsabet, M., and Jerkiewicz, G. (2012). Surface science and electrochemical analysis of nickel foams. **ACS Applied Materials and Interfaces**. 4(6): 3012-3021.
- Gregg, S. J., and Sing, K. S. W. (1982). **Adsorption, surface area and and porosity**. London, Academic Press INC.
- Hall, D. S., Lockwood, D. J., Bock, C., Macdougall, B. R., and Lockwood, D. J. (2015). Nickel hydroxides and related materials : a review of their structures , synthesis and properties. **Proceedings of the Royal Society A: Mathematical, Physical and Engineering Sciences**. 471: 1-64.
- Harding, J. H., Freeman, C. L., and Duffy, D. M. (2014). Oriented crystal growth on organic monolayers. **Crystal Engineering Communication**. 16: 1430-1438.
- He, S., Hu, X., Chen, S., Hu, H., Hanif, M., and Hou, H. (2012). Needle-like polyaniline nanowires on graphite nanofibers: hierarchical micro/nano-architecture for high performance supercapacitors. **Journal of Materials Chemistry**. 22(11): 5114-5120.

- Hu, G., Li, C., and Gong, H. (2010). Capacitance decay of nanoporous nickel hydroxide. **Journal of Power Sources**. 195(19): 6977-6981.
- Huang, J., Lei, T., Wei, X., Liu, X., Liu, T., Cao, D., Yin, J., and Wang, G. (2013). Effect of Al-doped β -Ni(OH)₂ nanosheets on electrochemical behaviors for high performance supercapacitor application. **Journal of Power Sources**. 232: 370-375.
- Huang, Y., Li, Y., Gong, Q., Zhao, G., Zheng, P., Bai, J., Gan, J., Zhao, M., Shao, Y., Wang, D., Liu, L., Zou, G., Zhuang, D., Liang, J., Zhu, H., Nan, C. (2018). Hierarchically mesostructured aluminum current collector for enhancing the performance of supercapacitors. **ACS Applied Materials and Interfaces**. 10(19): 16572-16580.
- Huang, Z., Wang, Z., Zheng, X., Guo, H., Li, X., Jing, Q., and Yang, Z. (2015). Structural and electrochemical properties of Mg-doped nickel based cathode materials $\text{LiNi}_{0.6}\text{Co}_{0.2}\text{Mn}_{0.2-x}\text{Mg}_x\text{O}_2$ for lithium ion batteries. **RSC Advances**. 5(108): 88773-88779.
- Hwang, J. Y., El-Kady, M. F., Li, M., Lin, C. W., Kowal, M., Han, X., and Kaner, R. B. (2017). Boosting the capacitance and voltage of aqueous supercapacitors via redox charge contribution from both electrode and electrolyte. **Nano Today**. 15: 15-25.
- Izadi-Najafabadi, A., Yasuda, S., Kobashi, K., Yamada, T., Futaba, D. N., Hatori, H., Yumura, M., Iijima, S., and Hata, K. (2010). Extracting the full potential of single-walled carbon nanotubes as durable supercapacitor electrodes operable at 4 V with high power and energy density. **Advanced Materials**. 22: 235-241.
- Jahromia, S. P., Pandikumar, A., Goha, B. T., Lima, Y. S., Wan Jeffrey Basirunb, H. N.

- L., and Huang, N. M. (2015). Influence of particle size on performance of nickel oxide nanoparticle-based supercapacitor. **RSC Advances**. 5: 14010-14019.
- Ji, J., Zhang, L. L., Ji, H., Li, Y., Zhao, X., Bai, X., Fan, X., Zhang, F., and Ruoff, R. S. (2013). Nanoporous Ni(OH)₂ thin film on 3D ultrathin-graphite foam for asymmetric supercapacitor. **ACS Nano**. 7(7): 6237-6243.
- Jia, H., Cai, Y., Lin, J., Liang, H., Qi, J., Cao, J., Feng J., and Fei, W. D. (2018). Heterostructural graphene quantum Dot/MnO₂ nanosheets toward high-potential window electrodes for high-performance supercapacitors. **Advanced Science**. 5(5): 1-10.
- Jiang, H., Zhao, T., Li, C., and Ma, J. (2011). Hierarchical self-assembly of ultrathin nickel hydroxide nanoflakes for high-performance supercapacitors. **Journal of Materials Chemistry**. 21(11): 3818-3823.
- Kiani, M. a., Mousavi, M. F., and Ghasemi, S. (2010). Size effect investigation on battery performance: Comparison between micro-and nano-particles of β -Ni(OH)₂ as nickel battery cathode material. **Journal of Power Sources**. 195(17): 5794-5800.
- Koningsberger, D. C., Mojet, B. L., van Dorssen, G. E., and Ramaker, D. E. (2000). XAFS spectroscopy; fundamental principles and data analysis. **Topics In Catalysis**. 10: 143-155.
- Kötz, R., and Carlen, M. (2000). Principles and applications of electrochemical capacitors. **Electrochimica Acta**. 45: 2483-2498.
- Kounaves, S. P. (2015). **Handbook of instrumental techniques for analytical chemistry: Voltammetric techniques**. Prentice Hall.
- Krishnan, S. G., Reddy, M. V, Harilal, M., Vidyadharan, B., Misnon, I. I., Rahim, M.

- H. A., Ismail, J., and Jose, R. (2015). Characterization of MgCo_2O_4 as an electrode for high performance supercapacitors. **Electrochimica Acta**. 161: 312-321.
- Kumar, S., Vikrant, U., Raj, S., Sharma, K., and Singh, G. (2015). High performance, all solid state, flexible supercapacitor based on Ionic liquid functionalized Graphene. **Electrochimica Acta**. 157: 245-251.
- Landers, M., Gräfe, M., Gilkes, R. J., Saunders, M., and Wells, M. A. (2011). Nickel distribution and speciation in rapidly dehydroxylated goethite in oxide-type lateritic nickel ores: XAS and TEM spectroscopic (EELS and EFTEM) investigation. **Australian Journal of Earth Sciences**. 58(7): 745-765.
- Lang, X., Hirata, A., Fujita, T., and Chen, M. (2011). Nanoporous metal/oxide hybrid electrodes for electrochemical supercapacitors. **Nature Nanotechnology**. 6(4): 232-236.
- Lee, E. S., Nam, K. W., Hu, E., and Manthiram, A. (2012). Influence of cation ordering and lattice distortion on the charge-discharge behavior of $\text{LiMn}_{1.5}\text{Ni}_{0.5}\text{O}_4$ spinel between 5.0 and 2.0 V. **Chemistry of Materials**. 24(18): 3610-3620.
- Kim, S. M., Ahn, C-Y., Cho, Y-H., Kim, S., Hwang, W., Jang, S., Shin, S., Lee, G., Sung, Y-E., and Choi, M. (2016). High-performance fuel cell with stretched catalyst-coated membrane: one-step formation of cracked electrode. **Scientific Reports**. 6(1): 1-7.
- Li, B., Ai, M., and Xu, Z. (2010). Mesoporous $\beta\text{-Ni}(\text{OH})_2$: synthesis and enhanced electrochemical performance. **Chemical Communications**. 46(34): 6267-6269.
- Li, D., Gong, Y., Zhang, Y., Luo, C., Li, W., Fu, Q., and Pan, C. (2015). Facile synthesis of carbon nanosphere/ NiCo_2O_4 core-shell sub-microspheres for high performance supercapacitor. **Scientific Reports**. 5: 1-8.

- Li, H. B., Yu, M. H., Wang, F. X., Liu, P., Liang, Y., Xiao, J., Wang C. X., Tong, Y. X., and Yang, G. W. (2013). Amorphous nickel hydroxide nanospheres with ultrahigh capacitance and energy density as electrochemical pseudocapacitor materials. **Nature Communications**. 4: 1-7.
- Li, H., Ma, J., Evans, D. G., Zhou, T., Li, F., and Duan, X. (2006). Molecular dynamics modeling of the structures and binding energies of α -nickel hydroxides and nickel-aluminum layered double hydroxides containing various interlayer guest anions. **Chemistry of Materials**. 18(18): 4405-4414.
- Li, K., Li, S., Huang, F., Lu, Y., Wang, L., Chen, H., and Zhang, H. (2018). Hydrothermally formed three-dimensional hexagon-like P doped Ni(OH)₂ rod arrays for high performance all-solid-state asymmetric supercapacitors. **Applied Surface Science**. 428: 250-257.
- Li, Tao, Gulzar, U., Bai, X., Lenocini, M., Prato, M., Aifantis, K. E., Capiglia, C., and Zaccaria, R. P. (2019). Insight on the failure mechanism of Sn electrodes for sodium-ion batteries: evidence of pore formation during sodiation and crack formation during desodiation. **ACS Applied Energy Materials**. 2(1): 860-866.
- Li, Taotao, Dang, N., Zhang, W., Liang, W., and Yang, F. (2018). Determining the degree of [001] preferred growth of Ni(OH)₂ nanoplates. **Nanomaterials**. 8(12): 1-8.
- Li, W., Xu, K., An, L., Jiang, F., Zhou, X., Yang, J., Chen, Z., Zou, R., and Hu, J. (2014). Effect of temperature on the performance of ultrafine MnO₂ nanobelt supercapacitors. **Journal of Materials Chemistry A**. 2(5): 1443-1447.
- Lindström Henrik, So, S., Solbrand, A., Hjelm, J., Hagfeldt, A., and Lindquist, S. (1997). Li⁺ ion insertion in TiO₂(Anatase). 2. voltammetry on nanoporous films.

Journal of Physical Chemistry B. 2(97): 7717-7722.

Lisdat, F., and Schäfer, D. (2008). The use of electrochemical impedance spectroscopy for biosensing. **Analytical and Bioanalytical Chemistry.** 391(5): 1555-1567.

Liu, F., Chu, X., Zhang, H., Zhang, B., Su, H., Jin, L., Wang, Z., Huang, H., and Yang, W. (2018). Synthesis of self-assembly 3D porous Ni(OH)₂ with high capacitance for hybrid supercapacitors. **Electrochimica Acta.** 269: 102-110.

Liu, G., Zheng, H., Song, X., and Battaglia, V. S. (2011). Particles and polymer binder interaction: a controlling factor in lithium-ion electrode performance. **Journal of The Electrochemical Society.** 159(3): A214-A221.

Liu, H., Zhang, J., Zhang, B., Shi, L., Tan, S., and Huang, L. (2014). Nitrogen-doped reduced graphene oxide-Ni(OH)₂-built 3D flower composite with easy hydrothermal process and excellent electrochemical performance. **Electrochimica Acta.** 138: 69-78.

Liu, J., Wang, J., Xu, C., Jiang, H., Li, C., Zhang, L., and Shen, Z. X. (2018). Advanced energy storage devices: basic principles, analytical methods, and aational materials design. **Advanced Science.** 5(1): 1-19.

Liu, X., Huang, J., Wei, X., Yuan, C., Liu, T., Cao, D., and Wang, G. (2013). Preparation and electrochemical performances of nanostructured Co_xNi_{1-x}(OH)₂ composites for supercapacitors. **Journal of Power Sources.** 240: 338-343.

Liu, Ying, Zhou, J., Chen, L., Zhang, P., Fu, W., Zhao, H., and Xie, E. (2015). Highly flexible freestanding porous carbon nanofibers for electrodes materials of high-performance all-carbon supercapacitors. **ACS Applied Materials and Interfaces.** 7(42): 23515-23520.

Liu, Yonghuan, Wang, R., and Yan, X. (2015). Synergistic effect between ultra-small

nickel hydroxide nanoparticles and reduced graphene oxide sheets for the application in high-performance asymmetric supercapacitor. **Scientific Reports**. 5: 1-12.

Long, J. W., Bélanger, D., Brousse, T., Sugimoto, W., Sassin, M. B., and Crosnier, O. (2011). Asymmetric electrochemical capacitors-Stretching the limits of aqueous electrolytes. **MRS Bulletin**. 36(7): 513-522.

Lu, K., Zhang, J., Wang, Y., Ma, J., Song, B., and Ma, H. (2017). Interfacial deposition of three-dimensional nickel hydroxide nanosheet-graphene aerogel on Ni wire for flexible fiber asymmetric supercapacitors. **ACS Sustainable Chemistry and Engineering**. 5(1): 821-827.

Lu, Z., Chang, Z., Zhu, W., and Sun, X. (2011). Beta-phased Ni(OH)₂ nanowall film with reversible capacitance higher than theoretical Faradic capacitance. **Chemical Communications**. 47(34): 9651-9653.

Lv, B., Liu, Z., Ding, R., Wu, D., and Xu, Y. (2013). Fast production of β -Ni(OH)₂ nanostructures with (001) and (100) plane exposure and their electrochemical properties. **Journal of Materials Chemistry A**. 1(18): 5695.

Mancini, M., Gabrielli, G., Axmann, P., and Wohlfahrt-Mehrens, M. (2016). Electrochemical performance and phase transitions between 1.5 and 4.9 V of highly-ordered LiNi_{0.5}Mn_{1.5}O₄ with tailored morphology: influence of the lithiation method. **Journal of The Electrochemical Society**. 164(1): A6229-A6235.

McCusker, L. B., Dreele, R. B. Von, Cox, D. E., Louer, D., and Scardie, P. (1999). Rietveld refinement guidelines. **Journal of Applied Crystallography**. 32: 36-50.

McEwen, R. S. (1971). Crystallographic studies on nickel hydroxide and the higher

- nickel oxides. **Journal of Physical Chemistry**. 75: 1782-1789.
- Mei, W., Chen, H., Sun, J., and Wang, Q. (2019). The effect of electrode design parameters on battery performance and optimization of electrode thickness based on the electrochemical-thermal coupling model. **Sustainable Energy and Fuels**. 3(1): 148-165.
- Melbourne, P. (1978). A study of ruthenium electrodes by cyclic voltammetry and X-ray emission spectroscopy. **Journal of Electroanalytical Chemistry**. 89: 11-27.
- Meráz, J. S., Fernández, F., and Magaña, L. F. (2005). A method for the measurement of the resistance of electrolytic solutions. **Journal of The Electrochemical Society**. 152(4): E135-E137.
- Merlet, C., Rotenberg, B., Madden, P. A., Taberna, P., Simon, P., Gogotsi, Y., and Salanne, M. (2012). On the molecular origin of supercapacitance in nanoporous carbon electrodes. **Nature Materials**. 11(4): 306-310.
- Mphuthi, N. G., Adekunle, A. S., Fayemi, O. E., Olanikanmi, L. O., and Ebenso, E. (2017). Phthalocyanine doped metal oxide nanoparticles on multiwalled carbon nanotubes platform for the detection of dopamine. **Scientific Reports**. 7: 1-23.
- Nagaraju, G., Cha, S. M., and Yu, J. S. (2017). Ultrathin nickel hydroxide nanosheet arrays grafted biomass-derived honeycomb-like porous carbon with improved electrochemical performance as a supercapacitive material. **Scientific Reports**. 7: 1-11.
- Navarro Pardo, F., Benetti, D., Zhao, H. G., Castaño, V. M., Vomiero, A., and Rosei, F. (2016). Platinum/Palladium hollow nanofibers as high-efficiency counter electrodes for enhanced charge transfer. **Journal of Power Sources**. 335: 138-145.

- Nie, H., Fu, L., Zhu, J., Yang, W., Li, D., and Zhou, L. (2018). Excellent tribological properties of lower reduced graphene oxide content copper composite by using a one-step reduction molecular-level mixing process. **Materials**. 11(4). 1-14.
- Nithya, V. D., Selvan, R. K., Kalpan, D., Vasylechko, L., and Sanjeeviraj, C. (2013). Synthesis of Bi_2WO_6 nanoparticles and its electrochemical properties in different electrolytes for pseudocapacitor electrodes. **Electrochimica Acta**. 109: 720-731.
- Oliva, P., Leonardi, J., Laurent, J. F., Delmas, C., Braconnier, J. J., Figlarz, M., and Guibert, A. de. (1982). Review of the structure and the electrochemistry of nickel hydroxides and oxy-hydroxides. **Journal of Power Sources**. 8(2): 229-255.
- Ozkendir, O. M., and Bozgeyik, M. S. (2010). Electronic structure difference of stoichiometric and off-stoichiometric SBT. **European Physical Journal B**. 76(2): 203-208.
- Pandya, K. I., O'Grady, W. E., Corrigan, D. A., McBreen, J., and Hoffman, R. W. (1990). Extended X-ray absorption fine structure investigations of nickel hydroxides. **Journal of Physical Chemistry**. 94: 21-26.
- Park, J. H., Kim, S., Park, O. O., and Ko, J. M. (2006). Improved asymmetric electrochemical capacitor using Zn-Co co-doped $\text{Ni}(\text{OH})_2$ positive electrode material. **Applied Physics A: Materials Science and Processing**. 82: 593-597.
- Pecharsky, V. K., and Zavalij, P. Y. (2009). **Fundamentals of powder diffraction and structural characterization of materials**. New York, Springer Science & Business Media.
- Qu, Q., Zhang, P., Wang, B., Chen, Y., Tian, S., Wu, Y., and Holze, R. (2010). Electrochemical performance of MnO_2 nanorods in neutral aqueous electrolytes as a cathode for asymmetric supercapacitors. **Journal of Physical Chemistry**.

113: 14020-14027.

Ramesh, A., Jeyavelan, M., and Leo Hudson, M. S. (2018). Electrochemical properties of reduced graphene oxide derived through camphor assisted combustion of graphite oxide. **Dalton Transactions**. 47: 5406-5414.

Ramesh, T. N., and Kamath, P. V. (2008). The effect of cobalt on the electrochemical performance of β -nickel hydroxide electrodes. **Electrochimica Acta**. 53(28): 8324-8331.

Randviir, E. P., and Banks, C. E. (2013). Electrochemical impedance spectroscopy: an overview of bioanalytical applications. **Analytical Methods**. 5: 1098-1115.

Ratcliff, E. L., Meyer, J., Steirer, K. X., Garcia, A., Berry, J. J., Ginley, D. S., and Armstrong, N. R. (2011). Evidence for near-surface NiOOH species in solution-processed NiO_x selective interlayer materials: impact on energetics and the performance of polymer bulk heterojunction photovoltaics. **Chemistry of Materials**. 23: 4988-5000.

Ravikumar, C. R., Kumar, M. R. A., Nagaswarupa, H. P., Prashantha, S. C., Bhatt, A. S., Santosh, M. S., and Kuznetsov, D. (2018). CuO embedded β -Ni(OH)₂ nanocomposite as advanced electrode materials for supercapacitors. **Journal of Alloys and Compounds**. 736: 332-339.

Raymundo-Pinero, E., Azaïs, P., Cacciaguerra, T., Cazorla-Amorós, D., Linares-Solano, A., and Béguin, F. (2005). KOH and NaOH activation mechanisms of multiwalled carbon nanotubes with different structural organisation. **Carbon**. 43(4): 786-795.

Ren, Z., Li, J., Ren, Y., Wang, S., Qiu, Y., and Yu, J. (2016). Large-scale synthesis of hybrid metal oxides through metal redox mechanism for high-performance

- pseudocapacitors. **Scientific Reports**. 6(1): 20021.
- Sankar, K. V., Selvan, R. K., and Meyrick, D. (2015). Electrochemical performances of CoFe_2O_4 nanoparticles and a rGO based asymmetric supercapacitor. **RSC Advances**. 5(121): 99959-99967.
- Sankar, K. V., Surendran, S., Pandi, K., Allin, A. M., Nithya, V. D., and Lee, Y. S. (2015). RSC Advances de-intercalation mechanism of NiMn_2O_4 for high. **RSC Advances**. 5: 27649-27656.
- Senthilkumar, B., Sankar, K. V., Vasylechko, L., Lee, Y.-S., and Selvan, R. K. (2014). Synthesis and electrochemical performances of maricite- NaMPO_4 (M = Ni, Co, Mn) electrodes for hybrid supercapacitors. **RSC Advances**. 4(95): 53192-53200.
- Shanmugavani, A., Kalpana, D., and Selvan, R. K. (2015). Electrochemical properties of CoFe_2O_4 nanoparticles as negative and $\text{Co}(\text{OH})_2$ and $\text{Co}_2\text{Fe}(\text{CN})_6$ as positive electrodes for supercapacitors. **Materials Research Bulletin**. 71: 133-141.
- Shannon, R. D. (1976). Revised effective ionic radii in halides and chalcogenides. **Acta Crystallographica**. A32: 751-767.
- Shao, G., Yao, Y., Zhang, S., and He, P. (2009). Supercapacitor characteristic of La-doped $\text{Ni}(\text{OH})_2$ prepared by electrodeposition. **Rare Metals**. 28(2): 132-136.
- Shao, M., Ning, F., Zhao, Y., Zhao, J., Wei, M., Evans, D. G., and Duan, X. (2012). Core-shell layered double hydroxide microspheres with tunable interior architecture for supercapacitors. **Chemistry of Materials**. 24(6): 1192-1197.
- Sharma, A., Varshney, M., Shin, H. J., Lee, B., Chae, K. H., and Won, S. O. (2017). Effect of Cu insertion on structural, local electronic/atomic structure and photocatalyst properties of TiO_2 , ZnO and $\text{Ni}(\text{OH})_2$ nanostructures: XANES-EXAFS study. **Materials Chemistry and Physics**. 191: 129-144.

- Sim, C. K., Majid, S. R., and Mahmood, N. Z. (2015). Electrochemical performance of activated carbon derived from treated food-waste. **International Journal of Electrochemical Science**. 10(12): 10157-10172.
- Simon, P., and Gogotsi, Y. (2008). Materials for electrochemical capacitors. **Nature Materials**. 7(11): 845-854.
- Singh, A., and Chandra, A. (2016). Enhancing specific energy and power in asymmetric supercapacitors - a synergetic strategy based on the use of redox additive electrolytes. **Scientific Reports**. 6: 1-13.
- Singh, U., Banerjee, A., Mhamane, D., Suryawanshi, A., Upadhyay, K. K., and Ogale, S. (2014). Surfactant free gram scale synthesis of mesoporous Ni(OH)₂-rGO nanocomposite for high rate pseudocapacitor application. **RSC Advances**. 4(75): 39875-39883.
- Son, Y., Park, M., Son, Y., Lee, J. S., Jang, J. H., Kim, Y., and Cho, J. (2014). Quantum confinement and its related effects on the critical size of GeO₂ nanoparticles anodes for lithium batteries. **Nano Letters**. 14(2): 1005-1010.
- Song, Y., Zhou, D., Wang, Y., Wang, C., and Xia, Y. (2013). Preparation of nitrogen-containing mesoporous carbons and their application in supercapacitors. **New Journal of Chemistry**. 37(6): 1768.
- Soserov, L., Boyadzhieva, T., Koleva, V., Girginov, C., Stoyanova, A., and Stoyanova, R. (2017). Effect of the electrolyte alkaline ions on the electrochemical performance of α -Ni(OH)₂/activated carbon composites in the hybrid supercapacitor Cell. **Materials Science inc. Nanomaterials & Polymers**. 2: 6693-6698.
- Stern-Hamburg, H. O. (1924). The theory of the electrolytic double-layer.

ZEITSCHRIFT FOR ELEKTROCHEMIE. 30: 508-516.

Stoller, M. D., Park, S., Zhu, Y., An, J., and Ruoff, R. S. (2008). Graphene-Based Ultracapacitors. **Nano Letters.** 8: 3498-3502.

Stoller, M. D., and Ruoff, R. S. (2010). Best practice methods for determining an electrode material's performance for ultracapacitors. **Energy and Environmental Science.** 3(9): 1294-1301.

Sun, Wei, Wang, Z., Zaman, W. Q., Zhou, Z., Cao, L., Gong, X. Q., and Yang, J. (2018). Effect of lattice strain on the electro-catalytic activity of IrO₂ for water splitting. **Chemical Communications.** 54(8): 996-999.

Sun, Wenping, Rui, X., Ulaganathan, M., Madhavi, S., and Yan, Q. (2015). Few-layered Ni(OH)₂ nanosheets for high-performance supercapacitors. **Journal of Power Sources.** 295: 323-328.

Tang, S., Vongehr, S., Wang, Y., Chen, L., and Meng, X. (2010). Ethanol-assisted hydrothermal synthesis and electrochemical properties of coral-like β -Co(OH)₂ nanostructures. **Journal of Solid State Chemistry.** 183(9): 2166-2173.

Toby, B. H. (2006). R factors in Rietveld analysis : how good is good enough ?. **Powder Diffraction.** 12(1): 67-70.

Trasatti, S., and Buzzanca, G. (1971). Ruthenium dioxide: a new interesting electrode material. Solid state structure and electrochemical behaviour. **Journal of Electroanalytical Chemistry.** 9: A1-A5.

Tsuzuki, T., He, R., Dodd, A., and Saunders, M. (2019). Challenges in determining the location of dopants , to study the influence of metal doping on the photocatalytic activities of ZnO nanopowders. **Nanomaterials.** 9(481): 1-19.

Vijaya Sankar, K., Surendran, S., Pandi, K., Allin, a. M., Nithya, V. D., Lee, Y. S., and

- Kalai Selvan, R. (2015). Studies on the electrochemical intercalation/de-intercalation mechanism of NiMn_2O_4 for high stable pseudocapacitor electrodes. **RSC Advances**. 5(35): 27649-27656.
- Wagner, N., Friedrich, K. A., Park, D., and Ca, N. A. (2016). Novel solvent-free direct coating process for battery electrodes and their electrochemical performance. **Journal of Power Sources**. 306: 758-763.
- Wang, D.-W., Li, F., Liu, M., Lu, G. Q., and Cheng, H. M. (2008). 3D aperiodic hierarchical porous graphitic carbon material for high-rate electrochemical capacitive energy storage. **Angewandte Chemie - International Edition**. 47(2): 373-376.
- Wang, Jian, Zhou, Y., He, M., Wangyang, P., Lu, Y., and Gu, L. (2018). Electrolytic approach towards the controllable synthesis of NiO nanocrystalline and self-assembly mechanism of $\text{Ni}(\text{OH})_2$ precursor under electric, temperature and magnetic fields. **Crystal Engineering Communication**. 20(17): 2384-2395.
- Wang, Jianwei, Zhao, H., Xu, L., Yang, Y., He, G., and Du, Y. (2018). Three-electron redox enabled dithiocarboxylate electrode for superior lithium storage performance. **ACS Applied Materials and Interfaces**. 10(41): 35469-35476.
- Wang, John, Polleux, J., Lim, J., and Dunn, B. (2007). Pseudocapacitive contributions to electrochemical energy storage in TiO_2 (Anatase) nanoparticles. **Journal of Physical Chemistry C**. 111: 14925-14931.
- Wang, Jun, Gao, Z., Li, Z., Wang, B., Yan, Y., Liu, Q., Mann, T., Zhang, M., and Jiang, Z. (2011). Green synthesis of graphene nanosheets/ ZnO composites and electrochemical properties. **Journal of Solid State Chemistry**. 184(6): 1421-1427.

- Wang, Q., Moser, J. E., and Grätzel, M. (2005). Electrochemical impedance spectroscopic analysis of dye-sensitized solar cells. **Journal of Physical Chemistry B**. 109(31): 14945-14953.
- Wang, R., Lang, J., Liu, Y., Lin, Z., and Yan, X. (2015). Ultra-small , size-controlled Ni(OH)_2 nanoparticles : elucidating the relationship between particle size and electrochemical performance for advanced energy storage devices. **NPG Asia Materials**. 7(6): 1-7.
- Wang, X., Mathis, T. S., Li, K., Lin, Z., Vlcek, L., Torita, T., Osti, N. C., Hatter, C., Urbankowski, P., Sarycheva, A., Tyagi., M., Mamontov, E., and Gogotsi, Y. (2019). Influences from solvents on charge storage in titanium carbide MXenes. **Nature Energy**. 4: 241-248.
- Wang, X. W., Zheng, D. L., Yang, P. Z., Wang, X. E., Zhu, Q. Q., Ma, P. F., and Sun, L. Y. (2017). Preparation and electrochemical properties of $\text{NiO-Co}_3\text{O}_4$ composite as electrode materials for supercapacitors. **Chemical Physics Letters**. 667: 260-266.
- Wang, Y., Cao, D., Wang, G., Wang, S., Wen, J., and Yin, J. (2011). Spherical clusters of $\beta\text{-Ni(OH)}_2$ nanosheets supported on nickel foam for nickel metal hydride battery. **Electrochimica Acta**. 56(24): 8285-8290.
- Wei, L., Zhao, S. X., Wu, X., Zhao, S. J., and Nan, C. W. (2018). The existence form and synergistic effect of P in improving the structural stability and electrochemical performance of $\text{Li}_2\text{Mn}_{0.5}\text{Fe}_{0.5}\text{SiO}_4/\text{C}$ cathode materials. **Journal of Materiomics**. 4(3): 179-186.
- Wu, Z., Huang, X., Wang, Z.-L., Xu, J., Wang, H., and Zhang, X. (2015). Electrostatic induced stretch growth of homogeneous $\beta\text{-Ni(OH)}_2$ on graphene with enhanced

- high-rate cycling for supercapacitors. **Scientific Reports**. 4(1): 3669.
- Xiao, X., Song, H., Lin, S., Zhou, Y., Zhan, X., Hu, Z., and Yang, B. (2016). Holey two-dimensional transition metal oxide nanosheets for efficiency energy storage. **Nature Communications**. 7: 1-8.
- Xing, J., Liao, M., Zhang, C., Yin, M., & Song, Y. (2017). The effect of anions on the electrochemical properties of polyaniline for supercapacitors. **Physical Chemistry Chemical Physics**. 19: 14030-14041.
- Xing, W., Qiao, S., Wu, X., Gao, X., Zhou, J., and Zhuo, S. (2011). Exaggerated capacitance using electrochemically active nickel foam as current collector in electrochemical measurement. **Journal of Power Sources**. 196(8): 4123-4127.
- Xiong, X., Ding, D., Chen, D., Waller, G., Bu, Y., Wang, Z., and Liu, M. (2015). Three-dimensional ultrathin $\text{Ni}(\text{OH})_2$ nanosheets grown on nickel foam for High-performance supercapacitors. **Nano Energy**. 11: 154-161.
- Xu, J., Zhang, R., Chen, P., and Ge, S. (2014). Effects of adding ethanol to KOH electrolyte on electrochemical performance of titanium carbide-derived carbon. **Journal of Power Sources**. 246: 132-140.
- Yan, D., Li, Y., Liu, Y., Zhuo, R., Geng, B., Wu, Z., Wang, J., Ren, P., and Yan, P. (2015). Design and influence of mass ratio on supercapacitive properties of ternary electrode material reduced graphene oxide @ MnO_2 @poly(3, 4-ethylenedioxythiophene)-poly (styrene sulfonate). **Electrochimica Acta**. 169: 317-325.
- Yan, J., Sun, W., Wei, T., Zhang, Q., Fan, Z., and Wei, F. (2012). Fabrication and electrochemical performances of hierarchical porous $\text{Ni}(\text{OH})_2$ nanoflakes anchored on graphene sheets. **Journal of Materials Chemistry**. 22(23): 11494-

11502

- Yang, Y., Wang, H., Wang, L., Ge, Y., Kan, K., Shi, K., and Chen, J. (2016). A novel gas sensor based on porous α -Ni(OH)₂ ultrathin nanosheet/reduced graphene oxide composites for room temperature detection of NO_x. **New Journal of Chemistry**. 40(5): 4678-4686.
- Yin, H., and Tang, Z. (2016). Ultrathin two-dimensional layered metal hydroxides: an emerging platform for advanced catalysis, energy conversion and storage. **Chemical Society Reviews**. 45(18): 4873-4891.
- Yoshimura M., B. K. (2008). Hydrothermal processing of materials : past, present and future. **Journal of Materials Science**. 43: 2085-2103.
- Yu, A., Chabot, V., and Zhang, J. (2013). **Electrochemical supercapacitors for energy storage and delivery fundamentals and applications**. New York, Taylor & Francis Group.
- Yu, M., Wang, W., Li, C., Zhai, T., Lu, X., and Tong, Y. (2014). Scalable self-growth of Ni@NiO core-shell electrode with ultrahigh capacitance and super-long cyclic stability for supercapacitors. **NPG Asia Materials**. 6(9): 1-7.
- Yue, X., Pan, J., Sun, Y., and Wang, Z. (2012). Synthesis and electrochemical properties of nano-micro spherical β -Ni(OH)₂ with super high charge-discharge speed. **Industrial and Engineering Chemistry Research**. 51(25): 8358-8365.
- Zequine, C., Ranaweera, C. K., Wang, Z., Singh, S., Tripathi, P., Srivastava, O. N., Gupta, B. K, Ramasamy, K., Kahol, P. K., Dvornic, P. R., Gupta, R. K. (2016). High per formance and flexible supercapacitors based on carbonized bamboo fibers for wide temperature applications. **Scientific Reports**. 6: 1-10.
- Zhang, G., Wang, L., Liu, Y., Li, W., Yu, F., Lu, W., and Huang, H. (2016). Cracks

bring robustness: a pre-cracked NiO nanosponge electrode with greatly enhanced cycle stability and rate performance. **Journal of Materials Chemistry A**. 4(21): 8211-8218.

Zhang, J., Kong, L. B., Cai, J. J., Li, H., Luo, Y. C., and Kang, L. (2010). Hierarchically porous nickel hydroxide/mesoporous carbon composite materials for electrochemical capacitors. **Microporous and Mesoporous Materials**. 132: 154-162.

Zhang, L., and Gong, H. (2015). A cheap and non-destructive approach to increase coverage/loading of hydrophilic hydroxide on hydrophobic carbon for lightweight and high-performance supercapacitors. **Scientific Reports**. 5, 1-11.

Zhang, L. L., & Zhao, X. S. (2009). Carbon-based materials as supercapacitor electrodes. **Chemical Society Reviews**. 38(9): 2520-2531.

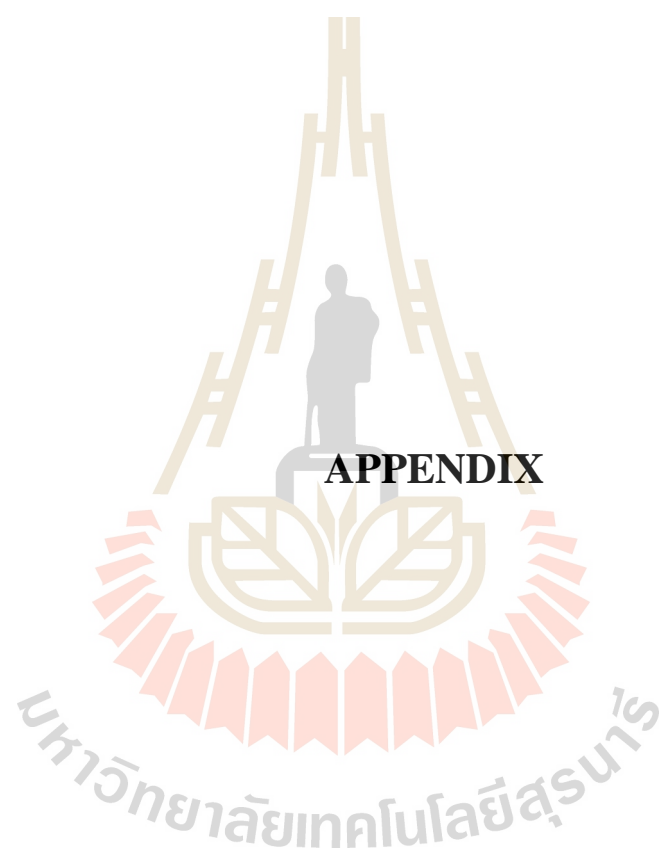
Zhang, Xiaojun, Gu, A., Wang, G., Fang, B., Yan, Q., Hu, J., Zhu, J., Sun, T., Ma, J., and Hng, H. H. (2011). Enhanced electrochemical catalytic activity of new nickel hydroxide nanostructures with (100) facet. **Crystal Engineering Communication**. 13: 188-192.

Zhang, Xiaoyan, Wang, X., Jiang, L., Wu, H., Wu, C., and Su, J. (2012). Effect of aqueous electrolytes on the electrochemical behaviors of supercapacitors based on hierarchically porous carbons. **Journal of Power Sources**. 216: 290-296.

Zhao, C., Zheng, W., Wang, X., Zhang, H., Cui, X., and Wang, H. (2013). Ultrahigh capacitive performance from both $\text{Co}(\text{OH})_2$ /graphene electrode and $\text{K}_3\text{Fe}(\text{CN})_6$ electrolyte. **Scientific Reports**. 3(1): 1-6.

Zhao, D. D., Bao, S. J., Zhou, W. J., and Li, H. L. (2007). Preparation of hexagonal nanoporous nickel hydroxide film and its application for electrochemical

- capacitor. **Electrochemistry Communications**. 9(5): 869-874.
- Zhao, Y., Zhang, X., He, Y., Liu, N., Tan, T., and Liang, C. (2017). Biomass derived nitrogen-doped highly porous carbon material with a hierarchical porous structure for high-performance lithium/sulfur batteries. **Materials**. 10(10): 1-11.
- Zheng, H., Li, H., Yu, M., Zhang, M., Tong, Y., Cheng, F., and Lu, X. (2017). Vertical bismuth oxide nanosheets with enhanced crystallinity: promising stable anodes for rechargeable alkaline batteries. **Journal of Materials Chemistry A**. 5(48): 25539-25544.
- Zhi, M., Xiang, C., Li, J., Li, M., and Wu, N. (2013). Nanostructured carbon-metal oxide composite electrodes for supercapacitors: a review. **Nanoscale**. 5(1): 72-88.
- Zhong, C., Deng, Y., Hu, W., Qiao, J., Zhang, L., and Zhang, J. (2015). A review of electrolyte materials and compositions for electrochemical supercapacitors. **Chemical Society Reviews**. 44(21): 7484-7539.
- Zhou, Q., Cui, M., Tao, K., Yang, Y., Liu, X., and Kang, L. (2016). High areal capacitance three-dimensional Ni@Ni(OH)₂ foams via in situ oxidizing Ni foams in mild aqueous solution. **Applied Surface Science**. 365: 125-130.
- Zhou, T., Cao, Z., Zhang, P., Ma, H., Gao, Z., Wang, H., Lu, Y., He, J., and Zhao, Y. (2017). Transition metal ions regulated oxygen evolution reaction performance of Ni-based hydroxides hierarchical nanoarrays. **Nature Publishing Group**. 7: 1-9.
- Zolotoyabko, E. (2009). Determination of the degree of preferred orientation within the March-Dollase approach. **Journal of Applied Crystallography**. 42(3): 513-518.



APPENDIX

APPENDIX

PUBLICATION AND PRESENTATIONS

A.1 List of publication

Sichumsaeng, T., Chanlek, R., and Maensiri S. (2018). Effect of various electrolytes on the electrochemical properties of Ni(OH)₂ nanostructures. **Journal of Applied Surface Science**. 446: 177-186.

A.2 List of oral presentations

Sichumsaeng, T., Pinitsoontorn, S., and Maensiri, S. (2015). Synthesis, characterization, and magnetic properties of KFeO₂ nanoparticles prepared by a simple egg white solution route. **The 10th International Conference on Surfaces, Coatings and Nanostructured Materials (NANOSMAT Manchester)**. Manchester, United Kingdom.

Sichumsaeng, T., Pinitsoontorn, S., Kidkhunthod, P., Chanlek, N., and Maensiri, S. (2016). Synthesis, characterization and electrochemical properties of KFeO₂ nanoparticles prepared by sol-gel method. **The 5th Thailand International Nanotechnology Conference (Nano Thailand 2016)**. Nakhon Ratchasima, Thailand.

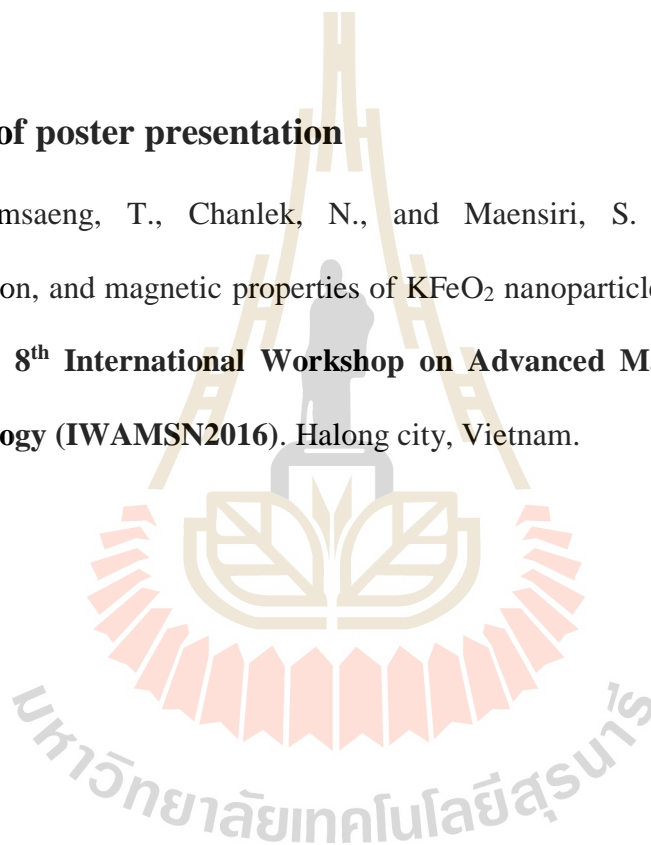
Sichumsaeng, T., Chanlek, N., and Maensiri, S. (2017). Synthesis, characterization, and electrochemical properties of Ni(OH)₂ nanostructures on GDL

substrates. **The First Materials Research Society of Thailand International Conference (1st MRS Thailand International Conference)**. Chiang Mai, Thailand.

Sichumsaeng, T., Chanlek, N., and Maensiri, S. (2017). Effect of various electrolytes on the electrochemical properties of Ni(OH)₂ nanostructures. **The 12th International Conference on Surfaces, Coatings and Nanostructured Materials (NANOSMAT Paris)**. Paris, France.

A.3 List of poster presentation

Sichumsaeng, T., Chanlek, N., and Maensiri, S. (2016). Fabrication, characterization, and magnetic properties of KFeO₂ nanoparticles prepared by sol-gel method. **The 8th International Workshop on Advanced Materials Science and Nanotechnology (IWAMSN2016)**. Halong city, Vietnam.



CURRICULUM VITAE

Name	Miss Thongsuk Sichumsaeng
Date of birth	September 19, 1990
Place of Birth	9 Moo 10, Lam Sai Yong Sub-district, Nang Rong District, Buri Ram, Thailand, 31110
Education	
2013-2019	Ph.D. candidate in Physics School of Physics, Institute of Science, Suranaree University of Technology, Nakhon Ratchasima, Thailand.
2013-2009	B.Sc. in Physics Department of Physics, Faculty of Science, Ubon Ratchathani University, Ubon Ratchathani, Thailand.
Scholarship	
2009-2018	Science Achievement Scholarship of Thailand (SAST)
Research experience	
2018- 2019	Visiting Ph.D. student in Materials by Design group, Institute of Physical Chemistry, Justus-Liebig University of Giessen, Germany.